


Université de Lille

Doctoral School **Sciences de la Matière, du Rayonnement et de l'Environnement (EDSMRE)**

Laboratory **Physique des Lasers, Atomes et Molécules (PhLAM) UMR 8523**

Thesis defended by **Noureddin OSSEIRAN**

Defended on **December 14, 2021**

In order to become Doctor from Université de Lille

Academic Field **Chemistry**

Speciality **Theoretical, physical and analytical chemistry**

Spectroscopic characterization of molecules of atmospheric interest: internal dynamics and microsolvation with hydrogen sulfide (H_2S)

Thesis supervised by

Thérèse HUET	Supervisor
Pascal DRÉAN	Co-Monitor
Manuel GOUBET	Co-Monitor

Committee members

Referees	Isabelle KLEINER	Directrice de recherche at CNRS, Université Paris-Est	
	Pierre ASSELIN	Chargé de recherche HDR at CNRS, UPMC	
Examiners	Denis PETITPREZ	Professeur at Université de Lille	Committee President
	Robert GEORGES	Professeur at Université de Rennes 1	
	Marie-Aline MARTIN	Chargée de recherche at CNRS, Université Paris-Saclay	
Supervisors	Thérèse HUET	Professeure at Université de Lille	
	Pascal DRÉAN	Maître de conférences at Université de Lille	

Colophon

Doctoral dissertation entitled "Spectroscopic characterization of molecules of atmospheric interest: internal dynamics and microsolvation with hydrogen sulfide (H_2S)", written by Noureddin OSSEIRAN, completed on March 15, 2022, typeset with the document preparation system LaTeX and the yathesis class dedicated to theses prepared in France.




Université de Lille

Doctoral School **Sciences de la Matière, du Rayonnement et de l'Environnement (EDSMRE)**

Laboratory **Physique des Lasers, Atomes et Molécules (PhLAM) UMR 8523**

Thesis defended by **Noureddin OSSEIRAN**

Defended on **December 14, 2021**

In order to become Doctor from Université de Lille

Academic Field **Chemistry**

Speciality **Theoretical, physical and analytical chemistry**

Spectroscopic characterization of molecules of atmospheric interest: internal dynamics and microsolvation with hydrogen sulfide (H_2S)

Thesis supervised by

Thérèse HUET	Supervisor
Pascal DRÉAN	Co-Monitor
Manuel GOUBET	Co-Monitor

Committee members

Referees	Isabelle KLEINER	Directrice de recherche at CNRS, Université Paris-Est	
	Pierre ASSELIN	Chargé de recherche HDR at CNRS, UPMC	
Examiners	Denis PETITPREZ	Professeur at Université de Lille	Committee President
	Robert GEORGES	Professeur at Université de Rennes 1	
	Marie-Aline MARTIN	Chargée de recherche at CNRS, Université Paris-Saclay	
Supervisors	Thérèse HUET	Professeure at Université de Lille	
	Pascal DRÉAN	Maître de conférences at Université de Lille	




Université de Lille

École doctorale **Sciences de la Matière, du Rayonnement et de l'Environnement (EDSMRE)**

Laboratoire de **Physique des Lasers, Atomes et Molécules (PhLAM) UMR 8523**

Thèse présentée par **Noureddin OSSEIRAN**

Soutenue le **14 décembre 2021**

En vue de l'obtention du grade de docteur de l'Université de Lille

Discipline **Chimie**

Spécialité **Chimie théorique, physique, analytique**

Caractérisation spectroscopique de molécules d'intérêt atmosphérique : dynamique interne et microsolvatation avec le sulfure d'hydrogène (H_2S)

Thèse dirigée par	Thérèse HUET	Directrice
	Pascal DRÉAN	co-encadrant
	Manuel GOUBET	co-encadrant

Composition du jury

Rapporteurs	Isabelle KLEINER	Directrice de recherche au CNRS, Université Paris-Est	
	Pierre ASSELIN	Chargé de recherche HDR au CNRS, UPMC	
Examinateurs	Denis PETITPREZ	Professeur à l'Université de Lille	président du jury
	Robert GEORGES	Professeur à l'Université de Rennes 1	
	Marie-Aline MARTIN	Chargée de recherche au CNRS, Université Paris-Saclay	
Directeurs de thèse	Thérèse HUET	Professeure à l'Université de Lille	
	Pascal DRÉAN	Maître de conférences à l'Université de Lille	

This thesis has been prepared at

Physique des Lasers, Atomes et Molécules (PhLAM) UMR 8523

Bâtiment P5 campus Cité Scientifique
2 Avenue Jean Perrin
59655 Villeneuve d'Ascq cedex
France

☎ +33 (0)3 20 43 49 82
✉ marc.douay@univ-lille.fr
Web Site https://phlam.univ-lille.fr/

There are sadistic scientists who hurry to hunt down errors instead of establishing the truth.

Marie Curie

Dedication makes dreams come true.

Kobe Bryant

Spectroscopic characterization of molecules of atmospheric interest: internal dynamics and microsolvation with hydrogen sulfide (H_2S)

Abstract

Biogenic volatile organic compounds (BVOCs), and especially monoterpenes ($C_{10}H_{16}$), are molecules naturally occurring in the atmosphere, which have been linked to the formation of secondary organic aerosol (SOA). They can alter the physical and chemical properties in the atmosphere, have negative effects on human health and contribute to climate change. There exists a strong relationship between the structure of a molecular system and the inter- and intramolecular interactions present on the molecular scale. Hence, having in-depth information about the gas phase structure and internal dynamics of these molecules, or their molecular complexes, is important to better understand their reaction pathways and complexation patterns.

The synergic combination of quantum chemical calculations and Fourier transform microwave (FTMW) spectroscopy has been shown to be a reliable approach to examine the conformational landscape, structure and internal dynamics of several types of molecules of atmospheric interest, their oxidation products and their complexes.

In the framework of this thesis, we have applied this theoretical-experimental approach to characterize the complexes of two monoterpenoids: fenchol ($C_{10}H_{18}O$) and fenchone ($C_{10}H_{16}O$) with another atmospheric contaminant: the H_2S molecule. The gas phase stable conformations were identified in the pure rotational spectrum with the support of *ab initio* and DFT calculations. A comparative analysis of the observed complexes with their water analogues confirmed the presence of weaker hydrogen bonds. On top of that, we observed a large amplitude motion, that was qualitatively described. The stabilizing non-covalent interactions of the two complexes were also evaluated.

In a similar manner, and within the same general context, we also characterized the conformational landscape and methyl internal rotation in the case of limona ketone ($C_9H_{14}O$), which is a BVOCs originating from the oxidation of limonene. The experimental barrier height of the methyl torsion showed some deviation from the calculated values, which pushed towards a more thorough examination, that revealed the presence of an intramolecular interaction.

The second part of this thesis was dedicated to the construction and evaluation of a broadband chirped pulse FTMW spectrometer, operating in the range 6-18 GHz. A detailed technical description of the spectrometer is given herein. Moreover, the preliminary tests performed to evaluate the performance of the spectrometer are reported.

Keywords: rotational spectroscopy, quantum chemical calculations, microsolvation, large amplitude motions, chirped-pulse fourier transform microwave spectrometer

Physique des Lasers, Atomes et Molécules (PhLAM) UMR 8523
Bâtiment P5 campus Cité Scientifique – 2 Avenue Jean Perrin – 59655 Villeneuve d'Ascq cedex – France

Caractérisation spectroscopique de molécules d'intérêt atmosphérique : dynamique interne et microsolvatation avec le sulfure d'hydrogène (H_2S)

Résumé

Les composés organiques volatils biogéniques (COVBs), et en particulier les monoterpènes ($C_{10}H_{16}$), sont des molécules naturellement présentes dans l'atmosphère, qui sont liées à la formation d'aérosols organiques secondaires (SOA). Ils peuvent altérer les propriétés physiques et chimiques de l'atmosphère, avoir des effets négatifs sur la santé humaine et contribuer aux changements climatiques. Une forte relation existe entre la structure d'un système moléculaire et les interactions inter- et intramoléculaires présentes à l'échelle moléculaire. Par conséquent, l'accès aux informations sur la structure, en phase gazeuse, et à la dynamique interne pourrait être essentiel pour prédire les voies possibles de réaction ou de la formation de complexes et d'agrégats.
La spectroscopie micro-ondes à transformée de Fourier (FTMW) combinée aux calculs de chimie quantique, est une approche fiable pour étudier le paysage conformationnel, la structure et la dynamique interne de plusieurs types des molécules, et notamment les molécules d'intérêt atmosphérique, leurs produits d'oxydation et leurs complexes associés.
Dans le cadre de cette thèse, nous avons appliqué cette approche théorique-expérimentale pour caractériser les complexes de deux monoterpénoïdes : le fenchol ($C_{10}H_{18}O$) et la fenchone ($C_{10}H_{16}O$) avec un autre contaminant atmosphérique, à savoir le H_2S. Les conformations stables en phase gazeuse ont été identifiées dans le spectre de rotation pure à l'aide des calculs *ab initio* et DFT. Une analyse comparative des complexes observés avec leurs analogues hydratés a confirmé la présence d'une liaison hydrogène plus faible. De plus, nous avons observé un mouvement de grande amplitude, décrit qualitativement. Les interactions non covalentes stabilisantes des deux complexes ont également été évaluées.
De manière similaire, et dans le même contexte général, nous avons également caractérisé le paysage conformationnel et la rotation interne du groupe méthyle dans le cas de la limona cétone ($C_9H_{14}O$), qui est un CVOB issu de l'oxydation du limonène. La hauteur de barrière expérimentale de la torsion du méthyle a montré un certain écart par rapport aux valeurs calculées, ce qui nous a poussé vers une investigation plus approfondie, qui a révélé la présence d'une interaction intramoléculaire.
La deuxième partie de cette thèse a été consacrée à la construction et à l'évaluation d'un nouveau spectromètre FTMW à dérive de fréquence, large bande (6-18 GHz). Une description technique détaillée du spectromètre est donnée dans ce manuscrit. De plus, les tests préliminaires effectués pour évaluer les performances du spectromètre sont rapportés.

Mots clés : spectroscopie rotationnelle, calculs de chimie quantique, microsolvatation, mouvements de grande amplitude, spectromètre par dérive de fréquence à transformée de fourier

ACKNOWLEDGMENTS

This thesis couldn't have taken place without the financial support of Université de Lille and Région Hauts-de-France. Also, I appreciate the financial contributions from the Labex Cappa project as well as the CPER Climibio.

I would like to thank everybody who helped realize this work.

First of all, I would like to express my deepest gratitude to my supervisor Prof. Therese HUET, who gave me the opportunity to be a part of this very interesting project. I appreciate the time she dedicated to help me during the last three years, and the priceless advice. It was a pleasure to learn from and work with this extraordinary person.

I am grateful to my colleagues and team members from whom I gained knowledge that will remain with me all my life. Thank you Dr. Pascal DRÉAN for the nice ambiance you set in the lab, your funny jokes and for helping me at the beginning of my thesis. An enormous THANK YOU for Dr. Manuel GOUBET 'MANU!' for all the interesting discussions, the big technical experience I gained learning from you and of course all the funny expressions! Merci beacoup MANU! Thank you Jordan Claus for the fun moments and interesting discussions we had in the lab. Also, I would like the thank all the SPECTRO group members that I didn't mention by name, and with whom I had very interesting conversations. I can't forget as well the effort made by the technicians of the electronic and mechanical workshops in PhLAM laboratory, to troubleshoot and resolve the technical problems that occurred during the last years.

I would like to express my sincere gratitude to Dr. Isabelle KLEINER and Dr. Pierre ASSELIN for accepting to review this work, as well as to Pr. Robert GEORGES and Dr. Marie-Aline MARTIN-DRUMEL for accepting to be members of the PhD committee and to evaluate my work. A very deep and sincere thank you to Prof. Denis PETITPREZ for accepting to be the president of the jury, and who is one of the main reasons I pursued this career path in research related to atmospheric chemistry. He was responsible for the Labex Cappa Master program "atmospheric environment", which was a very fruitful learning experience. I am honored to have met and learned from this amazing man.

My sincere and deep gratitude to my colleagues and very dear friends Dr. Elias NEEMAN and Dr. Celina BERMUDEZ. The discussions that we had were very

interesting and fruitful, and I have learned a lot from these two incredible people. They were very supportive and their presence added a dynamic and comforting ambiance to the lab. Merci beacoup Elias for everything! Muchas Gracias Celina!

A big and sincere Thank you to Mohammad HELLANI, one of the closest and dear people in my life. It was a long and nice journey, and it was nice to have someone like you along the way. Thank you for all the support and encouragement throughout these years. I really appreciate all the experiences and memories that we have been through. I would like also to thank my dear friends Joelle AL ASEEL and Marwa SAAB for their support and all the enjoyable moments we had, which always lifts my spirits and drop any stress. I would like to thank my friends Ali HELLANI, Wissal ADHAMI, Ahmed CARACALLA, and Ali QAIS with whom I spend a wonderful time, despite the long distances.

I can't imagine passing through this experience without the presence of my beloved fiancée Siveen THLAIJEH. I am extremely grateful for the unconditional love, and for the endless motivation and encouragement you give me. Thank you for being my support through hard times and for your patience. I am thankful for your being there whenever I needed you. I am glad that we went through this experience together. Thank you for your presence to celebrate every achievement. I believe that you are the reason behind all the success that I achieved and will achieve. Looking forward to much more success together.

Last but not least, I believe there are not enough words that can express my deep and sincere gratitude for my family. My father Maher, my mother Shereen, my sister Reem and my brothers Mahdi and Samer, you have always been my backbone. Your sacrifices and your unconditional love are what pushed me this far. You were always by my side and helped me pursue my dreams. You believed in me and gave me all that I needed to thrive. I am forever grateful for everything you did for me.

ACRONYMS

AWG arbitrary waveform generator. 6, 84, 85, 89–92

BVOCs biogenic volatile organic compounds. ix, 2–5, 7, 8, 79, 127

. ix

CAM combined axis method. 135, 142

CP-FTMW chirped-pulse Fourier transform microwave. 82, 83, 85

DFT density functional theory. 38

EDA energy decomposition analysis. 122

FFT fast Fourier transform. 61, 63, 64, 87

FID free induction decay. 61, 65, 66, 85, 87–89, 98

FP-FTMW Fabry-Perot Fourier transform microwave. 62, 84, 101, 128, 146

FSR free spectral range. 69

FTMW Fourier transform microwave. ix, x, 1

FWHM full width half maximum. 79

LFP linear fast passage. 62, 63, 93

LNA low noise amplifier. 85, 87

NBO natural bonding orbitals. xiv, 118–120, 125, 147

NCI non covalent interactions. xiv, 102, 107–109, 117, 118, 121, 122, 125, 147

PES Potential Energy Surface. xiv, 51, 52, 115, 116, 128–130, 132, 138–142, 147, 148

QST2 quadratic synchronous transit. 52, 129

RADAR radio detection and ranging. 5

RAP rapid adiabatic passage. 62, 63, 93, 94

RF radio frequency. 7, 84, 89

RWA rotating wave approximation. 59, 61

S/N signal-to-noise ratio. 87, 90, 93, 95, 98, 146

SAPT Symmetry-adapted perturbation theory. xiv, 102, 118, 122–125, 147

SOA secondary organic aerosol. ix, 2, 3, 127, 128, 147

TS transition state. 52

TWTA travelling wave tube amplifier. 84–87, 89, 92, 93

VOC volatile organic compounds. 2

ZPE zero point energy. 103, 110, 111, 131, 132

CONTENTS

CHAPTER

ONE

GENERAL INTRODUCTION

The subject of the present thesis is to study molecules and molecular complexes of atmospheric interest using FTMW spectroscopy supported by theoretical computational methods. I will describe shortly in the present chapter the general aspects related to atmospheric chemistry, and then the present work in the field of physical chemistry. Finally, the structure of the manuscript will be given.

1.1 Atmosphere

The earth's atmosphere, by definition, is the layers of gases surrounding the terrestrial body. These gases can be major constituents such as nitrogen and oxygen, or some other gaseous traces like water vapor and carbon dioxide. The gases surrounding the earth are classified into five layers that are characterized by their temperature and pressure. The atmosphere plays a vital role in maintaining life on earth, by absorbing the har mful ultraviolet radiation from the sun through ozone that is concentrated in the stratosphere (second) layer. Also, it keeps the planet warm by insulating it and reflecting the heat generated by the surface. Furthermore, it prevents diurnal temperature variation. The troposphere (first) layer of the atmosphere is where most life concerning phenomena takes place, such as weather fluctuations and wind movements. In addition, this layer contains organic and inorganic compounds in trace amounts, apart from CO_2 and H_2O, that can

significantly alter several physical and chemical atmospheric processes.

Volatile organic compounds (VOC) are generally defined by being carbon compounds that are volatile at room temperature, and more specifically compounds that have a vapor pressure greater than 0.01 kPa at 293.15 K [1]. Usually, methane is excluded from this class of molecules due to its low reactivity, and to the fact that it is not toxic. The sources of VOCs emission into the atmosphere can be natural or due to anthropogenic activities, with the vegetation being the major contributor with more than 90 % of the total VOC emissions [2]. The VOCs coming from vegetation are usually called biogenic volatile organic compounds (BVOCs). Their annual emissions are estimated to be about 760 Tg(C) /year [3]. Despite their presence in trace concentrations, BVOCs can have a significant influence on the chemistry and physics of the atmosphere. The oxidation of BVOCs by ozone O_3, hydroxyl $OH^{\bullet}$ radicals or nitrate $NO_3^{\bullet}$ radicals give rise to oxygen containing molecules[4–6]. BVOCs and their oxidation products facilitate the growth of freshly nucleated species, or condense into existing particles [6], hence providing evidence for their contribution to secondary organic aerosol (SOA) formation.

Aerosols are airborne suspended solid and liquid particles, of various sizes and forms. They are composed of organic material and may include inorganic oxides. Aerosols are either emitted directly into the atmosphere, in which case they are called primary aerosols, or originate starting from gaseous organic compounds, thus called SOA. The aerosols, in general, are grouped in two main categories depending on their size: the first called PM_{10} corresponding to particulate matter with a diameter less than 10 µm, and $PM_{2.5}$ corresponding to particulate matter with a diameter less than 2.5 µm. Aerosols have been the center of extensive research over the last two decades, because of their influence on climate and human health. They are capable of absorbing thermal and solar radiation, thus affecting the atmospheric radiation forcing[7]. They also have been linked to several diseases and premature mortality [8, 9]. The mechanisms leading to the formation of SOA are still not definitive, and some of them are not clearly explained. The research about aerosols and their properties has been a hot topic, with different techniques being used to characterize and quantify them.

A general scheme showing natural and anthropogenic sources of BVOCs and aerosols, as well as some other trace gases or molecules that can be of interest, is

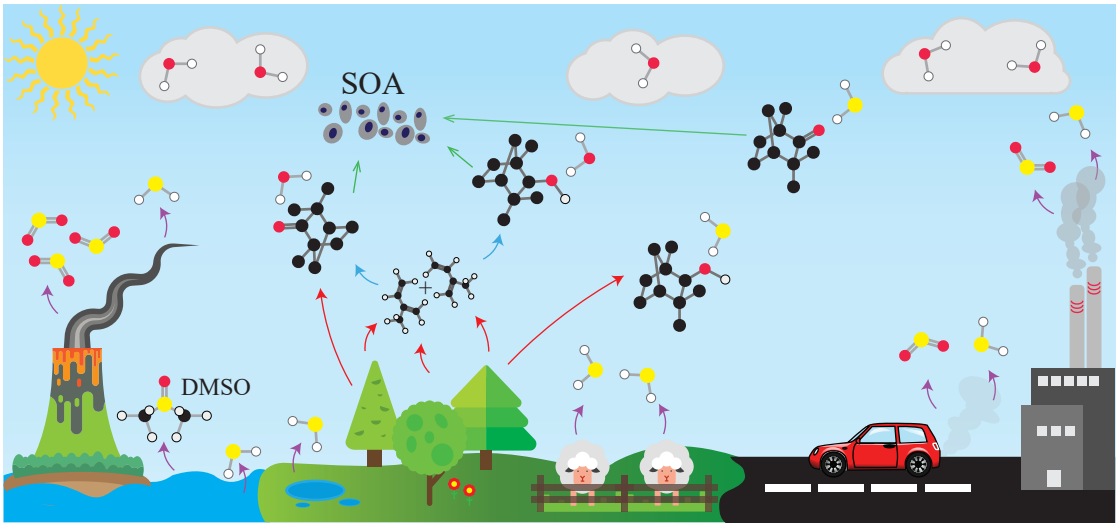

Figure 1.1: *A scheme illustrating the emission sources and examples of some interaction patterns of BVOCs with other species in the atmosphere. (Hydrogen, carbon, oxygen and sulfur atoms of the molecules are in white, black, red and yellow colors, respectively)*

given in fig. 1.1. Some of the elements in the scheme will be discussed after.

The contribution of BVOCs to SOA formation is not the only concern. These molecules and their oxygenated products can form hydrogen-bonded complexes with other molecules present in the atmosphere, such as water, and sulfur containing compounds. This can lead to changing the hygroscopic properties of different particles in the atmosphere. Their ability to form water complexes makes them good cloud condensation nuclei, which in turn can lead to the formation of more clouds that can induce some cooling effect on the earth. The micro-hydration, *i.e.* the process that allows water molecules to attach to the molecule of interest, of BVOCs in the atmosphere is a highly probable phenomenon, as water vapor is abundant in the atmosphere, and the water molecule can form hydrogen bonds very easily. The hydrogen bond, which can be differentiated from the general van der Waals interactions [10], is very important in stabilizing numerous molecular systems in the atmosphere, as well as inducing new particles formation.

Other than water, compounds containing electronegative atoms can form hydrogen bonds with BVOCs as well. To be exact, it is the difference of electronegativities of the two atoms which has to be considered: greater electronegativity of

the hydrogen bond acceptor of electrons will lead to an increase in hydrogen-bond strength. An interesting example can be sulfur containing compounds such as hydrogen sulfide H_2S, sulfur dioxide SO_2 and sulfuric acid H_2SO_4. An important point to consider is that oxygen and sulfur have remarkably different properties under ambient conditions despite being in the same group of the periodic table. It has been conventionally thought that oxygen is capable of hydrogen bonding while sulfur is not. The modern view is that both are capable of being hydrogen bond donors/acceptors but with differences in their capabilities [10]. The fact that sulfur is less electronegative than oxygen rationalizes this difference, as hydrogen bonds formed with sulfur will be weaker than those formed with oxygen. Volcanic activity represents the major source for these sulfur containing gases. Sulfur is important for biogeochemical processes, yet it is an evident pollutant contributing to acid rain [11]. SO_2 dominates the sulfur chemistry in the atmosphere, and it is one of the most emitted sulfur species. H_2S originates from natural and anthropogenic sources [12–14]. Examples of natural sources include volcanoes and geothermal vents, whereas fossil fuel burning and livestock production can be considered as sources coming from human activities. H_2S is a trace gas that is found globally in the atmosphere, yet it can play an important role in shaping the earth's atmosphere. It is very important for plants [12]. The higher interest in this molecule compared to other sulfur compounds is due to its structure that resembles that of water [15]. Theoretically speaking, the H_2S molecule is capable of forming hydrogen-bonded complexes with airborne molecules, which could be of great importance for atmospheric research as it will give the chance to understand the interaction occurring at the molecular scale and thus to predict structures of complexes of BVOCs. Despite the importance of sulfur containing compounds, their complexes with organic molecules remain scarce in the literature. A few examples have been reported including the complexes of benzene (C_6H_6) [16] and phenylacetylene (C_6H_6CCH) with H_2S [17]. In the scope of this work, complexes of BVOCs and especially monoterpenoids with H_2S will be examined, to see how they behave and differ compared to water molecules.

The direct and indirect effects of the different BVOCs on the air quality and human health highlighted above make them an interesting area of study to have a wider knowledge about the behavior of such molecules in the air. The understand-

ing of the physical and chemical properties of these molecules and their complexes requires an in-depth knowledge of their structure and internal dynamics. Structural information eases the prediction of reaction pathways or bonding capabilities, due to the strong correlation between molecular structure and inter and intramolecular forces occurring at the molecular scale. Many techniques have been used to characterize atmospheric BVOCs and their gas phase reaction pathways. Among these are spectroscopic techniques that have proved to be very reliable in several fields of application. In general, spectroscopy exploits the interaction of matter with light, at different wavelengths, to determine the electronic and structural properties of the molecular systems. Among the different techniques, rotational spectroscopy is a powerful technique that gives unmatched accuracy in structural determination, among other advantages that will be discussed in the following.

1.2 Microwave spectroscopy

The first microwave investigations date back to the year 1946. The spectrometers started to emerge in that period, by taking advantage of the advancements in radio frequency technology before and during the Second World War, especially the extensive research and development of radio detection and ranging (RADAR). The first few spectrometers used a gas cell or waveguide to measure the absorption of monochromatic radiation. Klystrons, magnetrons and traveling wave tubes were the sources of radiation at that time, and the detectors were semiconductor crystals [18]. In such types of spectrometers, the excitation or absorption frequencies, or excitation intensities were modulated by the Stark or Zeeman effects to enhance the sensitivity with the use of lock-in amplifiers [18].

was the first molecule to be studied by microwave spectroscopy. The interest in this molecule was due to its possession of two spectroscopic challenging features: the inversion splitting [19, 20] and the hyperfine structure arising from the quadrupolar moment of the nitrogen atom [21]. The extensive focus on ammonia led to the further development of stimulated emission techniques [22].

In 1953, Kraitchman was the first to present a theoretical approach that permits to determine the position of atoms in a molecule starting from spectroscopic measurement of isotopic species [23]. The Kraitchman method is still used up till

now to determine the equilibrium, substitution and mass-dependent structures of molecular systems.

Rotational spectroscopy witnessed several enhancements regarding sensitivity and resolution (line width), with the introduction of time-domain emission spectrometers, which were further enhanced by using pulsed microwave sources [24–27].

One of the most important steps in the history of microwave spectroscopy was in the 1980s when Balle and Flygare introduced a spectrometer that combines pulsed time-domain technique with a Fabry-Pérot optical cavity [28] to achieve unprecedented sensitivity and resolution. They also coupled the spectrometer to a supersonic expansion [28] which permitted to reach very low vibrational and rotational temperatures. This eliminated the drawbacks of pressure line broadening and low intensities due to poor population distribution at room temperature. The design was later enhanced in 1996 by adapting a coaxial alignment of the supersonic jet and the excitation microwave electromagnetic field [29]. This arrangement minimizes the Doppler broadening by replacing the perpendicular interaction and permits to achieve narrower line widths. Laboratories worldwide still to this day operate spectrometers that are inspired by the Balle-Flygare design.

In 2008, the field of Fourier transform microwave spectroscopy was revolutionized by the invention of a chirped-pulse spectrometer by the group of Brooks Pate [30]. The new spectrometer made use of new fast electronics and utilizes a high sampling rate arbitrary waveform generator (AWG) to generate a broadband chirp (frequency swept) signal having a bandwidth up to 12 GHz. The technique was a huge breakthrough concerning the bandwidth, flexibility and measurements times. The experimental time needed to record a spectrum was massively reduced, because the whole range can be acquired in one shot, and no moving parts are necessary due to the elimination of the optical cavity. Many groups adapted the new technique since then, and the construction of new spectrometers was reported with slight variations from the initial design, that exploit the rapid advancements in electronics and latest generation AWGs and oscilloscopes [31–40].

The exceptional accuracy of rotational spectroscopy in determining molecular structure is not its only strength. In fact, it is adapted to highlight the conformational flexibility of molecular systems as well as providing information about

the intramolecular forces. This can be accessed by the effects of the centrifugal forces, internal rotation and vibrations on the rotational Hamiltonian. Also, we can have some information about the electronic structure through dipole moments and quadrupole coupling. Microwave spectroscopy has also been employed to study complex intra and intermolecular dynamics [41, 42].

The invention of the chirped-pulse technique opened the door for new types of experiments that were not possible with the cavity technique. The novel applications include differentiation of enantiomers by three-wave radio frequency (RF) mixing [43, 44], two dimensional microwave spectroscopy [45] and isomerization dynamics [46, 47].

It is clear that microwave spectroscopy can be undoubtedly used to study molecular systems of atmospheric relevant species. The structure, conformational landscape and internal dynamics information that can be extracted from experimental rotational spectra are very useful in giving an idea about the reaction pathways and possible complex formations of BVOCs in the atmosphere. An understanding of the interaction sites and possible dynamics of atmospheric species can predict possible sinks for these molecules, and consequently can be used as entries for atmospheric models predicting concentrations of different families of molecules. The fingerprint rotational lines can also be used as database elements for the detection of such molecules.

It is worth mentioning that microwave spectroscopy has several important applications other than studying atmospheric species. In fact, it is widely used in astrophysics and astrochemistry to detect and characterize molecules that are found in interstellar media. It is often challenging to analyze the molecular signals, that are usually detected by large telescopes, for several reasons. The molecules in outer space are far from thermal equilibrium which means that their internal energies are spread over several vibrational levels. Also, it is not easy to reproduce the harsh environmental conditions that induce the formation of molecules in outer space inside the laboratory. Nonetheless, recent reports suggest that a discharge is a promising and efficient approach for producing unstable molecules of astrophysical interest in the jet-cooled conditions of Fourier transform microwave spectroscopy [48].

The work conducted throughout this thesis and present herein is composed

mainly of two parts. The first is to contribute to the construction and characterization of a new chirped-pulse spectrometer functioning in the 6-18 GHz range, which is described in detail in chapter 3. The second part is composed of a combined experimental and theoretical microwave spectroscopic study of complexes of BVOCs with H_2S molecule, as well as the conformational landscape and internal dynamics of a molecule of atmospheric interest. The manuscript incorporates four chapters other than this introductory one.

In chapter 2 I will present a theoretical background about rotational spectroscopy, including all the assumptions and approximations needed to derive the Hamiltonian used, as well as about quantum chemical calculations.

Chapter 3 is a detailed description of the cavity-based spectrometers available and operating in the PhLAM laboratory, along with a thermodynamic representation of the supersonic jet expansion technique. It also includes the technical characteristics and schemes of the newly constructed chirped-pulse spectrometer. At the end of the chapter is a summary of the experimental methods and conditions used to obtain the reported results in chapters 4 and 5.

Chapter 4 is dedicated to the theoretical and experimental results of the observed complexes of two monoterpenoids: fenchol and fenchone with H_2S molecule. A comparison of the two complexes with water analogs and with themselves through the employment of energetic analysis tools will also be presented in this chapter.

Chapter 5 reports the spectroscopic investigation of the conformational landscape and internal dynamics of limona ketone, which is an oxygenated monoterpene resulting mainly from limonene ozonolysis.

A general summary of the conducted work will be given at the end of these chapters.

CHAPTER

TWO

THEORETICAL BACKGROUND

In this chapter a theoretical description of the rotational Hamiltonian is given, starting from fundamental notions of quantum mechanics, and discussing the approximations needed for the derivation of the Hamiltonian. Also, a theoretical description of the internal rotation related to the presence of a methyl group is given. Following, a theoretical presentation of the quantum chemical calculations used throughout this work and a summary of the different methods and basis sets employed for the studied systems are presented. The last part of this chapter includes a few points about the interplay between theory and experiment and some of the programs used for fitting the experimental data.

2.1 Fundamentals of molecular spectroscopy

Spectroscopy is the study of the interaction between a physical system (molecules, atoms) and electromagnetic radiation (*i.e.* light). It is a probe, using static or dynamic electromagnetic fields, of the energy eigenvalues of a quantum system, or in other words, the energy difference between the quantum levels. The state of a molecular system having M nuclei and N electrons is described in quantum mechanics by a wave function Ψ satisfying Schrödinger equation:

$$i\hbar\frac{\partial\Psi}{\partial t} = \hat{H}\Psi \tag{2.1}$$

In this work, we deal with stationary electronic states and consequently, the molecular system can be described by the time-independent Schrödinger equation:

$$\hat{H}\Psi(\overrightarrow{x_n}, \overrightarrow{x_e}) = E\Psi(\overrightarrow{x_n}, \overrightarrow{x_e}) \tag{2.2}$$

where

- $\overrightarrow{x_n}$ and $\overrightarrow{x_e}$ are vectors describing the nuclear and electronic coordinates respectively
- Ψ is the wave function representing the eigenfunctions of the Hamiltonian operator $\hat{H}$
- E is the energy associated with the eigenvalues of Ψ

In the absence of an external field, the Hamiltonian can be divided into a kinetic energy term $\hat{T}$ and a potential energy term $\hat{V}$[49]. Each term can be decomposed into the interaction energies between the nuclei and electrons as follow:

$$\hat{H} = \hat{T} + \hat{V} = T_N + T_e + V_{NN} + V_{ee} + V_{Ne} \tag{2.3}$$

where:

- T_N is the kinetic energy of the nuclei:

$$T_N = \sum_{i=1}^{M} \frac{-\hbar^2}{2M_{n_i}} \overrightarrow{\nabla_{n_i}}^2 \tag{2.4}$$

  with M being the mass, and i represents the ith nucleus
- T_e is the kinetic energy of the electrons:

$$T_e = \sum_{i=1}^{N} \frac{-\hbar^2}{2m_{e_i}} \overrightarrow{\nabla_{e_i}}^2 \tag{2.5}$$

- V_{NN} is the potential energy associated with the electrostatic repulsion between two nuclei i and j:

$$V_{NN} = \sum_{i,j>i} \frac{Z_{n_i} Z_{n_j} e^2}{4\pi\epsilon_0 R_{n_i n_j}} \tag{2.6}$$

- V_{eN} is the potential energy of electrostatic attraction between nucleus and electrons:

$$V_{eN} = \sum_{i=1}^{n} \sum_{j=1}^{N} \frac{-Z_{n_i} {e_j}^2}{4\pi\epsilon_0 r_{n_i e_j}} \tag{2.7}$$

- V_{ee} is the potential energy of electrostatic interaction between electrons:

$$V_{ee} = \sum_{i,j>i} \frac{e^2}{4\pi\epsilon_0 r_{e_i e_j}} \tag{2.8}$$

  with i and j refer to the electrons

where

- M_n is the mass of the nuclei
- m_e is the mass of the electrons
- Z is the atomic number
- e is the charge of the electron
- $R_{n_i n_j}$ is the inter-nucleic distance
- $r_{n_i e_j}$ is the distance between nucleus i and electron j
- $r_{e_i e_j}$ is the inter-electronic distance

The energy eigenvalues are mainly influenced by molecular dynamics including electronic movements and molecular rotations and vibrations. However, these motions occur at different timescales because the mass of the proton is around 1836 times that of the electron, and consequently the electrons move much faster than the nucleus. This leads to the well-known approximation in molecular spectroscopy: the Born-Oppenheimer approximation [50].

Within the Born-Oppenheimer approximation, the Hamiltonian can be evaluated by a two-step approach. This is possible by separating the electronic and nuclear motions, based on the fact that the nucleus barely moves during a period of electronic movement [50]. In the first step, the electronic part of the Hamiltonian is solved with a fixed position of the nucleus $\overrightarrow{x_\alpha}$. In the second step, the nuclear part is solved based on an average electronic potential derived from the first step. It becomes possible to write the Hamiltonian as:

$$\hat{H} = \hat{H}_{electronic} + \hat{H}_{nuclear} \tag{2.9}$$

and the wave function as:

$$\Psi(\overrightarrow{x_n}, \overrightarrow{x_e}) = \Psi_e(\overrightarrow{x_\alpha}, \overrightarrow{x_e})\Psi_N(\overrightarrow{x_n}) \tag{2.10}$$

with $\overrightarrow{x_\alpha}$ being the fixed positions vector of the nuclei. Likely, molecular vibrations occur much faster than molecular rotations, hence we can employ a similar logic for the separation of vibrational and rotational movements. This means that, in a first approximation, the average contribution of the vibrational motions can be separated from the rotational part of the Hamiltonian. Thus, the total Hamiltonian of the system can be represented by:

$$\hat{H} = \hat{H}_{elec}(\overrightarrow{x_e}, \overrightarrow{x_\alpha}) + \hat{H}_{rot}(\Phi, \Theta, \chi) + \hat{H}_{vib}(\overrightarrow{x_n}) + \hat{H}_{trans}(X, Y, Z) + \hat{H}_{ns} \tag{2.11}$$

where:

- (Φ,Θ,χ) are the Euler angles describing the orientation of the molecular system in the laboratory-fixed coordinate system (O, X, Y, Z) and which will be discussed after;
- $\overrightarrow{x_e}$ and $\overrightarrow{x_n}$ are position vectors describing the orientation of electrons and nuclei, respectively, in a molecule-fixed coordinate system (o, x, y, z)

We can notice that even with this separation, the Hamiltonian is still complex to solve, as a molecule with N atoms has $3N$ independent variables related to the nuclear rotation, vibration and translation motions. One way to simplify this problem is to construct the Hamiltonian in a laboratory-fixed coordinate system (O, X, Y, Z) which is related to the molecular coordinates system (o, x, y, z), in which the coupling between the above movements is minimized. Both coordinate systems coincide at the center of mass of the molecule itself. This permits to exclusion of the translational movement of the nuclei with respect to the center of mass, thus reducing the degrees of freedom to $3N-3$. In addition, the relation between the two systems allows the determination of the rotational energy of the molecule by solving the rotational Hamiltonian, and that will be discussed later. The orientation of both coordinate systems relative to each other is described by the three Euler angles Φ,Θ and χ shown in fig. 2.1. The transformation from (o, x, y, z) to (O, X, Y, Z) is done by three consecutive rotations about the axes as

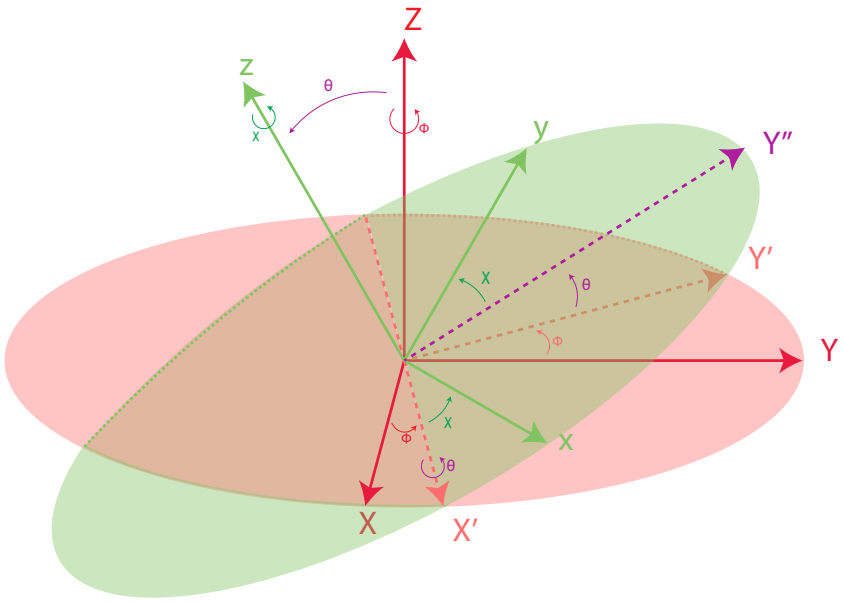

Figure 2.1: *Illustration of the Euler angles ϕ,θ,χ which designate the orientation of the molecular system (x,y,z) with respect to the laboratory frame (X,Y,Z)*

follows (rotation matrices can be found in Chapter 6 of reference [51]):

1. Rotate X and Y by angle ϕ about Z into X' and Y'
2. Rotate Y' and Z by angle θ about X' into Y'' and z
3. Rotate X' and Y'' by an angle χ about z into x and y

Since microwave spectroscopy, as employed in this work, is a probe of the rotational energy levels of a molecule, only the rotational part of the Hamiltonian is of interest, and it will be discussed in detail in the following section.

2.2 Rotational Hamiltonian

2.2.1 Rigid Rotor

In quantum mechanics, the rigid rotor Hamiltonian describes a molecule that rotates with fixed geometry. It is supposed that the molecule does not undergo any transformation during its rotation. A starting point to determine the Hamiltonian is the referral to classical mechanics, where the rotational energy of a rigid body

is given by:

$$E_{rot} = \frac{1}{2} I \omega^2 \tag{2.12}$$

where I is the inertia tensor, and ω is the angular velocity.

In a rigid molecule, the contribution of the electrons to the inertia tensor can be considered negligible, as their mass is much smaller than that of the nucleus. For a molecule with N atoms, each having mass m_i and coordinates (x_i,y_i,z_i) in a molecule-fixed axis system, the inertia tensor I can be expressed by:

$$I = \sum_{i=0}^{N} m_i \begin{pmatrix} {y_i}^2 + {z_i}^2 & -x_i y_i & -x_i z_i \\ -y_i x_i & {x_i}^2 + {z_i}^2 & -y_i z_i \\ -z_i x_i & -z_i y_i & {x_i}^2 + {y_i}^2 \end{pmatrix} = \begin{pmatrix} I_{xx} & I_{xy} & I_{xz} \\ I_{yx} & I_{yy} & I_{yz} \\ I_{zx} & I_{zy} & I_{xx} \end{pmatrix} \tag{2.13}$$

The above matrix can be simplified by diagonalization of the inertia tensor. This can be achieved by employing a molecule-fixed coordinates system called the principal axes system, which has its origin at the center of mass of the rotating molecule. The axes are denoted by a, b, c and they are unique to each molecule. The axes are designated in a manner that ensures the definition of the principal moments of inertia, which are the diagonal elements of I, with an increasing size $I_a \leqslant I_b \leqslant I_c$. The molecule-fixed axes (x,y,z) can be related to the principal axes (a,b,c) in six different ways. These representations are listed in table 2.1. These assignments will be of importance for the evaluation of the rotation Hamiltonian.

Table 2.1: *Possible identification of the molecular axes x, y, z with the principal axes a, b, c leading to six different representations. Superscripts r and l designate the right- and left-handed coordinate systems, respectively. Adapted from [52].*

	I^r	I^l	II^r	II^l	III^r	III^l
x	b	c	c	a	a	b
y	c	b	a	c	b	a
z	a	a	b	b	c	c

In the principal axes system the rotational energy can be written in the form:

$$E_{rot} = \frac{1}{2}(I_a \omega_a^2 + I_b \omega_b^2 + I_c \omega_c^2) = \frac{J_a^2}{2I_a} + \frac{J_b^2}{2I_b} + \frac{J_c^2}{2I_c} \tag{2.14}$$

where J_a^2, J_b^2 and J_c^2 are the components of the angular momentum along the principal axes a, b and c respectively.

The pathway from rotational energy in classical mechanics to the rigid rotor Hamiltonian in quantum mechanics is straightforward. It is done by employing the angular momentum operator $\hat{J}$, and the rotational Hamiltonian can be expressed as:

$$\hat{H}_{rot} = \frac{\hat{J}_a^2}{2I_a} + \frac{\hat{J}_b^2}{2I_b} + \frac{\hat{J}_c^2}{2I_c} \tag{2.15}$$

which can be rewritten in the form:

$$\hat{H}_{rot} = A\hat{J}_a^2 + B\hat{J}_b^2 + C\hat{J}_c^2 \tag{2.16}$$

with A, B and C being the rotational constants, expressed in Joules. They are inversely proportional to the principal moments of inertia and can be described by:

$$\begin{cases} A = \frac{\hbar^2}{2I_a} \\ B = \frac{\hbar^2}{2I_b} \\ C = \frac{\hbar^2}{2I_c} \end{cases}$$

As previously mentioned, the principal moments of inertia are chosen in increasing size. Hence, the rotational constants follow the inverse relation: $A \geqslant B \geqslant C$ Because rotational transitions and the corresponding energy levels are mostly in the frequency ranges of hundreds of MHz and GHz in rotational spectroscopy, the rotational constants are usually expressed in units of frequency (MHz or GHz) rather than units of energy. They can also be expressed in wavenumber (cm^{-1}). We can use the following expressions:

$$A(\mathrm{MHz}) = \frac{16.8576314}{I_a} \qquad A(\mathrm{cm}^{-1}) = \frac{505379.07}{I_a} \tag{2.17}$$

Here I_a is expressed in ($\mathrm{u\,\AA}^2$).

We can notice that the rotation Hamiltonian in eq. (2.16) solely depends on angular momentum operators, which are defined in the molecular axis system. It is necessary to relate the molecular (x,y,z) system to the laboratory-fixed (X,Y,Z) system, as explained in section 2.1 and shown in fig. 2.1, in order to calculate

the rotational energy of a molecule. The Cartesian components of the angular momentum operators can be thus expressed in terms of Eulerian angles in both systems. The angular momentum operators satisfy the following commutation relations [53]:

$$[\hat{J}_x, \hat{J}_y] = -i\hbar\hat{J}_z, \quad [\hat{J}_z, \hat{J}_x] = -i\hbar\hat{J}_y, \quad [\hat{J}_y, \hat{J}_z] = -i\hbar\hat{J}_x \tag{2.18}$$

$$[\hat{J}_X, \hat{J}_Y] = i\hbar\hat{J}_Z, \quad [\hat{J}_Z, \hat{J}_X] = i\hbar\hat{J}_Y, \quad [\hat{J}_Y, \hat{J}_Z] = i\hbar\hat{J}_X \tag{2.19}$$

$$[\hat{\mathbf{J}}^2, \hat{J}_x] = 0, \quad [\hat{\mathbf{J}}^2, \hat{J}_y] = 0, \quad [\hat{\mathbf{J}}^2, \hat{J}_z] = 0 \tag{2.20}$$

$$[\hat{\mathbf{J}}^2, \hat{J}_X] = 0, \quad [\hat{\mathbf{J}}^2, \hat{J}_Y] = 0, \quad [\hat{\mathbf{J}}^2, \hat{J}_Z] = 0 \tag{2.21}$$

$$[\hat{J}_i, \hat{J}_j] = 0 \qquad \text{with} \quad i = x, y, z \quad \text{and} \quad j = X, Y, Z \tag{2.22}$$

According to Heisenberg uncertainty principle, only the $\hat{\mathbf{J}}^2$ operator, one of the ($\hat{J}_x$, $\hat{J}_y$, $\hat{J}_z$) operators, and one of the ($\hat{J}_X$, $\hat{J}_Y$, $\hat{J}_Z$) operators can be measured simultaneously. The projections of the total angular momentum on the z-axis ($\hat{J}_z$) and the Z-axis ($\hat{J}_Z$) are chosen by convention in the rotational spectroscopy literature. The z-axis is assigned to the principal axis with the highest symmetry employing the appropriate representation in table 2.1. Starting from the commutation relations, a complete set of eigenfunctions $|JKM\rangle$ can be calculated for the operators $\hat{\mathbf{J}}^2$, $\hat{J}_z^2$ and $\hat{J}_Z^2$. The following eigenvalues can be derived with the help of the ladder operator $\hat{J}_\pm = \hat{J}_x \pm i\hat{J}_y$ [54, 55]:

$$\hat{\mathbf{J}}^2|JKM\rangle = J(J+1)\hbar|JKM\rangle \tag{2.23}$$

$$\hat{J}_z|JKM\rangle = K\hbar|JKM\rangle \tag{2.24}$$

$$\hat{J}_Z|JKM\rangle = M\hbar|JKM\rangle \tag{2.25}$$

where J, K and M are the quantum numbers such that:

- J is a positive integer starting from 0 $\quad\rightarrow\quad$ $J = 0, 1, 2, \ldots$
- K can take any integer value between $-J$ and $+J$ $\quad\rightarrow\quad$ $-J \leqslant K \leqslant +J$
- M can take any integer value between $-J$ and $+J$ $\quad\rightarrow\quad$ $-J \leqslant M \leqslant +J$

The quantum number J is the measure of the total angular momentum, and the quantum numbers K and M are the projection of the total angular momentum on the z-axis and Z-axis, respectively.

The knowledge of the angular momentum operator properties and their eigenstates and eigenfunctions makes it possible to solve the rotational Hamiltonian for different rigid rotor molecules, which will be classified below into different categories. It should be noted that the choice of the representation, in the following, has no effect on the eigenstates and the eigenfunctions, but assigning the z-axis to the principal axis with the highest symmetry decreases, dramatically, the complexity of computation of the Hamiltonian.

According to the symmetry of the molecule, some of its moments of inertia can be equal, or one of them might vanish. Therefore, in spectroscopy, molecules are classified into four main categories as follows:

Linear molecules: They are molecules having $B = C$ ($I_b = I_c$). They belong to point groups $C_{\infty v}$ or $D_{\infty h}$. Typical examples include carbonyl sulfide (OCS) and Hydrogen cyanide (HCN). The I^r representation of the rotation Hamiltonian gives:

$$\hat{H}_{rot} = B\hat{\mathbf{J}}^2 \tag{2.26}$$

with the eigenvalues:

$$E_{rot} = BJ(J+1) \tag{2.27}$$

The evaluation of the transition dipole moments leads to the selection rules of linear molecules [53]:

$$\Delta J = 0, \pm 1;\ \Delta M = 0, \pm 1$$

For linear molecules $K = 0$, so the corresponding energy levels are $(2J + 1)$ degenerate. The eigenvalues and the selection rules indicate that the rotational transitions will have a uniform spacing of $2B$ in the spectrum.

Spherical top molecules: They are molecules having all of their moments of inertia equal i.e. $A = B = C$ ($I_a = I_b = I_c$). They belong to the T_d, O_h or I_h point groups. Typical examples include methane (CH_4), carbon tetrachloride (CCl_4) and sulfur hexafluoride (SF_6). The Hamiltonian can be simply written as:

$$\hat{H}_{rot} = B\hat{\mathbf{J}}^2 \tag{2.28}$$

and the eigenvalues are:

$$E_{rot} = BJ(J+1) \tag{2.29}$$

The total degeneracy of the energy levels is $(2J+1)^2$. These molecules have a high degree of symmetry, and thus do not have a permanent dipole moment which make them not suitable to be studied by pure rotational spectroscopy.

Symmetric top molecules: They are molecules having two moments of inertia equal. They have C_n or S_4 symmetry. These molecules can be divided into two subcategories:

- Prolate symmetric tops: molecules having $A > B = C$ $(I_a < I_b = I_c)$. Since their symmetry lies mainly in the a-axis, they are described as having a cigar shape. Examples include chloroform (CH_3Cl) and propadiene (C_3H_4). With the a principal axis being the highest in symmetry and $B = C$, the rotational Hamiltonian in the I^r representation is given as:

$$\begin{aligned} \hat{H}_{rot} &= A\hat{J}_a^2 + B(\hat{J}_b^2 + \hat{J}_c^2) \\ &= B\hat{\mathbf{J}}^2 + (A-B)\hat{J}_z^2 \end{aligned} \tag{2.30}$$

  The matrix representation of H_{rot} is diagonal, and the eigenvalues are independent of M:

$$E_{rot} = BJ(J+1) + (A-B)K^2 \tag{2.31}$$

- Oblate symmetric tops: molecules having $A = B > C$ $(I_a = I_b < I_c)$. Since their symmetry lies mainly in the c-axis, they are described as having a disc shape. Examples include benzene (C_6H_6) and ammonia (NH_3). With the c principal axis being the highest in symmetry and $A = B$, the rotational Hamiltonian in the III^r representation is given as:

$$\begin{aligned} \hat{H}_{rot} &= C\hat{J}_c^2 + B(\hat{J}_a^2 + \hat{J}_b^2) \\ &= B\hat{\mathbf{J}}^2 + (C-B)\hat{J}_z^2 \end{aligned} \tag{2.32}$$

The matrix representation of $\hat{H}_{rot}$ is diagonal, and the eigenvalues are independent of M:

$$E_{rot} = BJ(J+1) + (C-B)K^2 \tag{2.33}$$

The evaluation of the transition dipole moments leads to the selection rules of pure rotational spectra of symmetric-top molecules [52]:

$$\Delta J = 0, \pm 1;\ \Delta K = 0;\ \Delta M = 0, \pm 1$$

In the absence of any external electromagnetic field, the corresponding energy levels E_{JKM} (with $K \neq 0$) are $(2J+1)$ degenerate in M and two-fold degenerate in K with $E_{JKM} = E_{J-KM}$ (K can be positive or negative). Considering the selection rule $\Delta K = 0$, we can say that the rotational transitions can be given by:

$$\nu = 2B(J+1)$$

But centrifugal distortion splits out the transitions with different K for a given $J \rightarrow J+1$ transition, which will be explained later in this section.

Asymmetric top molecules: They are molecules having all their rotational constants different $A \neq B \neq C$ ($I_a \neq I_b \neq I_c$). They are the largest class. An important subgroup of this class is planar molecules having $I_c - I_b - I_a = 0$. Examples of asymmetric molecules include water (H_2O) and phenol (C_6H_5OH, planar). All of the molecules studied in the scope of this work belong to this class of molecules. The rotation Hamiltonian of this class will be discussed in more detail than the other classes in the following paragraph.

One way to evaluate the energy levels of an asymmetric top is to examine how its behavior deviates from prolate and oblate symmetric tops, as two limiting cases [56]. An asymmetric top is characterized by Ray's asymmetric parameter κ which is commonly used to indicate the degree of asymmetry of the molecule.

$$\kappa = \frac{2B - A - C}{A - C} \tag{2.34}$$

The values of κ vary between -1 and 1 corresponding to the prolate and oblate symmetric-tops limits, respectively. If $\kappa = 0$ the molecule is very asymmetric. For asymmetric-top with $A > B > C$ the Hamiltonian cannot be solved analytically anymore. If the difference between B and C is small the top is called near prolate, and if the difference between A and B is small the top is called near oblate. The choice of representation for asymmetric tops, which is arbitrary, can enhance the stability of the numerical methods used to calculate it. The I^r and III^r representations are used for near prolate and near oblate tops, respectively. The Hamiltonian can be set up in terms of $\hat{\mathbf{J}}^2$, $\hat{J}_z^2$ and $\hat{J}_x^2 - \hat{J}_y^2$ as follows:

- In the I^r representation for near prolate tops:

$$\hat{H}_{rot} = \frac{1}{2}(B+C)\hat{\mathbf{J}}^2 + [A - \frac{1}{2}(B+C)]\hat{J}_z^2 + \frac{1}{2}(B-C)(\hat{J}_x^2 - \hat{J}_y^2) \tag{2.35}$$

- In the III^r representation for near oblate tops:

$$\hat{H}_{rot} = \frac{1}{2}(A+B)\hat{\mathbf{J}}^2 + [C - \frac{1}{2}(A+B)]\hat{J}_z^2 + \frac{1}{2}(A-B)(\hat{J}_x^2 - \hat{J}_y^2) \tag{2.36}$$

The matrix representation of the rotation Hamiltonian in eqs. (2.35) and (2.36) is block diagonal in J and has only off-diagonal elements in K. The non-vanishing terms are given by [52]:

- near prolate:

$$\langle JKM|\hat{H}_{rot}|JKM\rangle = \frac{1}{2}(B+C)(J(J+1) - K^2) + AK^2 \tag{2.37}$$

$$\langle JKM|\hat{H}_{rot}|JK \pm 2M\rangle = \frac{1}{4}(B-C)[(J(J+1) - K(K\pm 1))(J(J+1) - (K\pm 1)(K\pm 2))]^{\frac{1}{2}} \tag{2.38}$$

- near oblate:

$$\langle JKM|\hat{H}_{rot}|JKM\rangle = \frac{1}{2}(A+B)(J(J+1) - K^2) + CK^2 \tag{2.39}$$

$$\langle JKM|\hat{H}_{rot}|JK \pm 2M\rangle = \frac{1}{4}(A-B)[(J(J+1) - K(K\pm 1))(J(J+1) - (K\pm 1)(K\pm 2))]^{\frac{1}{2}} \tag{2.40}$$

Each J-level can be examined individually and for a given J value, the matrix will have $2J+1$ dimension. In comparison to symmetric-top eigenvalues, in the

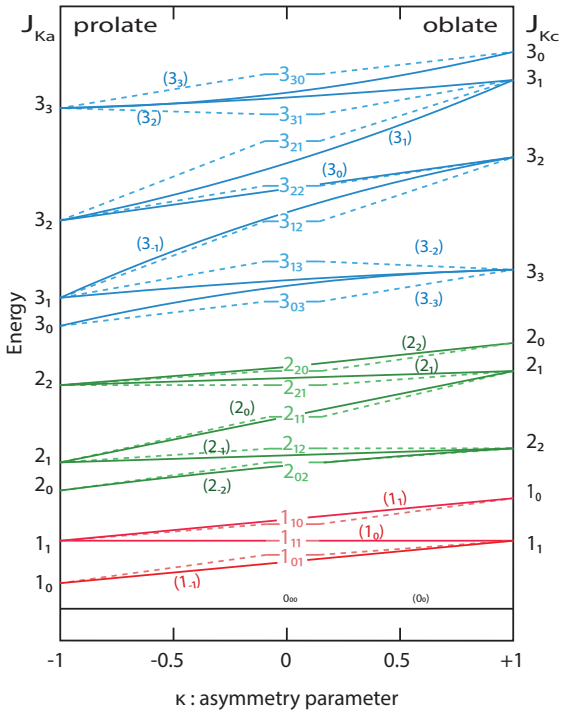

Figure 2.2: *Qualitative representation of rotational energy levels of an asymmetric-top molecule as function of Ray's asymmetry parameter κ. The J_{Ka} values at the prolate limit, and the J_{Kc} values at the oblate limit are shown on the left and right y-axes,respectively. The energy levels are labeled by J_{KaKc} notation (dashed lines) and by (J_{Ka-Kc}) notation which designate the energy ordering of a certain level within a J-stack.*

absence of an external electromagnetic field, the degeneracy $2J+1$ in M is still present, but the two-fold degeneracy in K is lifted.

For asymmetric-top molecules, the K quantum number is not suitable to label the energy levels, because the projection on the z-axis is not constant anymore. Hence, the rotation energy levels are labeled, using the King-Hainer-Cross notation, as $J_{K_aK_c}$ where K_a and K_c are the K values that the molecule would have in the limiting prolate and oblate cases, respectively. The values of $K_a - K_c$ give the position of the energy level ordering, which ranges from $-J$ to $+J$. A correlation diagram showing how the energy varies for different κ values can be found in fig. 2.2.

Returning to the original problem; an equivalent form of the Hamiltonian of

eq. (2.16)) is given by [52]:

$$\hat{H}_{rot} = \frac{1}{2}(A+C)\hat{\mathbf{J}}^2 + \frac{1}{2}(A-C)\hat{h}(\kappa) \tag{2.41}$$

where

$$\hat{h}(\kappa) = \hat{J}_a^2 + \kappa\hat{J}_b^2 - \hat{J}_c^2 \tag{2.42}$$

The matrix $\langle JK|\hat{h}(\kappa)|JK'\rangle$ has an ordered set of $2J+1$ eigenvalues $E_{J_\tau}(\kappa)$ called the reduced energies that are numbered with $-J \geqslant \tau \geqslant +J$. These eigen values have the property $E_{J_\tau} = -E_{J,\tau}(-\kappa)$ [52]. The eigenvalues of the asymmetric rotor are now expressed as:

$$E_{rot}(J_\tau) = \frac{1}{2}(A+C)J(J+1) + \frac{1}{2}(A-C)E_{J_\tau}(\kappa) \tag{2.43}$$

$E_{J\tau}$ is a numerical function, which should be evaluated for each particular system. By calculating the eigenvalues for a range of J levels, approximate expressions for low J have been tabulated and are listed in table 2.2 for $J \leqslant 3$ [56]. Computer programs are now available to calculate the asymmetric rotor energy levels in general.

A permanent dipole moment $\vec{\mu}$ is a necessity to observe the pure rotational spectra of any molecule. The selection rules for asymmetric tops are more complicated than for symmetric-tops, because all three dipole moments components can be nonzero along the principal axes. The selection rules for J and M are:

$$\Delta J = 0, \pm 1 \quad \text{and} \quad \Delta M = 0 \tag{2.44}$$

$\Delta J = -1, 0, +1$ constitute the P-,Q- and R-branches, respectively. The Q-branch appears in the spectrum of asymmetric-top molecules. The selection rules for K_a and K_c are obtained starting from group theory by writing the rotation wave functions and analyzing their components with respect to the D_{2h} group. Table 2.3 summarizes the different selection rules for K_a and K_c arising from the different dipole moment components. They are also shown in fig. 2.3.

Table 2.2: *Asymmetric-top rotational energies (J between 0 and 3)*

J_{KaKc}	$E(J_{KaKc})$
0_{00}	0
1_{01}	$B+C$
1_{11}	$A+C$
1_{10}	$A+B$
2_{02}	$2A+2B+2C+2\sqrt{B-C^2+(A-C)(A-B)}$
2_{12}	$A+B+4C$
2_{11}	$A+4B+C$
2_{21}	$4A+B+C$
2_{20}	$2A+2B+2C+2\sqrt{(B-C)^2+(A-C)(A-B)}$
3_{03}	$2A+5B+5C-2\sqrt{4(B-C)^2+(A-B)(A-C)}$
3_{13}	$5A+2B+5C-2\sqrt{4(A-C)^2-(A-B)(B-C)}$
3_{12}	$5A+5B+2C-2\sqrt{4(A-B)^2+(A-C)(B-C)}$
3_{22}	$4A+4B4C$
3_{21}	$2A+5B+5C+2\sqrt{4(B-C)^2-(A-B)(A-C)}$
3_{31}	$5A+2B+5C+2\sqrt{4(A-C)^2-(A-B)(B-C)}$
3_{30}	$5A+5B+2C+2\sqrt{4(A-B)^2+(A-C)(B-C)}$

2.2.2 Semi-rigid Rotor

In the previous section, and for the sake of simplicity, the rotation of molecules was modeled considering their geometry is rigid (fixed). However, molecules are flexible and the atoms' bond distances and angles will vary during their rotation due to centrifugal force. Also, the molecule might have some vibration and internal rotations along with its overall rotation. All of this can distort the geometry of a molecule from its equilibrium. It is worth mentioning that internal rotation and centrifugal distortion contribute to the angular momenta and hence they cannot be treated effectively. Internal rotation will be discussed later in section 2.3, and the centrifugal distortion will be discussed briefly in the following. The books cited in references [53, 56–58] can be consulted for further details.

The correction of centrifugal distortion can be done by the addition of higher order correction terms to the angular momenta, from perturbation theory, to the

Table 2.3: *Selection rules for asymmetric-top molecules*

	dipole	K_a, K_c	ΔJ	ΔK_a	ΔK_c
a-type	μ_a	$K_a = 0$	± 1	0, ± 2, … (even)	± 1, ± 3, … (odd)
		$K_a \neq 0$	0, ± 1	0, ± 2, … (even)	± 1, ± 3, … (odd)
b-type	μ_b		0, ± 1	± 1, ± 3, … (odd)	± 1, ± 3, … (odd)
c-type	μ_c	$K_c = 0$	± 1	± 1, ± 3, … (odd)	0, ± 2, … (even)
		$K_c \neq 0$	0, ± 1	± 1, ± 3, … (odd)	0, ± 2, … (even)

rotation Hamiltonian. Due to symmetry, only even order terms are non-vanishing, and hence for an asymmetric molecule the rotation Hamiltonian becomes:

$$\hat{H}^{sr}_{rot} = \hat{H}_{rot} + \hat{H}_{cd} = \hat{H}_{rot} + \frac{\hbar^4}{4} \sum_{\alpha\beta\gamma\delta} \tau_{\alpha\beta\gamma\delta} \hat{J}_\alpha \hat{J}_\beta \hat{J}_\gamma \hat{J}_\delta + O(6) + \dots \tag{2.45}$$

α, β, γ and δ can take any value of x, y or z in the molecule-fixed axes, and the parameters $\tau_{\alpha\beta\gamma\delta}$ are related to the force constants of bonds within a molecule. Watson demonstrated that the number of components of the correction term can be reduced to five determinable linear combinations of the fourth-order [59, 60], due to symmetry and commutation relations. Watson established two reduction schemes that are used in rotational spectroscopy: the (Asymmetric) A- and (Symmetric) S-reductions, which are best suited for asymmetric and symmetric (or slightly asymmetric) molecules, respectively. In the A-reduction, the rotation Hamiltonian can be written as [53]:

$$\begin{aligned} \hat{H}^{sr}_{rot} =& \frac{1}{2}(B^{(A)} + C^{(A)})\hat{J} + \left[A^{(A)} - \frac{1}{2}(B^{(A)} + C^{(A)})\right]\hat{J}_z^2 \\ &+ \frac{1}{2}(B^{(A)} - C^{(A)})(\hat{J}_x^2 - \hat{J}_y^2) - \Delta_J \hat{J}^4 - \Delta_{JK} \hat{J}^2 \hat{J}_z^2 - \Delta_K \hat{J}_z^4 \\ &- 2\delta_J \hat{J}^2(\hat{J}_x^2 - \hat{J}_y^2) + \delta_K \left[\hat{J}_z^2(\hat{J}_x^2 - \hat{J}_y^2) + (\hat{J}_x^2 - \hat{J}_y^2)\hat{J}_z^2\right] \\ &+ O(6) + \dots \end{aligned} \tag{2.46}$$

where Δ_J, Δ_{JK}, Δ_K, δ_J and δ_K are the five quartic centrifugal distortion constants. In the context of this work, only the A-reduced Hamiltonian was used,

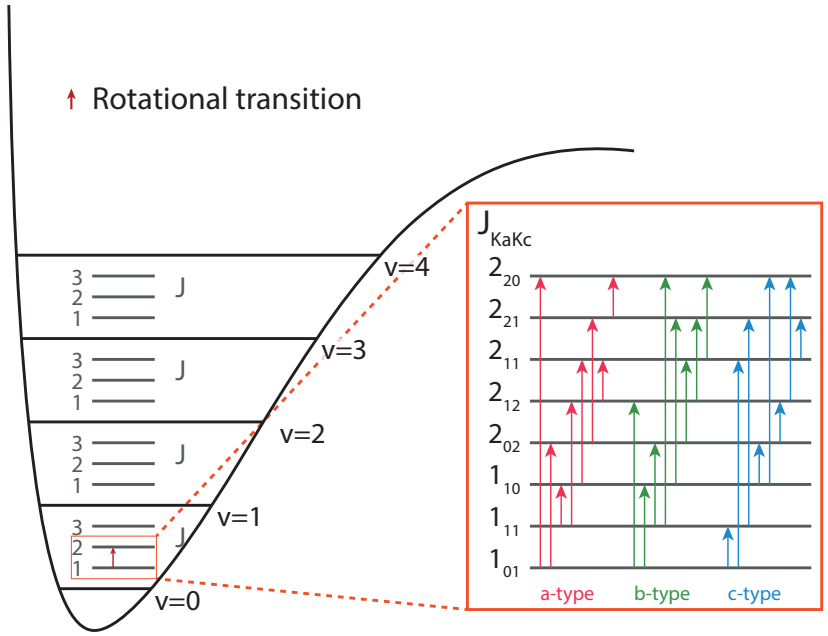

Figure 2.3: *Example of transition types based on the selection rules for asymmetric-top molecule for J=1 and J=2 rotational levels. The $v = 0, \ldots, 4$ are vibrational levels*

and a complete demonstration of the S-reduced Hamiltonian can be found in [53]. The distortion constants give an idea about the stiffness of the molecule, especially when compared with other molecules. They are usually smaller by three to six orders of magnitude than the rotational constants. They are beneficial in giving more accurate description of the rotation Hamiltonian. Also, it is necessary to consider the effect of the distortion terms in order to determine accurately the positions of rotational transitions in the experimental spectra, especially in high resolution measurements, and for high J and/or K values. The matrix representation of the semi-rigid Hamiltonian is diagonal in J and M with its elements as follows [53]:

$$\begin{aligned}\langle JKM|\hat{H}_{cd}^{(A)}|JKM\rangle =& A^{(A)}K^2 + \frac{1}{2}(B^{(A)} + C^{(A)})(J(J+1) - K^2) - \Delta_J J^2(J+1)^2 \\ & - \Delta_{JK} J(J+1)K^2 - \Delta_K K^4 + O(6) + \ldots\end{aligned} \tag{2.47}$$

$$\begin{aligned}\langle JKM|\hat{H}_{cd}^{(A)}|JK\pm 2M\rangle =& \Big\{\frac{1}{4}(B^{(A)}-C^{(A)})+\delta_J J(J+1)+\frac{1}{2}\delta_K[K^2+(K\pm 2)^2]\Big\} \\ & \times\Big[(J(J+1)-K(K\pm 1))(J(J+1)-(K\pm 1)(K\pm 2))\Big]^{\frac{1}{2}} \\ & +O(6)+\ldots\end{aligned} \tag{2.48}$$

Centrifugal distortion corrections shift the transitions in the observed spectra to lower frequencies than those predicted for the rigid rotor. These shifts are typically within a tenths kHz for $J \leqslant 10$, and might become more significant (order of several MHz) for higher J values. It is worth mentioning that the zero-order or 'rigid' rotational constants can be extracted from the 'nonrigid' rotational and centrifugal distortion constants [53]. This is useful for comparison with quantum chemistry calculation and structure determination.

2.3 Internal rotation

Additional features in the rotational spectrum of some flexible molecules may be observed, due to intramolecular large amplitude motions. These motions can be defined as internal movements with amplitudes on the order of the bond length. They may transform the molecule from one equivalent structure to another via tunneling. They are usually the result of shallow double or multi-well potentials, due to the coupling of conventionally isolated rotational and vibrational degrees of freedom. Internal rotation is an important example of these motions, and for this work only the internal rotation of the methyl group CH_3 (symmetric C_{3v} rotor) is of interest. The internal rotation is described in terms of α, named the internal rotation or torsion angle, which is the angle or rotation about the axis of the rotor, and $V(\alpha)$ which is the potential barrier. The following Schrödinger equation can describe the one-dimensional rotation of a methyl group in the molecular potential $V(\alpha)$:

$$\hat{H}\varphi(\alpha)=\left[-F\frac{\partial^2}{\partial\alpha^2}+V(\alpha)\right]\varphi(\alpha)=E\varphi(\alpha) \tag{2.49}$$

$V(\alpha)$ is periodic and vary within $[0, 2\pi]$, and it is repeated N-times where N is the number of equivalent configurations of the molecule, depending on its symmetry group. The potential $V(\alpha)$ can be represented by a Fourier series, with a period

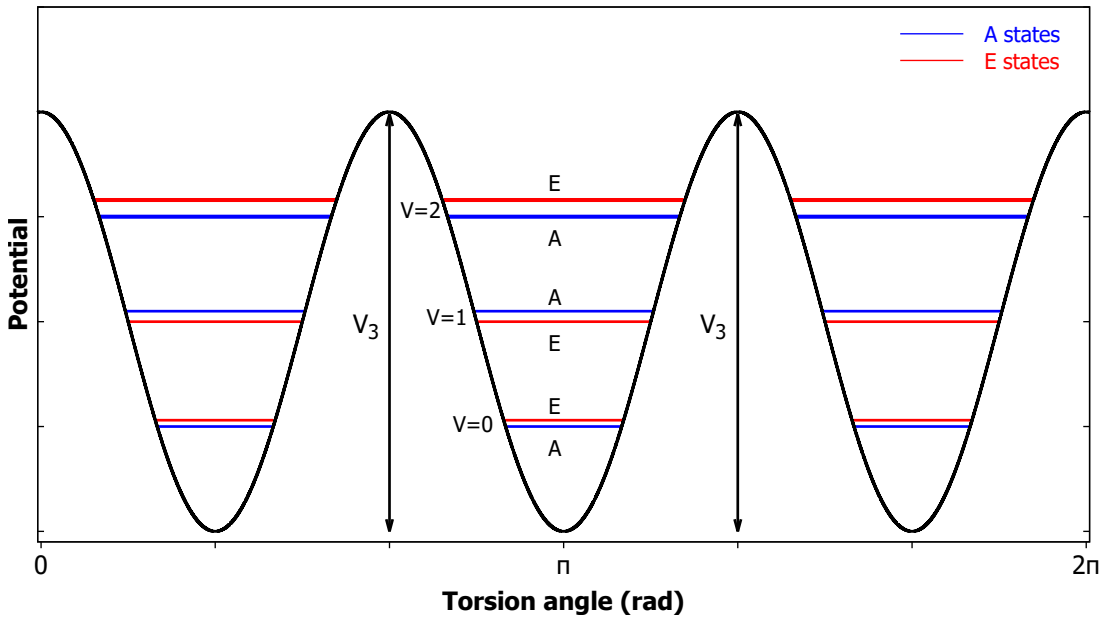

Figure 2.4: *Typical three fold barrier of the CH_3 (C_{3v} rotor). The horizontal lines represent the energy levels.*

of $\frac{2\pi}{N}$:

$$\begin{aligned} V(\alpha) &= \sum_k a_k \cos kN\alpha \\ &= \frac{V_N}{2}(1-\cos N\alpha) + \frac{V_{2N}}{2}(1-\cos 2N\alpha) + \ldots \end{aligned} \tag{2.50}$$

Because of the C_{3v} symmetry of the methyl group, its rotation is $\frac{2\pi}{3}$ periodic and the potential $V(\alpha)$ can be expanded in the following manner:

$$V(\alpha) = \frac{V_3}{2}(1-\cos 3\alpha) + \frac{V_6}{2}(1-\cos 6\alpha) + O(9) + \ldots \tag{2.51}$$

For most molecules, the expansion can be truncated after the first term, and for the sake of simplicity, only three-fold barriers are considered here. All but the V_3 terms vanish in the expansion. The shape of the three-fold methyl potential is represented in fig. 2.4. In this case, the rotation of the methyl leads to three equivalent minima and maxima in the potential surface energy along the torsion angle α. To derive the Hamiltonian which now includes the overall as well as the

internal rotation terms, one needs to consider the coupling of the two motions. By neglecting any distortion effects, the rotation Hamiltonian can be expressed in the principal axis system as [53]:

$$\hat{H}_{tot} = \hat{H}_{rot} + \hat{H}_{int} \tag{2.52}$$

Where

$$\hat{H}_{rot} = A\hat{J}_a^2 + B\hat{J}_b^2 + C\hat{J}_c^2 \tag{2.53}$$

and

$$\hat{H}_{int} = F(\hat{j}_\alpha - \rho_a\hat{J}_a - \rho_b\hat{J}_b - \rho_c\hat{J}_c)^2 + V(\alpha) \tag{2.54}$$

with

$$\hat{j}_\alpha = -i\frac{\partial}{\partial\alpha}, \quad \rho_x = \frac{\lambda_x I_\alpha}{I_x}, \quad \text{where } x = a, b, c \tag{2.55}$$

and

$$F = \frac{\hbar}{2rI_\alpha}, \quad r = 1 - \sum_{x=a,b,c} \lambda_x^2 \frac{I_\alpha}{I_x} \tag{2.56}$$

$\hat{j}_\alpha$ is the angular momentum operator of the internal rotor, and F is the rotational constant of the internal rotor, which can be calculated from I_α the moment of inertia of the internal rotor. The direction cosines λ_a, λ_b and λ_c give the orientation of the internal rotor in the principle axis system. In the case of high V_3 barrier (V_3 $> 1000\,\mathrm{cm}^{-1}$, $11\,\mathrm{kJ\,mol}^{-1}$), the internal motion due to CH_3 group is quenched, and the semi-rigid Hamiltonian given in eq. (2.46) can be used to describe the molecule. In the case of a low barrier, the CH_3 can rotate freely along the equivalent minima in the potential energy surface via tunneling. In the case of an intermediate barrier, the orientation of the CH_3 group and the height of the V_3 barrier can be calculated accurately. This was done in this work and will be discussed later.

Concerning the energy levels, they can be described by taking the solutions for the Hamiltonian in eq. (2.49) at the two limiting cases $V_3 \to 0$ and $V_3 \to \infty$:

- For the free rotor ($V_3 = 0$) case, the eigenfunctions $\varphi^{(0)}(\alpha)$ and the energy eigenvalues $E^{(0)}$ have the form [53]:

$$\varphi^{(0)}(\alpha) = Ae^{im\alpha} \tag{2.57}$$

$$E^{(0)} = Fm^2 \tag{2.58}$$

The values for the quantum number $m = 0, \pm1, \pm2, \ldots$ are obtained by applying the boundary conditions $\varphi^{(0)}(\alpha) = \varphi^{(0)}(\alpha + 2\pi)$. Each level is two-fold degenerate, which corresponds to the different directions of the rotation.

- For high barriers ($V_3 \to \infty$), the potential in eq. (2.51) can be expanded around small values of α in a Taylor series:

$$\cos 3\alpha = 1 - \frac{9}{2}\alpha^2 + \frac{27}{8}\alpha^4 + \ldots \tag{2.59}$$

If the expansion is truncated after the quadratic term, the well known harmonic oscillator wave functions are solutions for the Hamiltonian with the energies [53]:

$$E^{(\infty)} = \sqrt{3V_3 F}\left(\nu + \frac{1}{2}\right) \tag{2.60}$$

The quantum number ν can take integer values $0, 1, 2, \ldots$ and each of the vibrational sub-levels is triply degenerate, which corresponds to a vibration in every well of the potential.

If the barrier has finite height, tunneling can occur and the formerly triply degenerate vibrational sub-levels split into two degenerate levels designated with the symmetry label E (with quantum number $\sigma = \pm1$) and one non-degenerate level with symmetry label A (with quantum number $\sigma = 0$). Figure 2.4 shows the symmetry labeling of the sub-levels. Therefore, the quantum number σ defines the symmetry of the corresponding torsional wave function. Consequently, the transitions in the spectrum appear split into two components, and the separation between the two observed lines depends on the barrier height V_3. Transitions are only allowed between states having the same symmetry *i.e.* $A \leftarrow A$ or $E \leftarrow E$.

2.4 Quantum chemical calculations

The objective of this section is to present general notions about quantum chemical calculations used during my thesis, *i.e.* to predict the computational landscape of stable species with their equilibrium structures. In rotational spectroscopy, where

small and medium sized (< 20 heavy atoms) molecules are studied, the theoretical methods were shown to be of great asset and to have good accuracy. They are used to facilitate the analysis of microwave spectra and to have all the necessary molecular parameters to compare and discuss the experimental results. The possible benefits of such calculations will be discussed in more detail in section 2.6. For the derivation made in this section for the *ab initio* methods, one can refer to the two cited books [61, 62] for further details. Also, the cited books [63–65] can be referred to concerning DFT calculations.

The huge advancements in computation power and capabilities pushed quantum chemical calculations to be a very powerful tool in high resolution molecular spectroscopy. The algorithms and computer programs available to perform such calculations are numerous and show good results with different methods. The main methods can be classified into five major categories as follows:

Molecular mechanics (MM) These calculations are usually fast. They are based on classical physics, where the molecule is treated as a group of balls (atoms) held together by springs (bonds). If we know the length of each bond, the angles between the different bonds, as well as the force needed to compress or stretch these bonds, we can calculate the energy of the whole molecule. The lowest energy configuration can be determined by changing the geometry.

***ab initio* calculations** They are precise but relatively slow and costly. They are performed by solving the Schrödinger equation, which describes the behavior of electrons in a molecule by giving the energy and the wave function for every configuration. The wave function is a mathematical function that can be used to calculate the probability distribution of the electrons. The Schrödinger equation cannot be solved for molecules having more than one electron without using several approximations. *ab initio* calculations are founded uniquely over the theory of quantum mechanics.

Semi-empirical (SE) calculations They are slower than MM but faster than *ab initio* calculations. They are also based on solving the Schrödinger equation. They are a mixture between theory and experiment. They use empirical parameters to solve the Schrödinger equation, thus without computing the complex integrals like in *ab initio* calculations.

Density functional theory (DFT) calculations They are usually faster than *ab initio* but slower than SE calculations. They also solve the Schrödinger equation but, contrary to the *ab initio* and SE methods, without employing the wave function. Rather, they derive the electronic density function (electronic distribution) directly.

Molecular dynamics calculations They apply the laws of motion to the molecules.

The quantum chemical calculations listed above are performed by means of a finite set of basic functions that will be discussed in detail later in this section.

2.4.1 Molecular Hamiltonian

A small useful reminder will be recalling how the Hamiltonian in eq. (2.3) can be written as the sum of the different interactions occurring between the electrons and nuclei. By applying the Born-Oppenheimer approximation, which is used in all the developed approaches in what follows, the electronic wave functions are separated from the nuclei movements, and thus the electronic Hamiltonian in the position representation is written, in atomic units, as :

$$\hat{H}(r_1, r_2, \ldots, r_N) = \sum_{i}^{N} \hat{h}(r_i) + \frac{1}{2} \sum_{i}^{N} \sum_{i \neq j}^{N} \frac{1}{|r_i - r_j|} \tag{2.61}$$

where N is the total number of electrons, $\vec{r_i}$ the position coordinate and

$$\hat{h}(r_i) = -\frac{1}{2} \nabla_{r_i}^2 - \sum_{i=1}^{N} \frac{Z_n}{|r_i - R_n|} \tag{2.62}$$

is the single-electron contribution composed of the kinetic energy operator and of the nuclei-electron interaction with R_n and Z_n being the positions and charges of the nuclei. The stationary electronic states are determined by the time-independent Schrödinger equation:

$$\hat{H}(r_1, r_2, \ldots, r_N)\Psi(x_1, x_2, \ldots, x_N) = E\Psi(x_1, x_2, \ldots, x_N) \tag{2.63}$$

where $\Psi(x_1, x_2, \ldots, x_N)$ is a wave function written with space-spin electron coordinates $x_i = (r_i, \sigma_i)$ (with $r_i \in \mathbb{R}^3$ and $\sigma = \uparrow or \downarrow$) which is anti-symmetric with respect to the exchange of two coordinates, and E is the associated energy. We are interested in calculating an approximation for the wave function Ψ and the associated energy E of a specific state, most often the ground state wave function Ψ_0 and the ground state energy E_0.

2.4.2 Hartree-Fock method

The complexity of solving the Schrödinger equation arises from the presence of an electrostatic interaction term which involves the coordinates of two electrons. The first hypothesis to solve the Schrödinger equation is to consider the electrons as independent particles, thus simplifying the complex interaction of a multi-electron system. The quality of the solution to the Schrödinger equation depends on the form of the Hamiltonian $\hat{H}$, the form of the wave function Ψ and the numerical technique used.

Starting from the hypothesis presented above, if we neglect the Coulomb interaction term in the Hamiltonian of eq. (2.61), the single-electron Hamiltonian will be defined by a kinetic energy term and a potential energy term arising from nucleus-electron interaction. The total wave function Ψ can be written in the form of a product of single-electron functions $\Phi_i(x)$, where each function only depends on the coordinates $\vec{r}$ of the electron:

$$\Psi = \prod_{i=1}^{n} \Phi_i(x) = \Phi_1(x_1).\Phi_2(x_2)\ldots\Phi_{n-1}(x_{N-1})\Phi_n(x_N) \tag{2.64}$$

n represents the total number of single-electron functions $\Phi_i(x_i)$, and N the number of electrons. It should be noted that $n \neq N$ because virtual orbitals can be added. This approximation of independent particles was proposed by Douglas Hartree [66–68]: the wave function is a product of molecular orbitals that contain information about the spin, or simply the spin-orbitals.

This approximation is invalid from a physical point of view because it totally neglects the electron-electron interactions. Fock [69] showed that the Hartree wave function does not satisfy the Pauli exclusion principle. The electrons being

fermions with spin $\frac{1}{2}$, they should obey the Pauli exclusion principle, stating that two identical fermions cannot occupy the same quantum state simultaneously. Hence, the wave function describing the system should be anti-symmetric. He also proved that by using suitable additions and subtractions of all the permutations of Hartree products, we can construct a wave function that satisfies the exclusion principle.

In 1929, John Slater proposed a trial wave function that is nowadays known as the "Slater determinant", and that satisfies the anti-symmetric requirement as well as the electronic spin as it is composed of orthonormal spin orbitals. In this wave function, each electron is submitted to a potential created by the other $N-1$ electrons. The Slater determinant is written in the form:

$$\Psi^{HF} = \frac{1}{\sqrt{N!}} \begin{pmatrix} \chi_1(x_1) & \chi_2(x_1) & \cdots & \chi_N(x_1) \\ \chi_1(x_2) & \chi_2(x_2) & \cdots & \chi_N(x_2) \\ \vdots & \vdots & \ddots & \vdots \\ \chi_1(x_N) & \chi_2(x_N) & \cdots & \chi_N(x_N) \end{pmatrix} \tag{2.65}$$

where $\chi_i(x_i)$ are orthonormal spin orbitals. The orbitals are normalized by $\frac{1}{\sqrt{N!}}$. The HF total electronic energy, $E_{HF} = \langle \Psi_0 | H | \Psi_0 \rangle$, can be expressed in terms of integrals over these spin orbitals, using Slater's rules for calculating expectation values of Slater determinants:

$$E_{HF} = \langle \Psi_0 | H | \Psi_0 \rangle = \sum_{a}^{occupied} h_{aa} + \frac{1}{2} \sum_{a,b}^{occupied} \langle ab || ab \rangle \tag{2.66}$$

where the sum over a and b are over occupied spin orbitals, In this expression, h_{aa} are the single-electron integrals:

$$h_{aa} = \int dx \chi_a^*(x) h(r) \chi_a(x) \tag{2.67}$$

and $\langle ab||ab\rangle = \langle ab|ab\rangle - \langle ab|ba\rangle$ are the anti-symmetrized two-electron integrals (in physicists' notation) where:

$$\langle ij|kl\rangle = \iint dx_1 dx_2 \frac{\chi_i^*(x1)\chi_j^*(x2)\chi_k^*(x1)\chi_l^*(x2)}{|r_2 - r_1|} \tag{2.68}$$

The spin orbitals are obtained by minimizing the HF energy subject to the normalization constraints:

$$\min_{\{\chi_a\}} \left\{ E_{HF}[\{\chi_a\}] - \sum_{a}^{occupied} \epsilon_a \langle \chi_a | \chi_a \rangle \right\} \tag{2.69}$$

where ϵ_a are the orbital energies playing the role of Lagrange multipliers for the normalization constraints. This minimization leads to the HF eigenvalues equations:

$$f(x)\chi_i(x) = \epsilon_i \chi_i(x) \tag{2.70}$$

which determine both the occupied and virtual spin orbitals $\chi_i(x)$ and the associated orbital energies ϵ_i. In these equations, $f(x)$ is the one-electron HF Hamiltonian expressed as:

$$f(x) = h(r) + V^{HF}(x) \tag{2.71}$$

$V^{HF}(x)$ is the single-electron HF potential operator and is expressed with:

$$V^{HF}(x) = \sum_{a}^{occupied} J_a(x) - K_a(x) \tag{2.72}$$

with J_a being a coulomb operator defined by:

$$J_a(x_1) = \int dx_2 \frac{\chi_a^*(x_2)\chi_a(x_2)}{|r_2 - r_1|} \tag{2.73}$$

and K_a being an exchange operator whose action on a spin orbital $\chi_i(x_1)$is given by:

$$K_a(x_1)\chi_i(x_1) = \int dx_2 \frac{\chi_a^*(x_2)\chi_i(x_2)}{|r_2 - r_1|} \chi_a(x_1) \tag{2.74}$$

The Hartree-Fock (HF) potential $V^{HF}(x)$ is a single-electron mean-field potential approximating the effect of the two-electron interaction ($\frac{1}{2}\sum_i^N \sum_{i \neq j}^N \frac{1}{|r_i - r_j|}$). In other words, the HF approximation only accounts for the electron-electron interaction in an averaged mean-field manner. The approach used is called self-consistent field (SCF). The HF theory is an *ab initio* method that is independent of any empirical parameters. The limitation of the single determinant model is that it does not adequately describe the global electronic structure and the effect on

this structure from instantaneous repulsion between the electrons. The effect of the electron-electron interaction beyond the HF approximation, which is the non-recovered energy, is called the correlation energy. The difference between the exact ground state total energy E_0 and the HF total energy is the correlation energy:

$$E_c = E_0 - E_{HF} \tag{2.75}$$

Even though E_c is a small percentage of the total energy, it makes a large and crucial contribution to energy differences (such as barrier heights). Therefore, for most applications in rotational spectroscopy, the HF method lacks accuracy, and it is important to go beyond the HF approximation and calculate the correlation energy, which is the goal of the post-HF methods. Some of them (those who are used in the context of this thesis) will be described after.

2.4.3 Møller-Plesset (MPn) perturbation theory

Møller-Plesset perturbation theory of n-th order (MPn) [70] is one of the theories developed to deal with the electronic correlation that is not included in the HF theory. It is a particular case of Rayleigh-Schrödinger perturbation theory [71] ($\hat{H} = \hat{H}^{(0)} + \lambda\hat{V}$), in which the zeroth-order Hamiltonian is chosen to be the many-electron Hartree-Fock Hamiltonian

$$\hat{H}^{(0)} = \sum_{i}^{N} \hat{F}(\vec{r_i}) \tag{2.76}$$

The corresponding perturbation operator $\hat{V}$ is thus the difference between the electron-electron Coulomb interaction and the HF potential

$$\hat{V}(x_1, x_2, \ldots, x_N) = \sum_{i}^{N}\sum_{i\neq j}^{N} \frac{1}{|r_i - r_j|} - \sum_{i}^{N} V^{HF}(x_i) \tag{2.77}$$

The zeroth-order ground state wave function is the HF single determinant Φ_0, and the zeroth-order excited state wave functions are the single, double,... excited determinants $\Phi_n = \Phi_a^r, \Phi_{ab}^r, \ldots$. The zeroth-order ground state energy $E_0^{(0)}$can be

given by the sum of the occupied orbital energies:

$$E_0^{(0)} = \Big\langle \Phi_0 \Big| \hat{H}_0 \Big| \Phi_0 \Big\rangle = \sum_a^{occupied} \epsilon_a \quad \text{with} \quad \langle \Phi_0 | \Phi_0 \rangle = 1 \tag{2.78}$$

The first-order energy correction is the expectation value of the HF determinant over the perturbation operator, which is calculated according to Slater's rules:

$$\begin{aligned} E_0^{(1)} &= \langle \Phi_0 | \hat{V} | \Phi_0 \rangle = \frac{1}{2} \sum_{a,b}^{occupied} \langle ab||ab\rangle - \sum_a^{occupied} \langle a|\hat{V}^{HF}|a\rangle \\ &= -\frac{1}{2} \sum_{a,b}^{occupied} \langle ab||ab\rangle \end{aligned} \tag{2.79}$$

which is according to the definition of the HF potential in eq. (2.72), we have used the fact that $\sum_a^{occupied} \langle a|\hat{V}^{HF}|a\rangle = \sum_{a,b}^{occupied} \langle ab||ab\rangle$. Therefore, the sum of the zeroth-order energy and first-order energy correction just give back the HF energy:

$$E_0^{(0)} + E_0^{(1)} = \sum_a^{occupied} \epsilon_a - \frac{1}{2}\langle ab||ab\rangle = \sum_a^{occupied} h_{aa} + \frac{1}{2}\langle ab||ab\rangle = E_{HF} \tag{2.80}$$

where we have used the fact that $\epsilon_a = h_{aa} + \sum_a^{occupied} \langle ab||ab\rangle$. The demonstration above shows that the correction to the HF energy starts from second-order terms.

The second-order energy correction, which is called in this context the second-order Møller-Plesset (MP2) correlation energy is:

$$E_0^{(2)} = E_c^{MP2} = -\sum_{n\neq 0} \frac{\left|\langle \Phi_0 | \hat{V} | \Phi_0 \rangle\right|^2}{E_n^{(0)} - E_0^{(0)}} \tag{2.81}$$

where Φ_n can be a priori single, double, triple, ... excited determinants. In fact, since $\hat{V}$ is a two-body operator, according to Slater's rules, triple and higher excitation with respect to Φ_0 give vanishing matrix elements $\langle \Phi_0 | \hat{V} | \Phi_0 \rangle$. In addition, it turns out that single excitation only gives a vanishing contribution as well. It thus remains only the double excitation $\Phi_n = \Phi_{ab}^{rs}$. Only the two-body part of the

perturbation operator gives a non-zero matrix element:

$$\langle \Phi_0 | \hat{V} | \Phi_{ab}^{rs} \rangle = \langle ab||rs \rangle \tag{2.82}$$

Besides, the zeroth-order energy corresponding to the doubly-excited determinant Φ_{ab}^{rs} is:

$$E_n^{(0)} = E_a b^{rs,(0)} = E_0^{(0)} + \epsilon_r + \epsilon_s - \epsilon_a - \epsilon_b \tag{2.83}$$

Using the two equations above, we arrive at the following expression for the MP2 correlation energy:

$$E_c^{MP2} = - \sum_{a<b}^{occupied} \sum_{r<s}^{virtual} \frac{|\langle ab||rs \rangle|^2}{\epsilon_r + \epsilon_s - \epsilon_a - \epsilon_b} \tag{2.84}$$

Using the anti-symmetry property of the integrals, i.e. $\langle ab||rs \rangle = -\langle ab||sr \rangle = -\langle ba||rs \rangle$, and the fact that $\langle ab||rs \rangle = 0$ if $a = b$ or $r = s$, the MP2 correlation energy can also be written without constraints in the sums as:

$$E_c^{MP2} = -\frac{1}{4} \sum_{a,b}^{occupied} \sum_{r,s}^{virtual} \frac{|\langle ab||rs \rangle|^2}{\epsilon_r - \epsilon_s - \epsilon_a + \epsilon_b} \tag{2.85}$$

Note that the MP2 correlation energy is always negative. The MP2 total energy can be simply given as $E_{MP2} = E_{HF} + E_c^{MP2}$. Since it is not a variational theory, the MP2 total energy is not necessarily above the exact ground-state total energy. It is also possible to calculate third- and fourth-order MP correlation energies in a similar manner, but it is usually considered not worthwhile in comparison to couple-cluster methods for example. In this work, the MP2 method gave good results without the need to use cluster corrections, to avoid the extensive use of computing resources and long calculation times.

2.4.4 Density functional theory (DFT)

The previous methods describe a system of N electrons and try to find the exact wave function, which is a function with $3N$, to solve the Schrödinger equation, thus requiring high computing resources to derive the solution. A very interesting

and successful approach is the density functional theory (DFT) which is based on a reformulation of the variational principle. It determines the electronic structure and the ground state energy by obtaining the electron density. This allows minimizing the dimensions of the calculated function down to 3 instead of $3N$. The references [63–65] cited herein can be used to have a detailed derivation of the theory and its equations.

To discuss the mathematical framework employed within the DFT theory, it is useful to start with a reminder about the Hamiltonian. If we consider an N-electron system within the Born-Oppenheimer approximation, the electronic Hamiltonian in the position representation, and in atomic units, can be written as:

$$\hat{H}(r_1, r_2, \ldots, r_N) = -\frac{1}{2}\sum_{i=1}^{N}\nabla_{r_i}^2 + \frac{1}{2}\sum_{i=1}^{N}\sum_{j=1}^{N}\frac{1}{|r_i - r_j|} + \sum_{i=1}^{N}\nu_{nc}(r_i) \tag{2.86}$$

where $\nu_{nc}(r_i) = -\sum_\alpha \frac{Z_\alpha}{|r_i - R_\alpha|}$ is the nuclei-electron interaction with R_α and Z_α being the position and charges of the nuclei. This Hamiltonian can be further written as:

$$\hat{H} = \hat{T} + \hat{W}_{ee} + \hat{V}_{ne} \tag{2.87}$$

where $\hat{T}$ is the kinetic energy operator, $\hat{W}_{ee}$ is the electron-electron interaction operator and $\hat{V}_{ne}$ is the nuclei-electron interaction operator.

The quantity of primary interest is the ground state energy E_0. The variational theorem establishes that E_0 can be obtained by the following minimization:

$$E_0 = \min_{\Phi}\langle\Phi|\hat{H}|\Phi\rangle \quad \text{with} \quad \langle\Phi|\Phi\rangle = 1 \tag{2.88}$$

the search is done over all N-electron anti-symmetric wave functions Φ.

DFT is based on a reformulation of the variational theorem in terms of the single-electron density, defined as:

$$n(r) = N\int\ldots\int|\Phi(x_1, x_2, \ldots, x_N)|^2 d\sigma dx_2 \ldots dx_N \tag{2.89}$$

which is normalized to the electron number $N = \int n(r)dr$.

The Hohenberg-Kohn theorem

Consider an electronic system with an arbitrary external local potential $\nu(r)$ in place of $\nu_{nc}(r)$. In 1964, Hohenberg and Kohn [72] showed that the ground state density $n(r)$ determines the potential $\nu(r)$, which in turn determines the Hamiltonian. In other words, the potential ν is a unique functional of the ground state density n, and all other properties as well. The ground state wave function Φ for the potential $\nu(r)$ is itself a functional of n, denoted by $\Phi(n)$, that was exploited by Hohenberg and Kohn to define the universal density functional $F(n)$ given by:

$$F(n) = \langle \Phi(n) | \hat{T} + \hat{W}_{ee} | \Phi(n) \rangle \tag{2.90}$$

which can be used to define the total electronic energy functional $E(n)$, for the specific external potential $\nu_{nc}(r)$ of the system considered, by :

$$E(n) = F(n) + \int \nu_{nc}(r) n(r) dr \tag{2.91}$$

The Kohn-Sham equations

The Hohenberg-Kohn theorem has proven the existence of a functional for the density, but was not able to solve it. Faced with the difficulty of directly approximating $F(n)$, Kohn and Sham (KS) [73] proposed to decompose $F(n)$ as:

$$F(n) = T_s(n) + E_{Hxc}(n) \tag{2.92}$$

where $T_s(n)$ is the non-interacting kinetic energy functional which can be defined with a constrained search formulation:

$$T_s(n) = \min_{\Phi \to n} \langle \Phi | \hat{T} | \Phi \rangle = \langle \Phi(n) | \hat{T} | \Phi(n) \rangle \tag{2.93}$$

with $\Phi \to n$ meaning that the minimization is done over normalized single-determinants wave functions Φ which yield the fixed density n. For a given density n, the minimizing single-determinant wave functions is called the KS wave function and is denoted by $\Phi(n)$. The remaining functional E_{Hxc} is called the Hartree-exchange-

correlation functional, and can be written as:

$$E_{Hxc}(n) = E_H(n) + E_{xc}(n) \tag{2.94}$$

with $E_H(n)$ the Hartree energy functional, representing the classical electrostatic repulsion energy for the charge distribution $n(r)$, given by:

$$E_H(n) = \frac{1}{2} \iint \frac{n(r_1)n(r_2)}{|r_1 - r_2|} dr_1 dr_2 \tag{2.95}$$

and $E_{xc}(n)$ is the exchange-correlation energy functional that needs to be approximated. It is often decomposed as:

$$E_{xc}(n) = E_x(n) + E_c(n) \tag{2.96}$$

with $E_x(n)$ being the exchange energy functional given by:

$$E_x(n) = \langle \Phi(n) | \hat{W}_{ee} | \Phi(n) \rangle - E_H(n) \tag{2.97}$$

and $E_c(n)$ being the correlation energy functional given by:

$$E_c(n) = \langle \Psi(n) | \hat{T} + \hat{W}_{ee} | \Psi(n) \rangle - \langle \Phi(n) | \hat{T} + \hat{W}_e e | \Phi(n) \rangle = T_c(n) + U_c(n) \tag{2.98}$$

Now if we write the total electronic energy in terms of spin-orbitals and integrate over the spin variables, we obtain:

$$E[\{\phi_i\}] = \sum_{i=1}^{N} \int \phi_i^*(r) \Big(-\frac{1}{2} \nabla^2 + \nu_{ne}(r) \Big) \phi_i(r) dr + E_{Hxc}(n) \tag{2.99}$$

where the density is expressed in terms of the orbitals as:

$$n(r) = \sum_{i=1}^{N} |\phi_i(r)|^2 \tag{2.100}$$

If we calculate this functional derivative we get:

$$\Big(-\frac{1}{2}\nabla^2+\nu_{ne}(r)\Big)\phi_i(r)+\frac{\partial E_{Hxc}(n)}{\partial\phi_i^*(r)}=\epsilon_i\phi_i(r) \tag{2.101}$$

Defining the Hartree-exchange-correlation potential $\nu_{Hxc}(r)$ as the functional derivative of $E_{Hxc}(n)$ with respect to $n(r)$ we have:

$$\nu_{Hxc}(r)=\frac{\partial E_{Hxc}(n)}{\partial n(r)} \tag{2.102}$$

which is itself a functional of the density, which leads us to the KS equations:

$$\left(-\frac{1}{2}\nabla^2+\nu_{ne}(r)+\nu_{Hxc}(r)\right)\phi_i(r)=\epsilon_i\phi_i(r) \tag{2.103}$$

The orbitals satisfying eq. (2.103) are called the KS orbitals and ϵ_i are their energies. They are eigen functions of the KS single-electron Hamiltonian:

$$h_s(r)=-\frac{1}{2}\nabla^2+\nu_s(r) \tag{2.104}$$

where ν_s is the KS potential, represented as:

$$\nu_s(r)=\nu_{ne}(r)+\nu_{Hxc}(r) \tag{2.105}$$

Following the decomposition of $E_{Hxc}(n)$ in eq. (2.94), the potential $\nu_{Hxc}(r)$ is decomposed as:

$$\nu_{Hxc}(r)=\nu_H(r)+\nu_xc(r) \tag{2.106}$$

where the Hartree potential is given by

$$\nu_H(r)=\frac{\partial E_H(n)}{\partial n(r)}$$

and the exchange-correlation potential is given by

$$\nu_{xc}(r)=\frac{\partial E_{xc}(n)}{\partial n(r)}$$

Similarly, following the decomposition of $E_{xc}(n)$ in eq. (2.96), the potential $\nu_{xc}(r)$ can be decomposed as:

$$\nu_{xc}(r) = \nu_x(r) + \nu_c(r) \tag{2.107}$$

where $\nu_x(r) = \frac{\partial E_x(n)}{\partial n(r)}$ is the exchange potential and $\nu_c(r) = \frac{\partial E_c(n)}{\partial n(r)}$ is the correlation potential. Thus, the Kohn-Sham equations are similar to the Hartree-Fock equations, with the difference that they involve a local exchange potential $\nu_x(r)$ instead of a non-local one and an additional correlation potential. The drawback of the Kohn-Sham method is the difficulty of evaluating the integrals which cannot be evaluated analytically, since the density involved in the functional is of fractional power. The integrals are usually evaluated over a grid of points in the three-dimensional space.

An important question that we can pose is: how can we express $\nu_{xc}(r)$ in a form suitable for all systems? Several approximations have been proposed to well-define the term $\nu_{xc}(r)$ and will be discussed herein.

The local density approximation (LDA) was introduced by Kohn and Sham [73], in which the exchange-correlation functional is approximated in a uniform electron gas as:

$$E_{xc}^{LDA}(n) = \int n(r)\epsilon_{xc}^{unif}(n(r))dr \tag{2.108}$$

where $\epsilon_{xc}^{unif}(n)$ is the exchange-correlation energy per particle of the infinite uniform electron gas with the density n. The function $\epsilon_{xc}^{unif}(n)$ can only be solved analytically and it is the sum of exchange ($\epsilon_x^{unif}(n)$) and correlation ($\epsilon_c^{unif}(n)$) contributions: $\epsilon_{xc}^{unif}(n) = \epsilon_x^{unif}(n) + \epsilon_c^{unif}(n)$. The exchange energy per particle of the uniform electron gas $\epsilon_x^{unif}(n)$ is associated with the names of Dirac [74] and Slater [75] and it can be calculated analytically by:

$$\epsilon_x^{unif}(n) = -\Big(\frac{3}{4}\Big)\Big(\frac{3}{\pi}\Big)^{\frac{1}{3}} n^{\frac{1}{3}} \tag{2.109}$$

However, the correlation energy per particle $\epsilon_c^{unif}(n)$ of the uniform electron gas cannot be calculated analytically. This quantity has been obtained numerically for a number of densities n using accurate quantum Monte Carlo calculations [76], and fitted to parameterized function of n. The two most used parameterizations are those of Vosko, Wilk and Nusair (VWN)[77] and

those of Perdew and Wang (PW92) [78].

Generalized-gradient approximation (GGA) was developed after the failure of gradient-expansion approximation (GEA) which will be described briefly herein. The GEA was the next logical step beyond the LDA and it was initiated by Kohn and Sham [79]. One way of deriving the GEA is to start from the uniform electron gas, introduce a weak and slowly varying external potential $\nu(r)$, and expand the exchange-correlation energy in terms of the gradients of the density to obtain:

$$E_{xc}^{GEA}(n) = E_{xc}^{LDA}(n) + \int C_{xc}(n(r))n(r)^{\frac{4}{3}}\left(\frac{\nabla_n(r)}{n(r)^{\frac{4}{3}}}\right)^2 dr \tag{2.110}$$

where $C_{xc}(n) = C_x + C_c(n)$ is the sum of the exchange and correlation coefficients of the expansion. The GEA should improve over the LDA providing that the reduced density gradient is small. Unfortunately, for real systems, the reduced density gradient can be large in some regions of space, and the GEA turns out to be a worse approximation than the LDA.

The failure of the GEA led to the development of generalized-gradient approximations (GGAs), which really started in the 1980s, of the generic form:

$$E_{xc}^{GGA}(n) = \int f(n(r), \nabla n(r))dr \tag{2.111}$$

where f is some function. The GGAs are semi-local approximations in the sense that f does not only use the local value of the density $n(r)$ but also its gradient $\nabla n(r)$.

Many GGA functionals have been proposed and the most widely known and used are those of Becke 88 (B88 or B) [80], Lee-Yang-Parr (LYP) [81], Perdew-Wang 91 (PW91) [82, 83] and Pedrew-Burke-Ernzerhof (PBE) [84]. The GDA methods are generally more efficient than LDA methods for the calculations of molecular structures, but they lack precision for the calculations of energies and barriers for transition-state.

Hybrid approximations They are based on the idea of combining the exchange

and correlation obtained in the GGA functionals with a fraction of HF exchange energy. This idea was proposed by Becke in 1993 [85, 86], and in particular, he introduced a three-parameter hybrid (3H) approximation of the form:

$$E_{xc}^{3H} = aE_x^{HF} + bE_x^{GGA} + (1-a-b)E_x^{LDA} + cE_c^{GGA} + (1-c)E_c^{LDA} \quad (2.112)$$

where the three parameters a,b and c are determined by fitting to experimental data. The notation HF is used to specify that the orbitals in these hybrid approximations are optimized in the HF way i.e. with a non-local HF exchange potential instead of a local one. This constitutes a slight extension of the usual KS methods. The main advantage of adding a fraction of HF exchange is to decrease the self-interaction error in the exchange functional.

The most famous and most used three-parameter hybrid approximation is B3LYP [87] which uses the B88 exchange functional and the LYP correlation functional, and the parameters $a = 0.20$, $b = 0.72$ and $c = 0.81$. In 1996, Becke proposed a simpler one-parameter hybrid (1H) approximation [88]:

$$E_{xc}^{1H} = aE_x^{HF} + (1-a)E_x^{DFA} + E_c^{DFA} \quad (2.113)$$

where E_x^{DFA} and E_c^{DFA} can be any (semi-local) density-functional approximations (DFA), and the fraction a of HF has to be determined. A strategy that has been used to construct approximations is to employ parameterized flexible functions for E_x^{DFA} and E_c^{DFA}, and systematically optimized all the parameters on large sets of physicochemical properties of molecular systems. For example, the Becke 97 (B97) exchange-correlation functional [89] is a hybrid GGA approximation containing 13 parameters optimized on atomic exchange and correlation energies, ionization potentials, and proton affinities. Another example is Becke 98 (B98) exchange-correlation functional [90] which is based on B97 and contains 10 optimized parameters. One more example is the so-called family on "Minnesota" functionals, and in particular M06 and M06-2X exchange-correlation functional [91] which are hybrid meta-GGA approximations containing 36 parameters optimized

on a very large set of diverse physicochemical properties concerning main-group thermochemistry, reaction barrier heights, non-covalent interactions, electronic spectroscopy and transition metal bonding. The particularity of the "Minnesota" functionals is that they integrate terms concerning interactions at mid-ranges. These mid-range terms, when combined with long-range interaction terms, are called dispersion forces. The dispersion plays a very important role in chemical systems and can give an idea of non-covalent interactions such as van der Waals interactions. The dispersion is not accounted for in the other functionals listed above, but can be considered, for example in B3LYP, by using the so-called "D3" correction of Grimme [92–94] combined with the Becke-Johnson damping function [95, 96].

Range-separated hybrid approximations A long-range correction scheme (LC) was proposed in 2001 by Iikura, Tsuneda, Yanai and Hirao [97] based on the ideas of Savin [98]. The LC energy is expressed as:

$$E_{xc}^{LC} = E_x^{lr,HF} + E_x^{sr,DFA} + E_c^{DFA} \tag{2.114}$$

where $E_x^{lr,HF}$ is the HF exchange energy for a long-range electron-electron interaction $W_{ee}^{lr}(r_{12}) = \frac{erf(\mu r_{12}}{r_{12}}$ with $r_{12} = |r_1 - r_2|$ is the inter-electronic distance and erf is the error function. An example of this class of approximations is the $\omega B97XD$ exchange-correlation functional [99] which is based on the B97 exchange-correlation functional with re-optimized parameters, and uses $a = 0.16$, $b = 1$ and $\mu = 0.3\, {a_0}^{-1}$

In the context of this thesis, a series of calculations was realized using the methods MP2, B3LYP, M06-2X and ωB97XD methods described above.

2.4.5 Basis sets

In all quantum chemical methods, the solution depends on describing the molecular orbitals (MO) as close to reality as possible. This is done by using a mathematical framework, named basis set, to describe the MO. A complete (infinite) basis set, can give an exact description of the MO, but in reality, this is impossible as the basis sets used are finite and approximations should be made according to

the computing resources available. Most methods express the MO as a linear combination of atomic orbitals (LCAO). It is convenient to define a particular set of basis functions for each nucleus, that share the characteristics of atomic orbitals (AO). The AO are described by two types of functions in literature:

- Slater type orbitals (STO) [100]. These were introduced by Slater in 1930 and they are described by:

$$\zeta_i(\xi, n, l, m, r, \theta, \phi) = N_{nlm\xi} r^{n-1} e^{-\xi r} Y_{lm}(\theta, \phi) \tag{2.115}$$

  where:

  - $N_{nlm\xi}$ is a normalization constant
  - r is the distance between nucleus and electron
  - n, l, m are orbital and magnetic quantum numbers
  - $Y_{lm}(\theta, \phi)$ constitute the angular part and are called the spherical harmonics. They describe the angular distribution of the orbital similar to the Hydrogen atom.
  - ξ is the radial power that characterizes the size of the orbital.

  It can be noted that the STO describe well the AO and vary in a similar way to the real wave functions. However, they are difficult to handle mathematically and require enormous computing power and resources.

- Gaussian type orbitals (GTO) [101]. These were proposed by Boys and McWeeny in 1950. The Gaussian functions are given by:

$$g(\alpha, a, b, c, r) = N_{abc\alpha} x^a y^b z^c e^{-\alpha r^2} \quad \text{with} \quad L = a + b + c \tag{2.116}$$

  where:

  - $N_{abc\alpha}$ is a normalization constant
  - r is the distance between nucleus and electron
  - x, y, z are Cartesian coordinates
  - α is the radial power

– a, b, c are exponents of the coordinates and their sum is used in a similar manner to the quantum number of atoms where $L = 0, 1, 2, 3$ indicate s-, p-, d- and f-type orbitals, respectively.

The Gaussian functions are much easier to handle computationally and are advantageous to calculate the mono- and bi-electronic integrals. However, they are far from having the same quality as the Slater functions in describing the AO. In fact, a linear combination (contraction) of several Gaussian functions (each is called a primitive) is needed to determine the form of an STO, according to the equation:

$$X^L(r) = N \sum_{k}^{K_A} c_k N_k x^{a_k} y^{b_k} z^{c_k} e^{-\alpha_k r^2} \tag{2.117}$$

where N is the normalization constant of the contraction and N_k is the normalization constant of each primitive. K_A refers to the degree of contraction, and c_k is the contraction constant that is specific to each basis and does not change throughout the calculation.

Minimal and multiple-zeta basis sets

A basis set is considered to be minimal if only one STO is used to describe a single AO in a molecule. Pople's STO-nG series of basis sets [102] is an example of a minimal basis set where the STO can be estimated by n GTOs (at least three).

An important aspect to consider concerning the AO, is the difference between valence and inner-shell electrons. Electrons close to the nucleus tend to be much more localized than valence electrons. Thus, it is common to describe the valence orbitals with more than one basis function, where each function can be composed of a fixed linear combination of primitive Gaussian functions. Basis sets that exploit this difference between core and valence electrons, and employ multiple GTOs to describe a STO, are generally called multiple-zeta (double-, triple-, quadruple-, ...) valence basis sets.

Polarization and diffuse functions

The flexibility of the electronic structure is an important feature to consider. Valence electrons take part in bond formation, as opposed to core electrons that are extremely localized, thus leading to deformation of the electronic cloud once an atom is placed near another atom or approached by a ligand, which is known as polarization. STOs, having quantum numbers higher than the highest occupied atomic orbital, are used to build polarization functions, that can be integrated into basis sets.

In certain types of molecules, such as anions, Van der Waals complexes or a hydrogen-bonded system, the valence electrons are loosely bound to the molecule, and they undergo long-range interactions. Thus, the atomic orbitals are very diffuse and need diffusion functions that can map the electron density correctly. These diffusion functions are characterized by their small ζ radial exponent that accounts for the long-range characteristics.

Many basis sets are available in the literature. In what follows, I will discuss the three main classes of basis sets used within the context of this thesis.

Pople-type basis sets

They are multiple-zeta valence basis sets introduced by John Pople [103, 104]. They are known to be intermediate between minimal and very high quality basis sets. These basis sets offer the flexibility to adjust the basis set for each study case. They describe the core orbitals with a linear combination of Gaussian primitives (one STO), and each valence orbital by two or more Gaussian primitives. The general nomenclature has the form: $N-XYZ\ldots$ where N is an integer giving the number of Gaussian primitives used to construct the STO of the core orbitals, and $X,Y,Z,\ldots$ are integers indicating the number of Gaussian primitives used to build each valence orbital. The number of integers after the dash indicates the multiple-zeta index of the basis set. Polarization functions can be added to these basis sets by adding the letter d followed by a bracket containing two letters indicating the angular momentum of the polarization function, and corresponding to the polarization orbitals of the second-row and hydrogen atoms, separated by a comma. Diffusion functions can be enclosed in the basis set by adding the "+"

symbol. Another "+" symbol signals that hydrogen atoms have diffuse orbitals as well. Here is an explanatory example of the 6-311++G(d,p) basis set used extensively throughout this work:

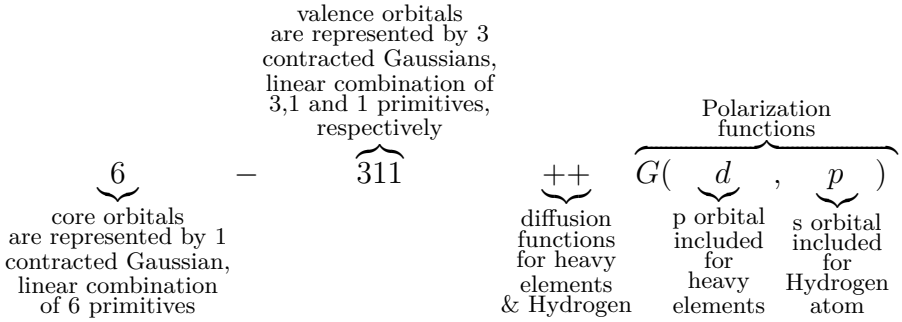

Dunning-type basis sets

They are also multiple-zeta valence basis sets, that were introduced by Dunning Jr. [105]. These basis sets take into account the electronic correlation, and they are specifically designed for correlation corrected methods. In addition, they are polarized basis sets. The base of their nomenclature is the abbreviation "cc" corresponding to correlation consistent. Meanwhile, the letter "p" symbolizes the polarization functions, and the expressions "VDZ, VTZ, VQZ, V5Z and V6Z" represent the number of contractions used to describe the valence orbitals (2, 3, 4, 5 and 6, respectively). It is also possible to add diffusion functions by adding the "aug-" prefix. An example of this class of basis sets is the aug-cc-pVTZ used in this work.

Ahlrichs' basis sets

In the context of this work, we are also interested in the second generation of the basis sets introduced by the Ahlrichs group at Karlsruhe [106, 107]. They are named as second-generation default or "def2". The radial exponents of these basis sets are those of Dunning cc-pVXZ. They are multi-zeta valence basis sets where the syntax "SV, TZV and QZV" correspond to split(double-zeta), triple-zeta and quadruple-zeta valence, respectively. A letter "P" after the valence syntax indicates the inclusion of polarization functions for elements other than hydrogen. Adding another "P" after the first indicates inclusion of polarization functions for

the hydrogen atoms as well. "def2TZVP" is an example of these basis sets, and it was used within this work. These basis sets are usually recommended to be used with DFT calculations.

2.5 Computational methods used in this work

Having the goal of avoiding unnecessary repetition of the same ideas in the different chapters, this section will report the common points of all the theoretical calculations made. The general approach is to group the standard operations performed in the same way for all the systems, in one place and in a simple representation. The remaining particularities, that cannot be grouped here, will be detailed in the corresponding chapter.

All calculations were performed using the Gaussian 16 software Revisions B.01 and C.01 [108], accessible on the high performance computing cluster available in PhLAM.

2.5.1 Complexes with H_2S

Most of the calculations for the two complexes analyzed within the context of this work were performed in a unified manner. Table 2.4 summarizes the methods used and the calculation types performed for the two complexes. The general strategy was to optimize the geometries of the possible conformers, followed by harmonic frequencies calculations of the optimized geometries. This permits to obtain the rotational constants of the different conformers, as well as the energy ordering to have an idea about the probability of observing the different structures and to ensure that the calculated geometry is the equilibrium geometry and not a transition state (absence of negative frequency). The obtained constants are used to predict molecular transitions that facilitate the search and assignment of experimental lines.

Table 2.4: *Calculations types performed for the two complexes at different levels of theory*

Fenchol$\cdots H_2S$ and Fenchone$\cdots H_2S$			
	Method	Basis set	Calculation types
ab initio	MP2[109–112]	6-311++G(d,p)[104]	opt[a], freq[b], wfx[c], NBO[a]
DFT	B3LYP [77, 87, 113, 114]	def2TZVP[106, 107]	opt[a], freq[b]
	M06-2X [91]	6-311++G(d,p)[104]	opt[a], freq[b]
	ωB97X-D[99]	6-311++G(d,p)[104]	opt[a], freq[b]

[a] Geometry optimization ;
[b] Harmonic frequencies;
[c] Wave function file (nci analysis);
[d] Natural bonding orbitals;

2.5.2 Limona ketone

The theoretical approach with LK was different, as only the molecule itself was the scope of the study. First, a PES was performed to determine the stable structures corresponding to real minima. Then, the geometries at these minima were optimized and harmonic frequencies calculations were made for the optimized geometries. The energy ordering and rotational constants of the possible conformers are obtained from these calculations, and they are used to predict and assign the experimental transitions. Also, transition state optimization calculations were needed for the treatment of internal rotation of the methyl group. The calculated barrier height is then used to predict and assign the lines. The used methods and calculation types are summarized in table 2.5.

2.5.3 Overview

The chemical quantum methods are indispensable tools to describe the electronic structure and geometries in the gas phase. The choice of the methods and basis sets is not straightforward, and there are no definite criteria to employ a universal and ideal combination of methods/basis sets. The choice is often based on experience and literature. The accuracy and reliability of the calculations vary with each

Table 2.5: *Calculation types performed for limona ketone at different levels of theory*

Limona ketone			
Method		Basis set	Calculation types
ab initio	MP2	6-311++G(d,p)	opt[a], freq[b], QST2[c]
		aug-cc-pVTZ[105]	opt[a], freq[b], QST2[c]
DFT	B3LYP	def2TZVP	opt[a], freq[b], QST2[c]
	B98[90]	aug-cc-pVTZ	PES[d], opt[a], freq[b], QST2[c]
	M06-2X	6-311++G(d,p)	opt[a], freq[b], QST2[c]

[a] Geometry optimization ;
[b] Harmonic frequencies;
[c] Quadratic synchronous transit (QST2) method for transition state (TS) optimization;
[d] Potential Energy Surface (PES);

molecular system, and the outcome should be compared carefully to experimental results. A comparison between calculated and experimental molecular parameters, for different molecules and complexes and using different methods and basis sets, will be reported in the corresponding chapters.

2.6 The interplay between rotational spectroscopy and theory

The exchange between theory and rotational spectroscopy occurs over many levels. Theoretical methods have achieved high accuracy that allows them to guide and facilitate experimental investigations. They can help as well to untangle challenging situations that cannot be overcome through experimental protocols alone. Also, theoretical outcomes, and especially molecular parameters, permit to predict rotational spectra which ease their assignment. At the same time, experiments constitute a high standard to benchmark the quantum chemical approaches and contribute to further improvements of these approaches and the implementation of new ones.

A review and an article, shedding the light on the role of theory in support-

ing rotational spectroscopy were published by Cristina Puzzarini [115, 116]. The following discussions highlight some of the important aspects of interchange between theory and experiment, that have been useful for the general aspect of this dissertation.

Molecular structures: Quantum chemical calculations are usually employed to optimize the geometry of a molecule at an equilibrium state using different methods and basis sets. After the convergence into equilibrium structure, molecular parameters such as the total electronic energies and the rotational constants, which are by far the most important parameters obtained from quantum methods, can be extracted. The energies can be used to predict the relative stability of different conformers, and the frequencies of the rotational transitions are predicted starting from calculated rotational constants. The prediction of the spectral patterns aids later in the experimental assignment of transitions. Moreover, comparing the experimental and theoretical rotational constants can help in deducing the experimental structure of the molecule. However, isotopic substitution remains the best method to determine the effective structure of a molecule, but it is not in the scope of this work.

Force Fields: The calculation of the harmonic and anharmonic force fields can be very useful in rotational spectroscopy. In particular, the harmonic force fields are necessary to determine the quartic centrifugal distortion constants. The force fields are also used to calculate the ro-vibrational frequencies. Another important point is the ability to derive and apply the zero-point corrections to the ground state energy of a molecule in its lowest vibrational state. Zero-point energy (ZPE) is the lowest energy a quantum system can have, and it arises from fluctuations in the lowest energy state due to Heisenberg uncertainty principle. Hence, the total energy of the system will be the calculated electronic energy plus ZPE. The influence of zero-point vibrations can be reflected as changes in the ground state energy and potential energy surfaces, and it can alter the energy ordering of non-rigid structural isomers.

Potential energy surfaces (PES): A molecule can exist in several stable conformers, and even in the low temperatures of a free supersonic jet, several of

these conformers can still be populated enough to be observed in the spectra. Hence, it might be useful in some cases to have in-depth information about the relative energies of different conformers, as well as the barrier heights for the conformational change. Such information can give a preliminary idea about what to expect to observe in the experimental spectra. The PES can be obtained in several ways, but as you will see in the upcoming chapters, it can be calculated by scanning along a geometry coordinate (e.g. bond length, bond angle or dihedral angle). This is only possible when the molecular flexibility and conformational change are restricted to a few coordinates. The complexity of the PES varies with the flexibility of the molecule or the molecular system.

Dipole moments: are another useful parameters that are obtained from quantum chemical calculations, including principal axes components as well as the total dipole moment. This can be very useful in the experiment, by knowing the polarization power needed for each transition type. It can also aid in assigning complex spectra, by establishing a link between the experimental lines and the different transition types of asymmetric-top molecules. The link can be done by comparing line intensities with calculated values (needs to be in principal axes representation), thus making it easier to assign experimental transitions to the calculated structure.

2.7 Spectral analysis and fitting

In the world of molecular spectroscopy, there is one central keyword that is the key to successful analysis: the Hamiltonian. The success of analysis is directly related to the choice of the correct Hamiltonian. In rotational spectroscopy it is not any different, the main goal is to find the appropriate rotational Hamiltonian that best describes the system under study. The Hamiltonian should incorporate the different quantum mechanical effects probed with the experimental method employed. There are different parameters and effects in play, and the experimental spectrum can be affected by several phenomena. For example, the average molecular charge distribution, can alter the molecular structure and consequently can

influence the experimental rotational constants. Other examples that can greatly influence the experimental spectrum include large amplitude motions, internal rotation and Coriolis coupling. In such cases, the coupling between vibrational and rotational levels cannot be ignored, and its description terms should be implemented in the Hamiltonian. An important factor to consider when choosing the Hamiltonian is the instrumental accuracy and frequency resolution of the setup. The influence of these factors can be attributed to the magnitude of separation of spectral features arising from the different physical quantities being probed. Higher resolution means probing weaker interactions, and thus including additional terms in the Hamiltonian. To be able to determine if the analysis is successful, one can ask the question: Does my Hamiltonian treat all the resolved physical features in my spectrum?

Sometimes, a compromise must be made to overcome a problem in the Hamiltonian particular to a molecular system. This compromise depends on the interest and goal behind the investigation. It is usually a trade-off between two main factors. The first one is the complexity of solving a Hamiltonian, and its capacity to well describe a system, and the second is the access to spectroscopic quantities of interest and the depth and significance of the information needed.

The assignment of rotational spectra is mainly done through well-known and documented software. There are many programs and codes available, matching different spectral problems and treating different interactions. These programs usually have implemented Hamiltonians, and operate by applying the least square method to optimize and reach a minimum set of parameters of the Hamiltonian capable of reproducing the spectrum up to instrumental accuracy. This is done after successfully assigning experimental transitions to the predicted ones, using their corresponding quantum numbers. The errors of the fitted parameters depend on several factors including the experimental accuracy, the number of transitions and the quality of the Hamiltonian chosen. Two programs have been used throughout this thesis:

SPFIT/SPCAT: It is a program suite developed by H.Pickett [117], and perhaps the most prominent and widely used tool for the prediction, fitting and analysis of high resolution rotational spectra. One of its key features is

its ability to deal with multiple molecular problems, as it is flexible in the construction of the Hamiltonian. It can be used with A- and S-reductions of Watson, and it implements centrifugal distortion along with other molecular interaction schemes such as quadrupole, spin-rotation, and Coriolis coupling as well as Fermi resonances.

XIAM: It is a program for the prediction and fitting of internal rotation data. It was developed by H. Hartwig [118], where it uses the extended Internal Axis Method proposed by Woods to treat internal rotation in an asymmetric-top molecule. It is widely used in the rotational spectroscopy community, and its popularity can be mainly attributed to its speed, ease of use and the ability to fit up to three symmetric internal rotors. It also includes other useful features such as quadrupole coupling of one nucleus with weak interaction and centrifugal distortion. Some empirical parameters were programmed in 1999 and can be found in the reference [119].

Any important and unmentioned information about the above two programs and their application to specific problems will be addressed further in the upcoming chapters, as needed.

CHAPTER

THREE

EXPERIMENTAL METHODS

This chapter will start with a theoretical description of the interaction of light with a molecular system, and the different techniques used to probe the polarization of molecules. Furthermore, the experimental details of the current Fabry-Pérot Fourier transform microwave spectrometers available in Lille [120, 121] will be reported, followed by a thermodynamic description of the supersonic expansion technique. In this chapter also, one can find the description, technical details and experimental performance of a chirped-pulse spectrometer that is newly constructed within the framework of this thesis. The last part will include a summary of the experimental conditions used for the different complexes and molecules studied throughout this thesis.

3.1 Bloch equations

In the previous chapter, the Hamiltonian was given for a molecule in the absence of an external field and it was considered unperturbed. However, this is not true if we want to obtain experimental spectroscopic information. In spectroscopic measurements, the interaction between the molecular system and the external electromagnetic field should be considered, and this is usually done by adding a time-dependent interaction term $\hat{V}(t)$ to the unperturbed Hamiltonian $\hat{H}_0$ [122]. In what follows, and for the sake of simplicity, a two-level quantum system will be

used to describe the physical systems. The system considered here is an isolated system with two non-degenerate levels $|a\rangle$ and $|b\rangle$, the lower and upper eigenstates, respectively.

The interaction is due to a linearly polarized electromagnetic wave F, propagating along the y-axis and having an amplitude $\mathcal{E}(r,t)$ (with r and t being position and time parameters):

$$F = \left(\frac{1}{2}\mathcal{E}(r,t)\mathrm{e}_z e^{i(ky-\omega t)} + \frac{1}{2}\mathcal{E}^*(r,t)\mathrm{e}_z e^{-i(ky-\omega t)}\right) \tag{3.1}$$

where ω is the angular frequency and k_y is the wave vector along the y-axis. In this example, the amplitude $\mathcal{E}$ is real and constant in space and time. Also, by applying the electric dipole approximation (interaction volume << wavelength of radiation), the propagation term ky can be neglected. F can be written as:

$$F = \frac{1}{2}\mathcal{E}\mathrm{e}_z(e^{i\omega t} + e^{-i\omega t}) \tag{3.2}$$

The interaction Hamiltonian $\hat{V}(t)$ is given by the product of the dipole moment operator $\hat{\mu}$ and the electromagnetic field F:

$$\hat{V}(t) = \hat{\mu} \cdot F = \begin{pmatrix} 0 & \mu_{ab} \\ \mu_{ba} & 0 \end{pmatrix} \cdot F = \begin{pmatrix} 0 & \mu \\ \mu & 0 \end{pmatrix} \tag{3.3}$$

The transition dipole moment μ_{ab} is the complex conjugate of μ_{ba}, and thus if μ_{ab} is real ($\mu_{ab} = \mu_{ba}^* = \mu_{ba} \equiv \mu$), and if the quantization axis of the molecule is chosen along the z-axis (parallel to the electromagnetic radiation), the total Hamiltonian $\hat{H}$ can be written as :

$$\hat{H} = \hat{H}_0 + \hat{V} = \begin{pmatrix} E_a & -\frac{1}{2}\mu\mathcal{E}(e^{i\omega t} + e^{-i\omega t}) \\ -\frac{1}{2}\mu\mathcal{E}(e^{i\omega t} + e^{-i\omega t}) & E_b \end{pmatrix} \tag{3.4}$$

The interaction of such two-level system with a resonant radiation is best described by density matrix formalism, introduced by von Neumann [123], where the density operator is defined by:

$$\hat{\rho} = \sum_n \mathrm{p}_n |\psi_n\rangle\langle\psi_n| \tag{3.5}$$

where p_n is the probability to encounter a quantum system in the state ψ_n. The Liouville equation is used to derive the time evolution of the density matrix of the isolated system:

$$i\hbar\frac{\partial\hat{\rho}(t)}{\partial(t)} = \left[\hat{H}(t), \hat{\rho}(t)\right] \tag{3.6}$$

The density matrix is defined by:

$$\hat{\rho} = \begin{pmatrix} \rho_{aa} & \rho_{ab} \\ \rho_{ba} & \rho_{bb} \end{pmatrix} \tag{3.7}$$

The Hamiltonian can be simplified by applying the rotating wave approximation (RWA), which is done within the interaction by convention[124]. The evaluation of the Liouville equations yields the following equations:

$$\frac{\partial\rho_{aa}}{\partial t} = -i\frac{\Omega}{2}(\rho_{ab}e^{-i\omega t} - \rho_{ba}e^{i\omega t}) \tag{3.8}$$

$$\frac{\partial\rho_{bb}}{\partial t} = -i\frac{\Omega}{2}(\rho_{ab}e^{-i\omega t} - \rho_{ba}e^{i\omega t}) \tag{3.9}$$

$$\frac{\partial\rho_{ab}}{\partial t} = i\omega_0\rho_{ab} - i\frac{\Omega}{2}(\rho_{aa}e^{-i\omega t} - \rho_{bb}e^{i\omega t}) \tag{3.10}$$

$$\frac{\partial\rho_{ba}}{\partial t} = i\omega_0\rho_{ba} - i\frac{\Omega}{2}(\rho_{aa}e^{-i\omega t} - \rho_{bb}e^{i\omega t}) \tag{3.11}$$

where $\Omega = \frac{\mathcal{E}\mu}{\hbar}$ is the Rabi frequency, and $\omega_0 = \frac{E_b - E_a}{\hbar}$ is the resonance frequency. The transformation into a rotating frame can eliminate the rapid oscillations at the optical frequency ω:

$$\varrho_{aa} = \rho_{aa} \tag{3.12}$$

$$\varrho_{bb} = \rho_{bb} \tag{3.13}$$

$$\varrho_{ab} = \rho_{ab}e^{i\omega t} \tag{3.14}$$

$$\varrho_{ba} = \rho_{ba}e^{-i\omega t} \tag{3.15}$$

The resulting equations are the so-called Bloch equations:

$$\frac{\partial \varrho_{aa}}{\partial t} = -i\frac{\Omega}{2}(\varrho_{ab} - \varrho_{ba}) \tag{3.16}$$

$$\frac{\partial \varrho_{bb}}{\partial t} = -i\frac{\Omega}{2}(\varrho_{ab} - \varrho_{ba}) \tag{3.17}$$

$$\frac{\partial \varrho_{ab}}{\partial t} = -i\delta\varrho_{ab} - i\frac{\Omega}{2}(\varrho_{aa} - \varrho_{bb}) \tag{3.18}$$

$$\frac{\partial \varrho_{ba}}{\partial t} = i\delta\varrho_{ba} - i\frac{\Omega}{2}(\varrho_{aa} - \varrho_{bb}) \tag{3.19}$$

where $\delta = \omega - \omega_0$ is the detuning from the resonance of the incident radiation. The time dependence of the density matrix elements of a two-level system can be described by the Bloch vector Θ precessing about the effective field vector Λ [124]:

$$\frac{\partial \Theta}{\partial t} = \Lambda \times \Theta \quad \text{with} \quad \Theta = \begin{pmatrix} u \\ v \\ w \end{pmatrix} = \begin{pmatrix} \varrho_{ab} + \varrho_{ba} \\ i[\varrho_{ab} - \varrho_{ba}] \\ \varrho_{aa} - \varrho_{bb} \end{pmatrix} = \begin{pmatrix} 2 \cdot \Re(\varrho_{ab}) \\ 2 \cdot \Im(\varrho_{ab}) \\ \Delta N \end{pmatrix} \tag{3.20}$$

and

$$\Lambda = \begin{pmatrix} -\Omega \\ 0 \\ \delta \end{pmatrix} \tag{3.21}$$

A pure two-state system is usually described by the so-called Bloch sphere, which is a unit sphere with the Bloch vector having a unit length. Upon interacting with the surroundings, the system cannot stay in its pure state as it undergoes population and coherence damping. Hence, it cannot be described by a single state vector any more, but rather by mixed states that lie within the Bloch sphere. Examples of damping mechanisms include spontaneous emission (inelastic collisions) which alter the populations and coherence. These can be accounted for, in the Bloch equations, by the damping constant γ_1 [125]. On the other hand, elastic collisions are an example that alter the coherence terms due to phase changes. A second damping constant Γ is used to account for these processes, and the damping constants γ_1 and Γ are combined into the damping constant $\gamma_2 = \frac{\gamma_1}{2} + \Gamma$. The Bloch equations describing a two-state system with damping terms can be written

as:

$$\frac{\partial \varrho_{aa}}{\partial t} = -i\frac{\Omega}{2}(\varrho_{ab} - \varrho_{ba}) + \gamma_1 \varrho_{bb} \tag{3.22}$$

$$\frac{\partial \varrho_{bb}}{\partial t} = -i\frac{\Omega}{2}(\varrho_{ab} - \varrho_{ba}) - \gamma_1 \varrho_{bb} \tag{3.23}$$

$$\frac{\partial \varrho_{ab}}{\partial t} = -(i\delta + \gamma_2)\varrho_{ab} - i\frac{\Omega}{2}(\varrho_{aa} - \varrho_{bb}) \tag{3.24}$$

$$\frac{\partial \varrho_{ba}}{\partial t} = (i\delta - \gamma_2)\varrho_{ba} - i\frac{\Omega}{2}(\varrho_{aa} - \varrho_{bb}) \tag{3.25}$$

In spectroscopic experiments, the polarization $\hat{P}$ is the probed observable and its expectation value is [124]

$$\left\langle \hat{P} \right\rangle = N \cdot \mathrm{Tr}(\hat{\rho}\hat{\mu}) \tag{3.26}$$

where N is the total number of molecules probed. The derivation of Bloch equations for a two-level system can be extrapolated to a multi-state system, through straightforward application of the RWA and transformation into a rotating frame. However, the complexity of these equations increases quickly.

There are several experimental techniques to probe the molecular transitions and they are discussed in the following.

Transient absorption

In these measurements, the molecules are subjected to monochromatic light, and the depletion in the light source, due to molecular absorption, is observed. It is also possible to observe optical nutation (Rabi oscillations) if the temporal resolution is enough.

Transient emission

In this technique, the molecules are excited by a short pulse (monochromatic) which is less than the relaxation times (damping constants). The molecules absorb the resonance frequencies, and re-emit damped signals that are called free induction decay (FID). The FID is observed in the time domain, and then a fast Fourier transform (FFT) is applied to obtain frequency spectra. In emission experiments, a perfect π-pulse is achieved for zero detuning and vanishing damping

mechanisms. It is not used, as it leads to population inversion and vanishing emission signal. A $\frac{\pi}{2}$-pulse is usually used since it yields maximum emission signal, and it can be achieved by choosing the pulse duration to satisfy the condition $\Omega \cdot t = \frac{\pi}{2}$.

Fast passage excitation

In such type of excitation, the frequency of the incident radiation is swept over the duration of the excitation pulse to match the molecular resonance. In this case, the effective field vector varies during the pulse and it is not constant anymore. In fast passage excitation, two regimes can be identified as follows:

Rapid adiabatic passage (RAP): In this regime, the Rabi frequency is large, leading to strong coupling that allows the Bloch vector to adiabatically follow the effective field vector. This can lead to population inversion (π-pulse condition).

Linear fast passage (LFP): In this regime, the Bloch vector cannot follow the effective field vector due to weak coupling, and thus no π-pulse can be achieved.

An illustration of the behavior of the Bloch vector in the two cases of fast passage excitation is represented in fig. 3.1.

Throughout this thesis, transient emission was used mainly to characterize the **fenchol-H_2S** and **fenchone-H_2S** complexes, as well as **limona ketone**. Also, the LFP excitation was used for the characterization of the newly built chirped-pulse spectrometer that will be discussed later.

3.2 The pulsed microwave spectrometer

Fabry-Perot Fourier transform microwave (FP-FTMW) (FP-FTMW) spectroscopy is a black background study of molecules that are mixed and diluted in an inert carrier gas (usually Argon, Neon or Helium). The gas-molecule mixture is expanded into a resonant Fabry-Pérot cavity, maintained under high vacuum, by a pulsed injector with a small orifice thus creating a supersonic expansion. A short microwave pulse is used to polarize the molecular ensemble and the cavity-

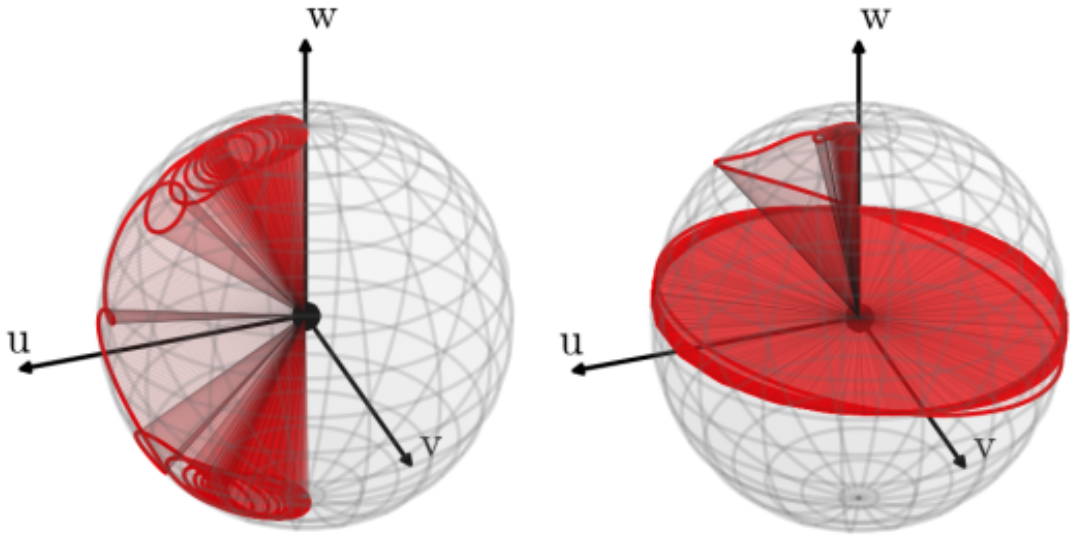

(a) **(b)**

Figure 3.1: *Bloch sphere representations, in the rotating frame, of a chirped-pulse in (a) the RAP regime where the Bloch vector can follow the driving vector smoothly as the chirped-pulse pass through resonance, leading to population inversion, and (b) the LFP regime where the Bloch vector cannot follow the driving vector smoothly anymore due to weak coupling. The LFP regime is best suited for maximizing the polarization of the molecular ensemble. The two figures have been reproduced from the thesis dissertation of David Schmitz.[126]*

amplified molecular response is recorded in the time domain and then converted into a frequency domain spectrum by applying an FFT.

A detailed description of the technique can be found in the reference [127]. Also, the PhD dissertation of S. KASSI [128], the HDR manuscript of D. PETITPREZ [129] and the reference [121] could be consulted by the reader for further details about the two spectrometers in Lille.

An overall synoptic of the spectrometer showing the main instruments as well the trigger and reference clock lines is illustrated in fig. 3.2.

3.2.1 Basis of operation

The two spectrometers operating in the PhLAM laboratory are based on the transient emission technique described in the previous section. This technique is com-

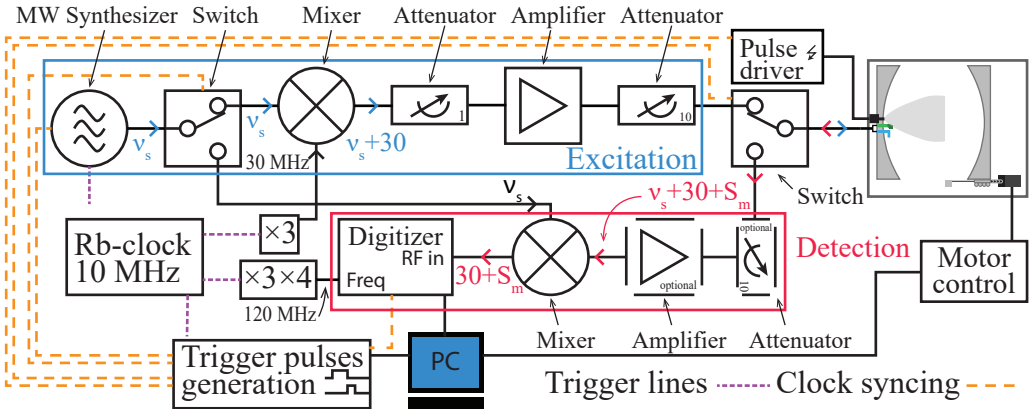

Figure 3.2: *Simplified scheme of the experimental setup of the pulsed microwave spectrometer. The signal is generated by a microwave synthesizer, added to 30 MHz and transmitted into the optical cavity by an L-shaped antenna. The difference between the transition frequency and the polarization frequency is transmitted from the cavity by the same antenna, heterodyned and recorded by a 14-bit digitizer card integrated into a computer. A 10 MHz Rb-frequency standard is used to phase lock the instruments, as well as in multiplication chains to obtain the necessary frequencies for mixing and digitizing. Triggering pulses are generated by a NI digital I/O device. The timing parameters are defined in a computer program, that is used to control to automate the spectrometer, and applies an FFT to obtain the frequency domain spectrum.*

posed of two main phases:

Excitation phase: Where the molecules, being in the gas phase, having a permanent dipole moment μ are polarized by a short microwave pulse. In this technique the population n of the gas formed by N molecules and oscillating as a function of time t, and the macroscopic polarization P of the system (considered as a two-level system) can be written as:

$$\begin{cases} n(t) = n_0 \cos(\Omega t) \\ P(t) = -i\mu n_0 \sin(\Omega t) \end{cases}$$

where n is the number of molecules interacting with the exciting wave and proportional to the population difference (of the two energy levels in the simplified system), n_0 is the value of n at thermodynamic equilibrium tem-

perature T_0 of the gas and Ω is the Rabi frequency. The maximum polarization is achieved by the $\frac{\pi}{2}$ condition i.e. $t = \frac{h}{4\mu E_0}$. When this condition is verified, the projection of the dipole moments (μ) on the principal inertia axes of all the molecules are aligned and produce maximum polarization of the gas (see fig. 3.3). In our experimental setup, the excitation branch is composed primarily of a microwave synthesizer (Agilent E8247C) which provide monochromatic radiation (called ν_s) starting from 1 up to 20 GHz. The signal is then transmitted either into the excitation line or to the detection line (which will be described later) by a fast single pole double throw switch (L3 Narda-MITEQ S238B 1). After the switch, the excitation signal is attenuated and then mixed with a 30 MHz signal produced by a multiplication ($\times 3$) of a 10 MHz signal, that is supplied by a 10 MHz rubidium frequency standard clock (SRS FS725), by an up-converter (L3 Narda-MITEQ SM0218LC1MD). The resulting signal (ν_s+30 MHz) is amplified by a fixed gain amplifier placed between two manual attenuators (Agilent 8494B and 8495B) that permit adjusting the polarizing power between -50 and 10 dBm. The signal is then transmitted by another rapid single pole double throw switch (L3 Narda-MITEQ S238B 2) into the cavity containing the molecular gas through an L-shaped antenna.

Detection phase: starts after the cut-off of the excitation pulse, where the non-zero polarization of the gas decreases exponentially as a function of time while oscillating at the frequency of the excitation wave. This frequency is known as the molecular transition frequency. The obtained signal is called free induction decay (FID), and the mechanism producing it is known as optical precession. The polarization at any time can be expressed by:

$$P(t) = P_0 e^{\frac{-t}{\gamma_2}} \cos(\omega_0 t) \tag{3.27}$$

with γ_2 being the coherence damping time, which is the time needed to reach zero polarization. It is usually in the order of hundreds of micro-seconds. The sinusoidal emitted signal, corresponding to the frequency of the rotation of the molecule, can be detected directly by an antenna. The amplitude of the field received by the antenna is proportional to the macroscopic oscillation

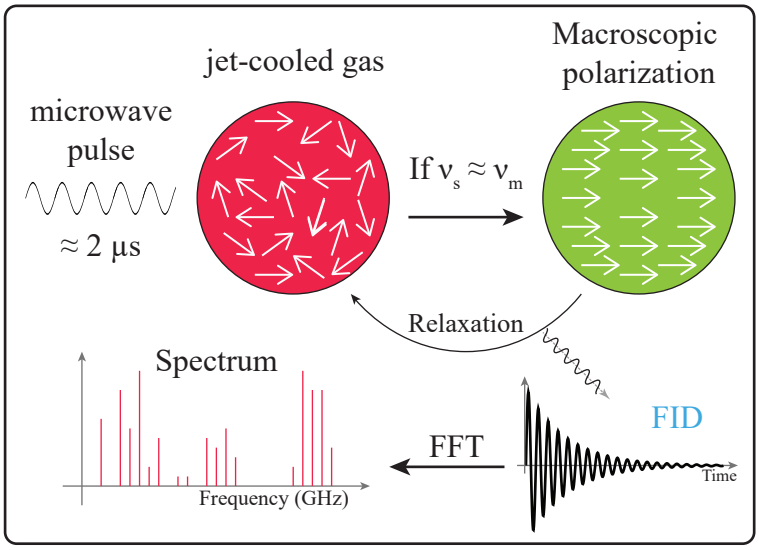

Figure 3.3: *A scheme illustrating the phases of transient emission experiment. ν_s and ν_m correspond to the frequencies of the excitation pulse and molecular transition, respectively.*

of the dipole moment and can be written as:

$$S(t) \propto P(t) = n_0 \mu e^{\frac{-t}{\gamma_2}} \cos(\omega_0 t) \tag{3.28}$$

Figure 3.3 can be consulted for the general FID signal emission and detection. In our experimental setup, the detection branch starts with the same L-shaped antenna that is used for the polarization signal. The molecular FID signal is called ν_m. It is important to keep in mind that the cavity acts like a pass-band filter with a maximum width of 1 MHz. This means that the cavity will be resonant only for molecular signals having a frequency difference less than 1 MHz from the polarization frequency. Thus, all the molecular signals detected will have a frequency ν_m close to the polarizing frequency ν_s such that $S_m = |\nu_s - \nu_m| < 1$ MHz. So, the total signal (ν_s+ 30 MHz +S_m) is transmitted by the antenna to the rapid switch (L3 Narda-MITEQ S238B 2) which directs the electric signal towards an optional manual attenuator (Agilent 8465B) followed by an optional (necessary for very weak signals) amplifier (L3 Narda-MITEQ MPN4). In our setup, the molecular signal,

between 2 and 20 GHz, must be down-converted to low frequencies (heterodyne) to be visualized and measured. This is done by a mixer (L3 Narda-MITEQ IRB0218LC1A) which subtracts ν_s from the total detected signal. Thus the remaining signal $(30 + S_m)$ is amplified (L3 Narda-MITEQ AU-2A-0110) and sampled by an acquisition card (AlazarTech ATS460) which is placed inside a PC. The card samples with a frequency of 120 MHz that is supplied and ensured in phase by employing a multiplication circuit (×3,×4) on the 10 MHz signal of the Rb reference. The memory of the card permits to record a maximum of 262 144 points, corresponding to 1 point every 0.46 kHz (see table 3.1).

Table 3.1: *Measurement resolution as a function of the number of points recorded by the 14-bit acquisition card. resolution (kHz)* $= \frac{120\times10^3}{N}$

Number of points	8192	16384	32768	65536	131072	262144
Resolution (kHz)	14.65	7.32	3.66	1.83	0.92	0.46

The automation of the spectrometer is achieved by a computer program written in LabVIEW, that controls the timing sequence of the experiment as well as the motor responsible for the movement of the mirror. A NI card (PCI-DIO-32HS) is used to generate the pulses that trigger the synthesizer to operate, change the switches' positions between excitation and detection, trigger the pulse drivers to open the gas valves and finally trigger the acquisition card to accumulate data. High phase stability is required throughout the experiment, and for this goal the instruments are phase-locked to an Rb-frequency standard.

3.2.2 Fabry-Perot resonant cavity

The optical cavity of type Fabry-Perot is made up of two identical spherical mirrors. The mirrors are characterized by their diameter d and radius of curvature R. One of the mirrors is fixed and the second can be moved horizontally by a step-by-step motor, thus changing their distance of separation denoted by L. The Fabry-Perot cavity acts as an amplifier that permits to enhance the signal quality, as the energy distribution inside the cavity follows well-defined rules. A spatial

distribution of the electromagnetic field corresponding to a resonance frequency is called a resonance mode. The three dimensional distribution of the energy in the cavity can be characterized by the notation TEM_{mnq} where TEM_{mn} describes the transversal modes corresponding to two dimensions, and q is a parameter describing the longitudinal structure of the mode. A resonant frequency ν_{mnq} can be associated for each mode in the cavity such that:

$$\nu_{mnq} = \frac{c}{2L}\Big[q + \frac{1}{\pi}(m+n+1)\arccos(\pm\sqrt{g_1 g_2})\Big] \tag{3.29}$$

with m,n and q being integers characterizing the mode and g_i ($i = 1,2$) being a parameter depending on the geometry of the cavity:

$$g_i = 1 - \frac{L}{R_i} \tag{3.30}$$

This parameter can be omitted as the two mirrors used are identical and thus $g_1 = g_2$. The modes inside the cavity are divided into two categories:

- Transversal modes also called Hermite-Gauss modes: it is the case where $m + n > 0$ and the modes are designated by TEM_{mn}. The energy is not concentrated over the axis of the cavity. In the case where m and n are even, their energy distribution is null along the axis.

- Longitudinal modes, or Gaussian modes: in this case $m = n = 0$, and the modes are designated by TEM_{00q}. The energy distribution has cylindrical symmetry, and its maximum is concentrated along the axis of the cavity. They are also called the fundamental modes.

We are interested in the fundamental modes as the onic jet in our experimental setup is directed parallel to the axis of the cavity. Thus, in order to have maximal amplification, we should have the energy distribution compatible with the gas distribution inside the cavity, meaning it should be concentrated over the axis of the cavity.

Going back to eq. (3.29), we can see that it is composed of two terms. The first term, which only depends on q, gives the expression of the resonance frequencies

of a plane-parallel resonator:

$$\nu_q = q\frac{c}{2L} \qquad \text{with} \qquad q = 1, 2, \cdots \tag{3.31}$$

This permits to define the frequency difference between two successive modes, known as the free spectral range (FSR) given by:

$$FSR = \frac{c}{2L} \tag{3.32}$$

where c is the speed of light in vacuum and L is the distance between the two mirrors.

As previously mentioned, the gas is expanded along the optical axis of the cavity, thus the maximum concentration of the molecules is found along this axis. Hence, it is preferable to excite the molecules using the fundamental modes. This necessitates that the central frequency of the mode is close to the frequency of the molecular transition while satisfying the $\frac{\pi}{2}$ condition. This can be achieved by moving the mobile mirror of the cavity, and the distance L necessary for each value of q can be calculated by eq. (3.29). As the motor used to move the mobile mirror is controlled by a PC, and the distance for each mode can be estimated, it is thus possible to perform an automatic scan of defined frequency step over all the spectral range of the spectrometer.

Despite being an amplifier that enhances the signal, the Fabry-Perot cavity possesses a physical limitation that can cause signal loss or reduction due to the phenomenon of auto-diffraction. It is necessary then to have the dimensions of the mirrors larger than the wavelength used. The Fresnel number N can be used to control or reduce the loss due to diffraction. N is defined as a function of the diffraction spot size by a circular aperture R, aperture radius d and the wavelength λ:

$$N = \frac{d^2}{\lambda R} \tag{3.33}$$

In order to minimize the loss by diffraction, d should be large compared to R to respect the condition $N >> 1$. For the limiting case of $N = 1$ we can obtain the low cutoff frequency:

$$\nu_{LF} = \frac{cR}{d^2} \tag{3.34}$$

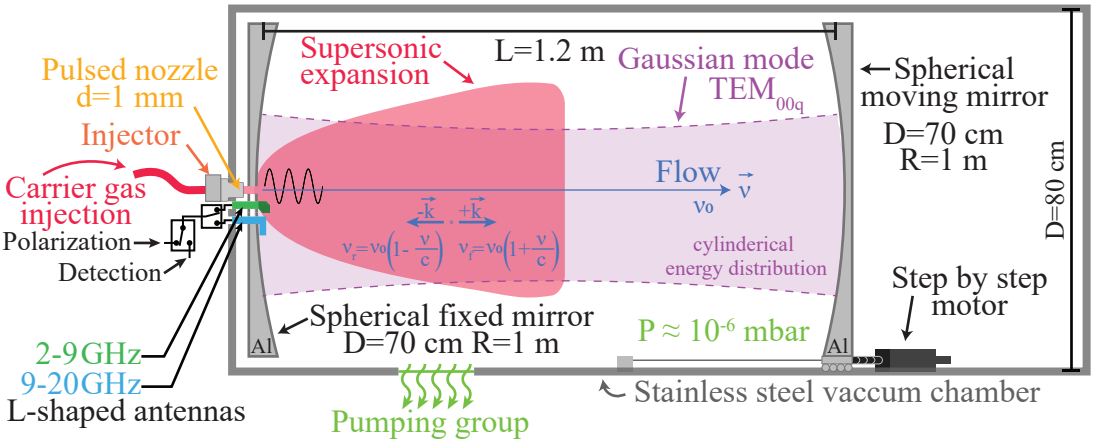

Figure 3.4: *Schematic representation of the optical cavity and the vacuum chamber of the SIMO2 spectrometer.*

Other losses also exist inside the cavity, and they are mainly due to deformations in the mirrors' geometry and to the presence of antennas. The quality of the resonator can be described by a quality factor Q defined as the ratio of the central frequency ν of the mode and its width at half maximum $\Delta\nu$:

$$Q = \frac{\nu}{\Delta\nu} \tag{3.35}$$

The fixed mirror has a hole in its center to insert the nozzle of the injector. Just below it is another hole where an L-shaped wired antenna is inserted. This antenna serves for the conversion of the electric wave from the cables into free electromagnetic radiation inside the Fabry-Perot cavity (and vice-versa for detection). As a general rule, the optimum antenna dimensions are equal to $\frac{\lambda}{4}$ over the short edge and $\frac{\lambda}{2}$ over the long edge . In one of our spectrometers, the fixed mirror has a third hole where a second antenna is inserted. This eliminates the tedious changing of antennas when going up or down the frequency range.

PhLAM possesses two spectrometers. The first is called SIMO (Spectromètres à impulsions micro-ondes in French). It has two mirrors with dimensions: d=0.4 m, R=0.8 m and L=1.2 m. It possesses one antenna and operates in the range 4-20 GHz. The second is called SIMO2. It has two mirrors with the following dimensions: d=0.7 m, R=1 m and L=1.2 m. It possesses two antennas one that functions over

the range 1 to 9 GHz and another that functions over the remaining range of 9 to 20 GHz. The lower cutoff frequencies of the two spectrometers are governed by the geometries of their mirrors, and the upper cutoff limits are due to the maximum limit of the microwave synthesizer. A general descriptive schematic of the SIMO2 spectrometer is illustrated in fig. 3.4.

Throughout this thesis, the two spectrometers have been used in the following manner: for the Fenchone$\cdots H_2S$ and Fenchol$\cdots H_2S$ complexes only the SIMO2 spectrometer have been used, whereas for the limona ketone molecule both spectrometers were used.

3.3 Supersonic jet expansion

The coupling of microwave spectrometers to atomic and molecular beam techniques, since 1975, improved the sensibility and the resolution of FTMW spectrometers vastly. The employment of gas expansion techniques is not limited to one type of spectrometer, and it can be applied to several types of spectrometers. The use of such techniques, especially the supersonic expansion that is used in our three spectrometers, is advantageous on many levels which will become more clear by the end of this section.

Atomic and molecular beams, and in our case free jets, are different types of gas expansion. In general, they occur when gas is expanded from a high pressure medium to vacuum through a small opening. The pressure in the container P_0 and the diameter of the opening D are two factors that determine the type of the expansion. Two cases are possible:

Effusive beam: It is formed when $D <<$ the mean free path length λ

Supersonic beam: It is formed when $D >> \lambda$

In this work, we are only interested in supersonic jets, and thus no further discussion about effusive beams will be made.

In the supersonic jet, cooling of the internal degrees of freedom is achieved by transforming the internal energies into kinetic translational energies through collisions. We can explain that by a thermodynamic point of view. First of all, we

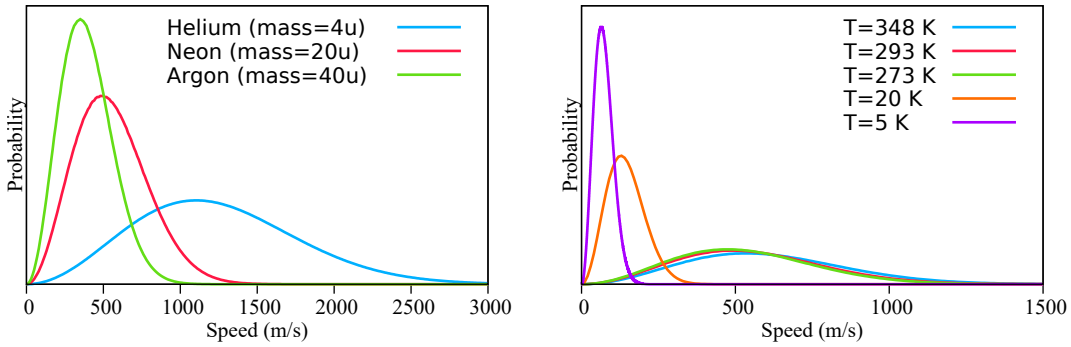

Figure 3.5: *(a) Maxwell-Boltzmann velocity distributions of different rare noble gases at room temperature (293 K) and (b) Maxwell-Boltzmann velocity distributions of Neon gas at different temperatures.*

are concerned with the velocity distribution inside the jet, as we are speaking of translational energies. Before the expansion, the velocity distribution in the high pressure container, of an ideal monoatomic gas, follows the Maxwell-Boltzmann distribution and depends only on the atomic mass and temperature as follows:

$$P(v) = 4\pi \left(\frac{m}{2\pi k_B T} \right)^{\frac{3}{2}} v^2 e^{-\frac{mv^2}{2k_B T}} \tag{3.36}$$

The effect of atomic mass on the velocity distribution can be observed in fig. 3.5a and the effect of temperature can be observed in fig. 3.5b. During the expansion, the collisions transfer energy leading to lower temperatures and narrower velocity distribution. The expansion is considered adiabatic, thus the transfer can be characterized by conservation of the sum of enthalpy and kinetic energy according to the following equation:

$$h_0 = h + \frac{v^2}{2} \tag{3.37}$$

where h_0 is the total enthalpy of the gas (per unit of mass), h is the enthalpy (per unit of mass) and v is the velocity of the flow of the gas. By definition, enthalpy is the fraction of internal energy of a fluid susceptible to being transformed into kinetic energy. For an ideal gas, a small variation in enthalpy can be expressed as

a function of the specific heat c_p and variation in temperature by :

$$dh = c_p dT \tag{3.38}$$

and the differential equation from eq. (3.37) leads to:

$$c_p T_0 = c_p T + \frac{v^2}{2} \tag{3.39}$$

This equation shows that the velocity of the gas is complementary to the temperature. Thus, an increase in the velocity will be accompanied by a decrease in the temperature. If the enthalpy is completely transformed into a directed mass flow, the terminal velocity of the ideal gas v_{max} can be expressed by:

$$v_{max} = \sqrt{\frac{2R\gamma(T_0 - T)}{(\gamma - 1)M_m}} \tag{3.40}$$

where R is the ideal gas constant, γ is the specific heat ratio defined by: $\gamma = \frac{C_p}{C_v}$ and $\gamma = \frac{5}{3}$ for a monoatomic gas, T_0 is the temperature of the container, T is the temperature in the jet and M_m is the molar mass of the gas. Considering the gas is monoatomic, the equation for v_{max} at the limiting case of $T << T_0$ can be rewritten as:

$$v_{max} = \sqrt{\frac{5RT_0}{M_m}} \tag{3.41}$$

eq. (3.41) is an approximation considering $T \to 0\,\mathrm{K}$. The expansion is not complete, and the most probable velocity of the gas corresponding to the maximum velocity of its Maxwell-Boltzmann distribution can be estimated by:

$$v_{mp} = \sqrt{\frac{2RT}{M_m}} \tag{3.42}$$

which means that after the expansion, the distribution is very narrow. The effects of mass and temperature on the velocity distribution are illustrated in figs. 3.5a and 3.5b, respectively.

The supersonic expansion is a very dynamic process, and many parameters that affect the collisions come into play within the jet. However, there exist ana-

lytical and empirical formulas to characterize the thermodynamic properties such as temperature, pressure or density for all the jet, in a position-dependent manner. This means that such properties can be estimated depending on the position downstream the jet, and this will be discussed after.

The jet can be divided into different regimes according to the Mach number which is the ratio of the velocity of the jet v to the velocity of sound a, and which is written as:

$$M = \frac{v}{a} \tag{3.43}$$

The comparison with the speed of sound is due to the fact that the Mach number expresses the amount of thermal energy transformed into kinetic energy. A qualitative scheme of the jet can be found in fig. 3.6. Three main zones can be identified in the expansion:

$M << 1$ This zone is inside the container. The frequency of collisions between the molecules in this zone is high due to the high pressure and temperature. Thus, the mean particle velocity is much smaller than the speed of sound.

$M = 1$ This zone can be considered at the exit of the orifice. The pressure difference between the container and the vacuum chamber causes the particle to accelerate. Due to this acceleration and to the reduction in the section while passing through the orifice, the speed of the gas is the same as the speed of sound.

$M >> 1$ This zone starts after the orifice exit. The collisions become negligible as the density decreases, and the jet reaches high terminal velocities that are much higher than the speed of sound, which makes the expansion supersonic. The jet has a barrel shape, and the collisions with the background gas cause shock waves to form at the boundaries. These shock waves play an important role in protecting the molecules inside the jet from colliding with the warm background gas. The central zone of the jet surrounded by the shock waves, and where no collisions take place, is called the silence zone. Interaction with polarizing radiation takes place inside this zone where the temperatures are the lowest.

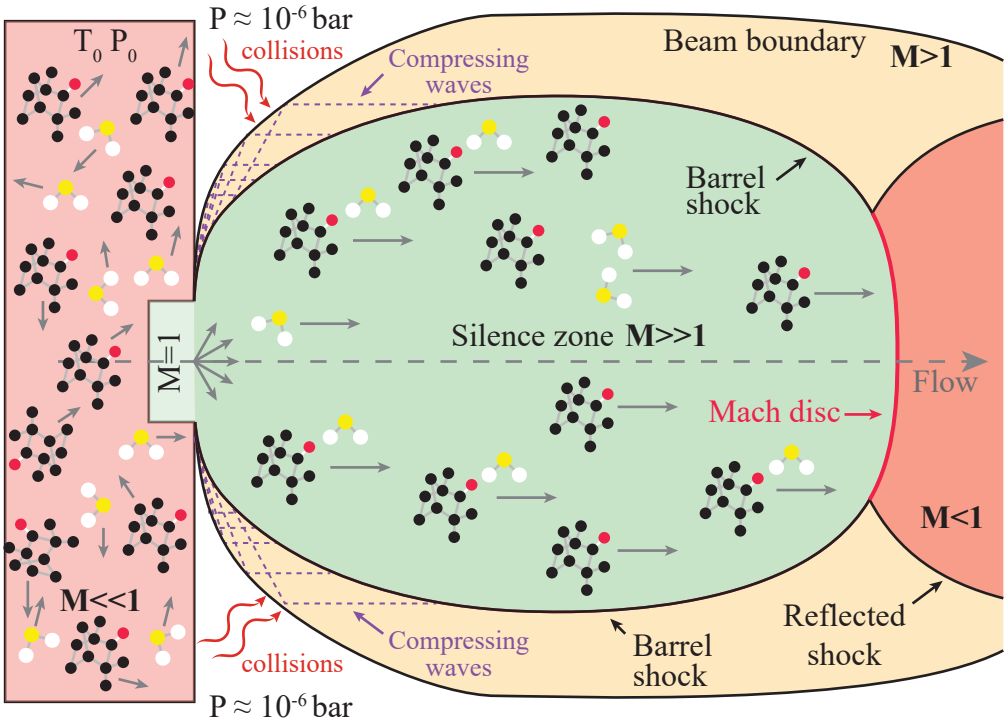

Figure 3.6: *Scheme representing the different parts of a supersonic expansion and the value of the Mach number in each region. The barrel shock wave is formed around the jet due to collisions of the expanding molecules with the background gas. The central shock wave called the Mach disk, and the barrel shock waves represent the limits of the jet. The silence zone, in the center, is the ideal region for spectroscopic measurements, where there is no interactions due to low particle density. A low static temperature is reached in the silence zone. The scheme includes an example of fenchone and H_2S molecules in the jet.*

The length of the silence zone is determined by the central shock wave called the Mach disk, whose position can be determined by the following empirical formula [130]:

$$x_m = 0.67D\sqrt{\frac{P_0}{P_b}} \tag{3.44}$$

where x_m is the position of the Mach disk downstream the jet (length of the silence zone), D is the diameter of the orifice, P_0 is the pressure in the container and P_b is the background pressure in the chamber vacuum. It is also possible to calculate the Mach number at different positions in the jet using the following empirical

relation[130]:

$$M = \left(\frac{x_m}{D}\right)^{\gamma-1}\left[3.606 - \frac{1.742}{x} + \frac{0.9226}{x^2} - \frac{0.2069}{x^3}\right] \tag{3.45}$$

where γ is the specific heat ratio and x is the distance downstream the jet. The cooling efficiency of the jet depends on the electronic structure of the molecule. This is due to the fact that the lower the energy difference between internal degrees of freedom, due to the fewer collisions are required to cross the energy gap and transform into translational energy. Based on this, the rotational energy levels are the most effectively cooled, as the energy differences are small. The vibrational cooling depends on the structure greatly and the low lying modes are efficiently cooled. At one point, the rate of collisions in the jet becomes so small that the internal degrees of freedom become frozen, meaning that the internal energy distribution is no longer changing. The vibrational energy is frozen before the rotational energy. Also, the order of magnitude of the different temperatures is as follows: $T_{vib} >> T_{rot} > T_{trans}$. This is due to the efficiency of collisions in transferring into translational energy of the different modes. In general, the order of magnitude of the rotational temperature is lower than 10 K.

The efficiency of the jet can be characterized by three parameters: Temperature, pressure and molecular density. These can be estimated analytically depending on their position downstream the jet according to the following equation [130]:

$$\frac{T}{T_0} = \left(\frac{P}{P_0}^{\frac{\gamma-1}{\gamma}}\right) = \left(\frac{\rho}{\rho_0}^{\gamma-1}\right) = \frac{1}{1+\frac{1}{2}(\gamma-1)M^2} \tag{3.46}$$

In the above equation, T_0, P_0 and ρ_0 are the temperature, pressure and density in the reservoir, respectively, while T, P and ρ are the same parameters but in the jet, γ is the specific heat ratio and M is the Mach number.

As mentioned above, the two body collisions that take place in the expansion are responsible for the cooling of the internal degrees of freedom. However, three body collisions can also occur leading to the formation of clusters. The collision rates Z_2 and Z_3 of the two types of collisions scale differently as follows:

$$Z_2 = \frac{P_0 D}{T_0} \tag{3.47}$$

$$Z_3 = \frac{P_0^2 D}{T_0} \tag{3.48}$$

We can see that two body collisions are proportional to $P_0 D$ whereas three body collisions are proportional to $P_0^2 D$. We can then say that lower pressure and smaller orifice diameter can reduce clustering. The terminal velocities, at 300 K, are 1765, 790 and 560 $\mathrm{m\,s^{-1}}$ for He, Ne and Ar, respectively.

In the supersonic free jet experiments conducted throughout this thesis, the gas used is a rare atom gas (mainly Neon) doped with a small fraction of molecules to be investigated. The molecules in liquid and solid phases are heated inside the injector to increase their vapor pressure. The inert gas is then seeded with the vapor of these molecules. In the case of gas samples, a mixture of the inert gas with a fraction of molecular gas is prepared before the injector and then directly expanded into the vacuum chamber. In both cases, the fraction of the molecules in the carrier gas does not exceed 2 %. This ensures that the molecules do not alter the temperature and velocity distribution of the gas atoms, and exhibit similar thermodynamic behavior.

The pulsed supersonic expansion, which is used throughout this work, is an enhancement over the continuous jet providing better cooling. The mixture of carrier gas and molecules is injected into the cavity in a pulsed manner by a controlled valve (the details of the injector used will be discussed later). The diameter of the orifice is of the order of 1 mm. An advantage of the pulsed jet is the lower consumption of chemical products.

The advantages of coupling a pulsed supersonic expansion to microwave spectrometers are clearer now, and are summarized below:

Higher resolution: In the adiabatic expansion, very efficient cooling of the internal degrees of freedom of the molecule can be achieved. This leads to narrow velocity distribution inside the jet due to low translational temperatures, thus minimizing the thermal agitation causing the Doppler effect. Also, the high dilution inside the jet implies a low concentration of molecules, which eliminates the pressure broadening of the lines. Hence, the line widths are dominated by transient time (or natural) broadening and convective Doppler broadening due to radial velocities. This results in very narrow molecular transitions, of full width half maximum (FWHM) less than 10 kHz,

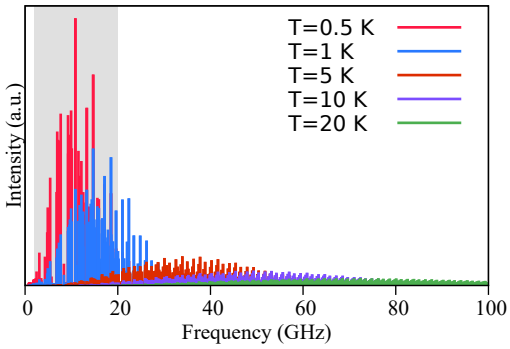

Figure 3.7: *Simulated rotational spectra of the monoterpenoid nopinone ($C_9H_{14}O$) at different rotational temperatures in thermal equilibrium. The rotational constants are taken from [131]. The portion of the graph in gray is the functioning zone of our spectrometers.*

permitting to perform high resolution molecular spectroscopy.

Simpler and more intense spectrum: The effective cooling of the vibrational and rotational degrees of freedom decreases the population of high energy levels and limits the population to the lowest levels ($J < 10$). The resulting spectrum is much simpler due to the limited number of populated levels, and also more intense as the population is now limited to a few rotational states. This facilitates the understanding and analysis of the spectra. We can explain the intensity of the states by the probability of population of a rotational state P_j in thermal equilibrium which is given by the Boltzmann distribution:

$$P_j = \frac{N_j}{N} = \frac{g_j e^{-\frac{E_j}{k_B T_R}}}{Q_R} \tag{3.49}$$

where N_j is the number of molecules in the rotational state having E_j, T_R is the rotational temperature and g_j is the quantum state degeneracy. Q_R is the rotational partition function which can be expressed as a function of the rotational temperature T_R and the three rotational constants A,B and C as follows [53]:

$$Q_R = 5.34 \times 10^6 \sqrt{\frac{T_R^3}{ABC}} \tag{3.50}$$

The 5.34×10^6 term is used to ensure the proper conversion of units, where A,B and C are in MHz and T is in K. The effect of the rotational temperature on the intensity and complexity of the spectrum is depicted in fig. 3.7.

Complexes formation: Three-body collisions that occur during the expansion favor the formation of non-covalent complexes and clusters. Clustering is not always a drawback, as van der Waals complexes and hydrogen-bonded complexes are easily formed in the cold conditions of the jet, and they are of interest for the context of this work, as we are interested in studying complexes of BVOCs with sulfur containing compounds. Therefore, supersonic expansion is an indispensable tool for studying van der Waals complexes and hydrogen-bonded complexes.

3.4 Doppler splitting

The translational speed of the molecules inside the cavity is much smaller than the speed of light ($v << c$). Thus, we can assume that the molecules are excited by a stationary electromagnetic field. This results in the superposition of two unidirectional waves: The first has an opposite direction to that of the wave vector and designated by $-\vec{k}$, and the second parallel to $\vec{v}$ and designated by $\vec{k}$. Hence, the recorded signal will be composed of two components, and the molecular emission signal ν_0 will be shifted by a magnitude of $\pm\frac{v}{c}\nu_0$. Therefore, the experimentally observed frequency will be the arithmetic average of the two Doppler components:

$$\nu_0 = \frac{\nu_r + \nu_f}{2} \tag{3.51}$$

where ν_r and ν_f are the reflected ($-\vec{k}$) and forward ($\vec{k}$) frequencies, respectively. This has been illustrated in fig. 3.4. The difference in frequency between the two components of the transition can be used to calculate the speed v of the molecules in the jet, by using the following formula:

$$v = \frac{c}{2}\frac{\Delta\nu_D}{\nu_0} \tag{3.52}$$

The difference in frequency $\Delta\nu_D = \nu_f - \nu_r$ varies depending on the carrier gas used (Ar, Ne or He), as well as the frequency value.

3.5 Injection system

This small section serves to describe the injection system employed to achieve jet-cooled conditions on the three spectrometers.

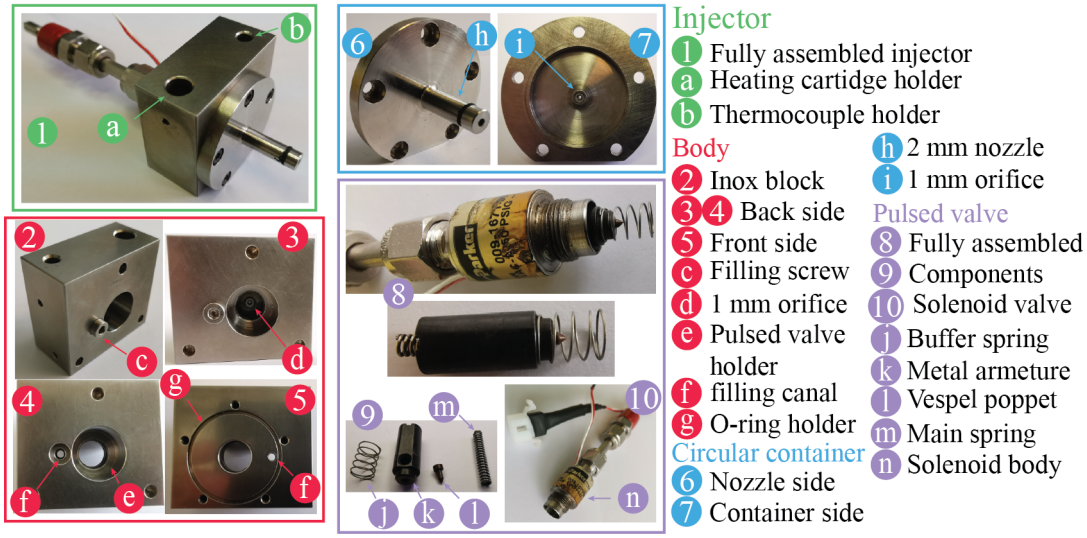

Figure 3.8: *The different components of the injector used throughout the experiments, from different viewing angles. The different parts have been classified into three main groups: the stainless steel body, the cylindrical container and the solenoid valve. A detailed explanation can be found in the text.*

The injection system used for the supersonic expansion in our experimental setup is placed outside the vacuum chamber, and it is universal for use on any of our spectrometers. The stainless steel injector is assembled from several parts. The central piece is a stainless steel block of dimensions 4.9 cm×4.3 cm×2.4 cm (L×W×D). From one side, a circular stainless steel piece with an extending nozzle of length 2 cm and diameter 2 mm, is connected by five small screws to the body. This part acts as the sample container with a central orifice of diameter 1 mm that extends along the nozzle. From the other side, a First Sensor series 9 pulse valve is attached through a central threaded hole. The pulsed valve is composed of a

solenoidal valve that drives a hollow metal armature containing a poppet that fits inside the orifice to control the flow of the gas. The poppet is fixed in place by a main spring that fits inside the armature. There is also a buffer spring between the armature head and the sample container around the orifice. The steel body also has a threaded canal that is used to fill liquid samples (and sometimes solid) into the container after the assembly and it is closed by a screw. O-rings are used to seal all the movable parts in order to prevent any leak. The steel body also has two holes on its top side that are used to insert a heating cartridge and a thermal sensor. This serves to heat and monitor the temperature of the injector when solid or liquid samples are used. The maximum temperature limit is determined by the threshold of the valve and the o-rings and is about 200 °C. The assembled injector is inserted into the optical cavity (maintained under vacuum) through a hole in the center of the fixed mirror and directly above the wired antenna. The carrier gas is seeded by a Teflon or stainless steel tube that connects the inert gas cylinder directly to the pulsed valve. An explanatory scheme of the injector is shown in fig. 3.8 above.

In the case of gas samples, a mixture is prepared beforehand in a sampling cylinder, and the cylinder is directly connected to the pulsed valve. More details will be given in the section of experimental conditions.

3.6 Chirped-Pulse spectrometer

In 1974, McGurk *et al.* introduced a fast passage excitation technique, in which they irradiated a molecular system with a fixed microwave frequency, and employed the Stark effect to quickly sweep the molecular transitions [26]. Another way to achieve fast passage excitation is to sweep the excitation frequency over the molecular resonance. Brown *et al.* were the first to successfully employ this frequency sweeping technique in the cm-wavelength region, by making use of the huge advancements in microelectronics to generate a digital microwave chirp (a pulse with a linear sweep of frequency over time) [30]. Both techniques should be fast compared to the relaxation time of the molecule.

One of the objectives of this thesis was to contribute to the development of a new chirped-pulse Fourier transform microwave (CP-FTMW) spectrometer oper-

ating in the 6-18 GHz range. A good starting point would be to describe what is a microwave chirp. By definition, a chirp is a signal in which the frequency increases (up-chirp) or decreases (down-chirp) with time. In this work, we are interested in linear chirps, whose waveform can be described by the following formula of the electric field:

$$\mathcal{E} = \mathcal{E}_0 e^{i(\omega_i t + \frac{\alpha t^2}{2})} \tag{3.53}$$

where $\mathcal{E}$ is the amplitude, $\mathcal{E}_0$ is the maximum amplitude, ω_i is the initial frequency and α is the chirp rate defined by the initial frequency ω_i, final frequency ω_f and the pulse duration τ_{pulse} by:

$$\alpha = \frac{\omega_f - \omega_i}{\tau_{pulse}} \tag{3.54}$$

at any time, the instantaneous frequency of the chirp can be obtained by:

$$\omega = \omega_i + \alpha t \tag{3.55}$$

At the weak field limit, that is when the Rabi frequency is slow relative to the sweep rate, there is no inversion of the population (as described before in the previous section). And, if we assume that the duration of the pulse is much less than the relaxation time, the polarization response $|P|$ for each transition within the chirped excitation pulse can be given by[132]:

$$|P| = \frac{2|\mu_{ab}|^2 \mathcal{E} \Delta N_0}{\hbar} \sqrt{\frac{\pi}{\alpha}} \tag{3.56}$$

with N_0 being the initial population difference of the two-level system. Consequently, the intensity of the emitted molecular signal, S, is proportional to:

- number of molecules N
- transition frequency ω
- square of transition dipole moment μ_{ab}
- amplitude of the excitation radiation $\mathcal{E}_0$
- population difference of the two states involved in the transition ΔN_0
- inverse square root of the chirp rate α

$$S \propto N \cdot \omega \cdot |\mu_{ab}|^2 \cdot \mathcal{E}_0 \cdot \Delta N_0 \cdot \sqrt{\frac{\pi}{\alpha}} \tag{3.57}$$

CP-FTMW spectrometer was first introduced by the group of Brooks Pate in 2006 [133] and described in detail in 2008 [30]. Since then, many groups adopted the new technique and it has been used widely. The newly constructed spectrometer presented here is inspired by the initial design, and makes use of the latest microelectronic and measurement devices. It covers the 6-18 GHz range, and a technical description of its different parts will be given in what follows.

Before the detailed description, a brief highlight of my personal contribution to this project might further clarify the objective of this dissertation. As the chirped-pulse technique has been applied for more than ten years, and many laboratories adapted this technique, this work started by building an extensive bibliography of the designs used in different groups, to point out key differences and get information of any possible difficulties or problems. The second step was to propose a timing sequence that takes into consideration the available instruments and the desired level of performance to achieve. Next, the assembly of the vacuum chamber and the pumping system took place, along with the physical connection and linking of the different electronic instruments that make up the spectrometer. After the full assembly and connection, basic tests were performed to characterize the polarization chirp, effectiveness of the proposed timing sequence and the detection capabilities. After the preliminary tests, a test spectrum of acetone was recorded between 6 and 18 GHz. Other more complicated tests are being performed in the meantime, but they are out of the time scale of writing this manuscript.

3.6.1 Technical characteristics of the spectrometer

The spectrometer can be described by separating it into four main parts: Chirp generation and amplification, polarization, detection and timing. The different instruments, electronics and materials that constitute the spectrometer have been summarized in the descriptive scheme of fig. 3.9. They have been grouped in a manner that highlights the different phases. A 10 MHz Rb-frequency standard is used to phase-lock the AWG, delay generator and the oscilloscope to ensure phase stability and consequently coherent averaging.

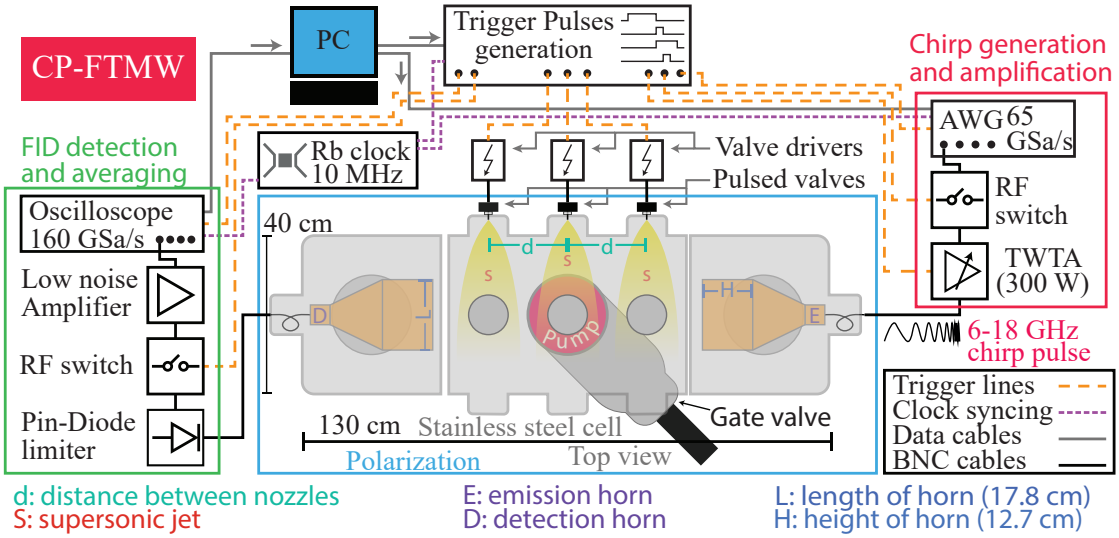

Figure 3.9: *Scheme of the general experimental setup of the new chirped-pulse Fourier transform microwave (CP-FTMW) spectrometer. The chirp is calculated by a PC program, generated by the AWG, amplified by the travelling wave tube amplifier (TWTA) and then transmitted into the vacuum chamber by a microwave horn. The molecular FID is collected with another identical horn, amplified by low noise amplifier (LNA) and recorded on an oscilloscope. The AWG, the triggering cards and the oscilloscope, which require high phase stability, are phase-locked to a 10 MHz Rb-frequency standard. The characteristics of vacuum chamber and the horns are listed. The different types of connections are explained by a legend inside the figure.*

Generation and amplification

The heart of the spectrometer is a 65 GSa/s AWG (Keysight M8195A), which is responsible for the generation of microwave chirps. The pulses usually have a bandwidth of 12 GHz, where they are linearly swept from 6 to 18 GHz (or the inverse) over a duration ranging typically between 1 and 4 µs. The chirps are generated numerically by a computer program and then sent to the AWG memory to be synthesized. Due to the absence of an optical cavity, as in the Fabry-Perot Fourier transform microwave (FP-FTMW) spectrometer described before, this type of spectrometer lacks the power amplification achieved by reflections in the optical cavity. Hence, an adjustable high power (300 W) TWTA (Instruments for Industry GT186-300) is needed to amplify the weak RF signal synthesized by

the AWG. A solid-state single pole single throw microwave switch (ATM S1517D) is placed between the AWG and the TWTA to better protect the sensitive detection devices by inhibiting the amplification of any undesired signal. The amplified chirp is introduced into the vacuum chamber, after amplification, by a microwave horn antenna (ATM 650-442-C3) that is rated for 6.5-18 GHz.

Polarization

The molecular system under study is polarized by the excitation pulse inside the vacuum chamber. The vapor of the molecular sample (solid, liquid or gas) is seeded into a noble gas mixture and supersonically expanded into the vacuum chamber through one, two or three pulsed injectors. The pulsed injectors are described in detail in section 3.5. In brief, they are composed of a pulsed valve (PARKER IOTA ONE pulse driver system, PARKER General Valve Series 9), a sample container that can be heated up to 160 °C and a 1 mm orifice. The three injectors are mounted on the side of a 130 cm stainless steel chamber, and they are separated by 20 cm. They are about 10 cm far from the edge of the horns. The mounting of the injectors can be seen in fig. 3.10b. The interest and advantages of studying the samples in jet-cooled conditions is described in section 3.3.

The vacuum chamber is a stainless steel cylinder with a diameter of 40 cm and a length of 130 cm. It is divided into three parts: A 60 cm central part and two 35 cm parts that attach to each side of the central piece. The chamber is sealed with ISO-K 400 to ISO-K 100 reducer flanges on each side, where the ISO-K 100 flanges have N-type microwave pass-throughs that are used to couple the output of the TWTA to the emission horn, and the receiving horn to the detection input outside of the chamber. The side pieces have ISO-K 200 flanges on their bottom side, each having an array of M6 screws that are used to mount the horns inside the chamber. The central piece has a total of 9 ISO-K 100 flanges (3 on the right, 3 on the top, 3 on the left sides). These are used to mount the injectors, pressure gauges and different pumping and venting valves. The central piece also has an ISO-K 200 flange that is used to connect the gate valve (VAT 12 146-PA44) and turbo-molecular pump (Leybold TURBOVAC MAG W 700 iP). The pumping speed of the turbo-molecular pump is $590\,\mathrm{L\,s^{-1}}$ (with N_2) and it is backed by a

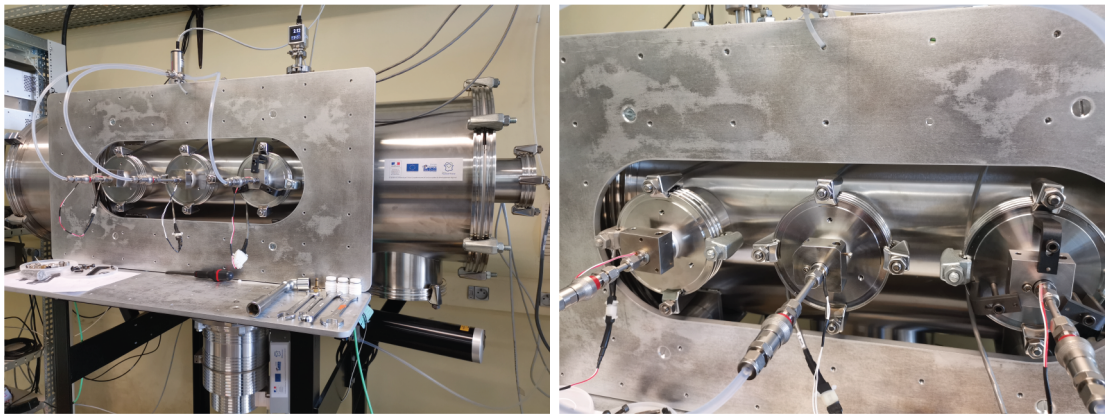

(a) **(b)**

Figure 3.10: *Part of the experimental setup of the chirped-pulse spectrometer showing (a) the stainless steel vacuum chamber and (b) the three injectors mounted on the side of the chamber*

mechanical booster pump (Edwards EH500) and a rotary vane pump (Leybold TRIVAC D 40 B). The pressure inside the chamber is monitored by a Pirani gauge (LEYBOLD TTR101N) for the primary vacuum and a cold-cathode gauge (LEYBOLD PTR225N) for the high vacuum. An image of the vacuum chamber with three mounted injectors is shown in fig. 3.10. The two horns inside the chamber are separated by 70 cm. The interaction of the internally cold molecules with the amplified microwave radiation, that is transmitted by the horn, takes place inside the vacuum chamber. A macroscopic dipole moment, resulting from the polarization of the molecule, is formed when a frequency lying within the chirp is resonant with a molecular transition.

Detection

The FID molecular signal, resulting from the relaxation of the macroscopic polarization of the molecules, is received by the second horn antenna (ATM 650-442-C3), amplified by an LNA (MITEQ JS42-6 001 800-20-10P) and recorded on a 160 GSa/s (63 GHz) oscilloscope (Keysight DSOZ634A). In order to protect the oscilloscope from the high power output of the TWTA during the excitation phase, a high power pin diode limiter (AMS/COBHAM ACLM-4537) is placed after the receiv-

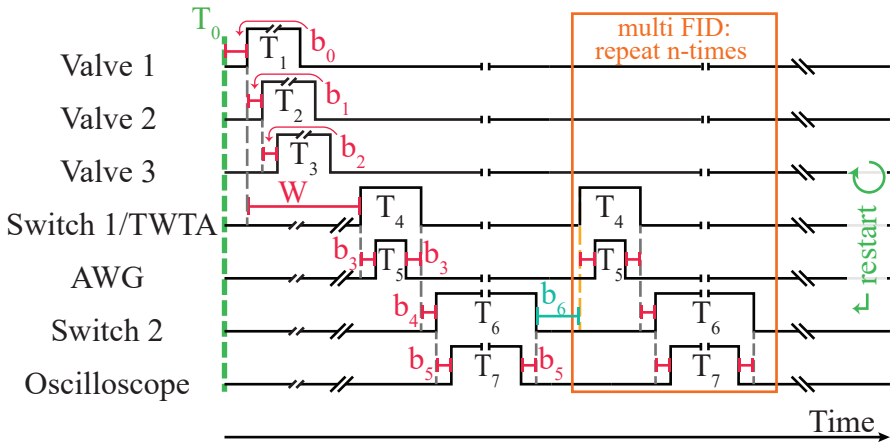

Figure 3.11: *Triggering pulse train of the experiment. The sequence order is from top to bottom, meaning that the first triggered instrument is the valve and the last is the oscilloscope. The numbered b constants are small time delays (buffers), of the order of 500 ns, and their objective is discussed in the text. The main timing parameters are the numbered T-letters. They indicate the pulse width during which the instruments are triggered. The repetitions (n-times) necessary to achieve multi-FID detection are shown in the scheme. Also, the repetition determining the repetition rate (injection frequency) are represented (m-times).*

ing horn. A solid-state single pole single throw microwave switch (ATM S1517D) is also used after the pin diode limiter to ensure full protection of the oscilloscope by blocking any excess leaking power. An FFT is performed on the collected time-domain FID signal by the oscilloscope and the frequency-domain signal is transferred into a computer for further analysis. Between hundreds and millions of averaged accumulations are required to achieve an acceptable signal-to-noise ratio (S/N), due to the low photon energy in the microwave region, and this is related to the magnitude of the dipole moment as well as the molecular density of the sample.

Timing

The experimental timing sequence of the spectrometer needs to be precisely controlled to achieve optimum results, by varying different factors. The timing sequence is a repetitive pulse train generated by a digital pulse and delay genera-

tor (Berkeley Nucleonics Corp Model 577). It can be triggered externally by NI counter/timer cards (National Instruments PCI-6602) integrated into the main computer, which runs the programs that control the experiment. The interest in triggering the delay generator is to have the possibility to perform multiple excitation and detection sequences within one gas pulse (multi-FID approach). The pulse train used to trigger the different instruments is depicted in fig. 3.11 and can be used to correlate the description given herein. The reference of time is determined by the T_0 parameter of the delay generator. First of all, a buffer time b_0 is introduced before any trigger signal to account for any delay during the rearming initialization. The valve driver is triggered and it keeps the valve open for time T_1. The other two valve drives are also triggered for the times T_2 and T_3 if the application of the three injectors is desired. T_1, T_2 and T_3 can be the same or different, and they can be delayed in between by the buffers b_1 and b_2, giving a wide margin of adjusting to achieve better signal optimization. The excitation begins after a waiting time W, representing the flight time delay, during which the molecules expand freely into vacuum. W can end before the gas pulse, considering the small distance available for the jet, and depend on the carrier gas used. For example, argon is expected to take longer time than neon. The excitation starts by closing the first RF switch and triggering the TWTA for a time T_4. Then, the AWG is triggered to fire the microwave chirp for a time T_5 corresponding to the pulse duration. A small delay b_3 before and after T_5 is provisioned to account for the ramp-up time of the TWTA and for the delay in response of the instruments. T_5 and b_3 is used to calculate T_4. The switch remains closed and the TWTA operates during the time T_4, but it only amplifies for the time the chirp is emitted. After that, and following a small delay b_4, the second microwave switch is closed for the duration T_6. The small delays ensures the proper stopping of the amplifier and that the sensitive detection electronics are well protected. The detection phase is started with the triggering of the oscilloscope, which records for the time T_7. It is triggered after a small wait b_5 relative to the switch to make sure there is no interference between the excitation pulse and the molecular FID. The switch is opened again after the same buffer b_5 to make sure all the signal was recorded and to reinitialize the sequence. The excitation/detection trigger pulses can be repeated in the case where multi-FID recording is desired. A buffer b_6 is used before

the repetition to ensure the stability of all instruments and to properly re-arm all triggers. Multi-FID serves to record multiple molecular signals in one gas pulse thus reducing the time needed for averaging dramatically. For the time of writing this manuscript, the multi-FID approach is not yet employed, and the corresponding sequence depicted in fig. 3.11 is just an anticipation of future employment. Without the multiple detection sequence, the repetition rate of the experiment is limited to the number of injections per second ($\approx 9\,\mathrm{Hz}$ with 1 injector and $\approx 4\,\mathrm{Hz}$ with 3 injectors) and is related to the capacity of the pumping system to maintain vacuum inside the chamber.

3.6.2 Experimental performance

This section presents the preliminary results of operating the new chirped-pulsed spectrometer. The performance of the spectrometer was characterized first by the ability of the AWG to generate a computer traced chirp, the quality of the signal emitted and received by the horns and the capabilities of the oscilloscope to record the signals. The timing sequence and delays were optimized to optimize the S/N ratio in the spectrum of acetone. The influence of using multiple nozzles injection on the intensity of signals was also examined. Finally, the performance of the oscilloscope regarding measurement times, sample rate and averaging are monitored to determine the optimum conditions.

Excitation chirp

The high sampling rate of the AWG ($65\,\mathrm{GSa/s}$) permits it to generate a chirp of $12\,\mathrm{GHz}$ bandwidth, between 6 and $18\,\mathrm{GHz}$. The frequency swept data points are generated by a computer program that uses the sine wave analog of eq. (3.53) to calculate, generate and send a data file to the AWG memory. The chirp generated by the AWG is amplified and then sent to the vacuum chamber. The transmitted signal represents the excitation pulse that is responsible of polarizing the molecules, thus it must cover the desired bandwidth to cover all the molecular transitions in the range. The evolution of a $4\,\mu\mathrm{s}$ pulse at different stages of the sequence is shown in fig. 3.12. The different steps start by numerically generating the 6-18 GHz chirp, detecting this generated chirp on the oscilloscope directly from the output of the

AWG, and also detecting the chirp on the oscilloscope after transmitting it through the horn antennas.

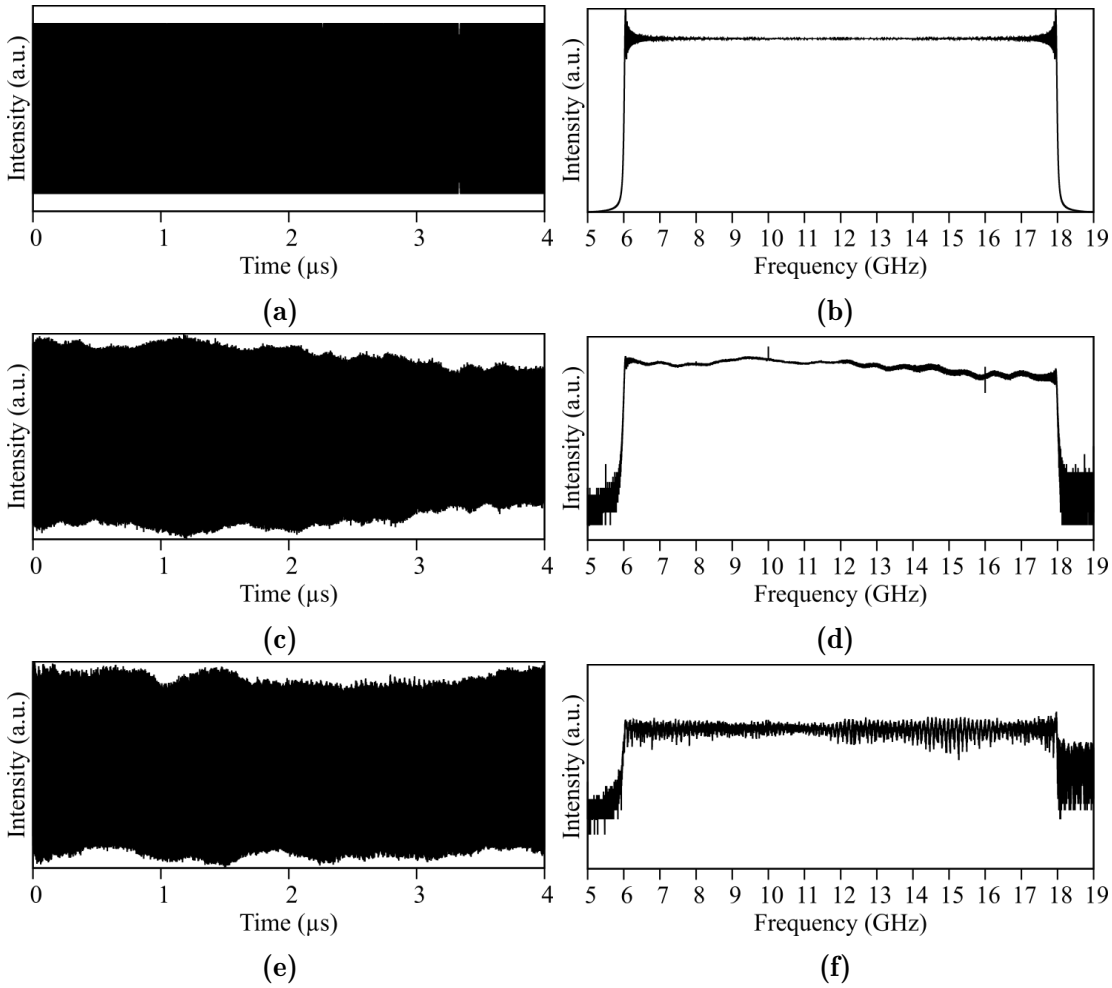

Figure 3.12: *Evaluation of the 4 μs microwave chirped-pulse (6-18 GHz) at different stages: (a) Time-domain chirp numerically generated by a computer program with a sampling rate of 64 GSa /s, and (b) its frequency waveform. (c) The signal is generated at the output of the AWG (with 64 GSa /s sampling rate) and recorded directly with the oscilloscope (no horn antennas), and (d) its frequency domain waveform. (e) The signal is recorded with the oscilloscope after being transmitted by the horns inside the stainless steel vacuum chamber, and (f) its frequency domain waveform.*

The calculated chirp signal was sampled at 64 GSa/s and its frequency spectrum appears to be perfectly flat because the sampling theory is fully satisfied. By

comparing the calculated waveform with the output signal of the AWG, which is recorded directly on the oscilloscope, we can see that the AWG is capable of reproducing the 12 GHz chirp without any significant change in the form. The intensity starts to decrease after 13 GHz, and this may be related to the specification of the cables and connections used. Also, some periodicity can be observed, which may be due to internal back reflections. Two strong peaks at 10 GHz and 16 GHz (see fig. 3.12d) are always observed in the spectrum, and their origin may be due to the channel bandwidth (33 GHz) of the oscilloscope.

The signal transmitted by the two horns seems to have better intensity distribution, where the intensity decrease at high frequencies is enhanced. However, a periodic oscillation appears in the baseline. This may be caused by reflections inside the stainless steel chamber, or to internal reflections that became more clear with lower power. The overall signal intensity is lower than the direct recorded signal.

Timing sequence, detection and averaging

The timing sequence of the spectrometer ensures the proper order of functionality of the different instruments involved. The configurable time parameters are listed in fig. 3.11. The spectrometer operation sequence reported here was optimized for the acetone molecule with argon as a carrier gas. Acetone was chosen because it is a simple molecule that was previously studied using microwave spectroscopy [134–136]. It has a large b-type dipole moment (2.9 D) which makes its observation with microwave spectroscopy very easy. Furthermore, it is a very volatile molecule, with a vapor pressure of ≈300 mbar at 25 °C. Hence, no further effort, such as heating, is required to seed a large number of molecules into the supersonic expansion, which simplifies the experimental setup. Moreover, acetone has complex spectroscopic features arising from its two interacting methyl internal rotors, which give characteristic splitting patterns that can be a good test of the performance of the spectrometer.

The experimental sequence starts by the opening of the gas valve to expand the molecules into vacuum. Typical opening times (T_1,T_2,T_3) ranged between 600 and 800 µs. The excitation phase starts afterward, when the first protective switch

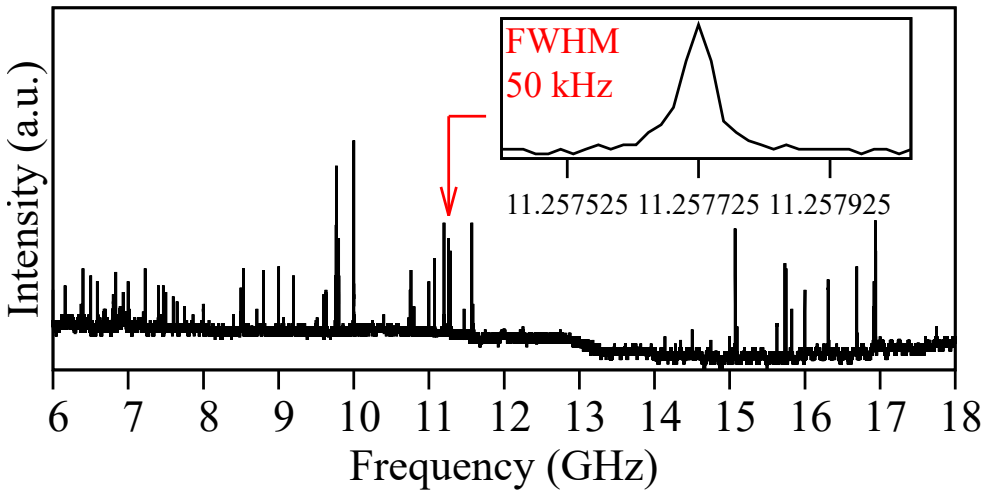

Figure 3.13: *Rotational spectrum of acetone recorded with the new chirped-pulse spectrometer in Lille, after 1 shot and using three gas valves simultaneously.*

closes after a flight time delay W between 400 and 700 µs from the opening of the valve and remains closed for T_4 =4.5 µs. After that, the TWTA is triggered to amplify after a short delay b_3 =50 ns for a duration T_4 =4.5 µs. The AWG is triggered to fire the chirp after a short delay b_3 =200 µs from the TWTA to account for the ramp-up time of the amplifier. The detection phase starts by the opening of the first protective switch and closing the second one, after a delay b_4 ranging between 1 and 2.5 µs. Switch 2 remains closed for a time T_6 between 11 and 81 µs depending on the desired detection duration. The oscilloscope is triggered to collect the data after a small buffer time b_5 =0.5 µs. The delay b_4 =2 µs, between the end of excitation and beginning of detection, was found to be optimum to minimize the detection of any resonances in the chamber.

Figure 3.13 shows the rotational spectrum of acetone, at room temperature, between 6 and 18 GHz after 1 shot with argon backing pressure of 2 bar. A three injectors arrangement permitted to increase the S/N, compared to one injector. The most intense signals of acetone appeared directly after one shot as can be seen in fig. 3.13. The spectrum was recorded for 30 µs at 80 GSa/s sampling rate. The spectrum also contains some spurious signals whose source and nature are still unidentified, around 6 GHz. No quantitative characterization of the intensities

or S/N ratios will be given here, as the results are still preliminary and further optimizations are still required.

Further tests will be based on a systematic approach to monitor the variation of the S/N ratio as a function of time and number of acquisitions. It will be interesting to know the number of acquisitions required to observe transitions of isotopic species for molecules with similar dipole moment values. Also, the effect of the carrier gas on the time parameters will be checked.

It is worth mentioning that the high amplifying power of the TWTA coupled to the large dipole moment values can drive the molecules into the rapid adiabatic passage (RAP) regime rather than the linear fast passage (LFP). The latter is required to have reliable intensity information as it induces no population changes. On the other hand, the RAP regime can lead to changes in populations and consequently to inversion of intensities due to multi-resonance effects which are enabled due to large perturbations on the populations and the large bandwidth of excitation. This influence on the populations can be examined by performing two sets of experiments: one with an increasing chirp rate (6-18 GHz) and another with a decreasing chirp rate (18-6 GHz). In this way the excitation chirp probes the population difference in various progressive series of transitions, once starting from the low frequency, and another time starting from the high frequency end. This test is to be anticipated in the future.

3.7 Experimental conditions

For the convenience of the reader, and for the sake of avoiding repetition in the following chapters, this section will include a summary of the different experimental conditions maintained throughout the investigations of the different molecules and complexes that are reported in this thesis. Figures, tables and text descriptions will be used to provide the best simplicity possible.

3.7.1 Complexes with H_2S

Table 3.2: *Information about the chemical species used throughout the experiments*

Species	IUPAC name	Formula	Supplier	Purity	State
Fenchol	1,3,3-Trimethylbicyclo [2.2.1]heptan-2-ol	$C_{10}H_{18}O$	Sigma-Aldrich	$\geqslant 99\,\%$	solid
Fenchone	1,3,3-Trimethylbicyclo [2.2.1]heptan-2-one	$C_{10}H_{16}O$	Sigma-Aldrich	$\geqslant 98\,\%$	liquid
H_2S	Dihydrogen sulfide	H_2S	Air liquide	$> 99.5\,\%$	gas
Neon	Neon	Ne	Air liquide	$99.999\,\%$	gas

Materials

Table 3.2 summarizes some useful information about the materials used for the formation of Fenchol$\cdots H_2S$ and Fenchone$\cdots H_2S$ complexes. All the chemical species were used as purchased and with no further purification.

Experimental conditions

The H_2S used to form complexes with fenchol and fenchone was conditioned in a gas cylinder. Thus, a premixture of H_2S and Ne was prepared beforehand and then flowed to the injector containing fenchol or fenchone. Table 3.3 shows the experimental conditions which were used to record the pure rotational spectra. The experimental approach is similar for both cases: A pressure of H_2S (P_{H2S}) is mixed with a great excess of Ne to reach a stagnation pressure (P_{gas}). The injector containing a certain volume of the molecule under study is maintained under this stagnation pressure, and it is heated to a certain optimum temperature that increases the vapor pressure of the molecule thus enhancing the molecular S/N. The seeded gas mixture is introduced into the cavity in a pulsed manner with a defined repetition rate (injection frequency). The conditions are given in table 3.3.

Table 3.3: *The experimental parameters used for recording the rotational spectra of the complexes with H_2S*

Species	P_{H_2S}[a]	P_{gas}[b]	Volume[c]	Gas[d]	Temp.[e]	Freq.[f]
Fenchol	50	3.5	< 0.3	Ne	348	1.5
Fenchone	50	3	< 0.3	Ne	348	1.5

[a] Pressure of H_2S (mbar) in the mixture;
[b] Backing pressure of carrier gas (bar);
[c] Sample Volume (mL) of the molecule in the container;
[d] Carrier gas used;
[e] Temperature (K) of the container;
[f] Injection frequency (Hz);

Premixing setup

As mentioned before, it was necessary to prepare a premixture of H_2S and Ne to ensure the correct mixing percentages (<2 % H_2S) at all times during the experiment. The setup consisted mainly of a 500 mL (Swagelok) sampling cylinder that was always maintained under vacuum when not in use. Rigid stainless steel tubes of defined length were used to connect the sampling cylinder to the 15 bar H_2S cylinder and the Ne cylinder, equipped with regulators, and a rotary pump. Several valves were used on the tubes to provide good control over the mixing process and to obtain a well-defined dead volume before the cylinder. A pressure gauge (accuracy of 0.5 mbar) is used to measure the pressure inside the cylinder and in the tubes. The ratio of the volume of the cylinder to the dead volume in the tubes is well known (around 20). This ratio is used to add the required pressure of H_2S into the pumped cylinder. Ne is then added until the optimum stagnation pressure for the supersonic expansion is reached. The premixing setup is shown in fig. 3.14.

3.7.2 Limona ketone

Materials and experimental conditions

Limona ketone was also used as purchased with no further purification. Table 3.4 includes information about the molecule itself as well as the experimental con-

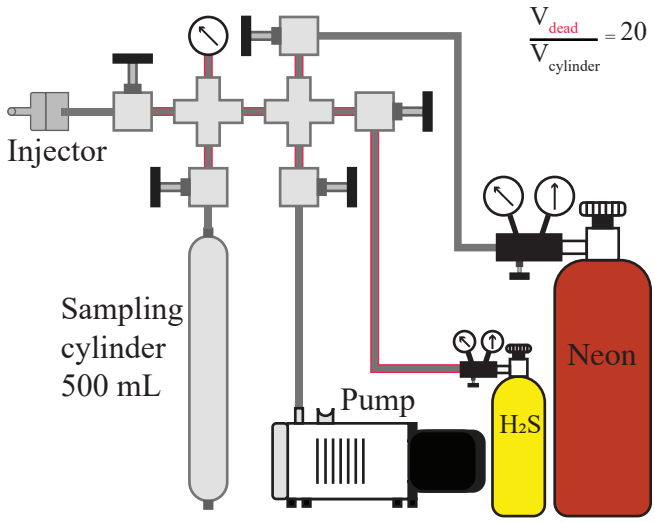

Figure 3.14: *Schematic representation of the premixing setup used with H_2S gas. The lines in red are the tubes used to calculate the volume in the closed line before the sampling cylinder, and it is called v_{Dead}. $V_{cylinder}$ is the volume of the empty sampling cylinder.*

ditions used while recording its spectrum. The experimental protocol here does not involve a premixture. Rather, the heated injector is maintained directly at a backing pressure of Neon (P_{gas}), and the seeded mixture is introduced into the cavity.

3.7.3 Strategy

In general, the experimental approach used was similar for all the systems studied. The first step includes running an automatic frequency scan in low resolution mode (point resolution of 15 kHz), of 250 kHz steps. The automatic scan is possible thanks to a program written in LabVIEW. The program can control all the instruments connected to the PC, and it gives the possibility to change several experimental parameters such as the injection duration (time for which the injector is open), flight time delay (waiting time before sending the polarization pulse), heterodyne delay (time before starting acquisition of the signal), microwave pulse duration, injection frequency, number of accumulations and the start and end frequency with the frequency step in case of automatic scan mode. During the

Table 3.4: *Materials and experimental parameters used for recording the rotational spectrum of limona ketone*

Limona ketone	
IUPAC name	1-(4-Methyl-3-cyclohexen-1-yl)ethanone
Formula	$C_9H_{14}O$
Supplier	Fluorochem
Purity	90 %
State	Liquid
Gas used	Ne
P_{gas}	4 bar
Sample volume	<0.15 mL
Temperature	343 K
Injection frequency	1 Hz

automatic scan, the program changes the frequency of the synthesizer according to the frequency step desired and then moves the mirror to the corresponding mode of the cavity. A screenshot of the Labview program is shown in fig. 3.15. The frequency zone is chosen around the predicted frequencies, from quantum calculations, of the most intense transitions. A 2 µs microwave pulse is used to polarize the molecules, and the polarizing power is adjusted to be compatible with the calculated dipole moments. As soon as there are enough lines to perform a predictive preliminary fit, the scan is stopped and the lines are then recorded at high resolution (2 or 1 kHz). Hundreds to thousands of accumulations (averaging) are usually required to reach high S/N.

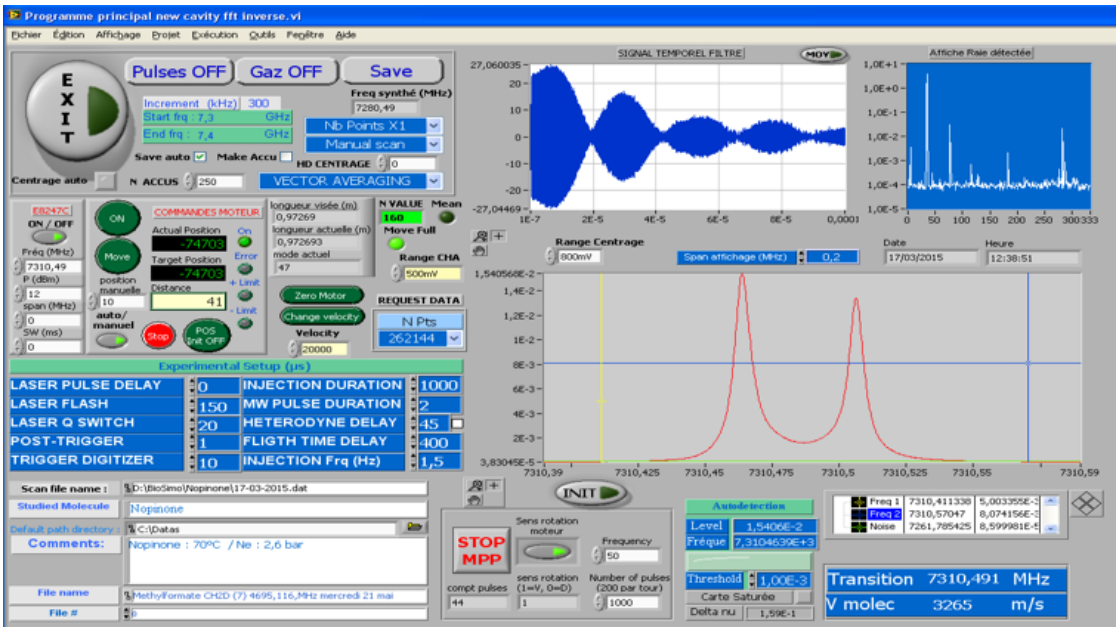

Figure 3.15: *The user interface of the LabVIEW program that permits to control the spectrometer. The modifiable timing parameters are the blue group on the middle left of the screen. The blue signal in the top is the time domain FID, and the central red signal is the frequency domain molecular transition. The signal corresponds to the molecule nopinone recorded in 2016. The white signal in the top right corner is the low resolution spectrum obtained from the automatic scan.*

CHAPTER

FOUR

THE COMPLEXES OF THE MONOTERPENOIDS FENCHOL AND FENCHONE WITH H_2S

4.1 Introduction

Monoterpenes are an important family of molecules present in the atmosphere. Their presence is dominated by natural emissions along with some minor emissions due to anthropogenic activities [3]. The wide structural variety of these compounds arises from the substitution and derivation of the main building block: isoprene (C_5H_8). The diversity of structures gives monoterpenes numerous chemical properties that can be applied in a wide range of fields of chemical and biological interest. Monoterpenes can give oxygenated products upon their reactions with ozone O_3, nitrogen oxides NO_x and hydroxyl radical $OH^\bullet$ [137, 138]. These oxygenated products are called monoterpenoids or terpenoids. The addition of an oxygen atom into these molecules can render them even more interesting. The oxygen-based functional groups as in alcohols (OH), aldehydes (CHO) and ketones (CO) open the door for new types of interactions for monoterpenoids. They can induce, for example, the formation of hydrogen-bonded complexes with other molecules present in the atmosphere such as water, sulfur containing compounds, halogen containing compounds, and alcohols.

The hydrogen bond, which is an intermediate range interaction, is very important. A hydrogen bond is defined as an attractive interaction between a hydrogen

atom in a molecule or fragment and an atom or group of atoms in the same or different molecule. It involves a proton donor represented by X-H and a proton acceptor represented by Y, where X and Y are more electronegative than H. An important condition for the hydrogen bond to be formed is that the acceptor should be a high electron density region, such as a lone pair of electrons on Y, or a π-bonded pair of electrons in a double or triple bond [139, 140]. Two atoms are considered hydrogen-bonded if the distance between them is less than the sum of their van der Waals radii [140]. The hydrogen bond is responsible for the stabilization of many vital molecular systems [141], and it is a main contributor to the formation of atmospheric relevant species [142].

Microwave spectroscopy is well suited to study the structures, interactions and dynamics of hydrogen-bonded complexes, due to its high resolution and unambiguous identification of structures and conformations. This can facilitate the understanding of the formation of secondary aerosol species that alter different processes in the atmosphere. The literature has expanded over the last decade with the addition of many studies of monoterpenoids complexes with water (and some other molecules). Examples of these complexes can be found in references [143–145], and other examples will be given throughout the text. Despite the extensive studies on complexes with water molecules, the information on organic complexes with sulfur containing molecules is scarce [17]. There is no report, to our knowledge, of a complex of a monoterpenoid with sulfur containing molecule in the literature. Sulfur is less electronegative than oxygen, and consequently, the hydrogen bond with sulfur is expected to be weaker and more difficult to establish.

We are intrigued by the questions: Is it possible to observe complexes of monoterpenoids with sulfur containing compounds? And if it is possible, how would that differ from the corresponding water-containing complex? Would the characteristics of the hydrogen bond change with different functional groups? The answers to these questions are not straightforward, and in order to be able to answer them, we need to choose a molecular system that can be compared to water. In 2018, the H_2S dimer was shown to have a similar structure to the H_2O dimer in the gas phase [15]. This finding provided a starting point to study complexes of monoterpenoids with sulfur. The complexes of monoterpenoids with H_2S can be compared to the extensively studied hydrates, which can provide a new and better

understanding of the interactions that can occur with this class of molecules. The choice of the molecular system depends on the field of interest, and the desired application. Based on the importance of monoterpenoids in the atmosphere, which was highlighted at the beginning of this introduction, we decided to study the complexes of atmospheric relevant species with H_2S. The choice of molecules was an alcohol (fenchol) and a ketone (fenchone) which were previously investigated with FTMW spectroscopy. These two molecules possess similar skeletal configurations, with the difference being the oxygenated functional group. The 2D structure of these two molecules is illustrated in fig. 4.1. The choice was influenced by our curiosity to see if the hydrogen bond behaves differently according to the interacting functional group.

In what follows, the experimental results of rotationally jet-cooled complexes of the hydrogen-bonded fenchol$\cdots H_2S$ and fenchone$\cdots H_2S$ complexes are reported. Moreover, a comparison between these complexes and the reported water complexes is established. A comparison between the two complexes themselves is also presented. Finally, a summary of the findings will be given at the end of this chapter.

4.2 Fenchol-H_2S

4.2.1 Motivation

Fenchol (1,3,3-Trimethylbicyclo[2.2.1]heptan-2-ol, $C_{10}H_{18}O$) is a monoterpenoid with a hydroxyl functional group (OH). It is an alcohol released by Eucalyptus globulus and Cedrus atlantica[146]. It can also be emitted from industrial materials such as the wood of pin radiata [147]. Fenchol possesses two stereoisomers: exo- and endo-fenchol. The structure of the conformers of the monomer of fenchol was previously determined by FP-FTMW spectroscopy [148], as well as the structure of the endo-fenchol monohydrate [149]. In this study, we aim at identifying the spectra of the conformers of the complex of fenchol with H_2S and establish a comparison with the monohydrates.

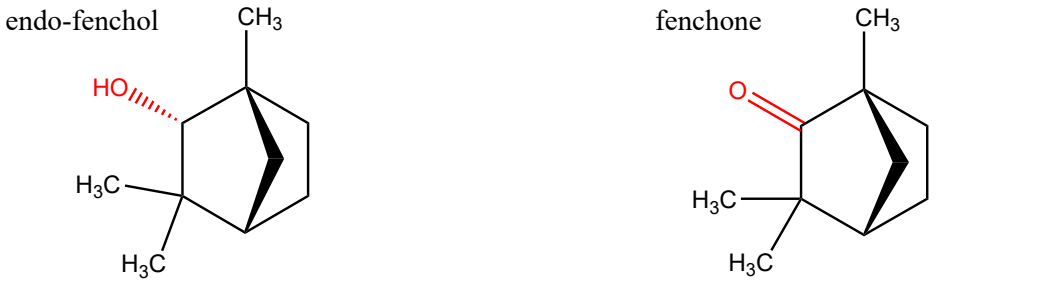

1,3,3-trimethylbicyclo[2.2.1]heptan-2-ol 1,3,3-trimethylbicyclo[2.2.1]heptan-2-one

Figure 4.1: *The 2D structure of fenchol (left) and fenchone (right). The corresponding IUPAC name is given under each structure.*

4.2.2 Methods

In order to determine the preferred structures for the complex, fast molecular mechanics calculations were first performed to have an idea about the possible conformers. The geometries of the obtained structures were optimized by Gaussian 16 [108] using the methods and basis sets listed on page 51. The H_2S molecule positions itself in a manner permitting to form a hydrogen bond between the hydrogen of the H_2S and the oxygen of the alcohol. The position of the H_2S, and mainly of the sulfur atom, can also be affected by factors other than the hydrogen bond, such as van der Waals interactions. These long and mid-range noncovalent interactions can contribute to the stability of the molecule, and alter some of the physical parameters such as the distance between the two groups of the complex. The non-covalent interactions can be characterized by NCI and Symmetry-adapted perturbation theory (SAPT), the results of which are reported later in this chapter.

4.2.3 Results

At first, the computational outcomes are reported, as they can be used as a starting point for predicting the contribution of different rotamers in the experimental spectra, and serve to facilitate the analysis of the obtained lines later. Four stable geometries were optimized. The structures of these conformers are depicted in fig. 4.2. The conformation arises from varying the position and orientation of the H_2S molecule with respect to the endo-fenchol molecule. The relative energies of

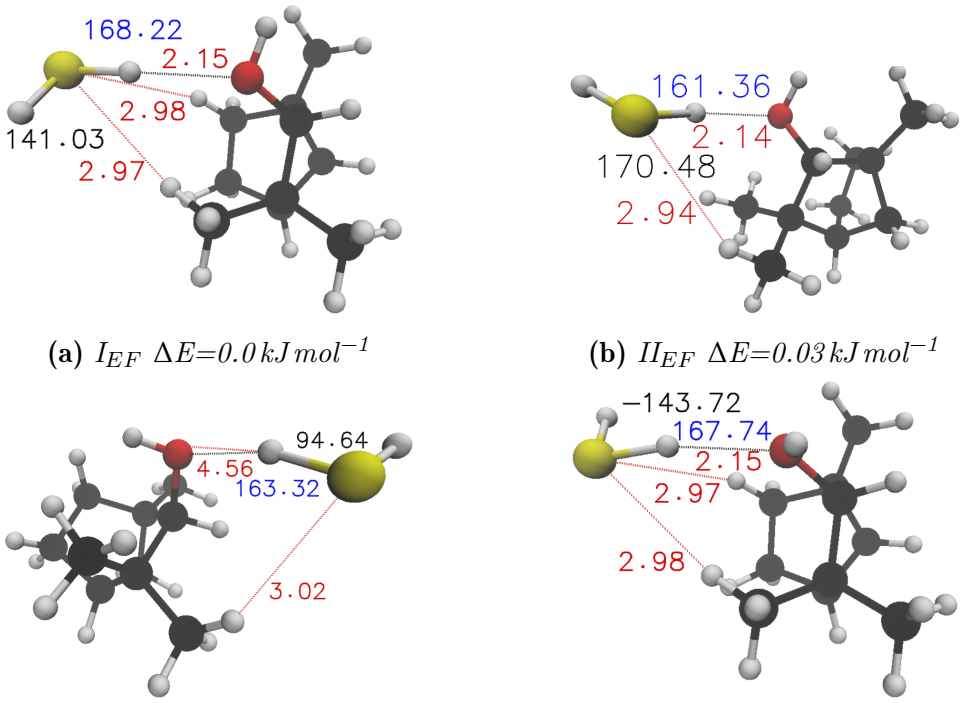

(a) I_{EF} ΔE=0.0 kJ mol^{-1} **(b)** II_{EF} ΔE=0.03 kJ mol^{-1}

(c) III_{EF} ΔE=0.11 kJ mol^{-1} **(d)** IV_{EF} ΔE=0.28 kJ mol^{-1}

Figure 4.2: *Optimized geometries of the endo-Fenchol$\cdots H_2S$ complex at the MP2/6-311++G(d,p). The relative energies displayed are ZPE corrected. The numbers displayed in red are the distances, in Å, between the atoms. The number displayed in blue is the angle OHS in degrees. The value displayed in black is the dihedral angle OHSH in degrees*

the four conformers are close with a maximum difference of 0.5 kJ mol^{-1} (MP2 method without zero point energy (ZPE) correction). The calculated rotational constants, dipole moment components and relative energies for the different conformers are listed in table 4.1 below. The energy ordering with such small value cannot be considered accurate, because it falls within the range of the error of calculation (around 0.5 kJ mol^{-1}).

The conformers are named by Roman numerals with 'EF' subscript referring to the abbreviation endo-fenchol, in increasing order of energy with respect to the MP2 method (I is the lowest in energy). The energy ordering of the conformers differs from one method to another, and it is not the same. It also changes when applying ZPE corrections or not. The ZPE corrected values of the MP2 method

was used as a reference to name the different conformers.

Table 4.1: *Rotational constants, absolute values of the dipole moments and relative energies of the different conformers of endo-fenchol$\cdots H_2S$ complex at the MP2/6-311++G(d,p), ωB97X-D/6-311++G(d,p) and B3LYP/def2TZVP levels of theory*

MP2/6-311++G(d,p)				
	I_{EF}	II_{EF}	III_{EF}	IV_{EF}
A (MHz)	992	1187.6	1182.3	993.9
B (MHz)	564.7	510.2	505.9	566.8
C (MHz)	492	445.4	439.6	492.8
μ_a (D)	2.1	1.6	2.7	2
μ_b (D)	0.1	0.8	0.02	0
μ_c (D)	0.9	0.2	0.1	0.7
ΔE (kJ mol^{-1})	0.14	0	0.29	0.53
ΔE_0[a](kJ mol^{-1})	0	0.03	0.11	0.28
ωB97X-D/6-311++G(d,p)				
	I_{EF}	II_{EF}	III_{EF}	IV_{EF}
A (MHz)	996.7	1201.7	1187.5	995.7
B (MHz)	550.3	494.7	498.4	553.8
C (MHz)	479.5	434.4	434.8	481.9
μ_a (D)	2.5	2.3	3	2.3
μ_b (D)	0	0.5	0.2	0
μ_c (D)	1	0.1	0.1	0.9
ΔE (kJ mol^{-1})	0.96	0.61	0	1.64
ΔE_0[a](kJ mol^{-1})	0.52	1.21	0	1.22
B3LYP/def2TZVP				
	I_{EF}	II_{EF}	III_{EF}	IV_{EF}
A (MHz)	994.4	1193	1192.7	995.5
B (MHz)	551.2	496.8	497.4	553.9
C (MHz)	479.7	435.7	434.9	481.3
$\lvert\mu_a\rvert$ (D)	2.1	2	2.5	1.9
$\lvert\mu_b\rvert$ (D)	0.1	0.6	0.1	0.1
$\lvert\mu_c\rvert$ (D)	1	0.1	0.1	0.9
ΔE (kJ mol^{-1})	1.47	0.49	0	1.48
ΔE_0[a](kJ mol^{-1})	1.38	0.86	0	1.39

[a] Zero-point energy corrections applied

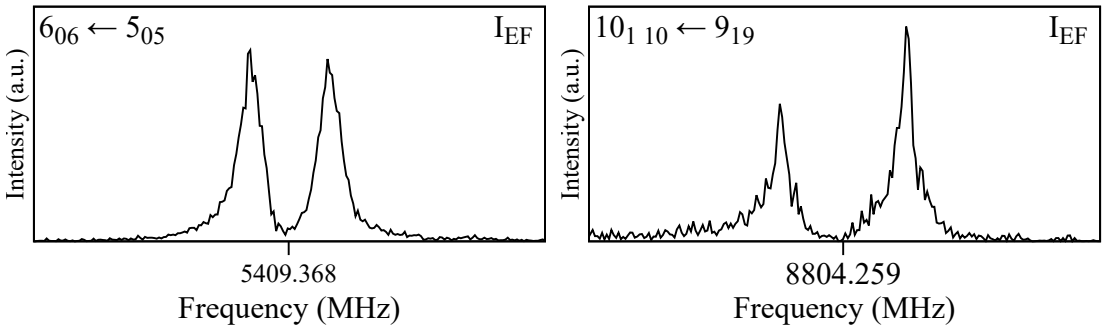

Figure 4.3: *An example of two transitions recorded at high resolution (frequency grid = 2 kHz) for the fenchol$\cdots H_2S$ complex. The assigned transition is shown in the top left corner in the form $J'_{K'_aK'_c} \leftarrow J''_{K''_aK''_c}$. The figure represents a 0.2 MHz span.*

A scaling factor, which derived from the differences between calculated and observed constants of the water complex (at the same level of theory), was applied to the calculated rotational constants. The scaled constants were used to obtain line predictions based on a semi-rigid asymmetric model for a near prolate top. This scaling methodology is usually used to decrease the difference between the experimental and predicted line transitions. Scans were made around the most intense predicted frequencies. The experimental signals were very weak and could not be distinguished from the baseline easily, in the low resolution auto scan mode. Therefore, it was not convenient to scan the full range of the spectrometer. The spectrum contained only a-type transitions, and 56 lines were assigned to molecular transitions. The recorded lines with their assigned transitions are presented in table A.1. An example of the lines recorded at high resolution can be found in fig. 4.3. The rotational constants were fitted to a semi-rigid model Watson Hamiltonian in the A-reduction and I^r representation, using Picketts's SPFIT/SPCAT suite of programs. The three transitions $8_{27} \leftarrow 7_{26}$, $8_{08} \leftarrow 7_{07}$ and $8_{18} \leftarrow 7_{17}$ were the first to be assigned to the experimental frequencies 7340.184 MHz, 7125.466 MHz and 7069.324 MHz, respectively. Further transitions up to $J = 13$ and $K_a = 4$ levels were then assigned to recorded lines to obtain the final fit. The fitted constants are shown in table 4.2. The identification of the observed conformer was not straightforward, since two conformers have similar theoretical rotational con-

Table 4.2: *Comparison between the experimental rotational and centrifugal distortion parameters of the ground state III_{EF} conformer of the fenchol$\cdots H_2S$ complex and the calculated values at a different level of theory*

Parameters	Exp.[a]	MP2[b]	B3LYP[c]	ωB97X-D[b]
$\boldsymbol{A}$ (MHz)	1161.2329(32)	1182.3	1192.7	1187.5
$\boldsymbol{B}$ (MHz)	494.214 34(11)	505.9	497.4	498.4
$\boldsymbol{C}$ (MHz)	430.006 772(86)	439.6	434.9	434.8
Δ_J (kHz)	0.206 03(35)	0.06	0.06	0.05
Δ_K (kHz)	−0.450 78 [e]	−0.46	−0.28	−0.36
Δ_{JK} (kHz)	0.8615(31)	0.75	0.48	0.58
δ_J (kHz)	0.032 87(22)	0.01	0.01	0.01
δ_K (kHz)	0.231(12)	0.29	0.17	0.29
$\lvert\mu_a\rvert$ (D)	observed	2.7	2.5	3.0
$\lvert\mu_b\rvert$ (D)	not observed	0.02	0.1	0.2
$\lvert\mu_c\rvert$ (D)	not observed	0.1	0.1	0.1
N[d]	56			
RMS (kHz)	1.44			
J_{max}/J_{min}	13/2			
Ka_{max}/Ka_{min}	4/0			
Kc_{max}/Kc_{min}	12/2			

[a] A-reduced Watson Hamiltonian in I^r representation
[b] 6-311++G(d,p) basis set
[c] def2TZVP basis set
[d] Number of lines used in fit
[e] fixed value obtained from MP2/6-311++G(d,p) calculation

stants. Both sets of parameters could be assigned to the experimental rotational constants (II_{EF} and III_{EF}; see table 4.1). However, these two conformers have different dipole moments: conformer II_{EF} is expected to have dominant a-type lines (1.6 D), weaker b-type lines (0.8 D; this can be usually observed in our setup) and no (very weak) c-type transitions (0.1 D; the lowest we can observe is around 0.5 D), whereas conformer III_{EF} is expected to have only a-type spectrum (dipole components along b and c axes are 0.1 and 0.3 D, respectively, which are too weak to be observed in our setup). Hence, having only a-type lines in the experimental spectrum, the observed rotamer was attributed to the calculated conformer III_{EF}.

The experimental rotational constants show good agreement with the different calculation methods used (see table 4.2). The MP2 method with the 6-311++G(d,p) basis set has the lowest difference, from the experimental value, on the A rotational constant: 1.8 % compared to 2.7 % and 2.3 % with B3LYP and ωB97X-D methods, respectively. On the other hand, the B rotational constant shows the lowest difference with the B3LYP and ωB97X-D methods: 0.6 % and 0.8 %, respectively compared to the 2.4 % with the MP2 method. Similarly, the C rotational constant is better predicted with B3LYP and ωB97X-D methods with the difference being 1.1 % for both, which is less than the 2.2 % difference with the MP2 method. The differences in the centrifugal distortion parameters are much larger and vary a lot between methods.

The stabilization of the complex is due to the hydrogen bond formed between the hydrogen atom of the H_2S molecule and the oxygen atom of the OH group in fenchol. The strength of this hydrogen bond can be characterized by the distance between the two atoms, and by the non-covalent interactions. The complex may also be stabilized by the dispersive interactions between the H_2S molecule and the fenchol monomer. Both types of interactions can be visualized by performing NCI analysis. This is usually done by nciplot software [150–152]. The calculated interactions can then be visualized by plotting the isosurface in the VMD visualization program. The NCI analysis of the fenchol$\cdots H_2S$ complex is shown in fig. 4.4.

4.2.4 endo-fenchol-H_2S vs. endo-fenchol-H_2O

Although oxygen and sulfur belong to the same group of the periodic table, they exhibit different chemical behavior in most cases. One of the main factors affecting their behavior in complexes is their electronegativity. Oxygen is more electronegative (3.44) than sulfur (2.58), which qualifies it to be a better proton donor in a hydrogen bond, and consequently, it is expected to have stronger hydrogen bonds. Considering that, to our knowledge, this is the first time a complex of a monoterpenoid with H_2S is observed with microwave spectroscopy, it is interesting to see how such complexes compare to those with water. Considering the better hydrogen bonding abilities of oxygen, the sulfur complexes are expected to be weaker and harder to observe.

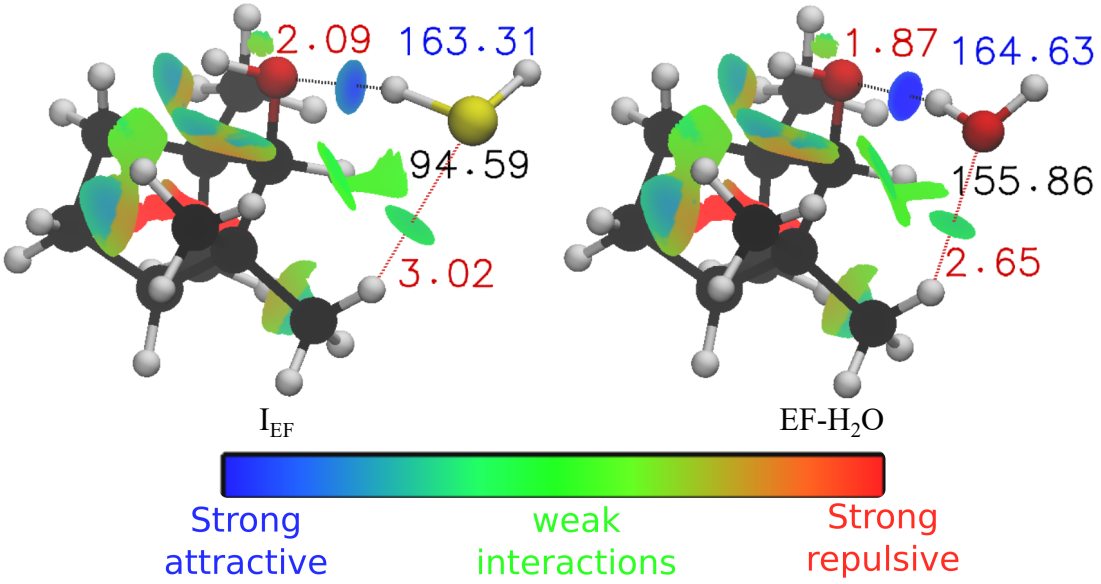

Figure 4.4: *The NCI isosurfaces of the EF···H_2S (left) and EF···H_2O (right) [149] complexes. The numbers displayed in red are the distances, in Å, between the atoms. The numbers displayed in blue are the angles OHS and OHO, in degrees. The value displayed in black are the dihedral angles OHSH and OHOH in degrees*

As previously mentioned, the endo-Fenchol···H_2O complex was previously studied [149], and only one conformer has been observed. It has also been shown to alter the position of the hydroxyl group in endo-fenchol upon complexation.

A first look at the two complexes gives the impression that they are similar from a structural point of view. The structure of the observed conformers of both complexes is illustrated in fig. 4.4. It is clear that the H_2S molecule approaches the molecule in a similar way that the H_2O does. The angles OHS and OHO, which can represent the of the sulfur and oxygen atoms with respect to the molecule, have close values. However, the dihedral angles OHOH and OHSH are different, and their values are 155.9° and 94.6°, respectively. This infers that the orientation of the free hydrogen of the H_2S in space is slightly different than that with water. This can be due to structural constraints due to several reasons. It can be interpreted for example by the difference in electronic structure between the two atoms, where sulfur has double the number of electrons (16) than that of oxygen, which means it has an extra valence orbital. Also, the covalent radii (oxygen:66 pm, sulfur:105 pm)

and the van der Waals radii (oxygen:152 pm, sulfur:180 pm) are different. This can explain the different distances in the two complexes, and especially the longer distances between the H_2S and the EF molecule, compared to the water complexes.

If we examine the NCI plot represented in fig. 4.4, we can deduce that the hydrogen bond in the water complex is much stronger (dark blue color) than that in the sulfur complex (light blue color). This can confirm the initial assumption based on the electronegativity of the atoms. The shorter hydrogen bond distance in the case of the water complex also confirms the stronger hydrogen bond. Another interesting information that can be extracted is the dispersive interactions between the sulfur or the oxygen and other atoms in the molecule. In both complexes, the interactions seem to be weak and of similar magnitude. The distance from the closest hydrogen atom in the molecule is shorter in the water complex. This can be due to the difference in sizes between oxygen and sulfur, which causes the sulfur to be placed farther away. In both cases, however, the O-H and S-H distances are on the limit of the sum of the corresponding van der Waals radii[153].

4.3 Fenchone-H_2S

4.3.1 Motivation

Fenchone, or 1,3,3-Trimethylbicyclo[2.2.1]heptan-2-one has the formula $C_{10}H_{16}O$. It belongs to the monoterpenoids family. It shares a similar structure with fenchol (see the previous section) with the difference of having a carbonyl CO group in place of the OH group. It is also an isomer of camphor, which has been investigated before with FTMW spectroscopy, along with its hydrates [154, 155]. Fenchone is the main component of the essential oils of fennel, cedar and lavender [156]. It is released into the atmosphere naturally from the previously listed species, or from its use in household products and pesticides. The structure of fenchone was determined by broadband microwave spectroscopy [156], and lately, its hydrates have also been reported [157]. In this work, we present the investigation of the complex of fenchone with H_2S, and we are intrigued to see how it behaves in comparison to water complexes and to fenchol complex with sulfur.

4.3.2 Methods

The initial guess of possible structures was done by fast molecular mechanics, followed by geometry optimization and frequency calculations using the methods and basis sets listed on page 51, as employed in the Gaussian 16 software [108]. The different conformations arise from the placement of the H_2S molecule around the fenchone monomer, in such a way that a weak hydrogen bond is formed between one of the hydrogen atoms of the H_2S and the oxygen of the ketone. The position of the sulfur atom can be affected by the van der Waals interactions and dispersive forces with the rest of the molecule. These forces can stabilize the complex, and their magnitude can influence the overall energy of the complex. The magnitude of these interactions and their ability to stabilize the complex against the repulsive interactions determine the possible positions responsible for the stable structures. The experimental conditions used to record the gas phase rotational spectra are listed on page 95.

4.3.3 Results

Computationally, six conformers were predicted to be stable for the fenchone$\cdots H_2S$ complex, by the different quantum chemical calculation methods performed. The six predicted conformers are shown in fig. 4.5. Four of these complexes are close in energy, and the relative energy difference between them is less than $0.5\,\mathrm{kJ\,mol^{-1}}$, while the other two are $4\,\mathrm{kJ\,mol^{-1}}$ higher in energy. Due to energy considerations, and the low probability of observing conformers with energy difference higher than $3\,\mathrm{kJ\,mol^{-1}}$ in our jet-cooled conditions, only the four lowest energy conformers were considered and expected to be observed. The conformers are labeled with roman numerals with the subscript "FEN" referring to fenchone abbreviation. The lowest roman number corresponds to the conformer with the lowest energy among the ZPE corrected values of the MP2 method. The calculated rotational constants and dipole moment components with all the methods used are summarized in table 4.3. A scan at low resolution, a portion of which is shown in fig. 4.6, permitted to observe lines corresponding to the complex. The first two observed lines at 6292.456 MHz and 6339.421 MHz were tried to be assigned to the transitions $6_{16} \leftarrow 5_{15}$ and $6_{06} \leftarrow 5_{05}$, respectively. This was done with the help of predicted line

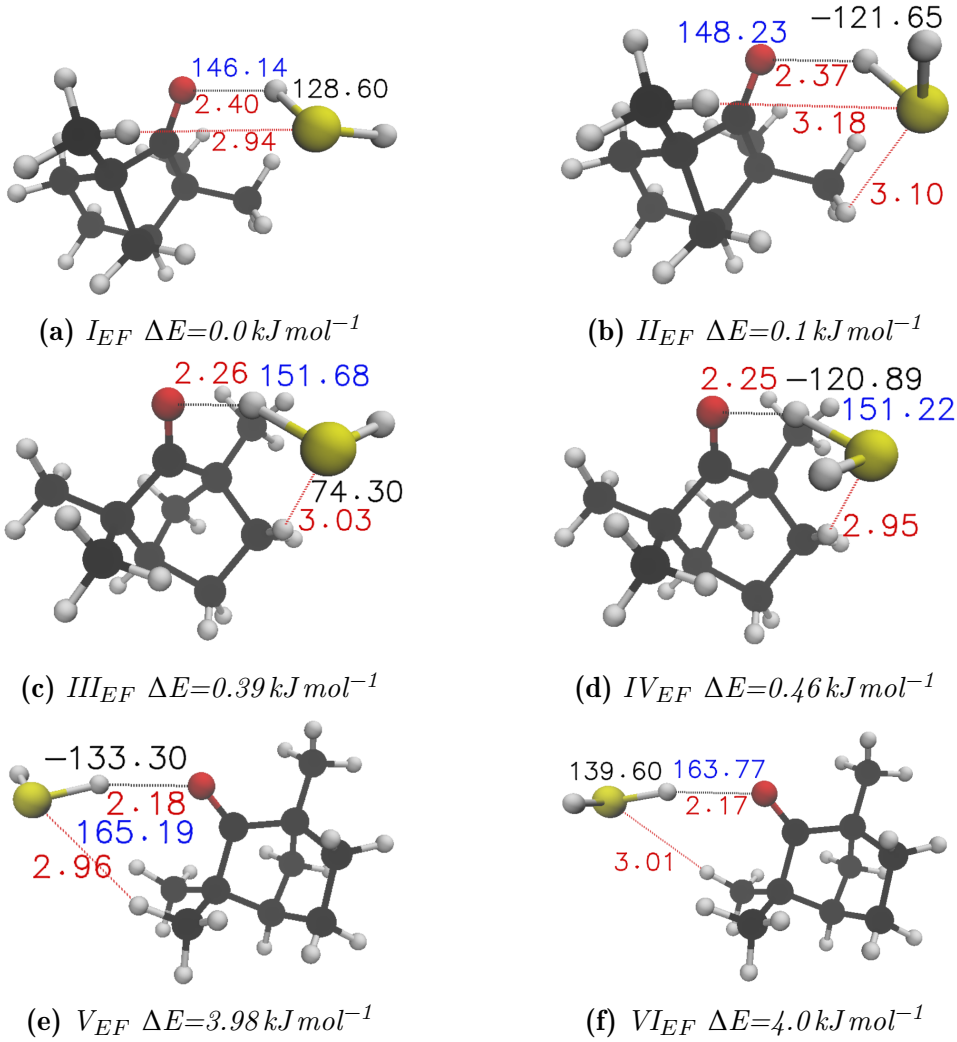

(a) I_{EF} ΔE=0.0 kJ mol^{-1} **(b)** II_{EF} ΔE=0.1 kJ mol^{-1}

(c) III_{EF} ΔE=0.39 kJ mol^{-1} **(d)** IV_{EF} ΔE=0.46 kJ mol^{-1}

(e) V_{EF} ΔE=3.98 kJ mol^{-1} **(f)** VI_{EF} ΔE=4.0 kJ mol^{-1}

Figure 4.5: *Optimized geometries of the Fenchone$\cdots H_2S$ complex at the MP2/6-311++G(d,p). The relative energies displayed are ZPE corrected. The numbers displayed in red are the distances, in Å, between the atoms. The number displayed in blue is the angle OHS in degrees. The value displayed in black is the dihedral angle OHSH in degrees*

frequencies obtained from calculated constants. A set of lines were recorded at high resolution (frequency resolution of 1 kHz) and was successively assigned to transitions with quantum numbers from $J = 2$ and $K_a = 0$ up to $J = 12$ and $K_a = 4$. The spectrum contained all a, b and c transition type lines. A splitting of the observed lines was obvious in the spectrum. This splitting ranged between a few

Table 4.3: *Rotational constants, absolute values of the dipole moments and relative energies of the different conformers of the fenchone$\cdots H_2S$ complex at the MP2/6-311++G(d,p), ωB97X-D/6-311++G(d,p) and B3LYP/def2TZVP levels of theory*

MP2/6-311++G(d,p)						
	I_{FEN}	II_{FEN}	III_{FEN}	IV_{FEN}	V_{FEN}	VI_{FEN}
A (MHz)	1092.9	1091.5	984.2	985.3	1261.9	1275.8
B (MHz)	610.7	610.6	597.2	599	473.1	474.4
C (MHz)	507.2	506.7	525.1	526.9	417.4	415
$\|\mu_a\|$ (D)	2	1.9	2.7	2.5	3.3	3.4
$\|\mu_b\|$ (D)	0.5	0.9	1.1	0.4	1.2	1.6
$\|\mu_c\|$ (D)	1.8	1.4	1.3	1.5	1.1	0.4
ΔE (kJ mol^{-1})	0	0.6	0.83	0.52	3.91	3.90
ΔE_0[a](kJ mol^{-1})	0	0.1	0.39	0.46	3.98	4.0
ωB97X-D/6-311++G(d,p)						
	I_{FEN}	II_{FEN}	III_{FEN}	IV_{FEN}	V_{FEN}	VI_{FEN}
A (MHz)	1103.7	1101.6	982.9	987.8	1265.7	1266.8
B (MHz)	595.9	597.7	594.6	592.7	476.8	476.4
C (MHz)	493.8	495.5	521.5	520.0	418	417.7
$\|\mu_a\|$ (D)	2.9	2.5	3.0	3.3	4.0	4.0
$\|\mu_b\|$ (D)	0.5	1.0	0.9	0.4	1.3	1.7
$\|\mu_c\|$ (D)	1.8	1.5	1.3	1.5	1.2	0.5
ΔE (kJ mol^{-1})	0.92	1.09	0.86	0.71	0	0.06
ΔE_0[a](kJ mol^{-1})	0.69	0.49	0	0.47	0.12	0.20
B3LYP/def2TZVP						
	I_{FEN}	II_{FEN}	III_{FEN}	IV_{FEN}	V_{FEN}	VI_{FEN}
A (MHz)	1104.9	1101.5	978.8	982.0	1268.1	1266.6
B (MHz)	597.5	604.5	604.7	597.3	478.7	478.1
C (MHz)	494.3	499.8	530.0	523.6	419.3	419.2
$\|\mu_a\|$ (D)	2.6	2.2	2.6	2.9	3.7	3.8
$\|\mu_b\|$ (D)	0.4	0.9	0.7	0.4	1.3	1.7
$\|\mu_c\|$ (D)	1.8	1.5	1.4	1.6	1.1	0.3
ΔE (kJ mol^{-1})	0.96	0.56	0.27	0.54	0	0.03
ΔE_0[a](kJ mol^{-1})	0.69	0.46	0	0.07	0.24	0.40

[a] Zero point energy corrections applied

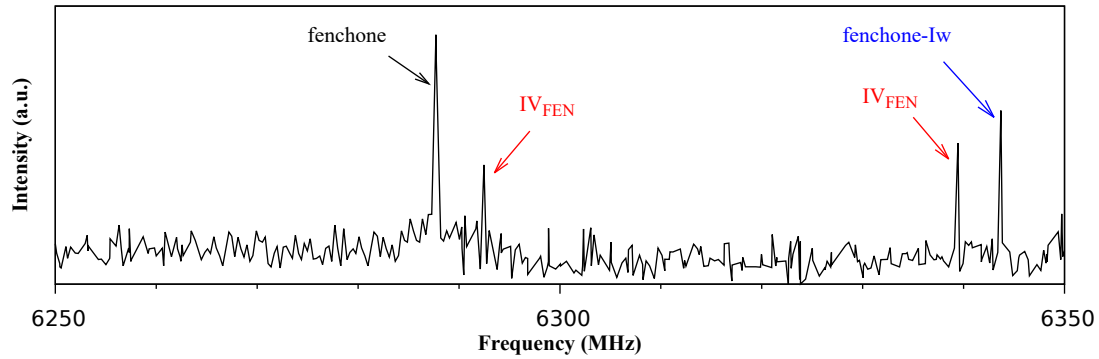

Figure 4.6: *100 MHz portion of the scan in low resolution mode, where the first two assigned lines of the fenchone$\cdots H_2S$ complex are shown. The other intense lines correspond to the fenchone molecule and fenchone$\cdots H_2O$ complex (Iw).*

kHz and up to 200 kHz, apart from the Doppler splitting that is normally observed in the cavity. The ratio of the intensities of the components on all transitions was 3:1. An example of this splitting is illustrated in fig. 4.7. This pattern is usually a characteristic of large amplitude motion. Two sets of transitions (split into two components) corresponding to one conformer were observed on the spectrum. The experimental lines were fitted to semi-rigid Hamiltonian using Pickett's suite of programs SPFIT/SPCAT[117], into two separate states 0^- for the stronger lines and 0^+ for the weaker lines. The two states were fitted while fixing the values of

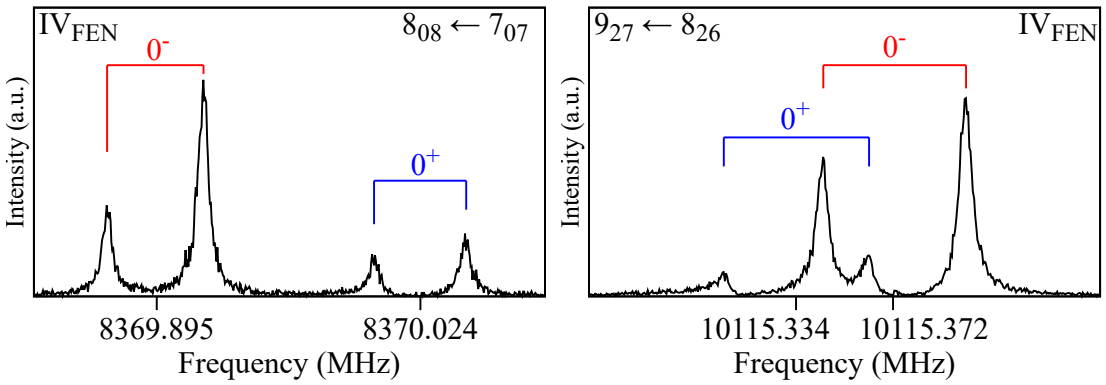

Figure 4.7: *An example of two transitions recorded at high resolution (frequency grid = 1 kHz) of fenchone$\cdots H_2S$ complex. The assigned transition is shown in the top left and right corners in the form $J'_{K'_aK'_c} \leftarrow J''_{K''_aK''_c}$. Each transition appears to split into two components.*

Table 4.4: *Comparison between the experimental rotational and centrifugal distortion parameters of the ground state IV_{FEN} conformer of the fenchone$\cdots H_2S$ complex and the calculated equilibrium values at different level of theory*

Parameters	Exp.[a]		MP2[b]	B3LYP[c]	ωB97X-D[b]
	0^-	0^+			
$\boldsymbol{A}$ (MHz)	983.403 41(13)	983.414 97(21)	985.3	982.0	987.8
$\boldsymbol{B}$ (MHz)	582.241 521(34)	582.232 474(64)	599.0	597.3	592.7
$\boldsymbol{C}$ (MHz)	511.007 220(30)	511.016 389(44)	526.9	523.6	520.0
Δ_J (kHz)	0.18499(14)		0.11	0.11	0.10
Δ_K (kHz)	-1.6012(59)		−0.74	−1.39	−1.13
Δ_{JK} (kHz)	1.4868(14)		0.71	1.34	1.12
δ_J (kHz)	0.015727(80)		0.01	0.01	0.01
δ_K (kHz)	0.7361(24)		0.31	0.58	0.46
$\lvert\mu_a\rvert$ (D)	observed intense		2.5	2.9	3.3
$\lvert\mu_b\rvert$ (D)	observed weak		0.4	0.4	0.4
$\lvert\mu_c\rvert$ (D)	observed medium		1.5	1.6	1.5
N[d]	99	70			
RMS (kHz)	1.72				
J_{max}/J_{min}	12/2				
Ka_{max}/Ka_{min}	4/0				
Kc_{max}/Kc_{min}	11/2				

[a] A-reduced Watson Hamiltonian in I^r representation
[b] 6-311++G(d,p) basis set
[c] def2TZVP basis set
[d] Number of lines used in fit

the centrifugal distortion constants for both states. A total of 169 lines were used to obtain the final fit (99 lines for 0^- and 70 lines for 0^+). The recorded lines along with their assigned transitions are reported in table A.2 of the Appendix. The fitted parameters are shown in table 4.4.

The obtained experimental rotational constants can be attributed to two of the calculated conformers: III_{FEN} or IV_{FEN}. The energy ordering was not the same with all methods, and the relative energy difference between the two conformers was less than $0.5\,\mathrm{kJ\,mol^{-1}}$ which is within the error margin of the quantum calculations. Therefore, The definite identification of which conformer is observed was not straightforward. A complementary approach was to compare the polarization power used in the experiment to the estimated value of the dipole moments components. Along the a-axis, the value of the dipole was rather close, and thus no useful information could be extracted. In contrast, along the b- and c-axes the

calculated dipole moments show that, depending on the method considered, for III_{FEN} conformer, the b-type transitions intensities would be around two times lower than c-type transitions. For the IV_{FEN} conformer, it is expected that c-type transitions will be three times more intense than b-type transitions. This is valid for all methods. In our experimental conditions, the polarizing power used to optimize b-type lines was three times lower than that used to optimize the c-type lines. Hence, we can say that the observed conformer was the IV_{FEN} conformer. The experimental constants are in good agreement with the calculated constants for the observed species, and this can be seen in table 4.4. The three methods predict the A rotational constant with similar accuracy, as the error was 0.14 %, 0.19 % and 0.45 % with B3LYP, MP2 and ωB97X-D, respectively. Concerning the B rotational constant, the ωB97X-D method has the lowest error of 1.8 %, followed by B3LYP (2.59 %) and MP2 (2.88 %). ωB97X-D seems to be the best at predicting the C rotational constant as well with a difference of 1.76 %, while among the other two methods B3LYP is better with a difference from the experimental value of 2.5 % compared to 3.1 % with MP2. It is worth mentioning that the other conformers were not observed. This may be due to relaxation by collisions in the jet, or due to very low intensities that are below the sensitivity limit of our spectrometer.

4.3.4 Large amplitude motion

As it was mentioned before, the experimental lines were split into two components. The explanation of this splitting should take into account the fact that only one conformer was observed, and thus the large amplitude motion present should give structures of the same energy. Also, the ratio of the intensities of the two components was 1 : 3. The only possible movement to give iso-energetic structures is the proton exchange in the H_2S molecule due to its internal rotation about its C_{2v} symmetry axis. This rotation permits the two hydrogen atoms to exchange their position giving two equivalent structures. This movement requires that the hydrogen bond S-H$\cdots$O is weak enough to break and form again with the other hydrogen.

In order to have more information about this motion, a PES was calculated and

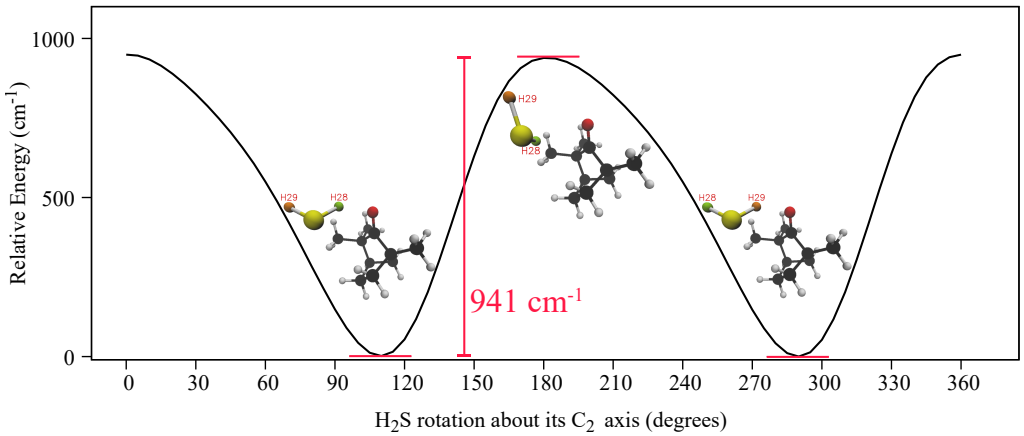

Figure 4.8: *Calculated PES for the fenchone$\cdots H_2S$ complex, showing the minima structures as well as the transition state structure. The PES is the result of rotating the H_2S molecule around its C2 symmetry axis, which is the axis passing through the sulfur atom and the plane HSH (axis between the two hydrogen atoms). The rotation of H_2S around this axis permits the two hydrogen atoms to give two equivalent structures by exchanging their positions through rotation by 180 °.*

is shown in fig. 4.8. The scan shows the two equivalent structures as two minima, having the same energy. The barrier height for this rotation was calculated to be 941 cm^{-1}. The height of this barrier is surprisingly high, but it cannot be said for sure if this magnitude corresponds to the experimental splitting observed since it requires the knowledge of the experimental energy potential. In the literature, the internal dynamics of similar systems is usually treated with the flexible model of Meyer [158, 159], but unfortunately, we do not have access to the program used for this treatment.

The reference [160] gives a very nice description of the cases where such kind of splitting occurs. According to the authors, the splitting is usually not observed in the case of strong O-H$\cdots$O hydrogen bond, but it is observed in the case of the weaker O-H$\cdots$halogen or O-H$\cdots\pi$ hydrogen bonds, where it is possible to break and reform the hydrogen bond while the water molecule is rotating along its symmetry axis. It is also possible to observe the splitting in the case where the water molecule acts as a proton acceptor in the hydrogen bond. An example that can be considered is the case of cyclohexanol and its water complex [161].

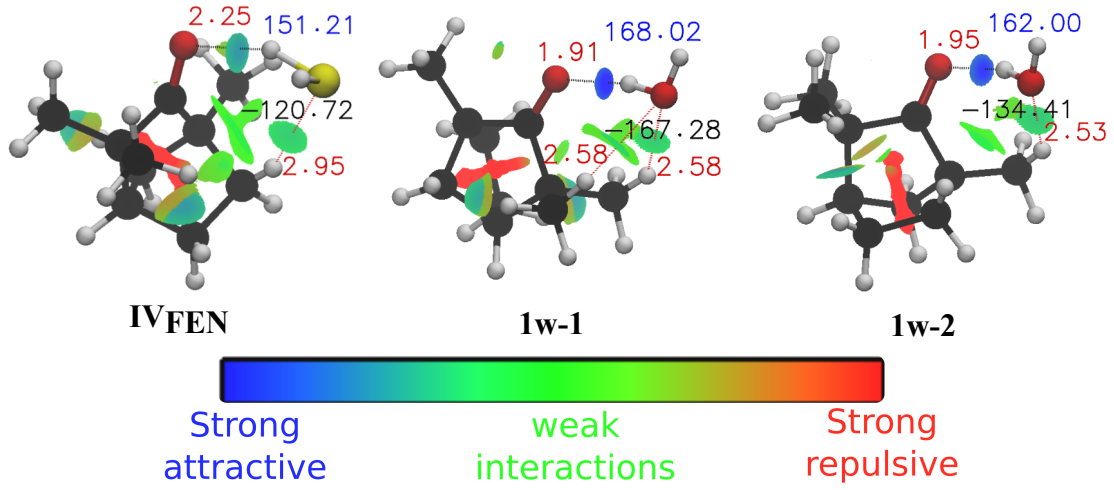

Figure 4.9: *The NCI isosurfaces of the FEN$\cdots H_2S$ (left), FEN$\cdots H_2O$(1) (middle) and FEN$\cdots H_2O$(2) complexes. The numbers displayed in red are the distances, in Å, between the atoms. The number displayed in blue is the angle OHS in degrees. The value displayed in black is the dihedral angle OHSH in degrees*

It seems that our case is similar to the halogen or π-bonding cases, where the S-H$\cdots$O is much weaker than the O-H$\cdots$O hydrogen bond. The weak hydrogen bond gives the H_2S molecule a margin of freedom permitting it to undergo internal rotation, breaking and reforming the hydrogen bond throughout the rotation.

4.3.5 Fenchone-H_2S vs. Fenchone-H_2O

One of the reasons to study complexes with sulfur containing compounds is to understand how the monoterpenoids would interact with sulfur instead of oxygen. And what even motivates more is the fact that complexes of monoterpenoids with one or multiple water molecules are extensively present in the literature. Some examples of these water aggregates include ketones such as camphor [155] and verbenone [162], and alcohols such as verbenol [163] and fenchol [149]. The hydrates of fenchone were also reported recently [157], and the mono-hydrates are of great interest as they permit to make a comparison with the observed complex with H_2S. The authors reported the observation of two monohydrates, which are shown in fig. 4.9 alongside the observed H_2S complex of the present work.

First, we can notice that the complex with sulfur is different from the two

complexes with water in the way the H_2S orients itself with respect to the molecule. This difference may be explained by referring to the difference in sizes between sulfur and oxygen, where the size may result in a constraint on the intermolecular distances. The difference in the structure of experimentally observable species can be a starting point to see if this behavior is functional group related, or due to some other reasons. If we take a look at the intermolecular distances that are shown in fig. 4.9, we can see that the distance between the oxygen atom and the closest hydrogen of the methyl groups in the skeleton, in the case of the monohydrate, is less than the distance between the sulfur atom and the closest hydrogen of the methylene group in the skeleton. This can prove the point discussed above, where the size of the atom causes the distances to be longer. The distances in both cases seem to be leading to a non-covalent interaction of similar magnitude, as can be inferred from the NCI isosurface (see fig. 4.9). The distances are on the limit of the sum of the van der Waals radii of the corresponding atoms and cannot be considered as hydrogen bonds.

Another point to consider is the hydrogen bond. The NCI analysis plot illustrated in fig. 4.9 shows clearly that the hydrogen bond in the case of H_2S is much weaker (light blue) than in the case of H_2O (dark blue). This was expected considering that oxygen is more electronegative than sulfur, which means it is capable of forming stronger hydrogen bonds. The weaker hydrogen bond can be a starting point to understand why the splitting, due to proton exchange, is observed only in the complex with H_2S, and not with water complexes where the strong hydrogen bond cannot be easily broken thus prohibiting the hydrogen atoms' rotation.

4.4 Comparison of the two complexes

In order to have an overall look at the difference between the two complexes observed in this work, this section will present some analysis of the non-covalent interactions occurring in the complexes. These include NBO, NCI and SAPT analyses.

4.4.1 NBO analysis

NBO can give describe the intermolecular interactions occurring in the molecular system, by reflecting the delocalization of electronic charge[164], which plays a role in stabilizing the different interactions occurring. It gives the energy of the different bonding, non-bonding and lone pair orbitals available. This analysis was done for both complexes at the MP2/6-311++G(d,p) level of theory as implemented in Gaussian 16, and the obtained orbitals of interest are visualized in fig. 4.10. An important interaction that we are interested in is the hydrogen bond.

Fenchol$\cdots$$H_2S$

In the case of fenchol, the hydrogen bond is stabilized by two interactions: First, the interaction between the lone pair (LP 1) on the oxygen atom and the anti-bonding orbital (BD*) of the S-H bond with its energy being $9.4\,\mathrm{kJ\,mol^{-1}}$. The second is the interaction between the second lone pair of electrons (LP 2) on the oxygen atom and the anti-bonding orbital (BD*) of the S-H bond with its energy being $15.4\,\mathrm{kJ\,mol^{-1}}$. There are also minor dispersive interactions that aids in stabilizing the complex, and these include the interaction between the lone pair electrons (LP 2) on the sulfur atom and the anti-bonding orbital (BD*) of the C-H bond in the methyl group, having an energy of $3.3\,\mathrm{kJ\,mol^{-1}}$, as well as the interaction between bonding orbital (BD) of the S-H bond and the anti-bonding orbital (BD*) of the O-H bond, having an energy of $0.9\,\mathrm{kJ\,mol^{-1}}$.

Fenchone$\cdots$$H_2S$

In the case of fenchone, the hydrogen bond is stabilized mainly by the interaction between the lone pair electron (LP 1) on the oxygen atom and the anti-bonding orbital (BD*) of the S-H bond, with an energy of $3\,\mathrm{kJ\,mol^{-1}}$. It may also be stabilized by the interaction occurring between the bonding orbital (BD 2) of the C-O bond and the anti-bonding orbital (BD*) of the S-H bond, which has an energy of $5.6\,\mathrm{kJ\,mol^{-1}}$. If we compare the common interaction of the lone pair electrons on the oxygen and the S-H bond in both complexes, we can say that the energy of this interaction is about three times lower (3 compared to $9.4\,\mathrm{kJ\,mol^{-1}}$)

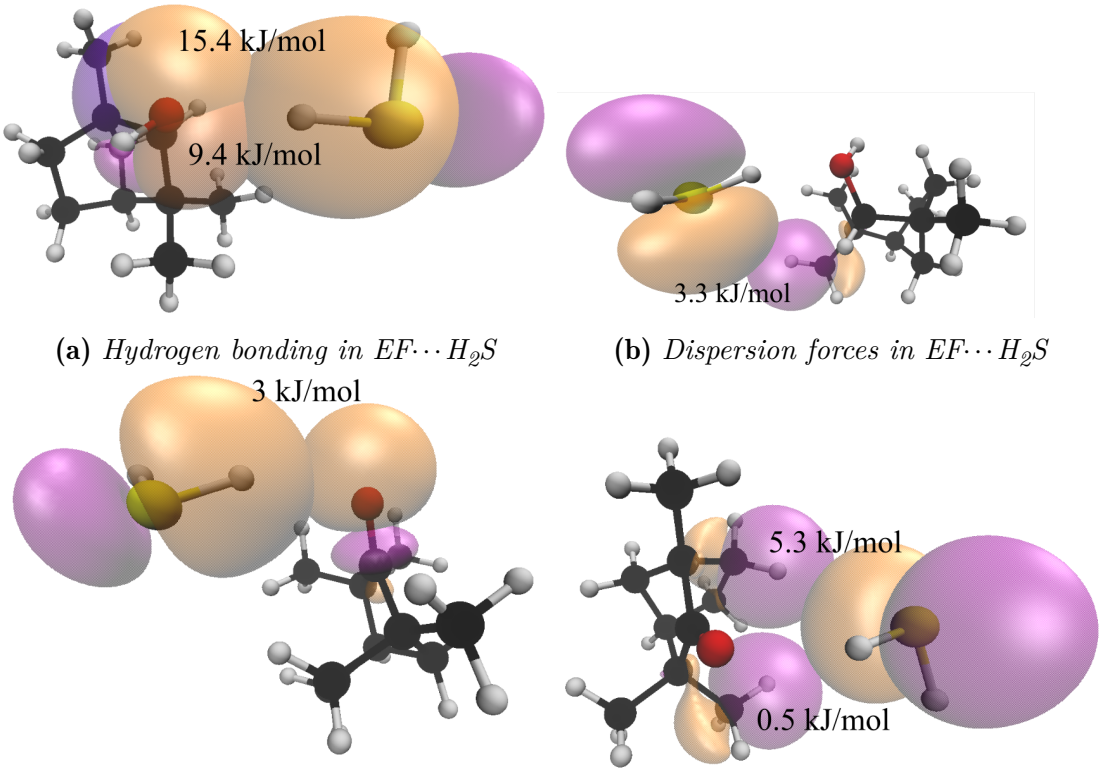

(a) *Hydrogen bonding in EF$\cdots H_2S$* **(b)** *Dispersion forces in EF$\cdots H_2S$*

(c) *Hydrogen bonding in FEN$\cdots H_2S$* **(d)** *Dispersion forces in FEN$\cdots H_2S$*

Figure 4.10: *The different orbitals involved with the hydrogen bonding and dispersion forces for the two complexes, along with their corresponding stabilization energy obtained from NBO analysis*

in the case of the fenchone complex. This can provide evidence that the hydrogen bond is not as strong with the ketone, which can explain the observation of the splitting only with this complex. Other dispersion interactions contribute to the stabilization of the complex. These include the interaction between the lone pair electrons (LP 2) on the sulfur atom and the anti-bonding orbital (BD*) of the C-H bond in the methylene group closest to the H_2S, having an energy of 5.3 kJ mol^{-1}, and also the interaction between the lone pair electrons (LP 2) on the sulfur atom and the anti-bonding orbital (BD*) of the C-H bond in the methyl group, with interaction energy of 0.5 kJ mol^{-1}.

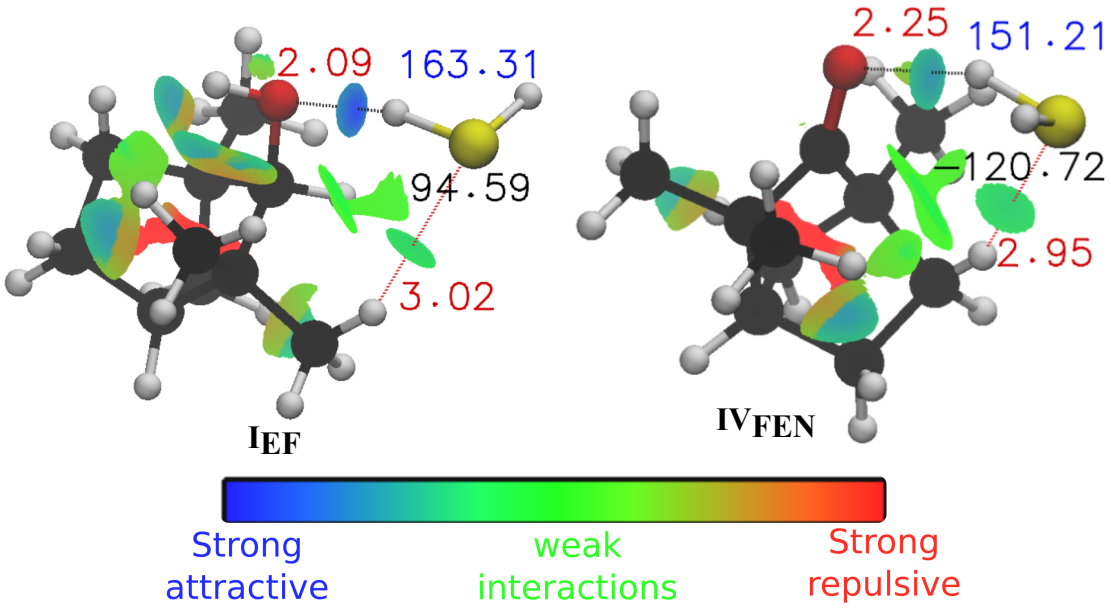

Figure 4.11: *The NCI isosurfaces of the EF$\cdots H_2S$ and FEN$\cdots H_2S$ complexes. The numbers displayed in red are the distances, in Å, between the atoms. The number displayed in blue is the angle OHS in degrees. The value displayed in black is the dihedral angle OHSH in degrees.*

4.4.2 NCI analysis

Another interesting method of characterizing inter-molecular interactions is to perform non covalent interactions (NCI) analysis [151]. It can provide a visual characterization of the strength of the different interactions taking place. The NCI plots for both complexes were previously shown in comparison with their analog water complexes, and they are visualized again, side by side in fig. 4.11, for the sake of comparison between the two complexes themselves. It can be inferred from the colored isosurfaces that the hydrogen bond in fenchol$\cdots H_2S$ complex is much stronger than the hydrogen bond in the fenchone$\cdots H_2S$ complex. This is another way to approve the reasoning behind the large amplitude motion occurring only with the ketone complex. Also in fig. 4.11, we can observe some van der Waals interactions, which are the dispersive forces that contribute to the stabilization of the complexes, by maintaining the position of the H_2S molecule. These interactions are weak in their nature but they contribute to the overall

stabilization. An example of these interactions is that between the sulfur atom and the hydrogen of one of the di-methyl groups in the fenchol$\cdots H_2S$ complex. The distance between the two atoms being around 3 Å is on the limit of their van der Waals sphere, and thus cannot be considered as a hydrogen bond (referring to the definition of the hydrogen bond given before). However, it is still an attractive interaction that aids in stabilizing the complex. Another similar example is the interaction between the sulfur atom and the hydrogen of the methylene group in the ring in the fenchone$\cdots H_2S$ complex. Similarly, it cannot be considered a hydrogen bond because it is on the limit of the van der Waals sphere of the two atoms. The NCI plot shows also the repulsive forces arising from the constraint in the ring, for both molecules. In brief, the van der Waals interactions observed with NCI analysis are slightly stronger in the fenchone$\cdots H_2S$ complex, whereas the hydrogen bond is stronger in fenchol$\cdots H_2S$ complex.

4.4.3 SAPT analysis

SAPT [165] permits to calculate the intermolecular interaction (non-covalent) energy, between two molecules, without computing the total energy of the monomer or the complex. It is one of the methods used for energy decomposition analysis (EDA). Furthermore, what is interesting about SAPT is that it provides a decomposition of the interaction energy into components that have a physical meaning. These components include the following terms:

Electrostatic: Which corresponds to the interaction between charged particles. It can be attractive or repulsive. It is also known as van der Waals interactions. These kinds of interactions are responsible for hydrogen bonding in general.

Exchange: It is a quantum mechanical effect that occurs between identical particles. In the case of electrons, which are fermions, the interaction is referred to as Pauli repulsion. It is repulsive in nature.

Induction: It is also known as electrostatic influence, and it is the effect caused by nearby charges which causes a redistribution of particles. It is generally known as polarization of the molecular orbitals.

Dispersion This type of interaction is attractive by nature, and it occurs between electrically symmetric atoms and molecules. They can be referred to as London dispersion forces, and they arise from the fluctuation in electron distribution that causes induced dipole forces.

SAPT analysis was done on the two observed complexes, as well their water analogs, at the $SAPT_{2+3}$ level based on the output of the optimization at the MP2/6-311++G(d,p) level of theory. The energies of the different terms for the analyzed species are presented in table 4.5. There is also a radar chart in fig. 4.12 that shows the contribution (in %) of each interaction term to the total SAPT energy.

Table 4.5: *The calculated energies (in $kJ\,mol^{-1}$) of the total and interaction terms obtained at the $SAPT_{2+3}$ level.*

Energy ($kJ\,mol^{-1}$)	EF$\cdots H_2S$	FEN$\cdots H_2S$	EF$\cdots H_2O$	FEN$\cdots H_2O$(*I*w-1)	FEN$\cdots H_2O$(*I*w-2)
Electrostatic	−29.23	−21.02	−48.79	−47.45	−39.76
Exchange	42.69	31.02	55.90	51.59	43.41
Induction	−10.07	−6.87	−16.62	−16.10	−13.59
Dispersion	−16.91	−15.95	−17.24	−15.68	−14.75
Total	−13.53	−12.83	−26.75	−27.64	−24.69

It can be seen that for the water complexes, the contribution of the electrostatic interaction to the total energy is noticeably higher than for the sulfur complexes. This can further confirm that hydrogen bonding in water complexes is much stronger. Dispersion forces in the water complexes are lower than those in the sulfur complexes, as well as the repulsive exchange terms. Thus, this can indicate similar stability but because of different reasons. If we want to compare the sulfur complexes only, we can see that the electrostatic contribution to the total energy in the fenchol$\cdots H_2S$ complex is higher than that in the fenchone$\cdots H_2S$ complex. This can provide another proof that the hydrogen bonding in fenchol is stronger, and one more explanation for the fact that splitting is only observed with fenchone. With respect to the other terms, the fenchone$\cdots H_2S$ complex has a higher contribution of the dispersion forces compared to the fenchol$\cdots H_2S$ complex. Meanwhile, the repulsive exchange forces have close values. For the induction terms, all the complexes showed close values.

4.5 Conclusion

In this chapter, the experimental observations allowing the identification of two complexes were presented. The first complex was that of the bicyclic alcohol fenchol with hydrogen sulfide, and the second was that of the bicyclic ketone fenchone with hydrogen sulfide. These findings show that it is possible to form complexes of monoterpenoids with the H_2S molecule. Such type of systems was not reported in the literature before, according to our knowledge. The complexes are formed by a hydrogen bond between the oxygen in the monoterpenoid and a hydrogen atom in the hydrogen sulfide. We can say that the H_2S molecule acts as a proton donor in this case. The hydrogen bond in the case of the ketone was weaker than that with the alcohol. This weak hydrogen bond gave the H_2S molecule enough freedom to perform a large amplitude motion in the form of a proton exchange due to its rotation along its C_2 symmetry axis. This large amplitude motion was reflected in the spectrum as a splitting of the molecular transition lines, where each line was split into two components. A comparison between the two observed complexes was done through several tools including NBO, NCI and SAPT analysis. All the analyses lead to a similar conclusion that the hydrogen bond is much stronger in the case of the alcohol complex compared to the ketone complex.

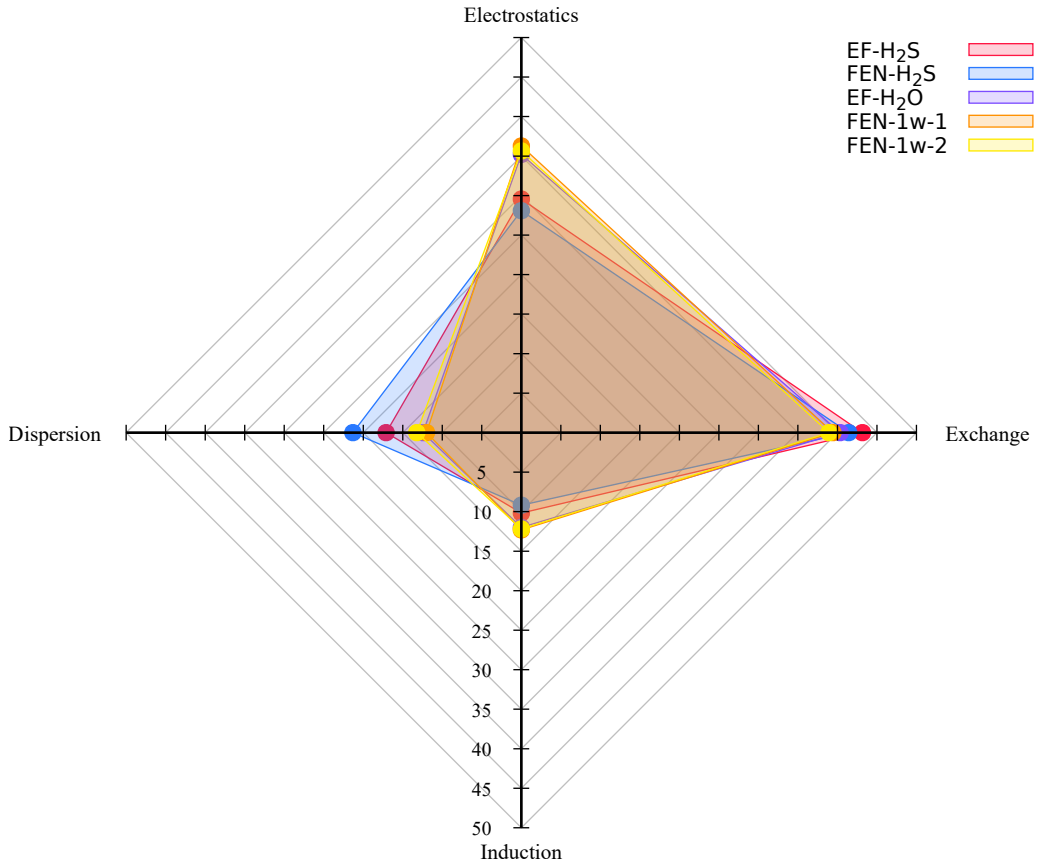

.

Figure 4.12: *Contribution of the different terms (in%) to the total SAPT energy. The values are derived from $SAPT_{2+3}$ level. The calculations for the water complexes were performed starting from the geometries reported in references [149, 157]*

CHAPTER

FIVE

CONFORMATIONAL LANDSCAPE AND INTERNAL DYNAMICS OF LIMONA KETONE

5.1 Introduction

As mentioned in the general introduction of this thesis, biogenic volatile organic compounds (BVOCs) are a class of molecules that is abundant in the atmosphere and is present mainly due to natural sources. Monoterpenes, which are a family of the BVOCs class, consist in combinations of two or more isoprene units, giving rise to a variety of structures and isomers. It was explained in the previous chapter that monoterpenes undergo oxidation in the atmosphere producing oxygenated compounds. These oxygenated compounds, called monoterpenoids, play an important role in atmospheric chemistry. The oxygenated functional groups can be very reactive and induce further reactions in the atmosphere.

Limonene ($C_{10}H_{16}$) is one of the most abundant monoterpenes in the atmosphere. It is usually released naturally from the trees of citrus fruits. It is an important and interesting molecule, due to its reactivity arising from the presence of two double bonds. An important aspect of limonene chemistry is its ozonolysis reaction. This reaction has been the subject of many studies [138, 166–170], as it has been shown to be a primary source of secondary organic aerosol (SOA) formation in the atmosphere [4, 5, 171]. Limonene can also undergo oxidation reactions with different molecules in the atmosphere [172, 173]. It's oxygenated products

are also very reactive themselves and can oxidize further in the atmosphere. Out of the various oxygenated products, only limonene oxide has been studied with FP-FTMW spectroscopy [174].

In order to understand the origin of a specific chemical behavior of a molecule, it is important to have access to information such as its molecular structure, the Potential Energy Surface (PES), its conformational flexibility and its internal dynamics. All of this information are accessible or can be verified by examining the pure rotational spectra using the FP-FTMW technique.

Within the atmospheric context of this work, we are interested in having information about the gas phase structure of one of the major ozonolysis products of limonene: Limona ketone. FP-FTMW spectroscopy permits unambiguous identification of the rotamers in the gas phase, which makes it a great tool for characterizing such types of molecules. In the following sections, a combined theoretical and experimental approach is used to analyze the pure rotational spectra of limona ketone, and to characterize its internal dynamics. The findings will be summarized at the end of this chapter.

5.2 Motivation

Limona ketone (1-(4-Methyl-3-cyclohexen-1-yl)ethanone, $C_9H_{14}O$, will be referred to as LK) is a monoterpenoid with a carbonyl CO group attached to a 1-methylcyclohexene ring. Its 2D structure is illustrated in fig. 5.1. It originates in the atmosphere as a product of oxidation or ozonolysis of limonene. It is an interesting molecule, and

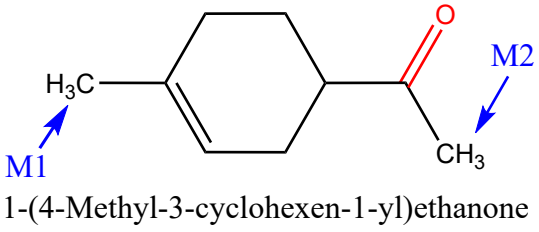

1-(4-Methyl-3-cyclohexen-1-yl)ethanone

Figure 5.1: *The 2D structure of limona ketone. The methyl group attached to the cyclohexene ring at position 1 is called M1, and the methyl moiety of the acetyl functional group is called M2. The IUPAC name is given under the structure.*

it has been shown to generate SOA [175]. Also, it is a short-lived reactive molecule that can further oxidize to give other products [173]. In this study, we want to explore the conformational landscape of LK as well as internal dynamics.

5.3 Methods

The general strategy for the investigation of LK started with theoretical exploitation of the conformational landscape of the molecule. In order to have an idea about the possible stable structures that can be observed in our jet conditions, a PES was calculated. The PES can be obtained by only one pathway which is rotating the acetyl group attached to the ring. This is the only movement that can give rise to stable rotamers. The dihedral angle rotated to obtain the conformations was that including the carbon atoms number 5, 4 and 8 as well as the oxygen atom labeled 10 (see fig. 5.3). This angle ensures the full rotation of the acetyl group. Two PES were calculated: one for the equatorial and one for axial positions. The geometries corresponding to the minima in the surface were then optimized and their harmonic frequencies were also calculated. The methods and basis sets used are summarized in table 2.5. As LK possesses two methyl groups, the barrier height for their internal rotation was calculated by optimizing a transition state through the QST2 method implemented in Gaussian 16.

5.4 Results

5.4.1 Theoretical calculations

The computational findings are reported first, due to their importance in complementing the assignment and analysis of the experimental spectra. The calculated PES for both equatorial and axial conformers are shown in fig. 5.2. In these graphs, the potential energy (in $\mathrm{kJ\,mol^{-1}}$) is plotted as a function of the rotation of the dihedral angle formed by the atoms C5, C4, C8 and O10. For the equatorial position, we can expect four stable structures, corresponding to four minima in the curve at the values around 105°, 140°, 275° and 325°. The conformers were named using numbers preceded by the EQ abbreviation, in increasing order of relative en-

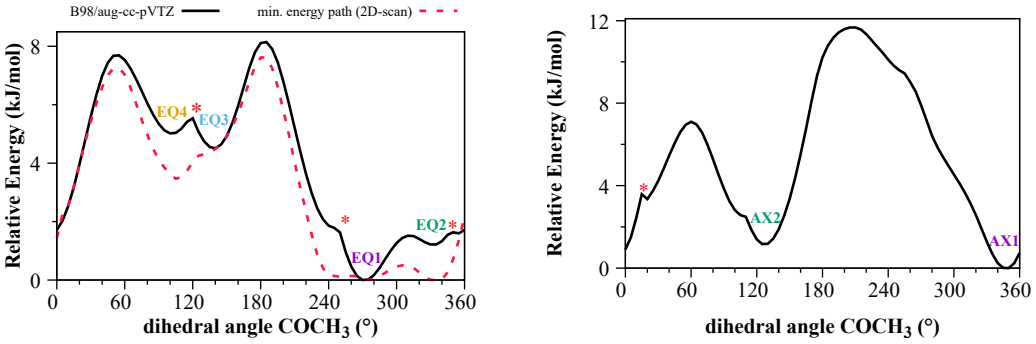

Figure 5.2: *PES for (a) equatorial and (b) axial configurations of limona ketone obtained with the B98 method and the aug-cc-pVTZ basis set*

ergy. This means that the lowest energy conformer is called EQ1 and the one with the highest energy is called EQ4. However, there were some unusual non-smooth points in the curve, and they were marked with a "*" symbol in the figure. These points could be problematic especially as they indicated the presence of the two conformers EQ3 and EQ4, where only one should be logically predicted. These points are unknown in nature and might not hold any physical significance. They will be discussed in more detail later throughout this chapter. The dashed line will also be discussed later. Concerning the axial conformers, two minima exist on the PES, thus two stable rotamers can be expected to be observed. They were named AX1 and AX2 with reference to their energy ordering. The PES for the axial position also showed some strange points, but they did not affect the general trend of the curve.

The structures of the stable conformers for both equatorial and axial conformers, optimized at the MP2/6-311++G(d,p) level of theory are shown in fig. 5.3. The figure also shows the dihedral angle values, and relative energy for each structure. The rotational constants as well as the dipole moment components, obtained from the geometry optimization using different methods and basis sets, for the equatorial conformers are represented in table 5.1. Those for axial conformers are similarly shown in table 5.2. For all the methods, the EQ1 conformer was predicted to have the lowest energy. On the other hand, the energy ordering of the other conformers is not the same with all the methods. A comparison between the

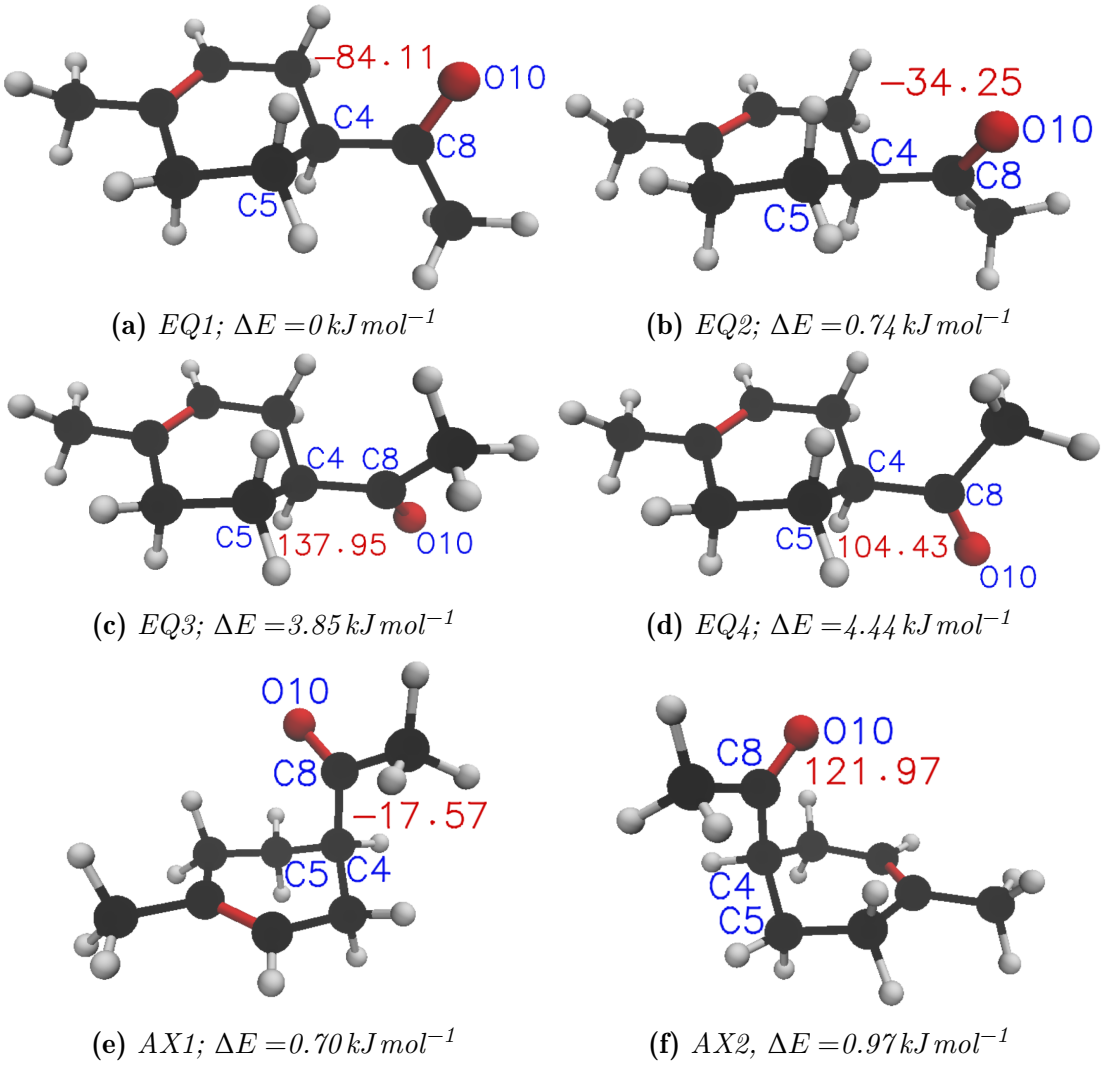

(a) *EQ1;* $\Delta E = 0\,kJ\,mol^{-1}$ **(b)** *EQ2;* $\Delta E = 0.74\,kJ\,mol^{-1}$

(c) *EQ3;* $\Delta E = 3.85\,kJ\,mol^{-1}$ **(d)** *EQ4;* $\Delta E = 4.44\,kJ\,mol^{-1}$

(e) *AX1;* $\Delta E = 0.70\,kJ\,mol^{-1}$ **(f)** *AX2,* $\Delta E = 0.97\,kJ\,mol^{-1}$

Figure 5.3: *Optimized geometries at the MP2/6-311++G(d,p) level of theory of the equatorial (EQ) and axial (AX) conformers of LK. The blue labels show the numbering of the atoms forming the dihedral angle responsible for the conformation. The red numbers represent the dihedral angle values, in degrees, on a scale from −180° to 180°. The* ΔE *value under each figure represents the ZPE corrected relative energy.*

relative energy with the different methods can be found in fig. 5.4.

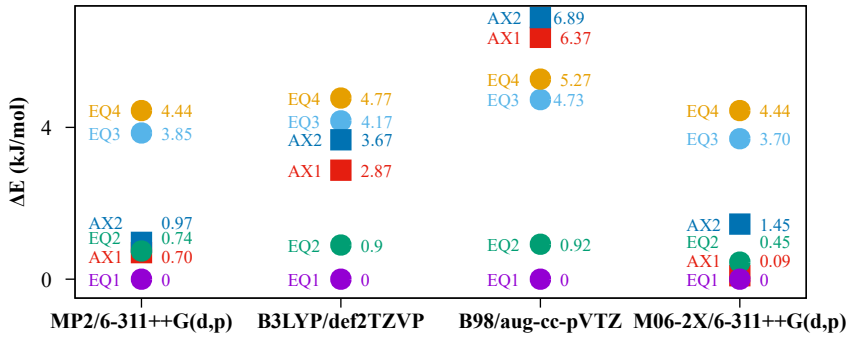

Figure 5.4: *Relative energies of the different axial (AX) and equatorial (EQ) conformers of limona ketone calculated with different methods and basis sets. The values are ZPE corrected.*

5.4.2 Experimental spectrum

The experimental conditions maintained throughout the manipulation of the setup are summarized in table 3.4. Experimentally, a set of transitions corresponding to one conformer was observed and assigned in the spectrum. Figure 5.5 shows a portion of the pure rotational spectrum of LK between 8000 and 9000 MHz, in which the transitions from EQ1, the lowest energy equatorial conformer, can be seen. The spectrum exhibits a, b and c-type transitions of a near prolate asymmetric rotor. The experimental lines were assigned with the help of a predicted spectrum, obtained starting from Watson's semi-rigid rotor Hamiltonian in the A-reduction, and employing the calculated rotational constants using the MP2 method. First, the most intense experimental a-type lines were assigned to the predicted transitions. After obtaining a preliminary fit, different series of lines of variable combinations of J, K_a and K_c values were added gradually to the fit, up to $J = 13$ and $K_a = 4$. Q-branch ($\Delta J = 0$) transitions were also observed and included in the fit. A global fit of 101 lines with an RMS of 1.32 kHz was achieved using Pickett's suite of programs SPFIT/SPCAT.

The identification of the observed conformer was straightforward. The calculated rotational constants of the axial conformers are very different from those of the equatorial conformers. The fitted rotational constants correspond clearly to equatorial constants. Concerning the equatorial conformers themselves, EQ3

Table 5.1: *Rotational constants and absolute values of the dipole moments of the different axial conformers of LK at the different levels of theory*

	EQ1				**EQ2**			
	MP2[a]	**B98[b]**	**B3LYP[c]**	**M06-2X[a]**	**MP2[a]**	**B98[b]**	**B3LYP[c]**	**M06-2X[a]**
A (MHz)	3151.24	3169.26	3184.07	3175.23	3153.10	3163.49	3178.18	3173.73
B (MHz)	732.36	727.51	734.05	738.52	725.85	724.53	732.07	737.49
C (MHz)	660.44	651.66	656.74	656.66	665.47	653.52	657.45	656.44
$\|\mu_a\|$ (D)	1.2	1.2	1.2	1.3	1.3	1.4	1.3	1.4
$\|\mu_b\|$ (D)	1.9	2.0	2.0	2.1	1.1	1.4	1.5	1.6
$\|\mu_c\|$ (D)	1.8	1.8	1.8	1.7	2.1	2.0	1.9	1.9
	EQ3				**EQ4**			
	MP2[a]	**B98[b]**	**B3LYP[c]**	**M06-2X[a]**	**MP2[a]**	**B98[b]**	**B3LYP[c]**	**M06-2X[a]**
A (MHz)	3120.87	3129.23	3146.49	3142.14	3118.12	3128.86	3145.67	3140.82
B (MHz)	722.41	716.56	722.86	727.31	724.75	719.02	725.07	730.2
C (MHz)	673.20	665.87	671.62	672.58	669.89	662.16	668.16	667.98
$\|\mu_a\|$ (D)	2.1	2.2	2.2	2.3	2.1	2.2	2.2	2.2
$\|\mu_b\|$ (D)	1.2	1.4	1.3	1.5	1.0	1.1	1.0	1.2
$\|\mu_c\|$ (D)	1.9	1.9	1.8	1.8	1.9	1.9	1.9	1.6

[a] 6-311++G(d,p) basis set; [b] aug-cc-pVTZ basis set; [c] def2TZVP basis set;

Table 5.2: *Rotational constants and absolute values of the dipole moments of the different axial conformers of LK at different levels of theory*

	AX1				**AX2**			
	MP2[a]	**B98[b]**	**B3LYP[c]**	**M06-2X[a]**	**MP2[a]**	**B98[b]**	**B3LYP[c]**	**M06-2X[a]**
A (MHz)	1938.77	2059.59	2022.85	1975.32	2106.94	2160.72	2142.76	2112.28
B (MHz)	1036.70	970.25	999.75	1025.97	984.42	941.93	964.78	984.59
C (MHz)	976.80	896.75	929.93	960.31	933.38	877.34	903.11	925.75
$\|\mu_a\|$ (D)	0.3	0.3	0.4	0.4	0.3	0.1	0.1	0.2
$\|\mu_b\|$ (D)	2.0	2.1	2.1	2.1	1.9	2.2	2.2	2.1
$\|\mu_c\|$ (D)	1.2	1.2	1.2	1.3	1.9	1.8	1.8	2.0

[a] 6-311++G(d,p) basis set; [b] aug-cc-pVTZ basis set; [c] def2TZVP basis set;

and EQ4 were predicted to have relative energies higher than $3.5\,\mathrm{kJ\,mol^{-1}}$. Conformers with this order of magnitude of energy difference are not usually observed in our experimental conditions. Also, if we examine the barrier height starting from EQ4 or EQ3, from the PES, we can see that its value is around $2.7\,\mathrm{kJ\,mol^{-1}}$

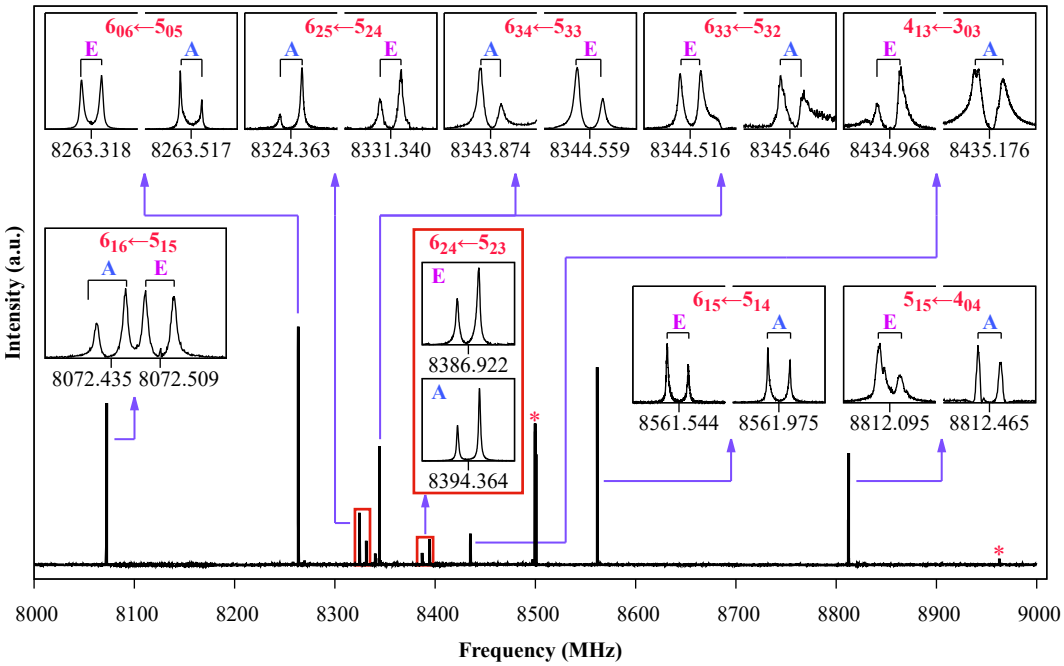

Figure 5.5: *Part of the rotational spectrum of limona ketone between 8 and 9 GHz showing the experimental lines obtained in the low resolution scan. The insets are the recorded high resolutions signals of the assigned transitions appearing in the scan, and showing splitting into A and E symmetry lines due to internal rotation of the methyl group. The transitions are represented in red with the following notation of quantum numbers:* $J'_{K'_aK'_c} \leftarrow J_{K_aK_c}$. *The central frequency of the Doppler doublets is shown under each inset. The * symbol corresponds to unassigned lines.*

which has a good probability to relax into EQ2. This relaxation assumption can be supported by the finding of the reference [176], as they propose that relaxation can occur for barriers lower than $4\,\mathrm{kJ\,mol^{-1}}$ at room temperature. With this, the two conformers EQ3 and EQ4 can be excluded from the picture and the identification is limited between EQ1 and EQ2. The energy difference between these two conformers is less than $1\,\mathrm{kJ\,mol^{-1}}$ with all the methods, which fall within the margin of error of the calculations, so we can't assign the conformer based on the energy factors alone. There is a difference in the calculated dipole moment on the b-axis, between the two conformers. This can give a hint that the observed conformer is EQ1, as the polarizing power used to probe the b-type transitions

Table 5.3: *The experimental and calculated rotational and centrifugal constants, and barrier height of methyl group internal rotation for limona ketone. The fitted internal rotation parameters obtained from XIAM are also given.*

	Exp. value[a]	**Exp.value**[b]	**MP2**[c]	**B98**[d]	**B3LYP**[e]	**M06-2X**[c]
A (MHz)	3159.788 66(11)	3159.509 939(292)	3151.24	3184.07	3169.26	3175.23
B (MHz)	735.407 909(45)	735.390 027(96)	732.36	734.05	727.51	738.52
C (MHz)	653.518 570(52)	653.512 896(91)	660.44	656.74	651.66	656.66
Δ_J (kHz)	0.030 16(18)	0.030 581(395)	0.03	0.03	0.03	0.02
Δ_{JK} (kHz)	0.0571(24)	0.052 08(312)	0.06	0.07	0.07	0.06
Δ_K (kHz)	0.3659(86)	0.3362(158)	0.44	0.38	0.39	0.37
δ_J (kHz)	0.001 516(74)	0.002 012(238)	0.003	0.002	0.002	0.001
δ_K (kHz)	0.834(21)	0.8315(260)	0.63	0.63	0.60	0.51
V_3 (cm^{-1})		298.39(25)	207.12	178.27	238.89	125.52
ϵ (rad)		2.615 051(959)	2.36	2.35	2.34	2.39
δ (rad)		2.230 887(506)	2.13	2.09	2.08	2.09
Dpi2- (kHz)		−317.622(807)				
F_0 (GHz)		163.561(115)				
N[f]	101	214				
RMS (kHz) [g]	1.32	3.36				

[a] A-reduced Watson Hamiltonian in I^r representation; [b] Internal rotation fit using combined axis method (CAM) employed in XIAM program; [c] 6-311++G(d,p) basis set; [d] aug-cc-pVTZ basis set; [e] def2TZVP basis set; [f] Number of lines used in fit; [g] root mean square value of observed - calculated line frequencies

of the molecules are in agreement with the values calculated for EQ1. Another fact that can lead toward the same conclusion is the shape of the potential energy curve. The barrier between EQ2 and EQ1 is very shallow and can be estimated to be less than $1\,kJ\,mol^{-1}$, which means that EQ2 will relax to EQ1 in the jet. Hence, the observed conformer was identified as EQ1. The experimental constants are shown in table 5.3, along with the calculated parameters obtained with the different methods used.

The calculated constants show good agreement with those obtained experimentally. The A constant is better predicted with the MP2 and B3LYP methods with difference about 0.3 %, followed by M06-2X method (0.5 %). The largest difference was with the B98 method. The B constant, on the other hand, was better predicted with the B98 method with a difference about 0.2 %. The MP2 and M06-2X methods had a slightly higher difference of 0.4 %, whereas the B3LYP method was the furthest away from the experiment constant (1.1 %). The B3LYP method gave the closest value of C constant with a difference of about 0.3 % from

the fitted value. The difference with the M06-2X and B98 methods was a little higher (0.5 %), whereas the MP2 value was the farthest away (1.1 %). The deviations of centrifugal constants from theoretical values are more important, but their sign and order of magnitude are consistent. This can be a reflection of the fact that the range of values of the J, K_a and K_c quantum numbers are limited in the microwave region.

The rotational spectra of LK showed splitting of the experimental lines, which ranged from few kHz up to few MHz. Figure 5.5 shows examples of the split lines of different types. The intensities of the two components were similar, which indicates a characteristic splitting due to the internal rotation of the methyl C_{3V} rotor. LK possesses two methyl groups: The first is attached directly to the cyclohexene cycle and we called it M1. The second is that of the acetyl moiety and it is attached to the carbonyl CO functional group, and we called it M2. The barrier heights for the internal rotation of M1 and M2 were computed through the difference in energy between the optimized transition state (QST2 in Gaussian) and the ground state optimized geometry of EQ1. For M1, the barrier height was calculated to be 789 cm^{-1} at the MP2/6-311++G(d,p) level of theory. This barrier is too high to induce an observable effect in the spectrum. Meanwhile, for M2 the barrier height (MP2/6-311++G(d,p)) was 207 cm^{-1}, which causes splittings that correspond to what we observe in our spectrum. The barrier height was also calculated using different methods and basis sets, and the values can be seen in table 5.3. The difference in the value between methods was significant.

As described before on page 26, a threefold rotation splits the energy levels into A and E symmetry states (see page 27), where the E symmetry level is doubly degenerate. These states vary with the change in rotational quantum numbers. The description of internal rotation motion is done by extending the rigid-rotor Hamiltonian to include the potential and kinetic energies of the internal rotor. In the case of methyl, which is a C_{3V} rotor, the potential energy V can be given in terms of the torsion angle α as follows (see eq. (2.51)):

$$V(\alpha) = \frac{V_3}{2}(1 - \cos(3\alpha)) + \frac{V_6}{2}(1 - \cos(6\alpha)) + \cdots \tag{5.1}$$

In the case of LK, the lack of symmetry makes only V_3 significant, thus it is

possible to truncate the expression of $V(\alpha)$ after the V_3 term. The implementation of the internal rotor potential into the molecular Hamiltonian is straightforward basically. Nonetheless, the transformation of the rotor into a suitable and efficient coordinate system remains a necessity. There are several propositions to perform such coordinate transformation, which can be consulted in references [177–183]. In this work, the program XIAM [118, 119] was chosen for its simplicity and efficiency in treating such systems. One of its advantages is its ability to treat up to three internal rotors with V_3 potential. It implements the extended internal axis method (IAM) proposed by Woods [182, 183]. As a first step, the rotational constants obtained from the semi-rigid model were used to predict the A and E symmetry lines with XIAM. Then, different series of lines were fitted gradually to reach an effective fit with an RMS 3.36 kHz. The total number of lines used in the fit was 214 including a, b and c-type lines of Q- and R-branches, with both A and E symmetry. The experimental value of the threefold barrier height was 298 cm^{-1}, which is not in agreement with the calculated values. This discrepancy will be discussed shortly after. The treatment of internal rotation gives access to information other than the barrier height, such as the orientation of the internal rotor. This is given by two angles δ and ϵ. They correspond to the angles between the internal rotation axis and the z principal axis, and between the projection of the internal rotation axis into the xy plane and the x principal axis, respectively. This means that in the case of a near prolate top and using the I^r representation, δ represents the angle between the a-axis and the rotor axis, and ϵ represents the angle between the b-axis and the projection of the rotor axis into the xy plane. The values of these two angles have been calculated based on the optimized geometries with different calculation methods, and have been fitted with XIAM as well. The calculated and experimental values are given in table 5.3. The rotational constant ($F = \frac{\hbar}{2I_\alpha}$) of the methyl group was also calculated and fitted.

5.4.3 Discussion

It was not possible to calculate a value of the barrier height in good agreement with the experimental findings, despite the multiple methods and basis sets used. This may be due to an interaction present between the methyl group and another

surrounding moiety, as XIAM treats the rotor as an isolated unit. In an attempt to see if this is the case, a potential energy scan in which only the methyl group was rotated while the geometry of the rest of the molecule was fixed, was performed using the MP2 method. This mimics the case of an isolated rotor. The obtained value of the barrier height was $442\,\mathrm{cm}^{-1}$. The experimental value is between the relaxed and "adiabatic" value: $V_3^{calc} < V_3^{exp} < V_3^{adb}$. This finding implies the presence of intramolecular interaction between the M2 internal rotation and the surrounding atoms and groups in the skeleton of the molecule. Such effects have been discussed before in the cases of methacrolein [184], 2-Acetyl-5-methylfuran [185], methylglyoxal [186] and nitrotoluene [187]. Thus it is only possible to achieve an effective fit to reach instrumental accuracy, due to the unavailability of any model that takes into account the interactions between large amplitude motions. The effective fit can be achieved by introducing empirical terms to the isolated rotation Hamiltonian. In our case, this is done by using the Dpi2- parameter, which is an empirical operator for internal rotation-overall rotation distortion, programmed into XIAM. The fitted value of this parameter is listed in table 5.3. This interaction will be supported by more arguments in the following section.

5.5 Intermolecular interaction

5.5.1 Conformational landscape

There are many indications in the theoretical and experimental aspects of this study that give an impression that an intermolecular interaction is present in LK. The characterization of this interaction requires a broader look at the conformational landscape of the molecule. First, it would be useful to check the fundamental information obtained from the PES. As pointed out at the beginning of this chapter, the PES showed some non-smooth points at certain angle values, and those can be seen as small bumps in the curve. A similar discontinuity was observed in the case of 2-Acetyl-5-methylfuran [185]. The first approach was to calculate PESs with different methods and basis sets to eliminate any artifact that might occur with the calculation method used. All the curves showed these bumps. In the case of axial configuration, these points did not disrupt the general trend of the curve.

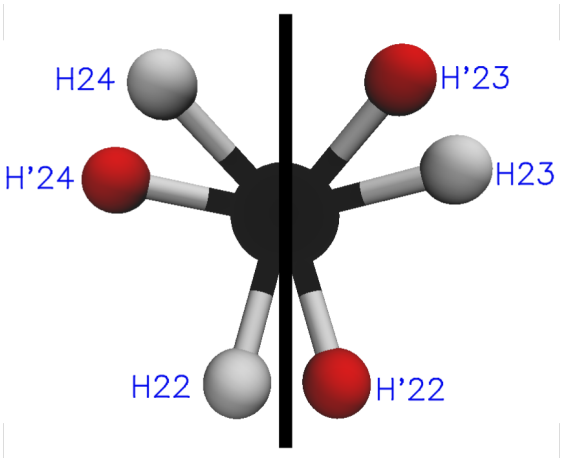

Figure 5.6: *The geometry of the methyl group M1 extracted from the relaxed PES at C5C4C8O10=119° and 120°. The white hydrogen atoms with the H labeling correspond to the 119° geometry, whereas the red hydrogen atoms with H' labeling correspond to the 120° geometry. The black line in the middle represents an imaginary plane of symmetry that allows the Hydrogen atoms to mirror themselves. The angle of rotation between each pair of H-H' is about 40°.*

However, in the case of the equatorial configuration, these points can be problematic. For example, at the dihedral angle value 120°, the discontinuity gave rise to a local maximum that indicates the presence of two stable structures. If these points have no significant physical meaning, it might be a different case where only one conformer is stable at this point. A further investigation was necessary to better understand the nature of these points. A second step was to check the geometry of the molecule at every point of the relaxed PES. Another tighter relaxed scan was made around 120° with rotation steps of 1°. This allows to follow the geometry more precisely. An interesting movement was noticed around the 120° limit. When the acetyl group rotation passed from 119° to 120°, the methyl group of the acetyl moiety rotated suddenly by an angle of about 40°. This movement is illustrated in fig. 5.6. What is important about this movement, is that the three hydrogen atoms of the methyl group seem to use this sudden rotation to mirror themselves through a quasi-symmetry plane passing through the CH bond. And what can be observed also is that the hydrogen atoms of the methyl are close to the hydrogen atoms of the methylene groups of the ring. Hence, it seems that the methyl group

tries to rotate itself as the acetyl is rotating to decrease the steric hindrence and avoid the repulsive interactions with other hydrogens in the skeleton, all while achieving an iso-energetic state. This kind of movement was observed at all the problematic points, and for the axial PES.

5.5.2 2D-PES

With the fact that the experimental barrier height of the methyl internal rotation was not in agreement with the calculated values (relaxed and adiabatic, see section 5.4.3), and that the geometrical observations are not enough to have a definite answer about the nature of the interaction or discontinuity points, we need another approach to tackle the problem. We decided to calculate a two dimensional PES, for the equatorial configuration, by varying two dihedral angles: The first is the one containing the acetyl ($COCH_3$) group (C5C4C8O10) and may be called D1, and the second is the one containing the methyl (CH_3) M2 group (C4C8C9H22) and may be called D2. The relaxed scan was made by steps of 5° for the two dihedral angles. This approach was supported by the findings reported in the case of nitrotoluene [187], where the authors used a 2D-PES iso-surface to point out the correlation effects between two large amplitude motions in the molecule. The map view of the calculated 2D-PES is shown in fig. 5.7. Having general look at the surface, we can see that there is no discontinuity or break from one point to another. If we examine the behavior of the isolated methyl group, *i.e.* at fixed values of the acetyl rotation, we can see a typical three fold potential of three equivalent minima as expected with internal rotation. Now considering the acetyl overall movements, the energy variation agrees qualitatively with that observed with the 1D-PES. However, the energy valleys exhibit a distorted diagonal orientation rather than the expected horizontal and vertical circular valleys in an interaction-free situation. This can be considered evidence of the presence of an interaction between the two movements. To examine the situation more closely, the lowest energy path in the 2D-PES was followed. This is done by starting from the minimum, which is in this case at D1=275° and D2=60°, and then moving point by point on the PES until full rotation of the acetyl group is reached. At each point, which represents D1+5°, the angle D2 corresponding to the lowest en-

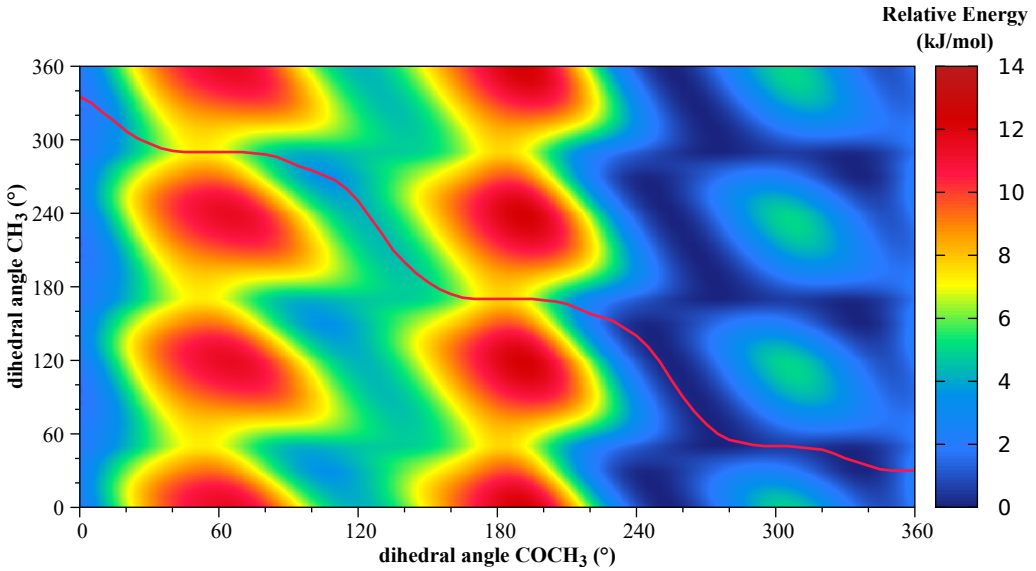

Figure 5.7: *2D-PES of limona ketone in equatorial position involving the rotation of the acetyl $COCH_3$ and the M2 methyl CH_3 groups. The red line represents the followed path with minimum energy values.*

ergy is marked. The obtained lowest energy path is traced as a red line in fig. 5.7. We can see that this path displays a diagonal trajectory down the energy valleys rather than the straight expected path. At certain points, the lowest energy is directed toward an alternative equivalent minimum rather than the minimum in the same valley. The points where the change of direction occurs are the same values where the bumps appear in the 1D-PES, *i.e.* 120°, 245° and 340°. The extracted energy path was plotted in fig. 5.2a to compare it with the 1D-PES. Several points can be noticed from this comparison. First, the bumps in the PES are no longer existing, which means that they did not have any significant physical meaning, and they can be just calculation artifacts. Another point that can be observed is that there is only one minimum around 105°, instead of the two assigned to EQ3 and EQ4. Indeed, it seems that there are two iso-energetic structures rather than two different conformers at this point, which changes the overall conformational landscape of the molecule. Furthermore, the potential well surrounding EQ1 and EQ2 seems to be very shallow in the extracted energy path. The fact that the 2D-PES

does not take into consideration any constraint between the followed groups and the rest of the molecules can explain this flat behavior.

The realistic energy potential can be thought of as an intermediate between the 1D-PES and the extracted minimum energy path, maybe closer to the relaxed PES but with no bumps. In brief, these observations can be used to qualitatively confirm the presence of an interaction between the M2 methyl group and the skeleton of LK molecule. This interaction can justify the discrepancy between the calculated and experimental torsion barrier height values, and the need to use the Dpi2- parameter in the fit.

5.6 Conclusion

In this chapter, the pure rotational analysis of the rotationally and vibrationally cold gas phase spectrum of LK, an ozonolysis product of limonene, was described. The assignment and fitting of the experimental lines between 3.8 and 19.3 GHz were supplemented with *ab initio* and DFT theoretical calculations. A conformer of the equatorial position, calculated to have the lowest energy, was the only species identified in the spectrum. The other calculated equatorial conformers are expected to relax to the observed conformer in our supersonic jet expansion conditions. The two stable conformers of the axial position were not observed, despite the low difference in relative energy. The experimental lines of the identified equatorial rotamer were split, with the magnitude of the splitting ranging between a few kHz up to tens of MHz. The 1:1 line splitting was contributed to the internal rotation of the methyl group M2 (see fig. 5.1). The experimental barrier height for this methyl torsion was obtained by fitting the A and E symmetry lines using the CAM method used in the XIAM program. However, the determination of the experimental barrier showed a poor agreement between the calculated and experimental values, which pushed us to further investigate the internal dynamics of the molecule. For this reason, a 2D-PES was calculated in an attempt to have a better understanding and recognition of any interaction taking place. The deduced information revealed the presence of intramolecular interaction, which was qualitatively described as being a repulsive interaction between the methyl group M2 and the nearest hydrogen atoms in the molecular skeleton. This leads

to the correlation between two movements: The rotation of both the acetyl and the methyl groups, where the methyl tends to rotate itself at some points during the overall acetyl rotation. This concerted movement can be interpreted as an attempt to minimize the repulsion due to steric hindrance.

The present data can be considered as a starting point for future micro-solvation or aggregation studies of LK, which can be very interesting from an atmospheric point of view. It can also be used as a basis for comparison with similar molecules that have an acetyl group attached to a ring.

CHAPTER

SIX

SUMMARY AND PERSPECTIVE

The physical properties and chemical reactivity of a molecule are mainly influenced by its structure, flexibility and internal dynamics. Thus, having accurate structural information is essential to predict and understand the interactions between the molecule and its surroundings or polarizing electromagnetic radiation. Rotational spectroscopy is a tool that is used, within the general context of this thesis, to determine the unambiguous gas phase structure of different types of molecules of atmospheric interest. The pure rotational spectra can be used as fingerprints for the detection of the studied systems in the atmosphere. Also, the structural flexibility and microsolvation patterns of the molecules represent a good starting point for understanding the formation and stability of secondary aerosols, that alter several atmospheric processes.

This thesis presents an overview of the spectroscopic characterization of biogenic monoterpenoids, employing a combined theoretical and experimental approach. The first step is the calculation and optimization of geometries with quantum chemical calculations in order to have access to the structural parameters such as rotational constants and dipole moments and in some cases barrier heights. This information is built upon to predict, assign and facilitate the analysis of the experimental gas phase pure rotational spectra, recorded with cavity-based spectrometers of type Balle-Flygare in the range 2-20 GHz. The computational methods in some cases are also used to support the discussions about the internal

dynamics and large amplitude motions.

This manuscript also includes the technical and experimental details of the construction and characterization of a new chirped-pulse Fourier transform microwave spectrometer. The performance characteristics presented for the new spectrometer represent a basis for the application of this powerful broadband spectroscopy technique for medium sized organic molecules. The instrumental ensemble is inspired from the initial design reported by the Pate group [30], and is adapted to operate in the frequency range 6-18 GHz. The performance of the signal sources and emitters has been characterized to visualize the quality of the excitation signal. The timing sequence has also been optimized to obtain a good S/N. The repetition rate of the experiment is mainly limited by the pumping speed, and in some cases by the data processing time. The spectrometer is equipped with three injectors that can be heated up to 520 K, and has a nozzle of 1 mm diameter. These injectors, which are placed outside the vacuum chamber, allow to supersonically expand the gas molecules into the vacuum chamber where excitation takes place. The low rotational temperatures in the jet ($<$5 K), as well as the collision free zone due to low molecular density, reduce the line broadening of the signals dramatically. The performance of the spectrometer was evaluated with acetone, which is a volatile molecule with interesting spectroscopic features. The primary tests presented here will be complemented by recording the spectra of more complex molecules with challenging features such as hyperfine structures of nitrogen containing species. Such types of tests can reveal the performance of the spectrometer in challenging situations and determine the maximum resolution that can be achieved. A projected improvement on the spectrometer is to use a sequence of multiple excitation/detection sequences for each gas pulse, which can reduce the accumulation time significantly. Furthermore, a computer program that integrates all the instruments and ensures the full automation of the spectrometer is in the progress.

Another aspect of this work was accomplished by employing the Fabry-Perot Fourier transform microwave (FP-FTMW) spectrometers available in Lille. The first subject under study included the microsolvation of two monoterpenoids with the H_2S molecule. The two chosen molecules were the alcohol fenchol and the ketone fenchone. One conformer for each of the fenchol$\cdots H_2S$ and fenchone$\cdots H_2S$

complexes were observed and identified with the help of theoretical computations. The two isolated molecules possess the same skeletal structure with a different functional group, yet their behavior toward the complexation with H_2S was different. The hydroxyl OH group formed a stronger hydrogen bond with the H_2S molecule compared to the carbonyl CO group. The weaker hydrogen bond in the ketone placed the H_2S group in a quasi-free state where splittings due to large amplitude motions were observed in the spectrum, and which were fitted to two states using Pickett's suite of programs SPFIT/SPCAT. The noncovalent interactions in both complexes were also examined through natural bonding orbitals (NBO), non covalent interactions (NCI) and Symmetry-adapted perturbation theory (SAPT) analysis. Those revealed that the dispersive forces in the ketone complex were stronger compared to the alcohol. The obtained complexes were compared to their analogs water complexes in terms of the general structure and noncovalent interactions. To our knowledge, no studies of complexes of monoterpenoids with H_2S were reported in the literature. This study is a proof that it is possible to observe such complexes, and opens the door for more experiments to explore the behavior of similar molecules with other functional groups, such as aldehydes and carboxylic acids, towards sulfur containing compounds. It can also be considered as an additional clue that aids in understanding the formation of SOAs starting from sulfur species. Future perspectives include the study of more complexes of monoterpenoids of atmospheric interest with sulfur containing compounds. The larger datasets may reveal some interesting features in the spectra, and lead to a more clear general image of the complexation patterns, that permits to make a solid comparison with water complexes. Also, we are curious to see if it is possible to form complexes with two or three H_2S molecules.

Another study, that falls within the same atmospheric context, involved the exploration of conformational landscape and internal dynamics of limona ketone (LK). LK is a short-lived major ozonolysis product of limonene, one of the most abundant monoterpenes in the atmosphere. First of all, relaxed Potential Energy Surface (PES) was calculated for the two possible equatorial and axial positions of the carbonyl CO group with respect to the cyclohexene ring. The optimized geometries of the minima, with different calculation methods, gave the rotational constants necessary to predict the frequencies of the transitions. Out of the four

equatorial and two axial conformers only the lowest energy equatorial conformer was observed in our experimental conditions, which confirms the assumptions of strong relaxation in the jet conditions. The experimental spectrum showed splitting of the lines into two components which is a characteristic of methyl (CH_3) internal rotation motion. The barrier heights of the torsion of the two methyl groups were calculated. It was inferred from the calculated barrier values that only the methyl group of the carbonyl moiety would cause observable splitting in our conditions. The A and E symmetry lines were fitted using XIAM program, and the experimental barrier height was determined. However, the experimental and theoretical values of the barrier were not in good agreement, and an empirical parameter was needed to reach instrumental accuracy. A geometry scan where the molecular parameters were fixed to mimic an isolated movement of the methyl was performed, to obtain an adiabatic value of the barrier height. The experimental value was between the fixed and relaxed values. This was an indication of a possible interaction in the molecule. A 2D-PES was calculated by scanning the dihedral angles of the acetyl and the methyl groups. The isosurface showed a diagonal pathway instead of the expected straight pathway down one valley. This was another indication of coupling between the two movements due to an interaction with the skeleton of the molecule. We followed the least energy path in the 2D-PES, and the obtained curve had no bumps and showed three instead of four minima. This is proof of the presence of an intramolecular interaction that cannot be interpreted by 1D-PES. The examination of the geometry at the problematic scan points showed that the methyl group undergoes a sudden rotation when it comes close to hydrogen atoms in the ring, to avoid the hindrance and achieve an isoenergetic position. In brief, the presence of repulsive interaction between the methyl group and the rest of the molecule forces a correlated movement of the acetyl and methyl groups. The methodology proposed in the present work should be of interest for other compounds containing acetyl moiety. Studying the microsolvation effects on LK is an interesting idea to check in the future, where complexation might induce structural or conformational changes.

Finally, I would like to acknowledge the presented work was funded by the Labex (Laboratoire d'Excellence) CaPPA (Chemical and Physical properties of the atmosphere) through the PIA (Programme d'Investissements d'Avenir) pro-

gram under the contract ANR-11-LABX-0005-01, by the Regional Council Hauts de France, by the European Funds for Regional Economic Development (FEDER), and by the French ministry of research higher education (Ministèrede l'Enseignement Supérieur et de la Recherche). It is also a contribution to the CPER research project CLIMIBIO and research project P4S.

BIBLIOGRAPHY

[1] A. Cicolella. "Les composés organiques volatils (COV) : définition, classification et propriétés". In: *Revue des Maladies Respiratoires* 25.2 (Feb. 1, 2008), pp. 155–163. ISSN: 0761-8425. DOI: 10.1016/S0761-8425(08)71513-4.

[2] A. Guenther, C. N. Hewitt, D. Erickson, R. Fall, C. Geron, T. Graedel, P. Harley, L. Klinger, M. Lerdau, W. A. Mckay, T. Pierce, B. Scholes, R. Steinbrecher, R. Tallamraju, J. Taylor, and P. Zimmerman. "A Global Model of Natural Volatile Organic Compound Emissions". In: *Journal of Geophysical Research: Atmospheres* 100.D5 (1995), pp. 8873–8892. ISSN: 2156-2202. DOI: 10.1029/94JD02950.

[3] K. Sindelarova, C. Granier, I. Bouarar, A. Guenther, S. Tilmes, T. Stavrakou, J.-F. Müller, U. Kuhn, P. Stefani, and W. Knorr. "Global Data Set of Biogenic VOC Emissions Calculated by the MEGAN Model over the Last 30 Years". In: *Atmospheric Chemistry and Physics* 14.17 (Sept. 9, 2014), pp. 9317–9341. ISSN: 1680-7316. DOI: 10.5194/acp-14-9317-2014.

[4] R. Atkinson and J. Arey. "Gas-Phase Tropospheric Chemistry of Biogenic Volatile Organic Compounds: A Review". In: *Atmospheric Environment. The 1997 Southern California Ozone Study (SCOS97-NARSTO). Dedicated to the Memory of Dr. Glen Cass (1947-2001)* 37 (Jan. 1, 2003), pp. 197–219. ISSN: 1352-2310. DOI: 10.1016/S1352-2310(03)00391-1.

[5] S. Koch, R. Winterhalter, E. Uherek, A. Kolloff, P. Neeb, and G. K. Moortgat. "Formation of New Particles in the Gas-Phase Ozonolysis of Monoterpenes". In: *Atmospheric Environment* 34.23 (Jan. 1, 2000), pp. 4031–4042. ISSN: 1352-2310. DOI: 10.1016/S1352-2310(00)00133-3.

[6] T. F. Mentel, J. Wildt, A. Kiendler-Scharr, E. Kleist, R. Tillmann, M. Dal Maso, R. Fisseha, T. Hohaus, H. Spahn, R. Uerlings, R. Wegener, P. T. Griffiths, E. Dinar, Y. Rudich, and A. Wahner. "Photochemical Production of Aerosols from Real Plant Emissions". In: *Atmospheric Chemistry and Physics* 9.13 (July 7, 2009), pp. 4387–4406. ISSN: 1680-7316. DOI: 10.5194/acp-9-4387-2009.

[7] P. Forster, V. Ramaswamy, P. Artaxo, T. Berntsen, R. Betts, D. Fahey, J. Haywood, J. Lean, D. Lowe, G. Myhre, J. Nganga, R. Prinn, G. Raga, M. Schulz, and R. Van Dorland. *Changes in Atmospheric Constituents and in Radiative Forcing Chapter 2*. United Kingdom: Cambridge University Press, 2007. ISBN: 978-0-521-70596-7. URL: http://inis.iaea.org/search/search.aspx?orig_q=RN:39002468.

[8] J. Lelieveld, J. S. Evans, M. Fnais, D. Giannadaki, and A. Pozzer. "The Contribution of Outdoor Air Pollution Sources to Premature Mortality on a Global Scale". In: *Nature* 525.7569 (7569 Sept. 2015), pp. 367–371. ISSN: 1476-4687. DOI: 10.1038/nature15371.

[9] Y. Ren, Z. Qu, Y. Du, R. Xu, D. Ma, G. Yang, Y. Shi, X. Fan, A. Tani, P. Guo, Y. Ge, and J. Chang. "Air Quality and Health Effects of Biogenic Volatile Organic Compounds Emissions from Urban Green Spaces and the Mitigation Strategies". In: *Environmental Pollution* 230 (Nov. 1, 2017), pp. 849–861. ISSN: 0269-7491. DOI: 10.1016/j.envpol.2017.06.049.

[10] M. Goswami and E. Arunan. "The Hydrogen Bond: A Molecular Beam Microwave Spectroscopist's View with a Universal Appeal". In: *Physical Chemistry Chemical Physics* 11.40 (Oct. 28, 2009), pp. 8974–8983. ISSN: 1463-9084. DOI: 10.1039/B907708A.

[11] P. Brimblecombe. "10.14 - The Global Sulfur Cycle". In: *Treatise on Geochemistry (Second Edition)*. Ed. by H. D. Holland and K. K. Turekian. Oxford: Elsevier, Jan. 1, 2014, pp. 559–591. ISBN: 978-0-08-098300-4. DOI: 10.1016/B978-0-08-095975-7.00814-7.

[12] T. Ausma and L. J. De Kok. "Atmospheric H2S: Impact on Plant Functioning". In: *Frontiers in Plant Science* 10 (2019). ISSN: 1664-462X. DOI: 10.3389/fpls.2019.00743.

[13] T. S. Bates, B. K. Lamb, A. Guenther, J. Dignon, and R. E. Stoiber. "Sulfur Emissions to the Atmosphere from Natural Sourees". In: *Journal of Atmospheric Chemistry* 14.1 (Apr. 1, 1992), pp. 315–337. ISSN: 1573-0662. DOI: 10.1007/BF00115242.

[14] S. F. Watts. "The Mass Budgets of Carbonyl Sulfide, Dimethyl Sulfide, Carbon Disulfide and Hydrogen Sulfide". In: *Atmospheric Environment* 34.5 (Jan. 1, 2000), pp. 761–779. ISSN: 1352-2310. DOI: 10.1016/S1352-2310(99)00342-8.

[15] A. Das, P. K. Mandal, F. J. Lovas, C. Medcraft, N. R. Walker, and E. Arunan. "The H2S Dimer Is Hydrogen-Bonded: Direct Confirmation from Microwave Spectroscopy". In: *Angewandte Chemie International Edition*

57.46 (2018), pp. 15199–15203. ISSN: 1521-3773. DOI: 10.1002/anie.201808162.

[16] E. Arunan, T. Emilsson, H. S. Gutowsky, G. T. Fraser, G. de Oliveira, and C. E. Dykstra. "Rotational Spectrum of the Weakly Bonded C6H6–H2S Dimer and Comparisons to C6H6–H2O Dimer". In: *The Journal of Chemical Physics* 117.21 (Dec. 1, 2002), pp. 9766–9776. ISSN: 0021-9606. DOI: 10.1063/1.1518999.

[17] M. Goswami and E. Arunan. "Microwave Spectrum and Structure of C6H5CCH H2S Complex". In: *Journal of Molecular Spectroscopy*. Philip R. Bunker and A. Robert W. McKellar 268.1 (July 1, 2011), pp. 147–156. ISSN: 0022-2852. DOI: 10.1016/j.jms.2011.04.011.

[18] C. H. Townes and A. L. Schawlow. *Microwave Spectroscopy*. Dover Publications, 2013. ISBN: 978-0-486-16231-7. URL: https://books.google.fr/books?id=f33CAgAAQBAJ.

[19] W. E. Good. "The Inversion Spectrum of Ammonia". In: *Physical Review* 69.9-10 (May 1, 1946), pp. 539–539. DOI: 10.1103/PhysRev.69.539.

[20] C. H. Townes. "The Ammonia Spectrum and Line Shapes Near 1.25-Cm Wave-Length". In: *Physical Review* 70.9-10 (Nov. 1, 1946), pp. 665–671. DOI: 10.1103/PhysRev.70.665.

[21] B. P. Dailey, R. L. Kyhl, M. W. P. Strandberg, J. H. Van Vleck, and E. B. Wilson. "The Hyperfine Structure of the Microwave Spectrum of Ammonia and the Existence of a Quadrupole Moment in ${\mathrm{N}}{14}$". In: *Physical Review* 70.11-12 (Dec. 1, 1946), pp. 984–984. DOI: 10.1103/PhysRev.70.984.

[22] J. P. Gordon, H. J. Zeiger, and C. H. Townes. "The Maser—New Type of Microwave Amplifier, Frequency Standard, and Spectrometer". In: *Physical Review* 99.4 (Aug. 15, 1955), pp. 1264–1274. DOI: 10.1103/PhysRev.99.1264.

[23] J. Kraitchman. "Determination of Molecular Structure from Microwave Spectroscopic Data". In: *American Journal of Physics* 21.1 (Jan. 1, 1953), pp. 17–24. ISSN: 0002-9505. DOI: 10.1119/1.1933338.

[24] R. H. Dicke and R. H. Romer. "Pulse Techniques in Microwave Spectroscopy". In: *Review of Scientific Instruments* 26.10 (Oct. 1, 1955), pp. 915–928. ISSN: 0034-6748. DOI: 10.1063/1.1715156.

[25] J. C. McGurk, R. T. Hofmann, and W. H. Flygare. "Transient Absorption and Emission and the Measurement of T1 and T2 in the J O→1 Rotational Transition in OCS". In: *The Journal of Chemical Physics* 60.7 (Apr. 1, 1974), pp. 2922–2928. ISSN: 0021-9606. DOI: 10.1063/1.1681462.

[26] J. C. McGurk, T. G. Schmalz, and W. H. Flygare. "Fast Passage in Rotational Spectroscopy: Theory and Experiment". In: *The Journal of Chemical Physics* 60.11 (June 1, 1974), pp. 4181–4188. ISSN: 0021-9606. DOI: 10.1063/1.1680886.

[27] J. Ekkers and W. H. Flygare. "Pulsed Microwave Fourier Transform Spectrometer". In: *Review of Scientific Instruments* 47.4 (Apr. 1976), pp. 448–454. ISSN: 0034-6748. DOI: 10.1063/1.1134647.

[28] T. J. Balle and W. H. Flygare. "Fabry–Perot Cavity Pulsed Fourier Transform Microwave Spectrometer with a Pulsed Nozzle Particle Source". In: *Review of Scientific Instruments* 52.1 (Jan. 1, 1981), pp. 33–45. ISSN: 0034-6748. DOI: 10.1063/1.1136443.

[29] J.-U. Grabow, W. Stahl, and H. Dreizler. "A Multioctave Coaxially Oriented Beam-resonator Arrangement Fourier-transform Microwave Spectrometer". In: *Review of Scientific Instruments* 67.12 (Dec. 1, 1996), pp. 4072–4084. ISSN: 0034-6748. DOI: 10.1063/1.1147553.

[30] G. G. Brown, B. C. Dian, K. O. Douglass, S. M. Geyer, S. T. Shipman, and B. H. Pate. "A Broadband Fourier Transform Microwave Spectrometer Based on Chirped Pulse Excitation". In: *Review of Scientific Instruments* 79.5 (May 1, 2008), p. 053103. ISSN: 0034-6748. DOI: 10.1063/1.2919120.

[31] L. Evangelisti, G. Sedo, and J. van Wijngaarden. "Rotational Spectrum of 1,1,1-Trifluoro-2-butanone Using Chirped-Pulse Fourier Transform Microwave Spectroscopy". In: *The Journal of Physical Chemistry A* 115.5 (Feb. 10, 2011), pp. 685–690. ISSN: 1089-5639. DOI: 10.1021/jp1089905.

[32] G. S. Grubbs, C. T. Dewberry, K. C. Etchison, K. E. Kerr, and S. A. Cooke. "A Search Accelerated Correct Intensity Fourier Transform Microwave Spectrometer with Pulsed Laser Ablation Source". In: *Review of Scientific Instruments* 78.9 (Sept. 1, 2007), p. 096106. ISSN: 0034-6748. DOI: 10.1063/1.2786022.

[33] M. K. Jahn, D. A. Dewald, D. Wachsmuth, J.-U. Grabow, and S. C. Mehrotra. "Rapid Capture of Large Amplitude Motions in 2,6-Difluorophenol: High-resolution Fast-Passage FT-MW Technique". In: *Journal of Molecular Spectroscopy*. Broadband Rotational Spectroscopy 280 (Oct. 1, 2012), pp. 54–60. ISSN: 0022-2852. DOI: 10.1016/j.jms.2012.07.006.

[34] S. Mata, I. Peña, C. Cabezas, J. C. López, and J. L. Alonso. "A Broadband Fourier-transform Microwave Spectrometer with Laser Ablation Source: The Rotational Spectrum of Nicotinic Acid". In: *Journal of Molecular Spectroscopy*. Broadband Rotational Spectroscopy 280 (Oct. 1, 2012), pp. 91–96. ISSN: 0022-2852. DOI: 10.1016/j.jms.2012.08.004.

[35] J. L. Neill, S. T. Shipman, L. Alvarez-Valtierra, A. Lesarri, Z. Kisiel, and B. H. Pate. "Rotational Spectroscopy of Iodobenzene and Iodobenzene–Neon with a Direct Digital 2–8GHz Chirped-Pulse Fourier Transform Microwave Spectrometer". In: *Journal of Molecular Spectroscopy* 269.1 (Sept. 1, 2011), pp. 21–29. ISSN: 0022-2852. DOI: 10.1016/j.jms.2011.04.016.

[36] C. Pérez, S. Lobsiger, N. A. Seifert, D. P. Zaleski, B. Temelso, G. C. Shields, Z. Kisiel, and B. H. Pate. "Broadband Fourier Transform Rotational Spectroscopy for Structure Determination: The Water Heptamer". In: *Chemical Physics Letters* 571 (May 20, 2013), pp. 1–15. ISSN: 0009-2614. DOI: 10.1016/j.cplett.2013.04.014.

[37] B. Reinhold, I. A. Finneran, and S. T. Shipman. "Room Temperature Chirped-Pulse Fourier Transform Microwave Spectroscopy of Anisole". In: *Journal of Molecular Spectroscopy* 270.2 (Dec. 1, 2011), pp. 89–97. ISSN: 0022-2852. DOI: 10.1016/j.jms.2011.10.002.

[38] D. Schmitz, V. Alvin Shubert, T. Betz, and M. Schnell. "Multi-Resonance Effects within a Single Chirp in Broadband Rotational Spectroscopy: The Rapid Adiabatic Passage Regime for Benzonitrile". In: *Journal of Molecular Spectroscopy*. Broadband Rotational Spectroscopy 280 (Oct. 1, 2012), pp. 77–84. ISSN: 0022-2852. DOI: 10.1016/j.jms.2012.08.001.

[39] A. J. Shirar, D. S. Wilcox, K. M. Hotopp, G. L. Storck, I. Kleiner, and B. C. Dian. "Impact of Molecular Conformation on Barriers to Internal Methyl Rotation: The Rotational Spectrum of m-Methylbenzaldehyde". In: *The Journal of Physical Chemistry A* 114.46 (Nov. 25, 2010), pp. 12187–12194. ISSN: 1089-5639. DOI: 10.1021/jp107679n.

[40] S. L. Stephens and N. R. Walker. "Determination of Nuclear Spin–Rotation Coupling Constants in CF3I by Chirped-Pulse Fourier-transform Microwave Spectroscopy". In: *Journal of Molecular Spectroscopy* 263.1 (Sept. 1, 2010), pp. 27–33. ISSN: 0022-2852. DOI: 10.1016/j.jms.2010.06.007.

[41] M. Schnell, U. Erlekam, P. R. Bunker, G. von Helden, J.-U. Grabow, G. Meijer, and A. van der Avoird. "Structure of the Benzene Dimer—Governed by Dynamics". In: *Angewandte Chemie International Edition* 52.19 (2013), pp. 5180–5183. ISSN: 1521-3773. DOI: 10.1002/anie.201300653.

[42] N. A. Seifert, D. P. Zaleski, C. Pérez, J. L. Neill, B. H. Pate, M. Vallejo-López, A. Lesarri, E. J. Cocinero, F. Castaño, and I. Kleiner. "Probing the C H Weak Hydrogen Bond in Anesthetic Binding: The Sevoflurane–Benzene Cluster". In: *Angewandte Chemie International Edition* 53.12 (2014), pp. 3210–3213. ISSN: 1521-3773. DOI: 10.1002/anie.201309848.

[43] S. Lobsiger, C. Perez, L. Evangelisti, K. K. Lehmann, and B. H. Pate. "Molecular Structure and Chirality Detection by Fourier Transform Microwave Spectroscopy". In: *The Journal of Physical Chemistry Letters* 6.1 (Jan. 2, 2015), pp. 196–200. DOI: 10.1021/jz502312t.

[44] V. A. Shubert, D. Schmitz, C. Pérez, C. Medcraft, A. Krin, S. R. Domingos, D. Patterson, and M. Schnell. "Chiral Analysis Using Broadband Rotational Spectroscopy". In: *The Journal of Physical Chemistry Letters* 7.2 (Jan. 21, 2016), pp. 341–350. DOI: 10.1021/acs.jpclett.5b02443.

[45] D. S. Wilcox, K. M. Hotopp, and B. C. Dian. "Two-Dimensional Chirped-Pulse Fourier Transform Microwave Spectroscopy". In: *The Journal of Physical Chemistry A* 115.32 (Aug. 18, 2011), pp. 8895–8905. ISSN: 1089-5639. DOI: 10.1021/jp2043202.

[46] B. C. Dian, G. G. Brown, K. O. Douglass, and B. H. Pate. "Measuring Picosecond Isomerization Kinetics via Broadband Microwave Spectroscopy". In: *Science* 320.5878 (May 16, 2008), pp. 924–928. DOI: 10.1126/science.1155736.

[47] B. C. Dian, G. G. Brown, K. O. Douglass, F. S. Rees, J. E. Johns, P. Nair, R. D. Suenram, and B. H. Pate. "Conformational Isomerization Kinetics of Pent-1-En-4-Yne with 3,330 Cm−1 of Internal Energy Measured by Dynamic Rotational Spectroscopy". In: *Proceedings of the National Academy of Sciences* 105.35 (Sept. 2, 2008), pp. 12696–12700. ISSN: 0027-8424, 1091-6490. DOI: 10.1073/pnas.0800520105. pmid: 18678910.

[48] M. C. McCarthy, K. L. K. Lee, P. B. Carroll, J. P. Porterfield, P. B. Changala, J. H. Thorpe, and J. F. Stanton. "Exhaustive Product Analysis of Three Benzene Discharges by Microwave Spectroscopy". In: *The Journal of Physical Chemistry A* 124.25 (June 25, 2020), pp. 5170–5181. ISSN: 1089-5639. DOI: 10.1021/acs.jpca.0c02919.

[49] F. Merkt and M. Quack. "Molecular Quantum Mechanics and Molecular Spectra, Molecular Symmetry, and Interaction of Matter with Radiation". In: *Handbook of High-resolution Spectroscopy*. American Cancer Society, 2011. ISBN: 978-0-470-74959-3. DOI: 10.1002/9780470749593.hrs001.

[50] M. Born and R. Oppenheimer. "Zur Quantentheorie Der Molekeln". In: *Annalen der Physik* 389.20 (1927), pp. 457–484. ISSN: 1521-3889. DOI: 10.1002/andp.19273892002.

[51] P. F. Bernath. *Spectra of Atoms and Molecules*. Oxford University Press, Apr. 20, 2020. 542 pp. ISBN: 978-0-19-009541-3. Google Books: e2HdDwAAQBAJ.

[52] A. Bauder. "Fundamentals of Rotational Spectroscopy". In: *Handbook of High-resolution Spectroscopy*. American Cancer Society, 2011. ISBN: 978-0-470-74959-3. DOI: 10.1002/9780470749593.hrs002.

[53] W. Gordy and R. L. Cook. *Microwave Molecular Spectra*. Wiley, 1984. ISBN: 978-0-471-08681-9.

[54] A. R. Edmonds. *Angular Momentum in Quantum Mechanics*. Princeton University Press, 2016. ISBN: 978-1-4008-8418-6. URL: https://books.google.fr/books?id=YEWPDAAAQBAJ.

[55] R. N. Zare and V. D. Kleiman. *Angular Momentum: Understanding Spatial Aspects in Chemistry and Physics*. Wiley, 1988. ISBN: 978-0-471-85892-8. URL: https://books.google.dk/books?id=kDQ31MBZxioC.

[56] C. H. Townes and A. L. Schawlow. *Microwave Spectroscopy*. Dover Publications, 1975. ISBN: 978-0-486-61798-5. URL: https://books.google.fr/books?id=3LFeBReoDh0C.

[57] P. R. Bunker and P. Jensen. *Fundamentals of Molecular Symmetry*. Taylor & Francis, 2004. ISBN: 978-0-7503-0941-7. URL: https://books.google.fr/books?id=jhIrUtaNiowC.

[58] H. W. Kroto. *Molecular Rotation Spectra*. Dover Publications, 2003. ISBN: 978-0-486-49540-8. URL: https://books.google.fr/books?id=fyjJwAEACAAJ.

[59] J. K. G. Watson. "Determination of Centrifugal Distortion Coefficients of Asymmetric-Top Molecules". In: *The Journal of Chemical Physics* 46.5 (Mar. 1, 1967), pp. 1935–1949. ISSN: 0021-9606. DOI: 10.1063/1.1840957.

[60] J. K. G. Watson. "Indeterminacies of Fitting Parameters in Molecular Spectroscopy". In: *Handbook of High-resolution Spectroscopy*. American Cancer Society, 2011. ISBN: 978-0-470-74959-3. DOI: 10.1002/9780470749593.hrs017.

[61] T. Helgaker, P. Jorgensen, and J. Olsen. *Molecular Electronic-Structure Theory*. Wiley, 2013. ISBN: 978-1-118-53147-1. URL: https://books.google.fr/books?id=APjLWFFxWkQC.

[62] A. Szabo and N. S. Ostlund. *Modern Quantum Chemistry: Introduction to Advanced Electronic Structure Theory*. Dover Publications, 1996. ISBN: 978-0-486-69186-2.

[63] R. M. Dreizler and E. K. U. Gross. *Density Functional Theory: An Approach to the Quantum Many-body Problem*. Springer, 1990. ISBN: 978-3-540-51993-5.

[64] W. Koch and M. C. Holthausen. *A Chemist's Guide to Density Functional Theory*. Wiley, 2001. ISBN: 978-3-527-30422-6.

[65] R. G. Parr and W. Yang. *Density-Functional Theory of Atoms and Molecules*. Oxford University Press, USA, 1994. ISBN: 978-0-19-509276-9.

[66] D. R. Hartree. "The Wave Mechanics of an Atom with a Non-Coulomb Central Field. Part III. Term Values and Intensities in Series in Optical Spectra". In: *Mathematical Proceedings of the Cambridge Philosophical Society* 24.3 (1928), pp. 426–437. ISSN: 1469-8064. DOI: 10.1017/S0305004100015954.

[67] D. R. Hartree. "The Wave Mechanics of an Atom with a Non-Coulomb Central Field. Part II. Some Results and Discussion". In: *Mathematical Proceedings of the Cambridge Philosophical Society* 24.1 (1928), pp. 111–132. ISSN: 1469-8064. DOI: 10.1017/S0305004100011920.

[68] D. R. Hartree. "The Wave Mechanics of an Atom with a Non-Coulomb Central Field. Part I. Theory and Methods". In: *Mathematical Proceedings of the Cambridge Philosophical Society* 24.1 (1928), pp. 89–110. ISSN: 1469-8064. DOI: 10.1017/S0305004100011919.

[69] V. Fock. "Näherungsmethode zur Lösung des quantenmechanischen Mehrkörperproblems". In: *Zeitschrift für Physik* 61.1 (Jan. 1, 1930), pp. 126–148. ISSN: 0044-3328. DOI: 10.1007/BF01340294.

[70] C. Møller and M. S. Plesset. "Note on an Approximation Treatment for Many-Electron Systems". In: *Physical Review* 46.7 (Oct. 1, 1934), pp. 618–622. DOI: 10.1103/PhysRev.46.618.

[71] E. Schrödinger. "Über Das Verhältnis Der Heisenberg-Born-Jordanschen Quantenmechanik Zu Der Meinem". In: *Annalen der Physik* 384.8 (1926), pp. 734–756. ISSN: 1521-3889. DOI: 10.1002/andp.19263840804.

[72] P. Hohenberg and W. Kohn. "Inhomogeneous Electron Gas". In: *Physical Review* 136 (3B Nov. 9, 1964), B864–B871. DOI: 10.1103/PhysRev.136.B864.

[73] W. Kohn and L. J. Sham. "Self-Consistent Equations Including Exchange and Correlation Effects". In: *Physical Review* 140 (4A Nov. 15, 1965), A1133–A1138. DOI: 10.1103/PhysRev.140.A1133.

[74] P. a. M. Dirac. "Note on Exchange Phenomena in the Thomas Atom". In: *Mathematical Proceedings of the Cambridge Philosophical Society* 26.3 (July 1930), pp. 376–385. ISSN: 1469-8064, 0305-0041. DOI: 10.1017/S0305004100016108.

[75] J. C. Slater. "A Simplification of the Hartree-Fock Method". In: *Physical Review* 81.3 (Feb. 1, 1951), pp. 385–390. DOI: 10.1103/PhysRev.81.385.

[76] D. M. Ceperley and B. J. Alder. "Ground State of the Electron Gas by a Stochastic Method". In: *Physical Review Letters* 45.7 (Aug. 18, 1980), pp. 566–569. DOI: 10.1103/PhysRevLett.45.566.

[77] S. H. Vosko, L. Wilk, and M. Nusair. "Accurate Spin-Dependent Electron Liquid Correlation Energies for Local Spin Density Calculations: A Critical Analysis". In: *Canadian Journal of Physics* 58.8 (Aug. 1, 1980), pp. 1200–1211. ISSN: 0008-4204. DOI: 10.1139/p80-159.

[78] J. P. Perdew and Y. Wang. "Erratum: Accurate and Simple Analytic Representation of the Electron-Gas Correlation Energy [Phys. Rev. B 45, 13244 (1992)]". In: *Physical Review B* 98.7 (Aug. 14, 2018), p. 079904. DOI: 10.1103/PhysRevB.98.079904.

[79] W. Kohn and L. J. Sham. "Self-Consistent Equations Including Exchange and Correlation Effects". In: *Physical Review* 140 (4A Nov. 15, 1965), A1133–A1138. DOI: 10.1103/PhysRev.140.A1133.

[80] A. D. Becke. "Density-Functional Exchange-Energy Approximation with Correct Asymptotic Behavior". In: *Physical Review A* 38.6 (Sept. 1, 1988), pp. 3098–3100. DOI: 10.1103/PhysRevA.38.3098.

[81] C. Lee, W. Yang, and R. G. Parr. "Development of the Colle-Salvetti Correlation-Energy Formula into a Functional of the Electron Density". In: *Physical Review B* 37.2 (Jan. 15, 1988), pp. 785–789. DOI: 10.1103/PhysRevB.37.785.

[82] K. Burke, J. P. Perdew, and Y. Wang. "Derivation of a Generalized Gradient Approximation: The PW91 Density Functional". In: *Electronic Density Functional Theory: Recent Progress and New Directions*. Ed. by J. F. Dobson, G. Vignale, and M. P. Das. Boston, MA: Springer US, 1998, pp. 81–111. ISBN: 978-1-4899-0316-7. DOI: 10.1007/978-1-4899-0316-7_7.

[83] J. P. Perdew, J. A. Chevary, S. H. Vosko, K. A. Jackson, M. R. Pederson, D. J. Singh, and C. Fiolhais. "Atoms, Molecules, Solids, and Surfaces: Applications of the Generalized Gradient Approximation for Exchange and Correlation". In: *Physical Review B* 46.11 (Sept. 15, 1992), pp. 6671–6687. DOI: 10.1103/PhysRevB.46.6671.

[84] J. P. Perdew, K. Burke, and M. Ernzerhof. "Generalized Gradient Approximation Made Simple". In: *Physical Review Letters* 77.18 (Oct. 28, 1996), pp. 3865–3868. DOI: 10.1103/PhysRevLett.77.3865.

[85] A. D. Becke. "A New Mixing of Hartree–Fock and Local Density-functional Theories". In: *The Journal of Chemical Physics* 98.2 (Jan. 15, 1993), pp. 1372–1377. ISSN: 0021-9606. DOI: 10.1063/1.464304.

[86] A. D. Becke. “Density-functional Thermochemistry. III. The Role of Exact Exchange”. In: *The Journal of Chemical Physics* 98.7 (Apr. 1, 1993), pp. 5648–5652. ISSN: 0021-9606. DOI: 10.1063/1.464913.

[87] P. J. Stephens, F. J. Devlin, C. F. Chabalowski, and M. J. Frisch. “Ab Initio Calculation of Vibrational Absorption and Circular Dichroism Spectra Using Density Functional Force Fields”. In: *The Journal of Physical Chemistry* 98.45 (Nov. 1, 1994), pp. 11623–11627. ISSN: 0022-3654. DOI: 10.1021/j100096a001.

[88] A. D. Becke. “Density-functional Thermochemistry. IV. A New Dynamical Correlation Functional and Implications for Exact-exchange Mixing”. In: *The Journal of Chemical Physics* 104.3 (Jan. 15, 1996), pp. 1040–1046. ISSN: 0021-9606. DOI: 10.1063/1.470829.

[89] A. D. Becke. “Density-Functional Thermochemistry. V. Systematic Optimization of Exchange-Correlation Functionals”. In: *The Journal of Chemical Physics* 107.20 (Nov. 22, 1997), pp. 8554–8560. ISSN: 0021-9606. DOI: 10.1063/1.475007.

[90] H. L. Schmider and A. D. Becke. “Optimized Density Functionals from the Extended G2 Test Set”. In: *The Journal of Chemical Physics* 108.23 (June 5, 1998), pp. 9624–9631. ISSN: 0021-9606. DOI: 10.1063/1.476438.

[91] Y. Zhao and D. G. Truhlar. “The M06 Suite of Density Functionals for Main Group Thermochemistry, Thermochemical Kinetics, Noncovalent Interactions, Excited States, and Transition Elements: Two New Functionals and Systematic Testing of Four M06-class Functionals and 12 Other Functionals”. In: *Theoretical Chemistry Accounts* 120.1 (May 1, 2008), pp. 215–241. ISSN: 1432-2234. DOI: 10.1007/s00214-007-0310-x.

[92] S. Grimme. “Accurate description of van der Waals complexes by density functional theory including empirical corrections”. In: *Journal of Computational Chemistry* 25.12 (2004), pp. 1463–1473. ISSN: 1096-987X. DOI: 10.1002/jcc.20078.

[93] S. Grimme. “Density Functional Theory with London Dispersion Corrections”. In: *WIREs Computational Molecular Science* 1.2 (2011), pp. 211–228. ISSN: 1759-0884. DOI: 10.1002/wcms.30.

[94] S. Grimme, J. Antony, S. Ehrlich, and H. Krieg. “A Consistent and Accurate Ab Initio Parametrization of Density Functional Dispersion Correction (DFT-D) for the 94 Elements H-Pu”. In: *The Journal of Chemical Physics* 132.15 (Apr. 16, 2010), p. 154104. ISSN: 0021-9606. DOI: 10.1063/1.3382344.

[95] E. R. Johnson and A. D. Becke. "A Post-Hartree–Fock Model of Intermolecular Interactions". In: *The Journal of Chemical Physics* 123.2 (July 8, 2005), p. 024101. ISSN: 0021-9606. DOI: 10.1063/1.1949201.

[96] E. R. Johnson and A. D. Becke. "A Post-Hartree-Fock Model of Intermolecular Interactions: Inclusion of Higher-Order Corrections". In: *The Journal of Chemical Physics* 124.17 (May 5, 2006), p. 174104. ISSN: 0021-9606. DOI: 10.1063/1.2190220.

[97] H. Iikura, T. Tsuneda, T. Yanai, and K. Hirao. "A Long-Range Correction Scheme for Generalized-Gradient-Approximation Exchange Functionals". In: *The Journal of Chemical Physics* 115.8 (Aug. 10, 2001), pp. 3540–3544. ISSN: 0021-9606. DOI: 10.1063/1.1383587.

[98] A. Savin. *In Recent Developments of Modern Density Functional Theory; Seminario, JM, Ed.* Elsevier: Amsterdam, 1996.

[99] J.-D. Chai and M. Head-Gordon. "Systematic Optimization of Long-Range Corrected Hybrid Density Functionals". In: *The Journal of Chemical Physics* 128.8 (Feb. 27, 2008), p. 084106. ISSN: 0021-9606. DOI: 10.1063/1.2834918.

[100] J. C. Slater. "Atomic Shielding Constants". In: *Physical Review* 36.1 (July 1, 1930), pp. 57–64. DOI: 10.1103/PhysRev.36.57.

[101] S. F. Boys and A. C. Egerton. "Electronic Wave Functions - I. A General Method of Calculation for the Stationary States of Any Molecular System". In: *Proceedings of the Royal Society of London. Series A. Mathematical and Physical Sciences* 200.1063 (Feb. 22, 1950), pp. 542–554. DOI: 10.1098/rspa.1950.0036.

[102] W. J. Hehre, R. F. Stewart, and J. A. Pople. "Self-Consistent Molecular-Orbital Methods. I. Use of Gaussian Expansions of Slater-Type Atomic Orbitals". In: *The Journal of Chemical Physics* 51.6 (Sept. 15, 1969), pp. 2657–2664. ISSN: 0021-9606. DOI: 10.1063/1.1672392.

[103] R. Ditchfield, W. J. Hehre, and J. A. Pople. "Self-Consistent Molecular-Orbital Methods. IX. An Extended Gaussian-Type Basis for Molecular-Orbital Studies of Organic Molecules". In: *The Journal of Chemical Physics* 54.2 (Jan. 15, 1971), pp. 724–728. ISSN: 0021-9606. DOI: 10.1063/1.1674902.

[104] R. Krishnan, J. S. Binkley, R. Seeger, and J. A. Pople. "Self-consistent Molecular Orbital Methods. XX. A Basis Set for Correlated Wave Functions". In: *The Journal of Chemical Physics* 72.1 (Jan. 1, 1980), pp. 650–654. ISSN: 0021-9606. DOI: 10.1063/1.438955.

[105] T. H. Dunning. "Gaussian Basis Sets for Use in Correlated Molecular Calculations. I. The Atoms Boron through Neon and Hydrogen". In: *The Journal of Chemical Physics* 90.2 (Jan. 15, 1989), pp. 1007–1023. ISSN: 0021-9606. DOI: 10.1063/1.456153.

[106] F. Weigend. "Accurate Coulomb-fitting Basis Sets for H to Rn". In: *Physical Chemistry Chemical Physics* 8.9 (Feb. 23, 2006), pp. 1057–1065. ISSN: 1463-9084. DOI: 10.1039/B515623H.

[107] F. Weigend and R. Ahlrichs. "Balanced Basis Sets of Split Valence, Triple Zeta Valence and Quadruple Zeta Valence Quality for H to Rn: Design and Assessment of Accuracy". In: *Physical Chemistry Chemical Physics* 7.18 (Aug. 30, 2005), pp. 3297–3305. ISSN: 1463-9084. DOI: 10.1039/B508541A.

[108] M. J. Frisch, G. W. Trucks, H. B. Schlegel, G. E. Scuseria, M. A. Robb, J. R. Cheeseman, G. Scalmani, V. Barone, G. A. Petersson, H. Nakatsuji, X. Li, M. Caricato, A. V. Marenich, J. Bloino, B. G. Janesko, R. Gomperts, B. Mennucci, H. P. Hratchian, J. V. Ortiz, A. F. Izmaylov, J. L. Sonnenberg, Williams, F. Ding, F. Lipparini, F. Egidi, J. Goings, B. Peng, A. Petrone, T. Henderson, D. Ranasinghe, V. G. Zakrzewski, J. Gao, N. Rega, G. Zheng, W. Liang, M. Hada, M. Ehara, K. Toyota, R. Fukuda, J. Hasegawa, M. Ishida, T. Nakajima, Y. Honda, O. Kitao, H. Nakai, T. Vreven, K. Throssell, J. A. Montgomery Jr., J. E. Peralta, F. Ogliaro, M. J. Bearpark, J. J. Heyd, E. N. Brothers, K. N. Kudin, V. N. Staroverov, T. A. Keith, R. Kobayashi, J. Normand, K. Raghavachari, A. P. Rendell, J. C. Burant, S. S. Iyengar, J. Tomasi, M. Cossi, J. M. Millam, M. Klene, C. Adamo, R. Cammi, J. W. Ochterski, R. L. Martin, K. Morokuma, O. Farkas, J. B. Foresman, and D. J. Fox. *Gaussian 16 Rev. C.01*. Wallingford, CT, 2016.

[109] M. J. Frisch, M. Head-Gordon, and J. A. Pople. "A Direct MP2 Gradient Method". In: *Chemical Physics Letters* 166.3 (Feb. 23, 1990), pp. 275–280. ISSN: 0009-2614. DOI: 10.1016/0009-2614(90)80029-D.

[110] M. J. Frisch, M. Head-Gordon, and J. A. Pople. "Semi-Direct Algorithms for the MP2 Energy and Gradient". In: *Chemical Physics Letters* 166.3 (Feb. 23, 1990), pp. 281–289. ISSN: 0009-2614. DOI: 10.1016/0009-2614(90)80030-H.

[111] M. Head-Gordon, J. A. Pople, and M. J. Frisch. "MP2 Energy Evaluation by Direct Methods". In: *Chemical Physics Letters* 153.6 (Dec. 30, 1988), pp. 503–506. ISSN: 0009-2614. DOI: 10.1016/0009-2614(88)85250-3.

[112] M. Head-Gordon and T. Head-Gordon. "Analytic MP2 Frequencies without Fifth-Order Storage. Theory and Application to Bifurcated Hydrogen Bonds in the Water Hexamer". In: *Chemical Physics Letters* 220.1 (Mar. 25,

1994), pp. 122–128. ISSN: 0009-2614. DOI: 10.1016/0009-2614(94)00116-2.

[113] A. D. Becke. "Density-functional Thermochemistry. III. The Role of Exact Exchange". In: *The Journal of Chemical Physics* 98.7 (Apr. 1, 1993), pp. 5648–5652. ISSN: 0021-9606. DOI: 10.1063/1.464913.

[114] C. Lee, W. Yang, and R. G. Parr. "Development of the Colle-Salvetti Correlation-Energy Formula into a Functional of the Electron Density". In: *Physical Review B* 37.2 (Jan. 15, 1988), pp. 785–789. DOI: 10.1103/PhysRevB.37.785.

[115] C. Puzzarini. "Rotational Spectroscopy Meets Theory". In: *Physical Chemistry Chemical Physics* 15.18 (Apr. 18, 2013), pp. 6595–6607. ISSN: 1463-9084. DOI: 10.1039/C3CP44301A.

[116] C. Puzzarini, J. F. Stanton, and J. Gauss. "Quantum-Chemical Calculation of Spectroscopic Parameters for Rotational Spectroscopy". In: *International Reviews in Physical Chemistry* 29.2 (Apr. 1, 2010), pp. 273–367. ISSN: 0144-235X. DOI: 10.1080/01442351003643401.

[117] H. M. Pickett. "The Fitting and Prediction of Vibration-Rotation Spectra with Spin Interactions". In: *Journal of Molecular Spectroscopy* 148.2 (Aug. 1, 1991), pp. 371–377. ISSN: 0022-2852. DOI: 10.1016/0022-2852(91)90393-O.

[118] H. Hartwig and H. Dreizler. "The Microwave Spectrum of Trans-2, 3-Dimethyloxirane in Torsional Excited States". In: *Zeitschrift für Naturforschung A* 51.8 (1996), pp. 923–932. ISSN: 0932-0784.

[119] N. HANSEN, H. MÄDER, and T. BRUHN. "A Molecular Beam Fourier Transform Microwave Study of 0-Tolunitrile: 14N Nuclear Quadrupole Coupling and Methyl Internal Rotation Effects". In: *Molecular Physics* 97.4 (Aug. 20, 1999), pp. 587–595. ISSN: 0026-8976. DOI: 10.1080/00268979909482857.

[120] S. Kassi, D. Petitprez, and G. Wlodarczak. "Microwave Fourier Transform Spectroscopy of T-Butylchloride and t-Butylbromide Isotopic Species". In: *Journal of Molecular Structure* 517–518 (Feb. 16, 2000), pp. 375–386. ISSN: 0022-2860. DOI: 10.1016/S0022-2860(99)00296-3.

[121] M. Tudorie, L. H. Coudert, T. R. Huet, D. Jegouso, and G. Sedes. "Magnetic Hyperfine Coupling of a Methyl Group Undergoing Internal Rotation: A Case Study of Methyl Formate". In: *The Journal of Chemical Physics* 134.7 (Feb. 18, 2011), p. 074314. ISSN: 0021-9606. DOI: 10.1063/1.3554419.

[122] M. O. Scully and M. S. Zubairy. *Quantum Optics*. Cambridge University Press, 1997. ISBN: 978-0-521-43595-6. URL: https://books.google.fr/books?id=20ISsQCKKmQC.

[123] J. Von Neumann. *Mathematical Foundations of Quantum Mechanics*. Investigations in Physics. Princeton University Press, 1955. ISBN: 978-0-691-08003-1. URL: https://books.google.fr/books?id=lggOnwEACAAJ.

[124] J.-U. Grabow. "Fourier Transform Microwave Spectroscopy Measurement and Instrumentation". In: *Handbook of High-resolution Spectroscopy*. American Cancer Society, 2011. ISBN: 978-0-470-74959-3. DOI: 10.1002/9780470749593.hrs037.

[125] J. C. Mcgurk, T. G. Schmalz, and W. H. Flygare. "A Density Matrix, Bloch Equation Description of Infrared and Microwave Transient Phenomena". In: *Advances in Chemical Physics*. John Wiley & Sons, Ltd, 1974, pp. 1–68. ISBN: 978-0-470-14377-3. DOI: 10.1002/9780470143773.ch1.

[126] D. Schmitz. "Structural Flexibility and Chirality of Polar Molecules Elucidated with Broadband Rotational Spectroscopy". Staats-und Universitätsbibliothek Hamburg Carl von Ossietzky, 2015.

[127] H. Dreizler. "Experiences with Microwave Fourier Transform Spectroscopy of Molecular Gases". In: *Molecular Physics* 59.1 (Sept. 1, 1986), pp. 1–28. ISSN: 0026-8976. DOI: 10.1080/00268978600101881.

[128] S. Kassi. "Développement d'un Spectromètre Micro-Ondes à Transformée de Fourier : Applications Spectroscopiques : Des Molécules Stables Aux Complexes de Van Der Waals". These de doctorat. Lille 1, Jan. 1, 2000. URL: http://www.theses.fr/2000LIL10143.

[129] D. Petitprez. *Spectroscopie à impulsions micro-ondes*. In collab. with Université Lille1 - Sciences et Technologies. 2002.

[130] G. Scoles. *Atomic and Molecular Beam Methods*. Oxford University Press, 1988. ISBN: 978-0-19-504281-8. URL: https://books.google.fr/books?id=vO5AAQAAIAAJ.

[131] E. M. Neeman, J.-R. Avilés-Moreno, and T. R. Huet. "The Quasi-Unchanged Gas-Phase Molecular Structures of the Atmospheric Aerosol Precursor -Pinene and Its Oxidation Product Nopinone". In: *Physical Chemistry Chemical Physics* 19.21 (May 31, 2017), pp. 13819–13827. ISSN: 1463-9084. DOI: 10.1039/C7CP01298E.

[132] G. B. Park and R. W. Field. "Perspective: The First Ten Years of Broadband Chirped Pulse Fourier Transform Microwave Spectroscopy". In: *The Journal of Chemical Physics* 144.20 (May 28, 2016), p. 200901. ISSN: 0021-9606. DOI: 10.1063/1.4952762.

[133] G. G. Brown, B. C. Dian, K. O. Douglass, S. M. Geyer, and B. H. Pate. "The Rotational Spectrum of Epifluorohydrin Measured by Chirped-Pulse Fourier Transform Microwave Spectroscopy". In: *Journal of Molecular Spectroscopy* 238.2 (Aug. 1, 2006), pp. 200–212. ISSN: 0022-2852. DOI: 10.1016/j.jms.2006.05.003.

[134] P. Groner, S. Albert, E. Herbst, F. C. D. Lucia, F. J. Lovas, B. J. Drouin, and J. C. Pearson. "Acetone: Laboratory Assignments and Predictions through 620 GHZ for the Vibrational-Torsional Ground State". In: *The Astrophysical Journal Supplement Series* 142.1 (Sept. 1, 2002), p. 145. ISSN: 0067-0049. DOI: 10.1086/341221.

[135] F. Oldag and D. H. Sutter. "The Rotational Zeeman Effect in Acetone, Its g-Tensor, Its Magnetic Susceptibility Anisotropics and Its Molecular Electric Quadrupole Moment Tensor; A High Resolution Microwave Fourier Transform Study". In: *Zeitschrift für Naturforschung A* 47.3 (Mar. 1, 1992), pp. 527–532. ISSN: 1865-7109. DOI: 10.1515/zna-1992-0315.

[136] R. Peter and H. Dreizler. "Das Mikrowellenspektrum von Aceton Im Torsionsgrundzustand". In: *Zeitschrift für Naturforschung A* 20.2 (Feb. 1, 1965), pp. 301–312. ISSN: 1865-7109. DOI: 10.1515/zna-1965-0224.

[137] J. Lelieveld, T. M. Butler, J. N. Crowley, T. J. Dillon, H. Fischer, L. Ganzeveld, H. Harder, M. G. Lawrence, M. Martinez, D. Taraborrelli, and J. Williams. "Atmospheric Oxidation Capacity Sustained by a Tropical Forest". In: *Nature* 452.7188 (7188 Apr. 2008), pp. 737–740. ISSN: 1476-4687. DOI: 10.1038/nature06870.

[138] D. F. Zhao, M. Kaminski, P. Schlag, H. Fuchs, I.-H. Acir, B. Bohn, R. Häseler, A. Kiendler-Scharr, F. Rohrer, R. Tillmann, M. J. Wang, R. Wegener, J. Wildt, A. Wahner, and T. F. Mentel. "Secondary Organic Aerosol Formation from Hydroxyl Radical Oxidation and Ozonolysis of Monoterpenes". In: *Atmospheric Chemistry and Physics* 15.2 (Jan. 28, 2015), pp. 991–1012. ISSN: 1680-7316. DOI: 10.5194/acp-15-991-2015.

[139] E. Arunan, G. R. Desiraju, R. A. Klein, J. Sadlej, S. Scheiner, I. Alkorta, D. C. Clary, R. H. Crabtree, J. J. Dannenberg, P. Hobza, H. G. Kjaergaard, A. C. Legon, B. Mennucci, and D. J. Nesbitt. "Definition of the hydrogen bond (IUPAC Recommendations 2011)". In: *Pure and Applied Chemistry* 83.8 (July 8, 2011), pp. 1637–1641. ISSN: 1365-3075. DOI: 10.1351/PAC-REC-10-01-02.

[140] P. A. Kollman and L. C. Allen. "Theory of the Hydrogen Bond". In: *Chemical Reviews* 72.3 (June 1, 1972), pp. 283–303. ISSN: 0009-2665. DOI: 10.1021/cr60277a004.

[141] G. R. Desiraju and T. Steiner. *The Weak Hydrogen Bond: In Structural Chemistry and Biology*. Oxford University Press, 2001. ISBN: 978-0-19-850970-7. URL: https://books.google.fr/books?id=aj-pjov8DW0C.

[142] H. Zhao, S. Tang, X. Xu, and L. Du. "Hydrogen Bonding Interaction between Atmospheric Gaseous Amides and Methanol". In: *International Journal of Molecular Sciences* 18.1 (Dec. 30, 2016), p. 4. ISSN: 1422-0067. DOI: 10.3390/ijms18010004. pmid: 28042825.

[143] A. Krin, C. Pérez, P. Pinacho, M. M. Quesada-Moreno, J. J. López-González, J. R. Avilés-Moreno, S. Blanco, J. C. López, and M. Schnell. "Structure Determination, Conformational Flexibility, Internal Dynamics, and Chiral Analysis of Pulegone and Its Complex with Water". In: *Chemistry – A European Journal* 24.3 (Jan. 12, 2018), pp. 721–729. ISSN: 0947-6539. DOI: 10.1002/chem.201704644.

[144] E. M. Neeman, J. R. A. Moreno, and T. R. Huet. "Gas-Phase Hydration of Nopinone: The Interplay between Theoretical Methods and Experiments Unveils the Conformational Landscape". In: *Physical Chemistry Chemical Physics* 23.33 (2021), pp. 18137–18144. DOI: 10.1039/D1CP02717D.

[145] S. I. Murugachandran, J. Tang, I. Peña, D. Loru, and M. E. Sanz. "New Insights into Secondary Organic Aerosol Formation: Water Binding to Limonene". In: *The Journal of Physical Chemistry Letters* 12.3 (Jan. 28, 2021), pp. 1081–1086. DOI: 10.1021/acs.jpclett.0c03574.

[146] N. Yassaa, B. Youcef Meklati, and A. Cecinato. "Evaluation of Monoterpenic Biogenic Volatile Organic Compounds in Ambient Air around Eucalyptus Globulus, Pinus Halepensis and Cedrus Atlantica Trees Growing in Algiers City Area by Chiral and Achiral Capillary Gas Chromatography". In: *Atmospheric Environment* 34.17 (Jan. 1, 2000), pp. 2809–2816. ISSN: 1352-2310. DOI: 10.1016/S1352-2310(99)00436-7.

[147] A. G. McDonald, J. S. Gifford, D. Steward, P. H. Dare, S. Riley, and I. Simpson. "Air Emission from Timber Drying: High Temperature Drying and Re-Drying of CCA Treated Timber". In: *Holz als Roh- und Werkstoff* 62.4 (Aug. 1, 2004), pp. 291–302. ISSN: 1436-736X. DOI: 10.1007/s00107-004-0494-x.

[148] E. M. Neeman and T. R. Huet. "Identification of the Maze in the Conformational Landscape of Fenchol". In: *Physical Chemistry Chemical Physics* 20.38 (2018), pp. 24708–24715. DOI: 10.1039/C8CP04011G.

[149] E. M. Neeman and T. R. Huet. "Conformational Changes in Hydroxyl Functional Groups upon Hydration: The Case Study of Endo Fenchol". In: *Physical Chemistry Chemical Physics* 23.3 (2021), pp. 2179–2185. DOI: 10.1039/D0CP06042A.

[150] R. Boto, F. Peccati, R. Laplaza, C. Quan, A. Carbone, J.-P. Piquemal, Y. Maday, and J. Contreras-García. "NCIPLOT4: A New Step Towards a Fast Quantification of Noncovalent Interactions". In: (Jan. 27, 2020). DOI: 10.26434/chemrxiv.9831536.v2.

[151] J. Contreras-García, E. R. Johnson, S. Keinan, R. Chaudret, J.-P. Piquemal, D. N. Beratan, and W. Yang. "NCIPLOT: A Program for Plotting Noncovalent Interaction Regions". In: *Journal of Chemical Theory and Computation* 7.3 (Mar. 8, 2011), pp. 625–632. ISSN: 1549-9618. DOI: 10.1021/ct100641a.

[152] E. R. Johnson, S. Keinan, P. Mori-Sánchez, J. Contreras-García, A. J. Cohen, and W. Yang. "Revealing Noncovalent Interactions". In: *Journal of the American Chemical Society* 132.18 (May 12, 2010), pp. 6498–6506. ISSN: 0002-7863. DOI: 10.1021/ja100936w.

[153] A. Bondi. "Van Der Waals Volumes and Radii". In: *The Journal of Physical Chemistry* 68.3 (Mar. 1, 1964), pp. 441–451. ISSN: 0022-3654. DOI: 10.1021/j100785a001.

[154] Z. Kisiel, O. Desyatnyk, E. Białkowska-Jaworska, and L. Pszczółkowski. "The Structure and Electric Dipole Moment of Camphor Determined by Rotational Spectroscopy". In: *Physical Chemistry Chemical Physics* 5.5 (2003), pp. 820–826. DOI: 10.1039/B212029A.

[155] C. Pérez, A. Krin, A. L. Steber, J. C. López, Z. Kisiel, and M. Schnell. "Wetting Camphor: Multi-Isotopic Substitution Identifies the Complementary Roles of Hydrogen Bonding and Dispersive Forces". In: *The Journal of Physical Chemistry Letters* 7.1 (Jan. 7, 2016), pp. 154–160. DOI: 10.1021/acs.jpclett.5b02541.

[156] D. Loru, M. A. Bermúdez, and M. E. Sanz. "Structure of Fenchone by Broadband Rotational Spectroscopy". In: *The Journal of Chemical Physics* 145.7 (Aug. 21, 2016), p. 074311. ISSN: 0021-9606. DOI: 10.1063/1.4961018.

[157] M. Chrayteh, E. Burevschi, D. Loru, T. R. Huet, P. Dréan, and M. Eugenia Sanz. "Disentangling the Complex Network of Non-Covalent Interactions in Fenchone Hydrates via Rotational Spectroscopy and Quantum Chemistry". In: *Physical Chemistry Chemical Physics* 23.36 (2021), pp. 20686–20694. DOI: 10.1039/D1CP02995A.

[158] R. Meyer. "Flexible Models for Intramolecular Motion, a Versatile Treatment and Its Application to Glyoxal". In: *Journal of Molecular Spectroscopy* 76.1 (June 15, 1979), pp. 266–300. ISSN: 0022-2852. DOI: 10.1016/0022-2852(79)90230-3.

[159] R. Meyer and W. Caminati. "Quartic Centrifugal Distortion Constants Derived from a Flexible Model for 3-Methylthietan". In: *Journal of Molecular Spectroscopy* 150.1 (Nov. 1, 1991), pp. 229–237. ISSN: 0022-2852. DOI: 10.1016/0022-2852(91)90206-P.

[160] L. Evangelisti and W. Caminati. "Internal Dynamics in Complexes of Water with Organic Molecules. Details of the Internal Motions in Tert -Butylalcohol–Water". In: *Physical Chemistry Chemical Physics* 12.43 (2010), pp. 14433–14441. DOI: 10.1039/C0CP01195A.

[161] M. Juanes, W. Li, L. Spada, L. Evangelisti, A. Lesarri, and W. Caminati. "Internal Dynamics of Cyclohexanol and the Cyclohexanol–Water Adduct". In: *Physical Chemistry Chemical Physics* 21.7 (2019), pp. 3676–3682. DOI: 10.1039/C8CP04455D.

[162] M. Chrayteh, A. Savoia, T. R. Huet, and P. Dréan. "Microhydration of Verbenone: How the Chain of Water Molecules Adapts Its Structure to the Host Molecule". In: *Physical Chemistry Chemical Physics* 22.10 (2020), pp. 5855–5864. DOI: 10.1039/C9CP06678K.

[163] S. Blanco, J. Carlos López, and A. Maris. "Terpenoids: Shape and Non-Covalent Interactions. The Rotational Spectrum of Cis -Verbenol and Its 1:1 Water Complex". In: *Physical Chemistry Chemical Physics* 22.10 (2020), pp. 5729–5734. DOI: 10.1039/D0CP00086H.

[164] J. P. Foster and F. Weinhold. "Natural Hybrid Orbitals". In: *Journal of the American Chemical Society* 102.24 (Nov. 19, 1980), pp. 7211–7218. ISSN: 0002-7863. DOI: 10.1021/ja00544a007.

[165] K. Szalewicz. "Symmetry-Adapted Perturbation Theory of Intermolecular Forces". In: *WIREs Computational Molecular Science* 2.2 (2012), pp. 254–272. ISSN: 1759-0884. DOI: 10.1002/wcms.86.

[166] L. Baptista, R. Pfeifer, E. C. da Silva, and G. Arbilla. "Kinetics and Thermodynamics of Limonene Ozonolysis". In: *The Journal of Physical Chemistry A* 115.40 (Oct. 13, 2011), pp. 10911–10919. ISSN: 1089-5639. DOI: 10.1021/jp205734h.

[167] M. Ehn, J. A. Thornton, E. Kleist, M. Sipilä, H. Junninen, I. Pullinen, M. Springer, F. Rubach, R. Tillmann, B. Lee, F. Lopez-Hilfiker, S. Andres, I.-H. Acir, M. Rissanen, T. Jokinen, S. Schobesberger, J. Kangasluoma, J. Kontkanen, T. Nieminen, T. Kurtén, L. B. Nielsen, S. Jørgensen, H. G. Kjaergaard, M. Canagaratna, M. D. Maso, T. Berndt, T. Petäjä, A. Wahner, V.-M. Kerminen, M. Kulmala, D. R. Worsnop, J. Wildt, and T. F. Mentel. "A Large Source of Low-Volatility Secondary Organic Aerosol". In: *Nature* 506.7489 (7489 Feb. 2014), pp. 476–479. ISSN: 1476-4687. DOI: 10.1038/nature13032.

[168] Y. Gong, Z. Chen, and H. Li. "The Oxidation Regime and SOA Composition in Limonene Ozonolysis: Roles of Different Double Bonds, Radicals, and Water". In: *Atmospheric Chemistry and Physics* 18.20 (Oct. 19, 2018), pp. 15105–15123. ISSN: 1680-7316. DOI: 10.5194/acp-18-15105-2018.

[169] D. Johnson and G. Marston. "The Gas-Phase Ozonolysis of Unsaturated Volatile Organic Compounds in the Troposphere". In: *Chemical Society Reviews* 37.4 (Mar. 25, 2008), pp. 699–716. ISSN: 1460-4744. DOI: 10.1039/B704260B.

[170] S. E. Sbai and B. Farida. "Photochemical Aging and Secondary Organic Aerosols Generated from Limonene in an Oxidation Flow Reactor". In: *Environmental Science and Pollution Research* 26.18 (June 1, 2019), pp. 18411–18420. ISSN: 1614-7499. DOI: 10.1007/s11356-019-05012-5.

[171] A. Calogirou, B. R. Larsen, and D. Kotzias. "Gas-Phase Terpene Oxidation Products: A Review". In: *Atmospheric Environment* 33.9 (Apr. 1, 1999), pp. 1423–1439. ISSN: 1352-2310. DOI: 10.1016/S1352-2310(98)00277-5.

[172] J. Arey, R. Atkinson, and S. M. Aschmann. "Product Study of the Gas-Phase Reactions of Monoterpenes with the OH Radical in the Presence of NO x". In: *Journal of Geophysical Research: Atmospheres* 95.D11 (1990), pp. 18539–18546. ISSN: 2156-2202. DOI: 10.1029/JD095iD11p18539.

[173] P. J. Gallimore, B. M. Mahon, F. P. H. Wragg, S. J. Fuller, C. Giorio, I. Kourtchev, and M. Kalberer. "Multiphase Composition Changes and Reactive Oxygen Species Formation during Limonene Oxidation in the New Cambridge Atmospheric Simulation Chamber (CASC)". In: *Atmospheric Chemistry and Physics* 17.16 (Aug. 22, 2017), pp. 9853–9868. ISSN: 1680-7316. DOI: 10.5194/acp-17-9853-2017.

[174] D. Loru, M. M. Quesada-Moreno, J. R. Avilés-Moreno, N. Jarman, T. R. Huet, J. J. López-González, and M. E. Sanz. "Conformational Flexibility of Limonene Oxide Studied By Microwave Spectroscopy". In: *ChemPhysChem* 18.3 (2017), pp. 274–280. ISSN: 1439-7641. DOI: 10.1002/cphc.201600991.

[175] N. M. Donahue, J. E. Tischuk, B. J. Marquis, and K. E. H. Hartz. "Secondary Organic Aerosol from Limona Ketone : Insights into Terpene Ozonolysis via Synthesis of Key Intermediates". In: *Physical Chemistry Chemical Physics* 9.23 (2007), pp. 2991–2998. DOI: 10.1039/B701333G.

[176] R. S. Ruoff, T. D. Klots, T. Emilsson, and H. S. Gutowsky. "Relaxation of Conformers and Isomers in Seeded Supersonic Jets of Inert Gases". In: *The Journal of Chemical Physics* 93.5 (Sept. 1, 1990), pp. 3142–3150. ISSN: 0021-9606. DOI: 10.1063/1.458848.

[177] P. Groner. "Effective Rotational Hamiltonian for Molecules with Two Periodic Large-Amplitude Motions". In: *The Journal of Chemical Physics* 107.12 (Sept. 22, 1997), pp. 4483–4498. ISSN: 0021-9606. DOI: 10.1063/1.474810.

[178] V. V. Ilyushin, Z. Kisiel, L. Pszczókowski, H. Mäder, and J. T. Hougen. "A New Torsion–Rotation Fitting Program for Molecules with a Sixfold Barrier: Application to the Microwave Spectrum of Toluene". In: *Journal of Molecular Spectroscopy* 259.1 (Jan. 1, 2010), pp. 26–38. ISSN: 0022-2852. DOI: 10.1016/j.jms.2009.10.005.

[179] I. Kleiner. "Asymmetric-Top Molecules Containing One Methyl-like Internal Rotor: Methods and Codes for Fitting and Predicting Spectra". In: *Journal of Molecular Spectroscopy* 260.1 (Mar. 1, 2010), pp. 1–18. ISSN: 0022-2852. DOI: 10.1016/j.jms.2009.12.011.

[180] C. C. LIN and J. D. SWALEN. "Internal Rotation and Microwave Spectroscopy". In: *Reviews of Modern Physics* 31.4 (Oct. 1, 1959), pp. 841–892. DOI: 10.1103/RevModPhys.31.841.

[181] H. M. Pickett, J. C. Pearson, and C. E. Miller. "Use of Euler Series to Fit Spectra with Application to Water". In: *Journal of Molecular Spectroscopy* 233.2 (Oct. 1, 2005), pp. 174–179. ISSN: 0022-2852. DOI: 10.1016/j.jms.2005.06.013.

[182] R. C. Woods. "A General Program for the Calculation of Internal Rotation Splittings in Microwave Spectroscopy". In: *Journal of Molecular Spectroscopy* 21.1 (Jan. 1, 1966), pp. 4–24. ISSN: 0022-2852. DOI: 10.1016/0022-2852(66)90117-2.

[183] R. C. Woods. "A General Program for the Calculation of Internal Rotation Splittings in Microwave Spectroscopy: Part II. The n-Top Problem". In: *Journal of Molecular Spectroscopy* 22.1 (Jan. 1, 1967), pp. 49–59. ISSN: 0022-2852. DOI: 10.1016/0022-2852(67)90147-6.

[184] O. Zakharenko, R. A. Motiyenko, J.-R. Aviles Moreno, A. Jabri, I. Kleiner, and T. R. Huet. "Torsion-Rotation-Vibration Effects in the Ground and First Excited States of Methacrolein, a Major Atmospheric Oxidation Product of Isoprene". In: *The Journal of Chemical Physics* 144.2 (Jan. 14, 2016), p. 024303. ISSN: 0021-9606. DOI: 10.1063/1.4939636.

[185] V. Van, W. Stahl, and H. V. L. Nguyen. "The Structure and Torsional Dynamics of Two Methyl Groups in 2-Acetyl-5-methylfuran as Observed by Microwave Spectroscopy". In: *ChemPhysChem* 17.20 (Oct. 18, 2016), pp. 3223–3228. ISSN: 1439-4235. DOI: 10.1002/cphc.201600757.

[186] S. Bteich, M. Goubet, R. A. Motiyenko, L. Margulès, and T. R. Huet. "Vibrational Dynamic and Spectroscopic Molecular Parameters of Trans-Methylglyoxal, a Gaseous Precursor of Secondary Organic Aerosols". In: *Journal of Molecular Spectroscopy*. Molecular Spectroscopy, Atmospheric Composition and Climate Change 348 (June 1, 2018), pp. 124–129. ISSN: 0022-2852. DOI: 10.1016/j.jms.2017.12.007.

[187] A. Roucou, M. Goubet, I. Kleiner, S. Bteich, and A. Cuisset. "Large Amplitude Torsions in Nitrotoluene Isomers Studied by Rotational Spectroscopy and Quantum Chemistry Calculations". In: *ChemPhysChem* 21.22 (Nov. 17, 2020), pp. 2487–2487. ISSN: 1439-4235. DOI: 10.1002/cphc.202000893.

APPENDIX

A

OBSERVED LINES OF THE COMPLEXES WITH H_2S

A.1 fenchol$\cdots$$H_2S$ complex

Table A.1: *The recorded experimental lines of the fenchol$\cdots H_2S$ complex used in the fit. The difference between predicted and observed frequencies were extracted from the PIFORM formatted output file of SPFIT/SPCAT.*

J	K_a	K_c	J	K'_a	K'_c	Frequency	$\Delta\nu^a$
3	0	3	2	0	2	2755.1185	0.0010
4	0	4	3	0	3	3653.8855	0.0004
4	1	4	3	1	3	3560.1331	−0.0005
5	2	3	4	2	2	4693.7287	−0.0012
5	1	4	4	1	3	4760.1133	−0.0021
6	1	6	5	1	5	5322.1969	0.0006
6	0	6	5	0	5	5409.3682	0.0000
6	2	5	5	2	4	5525.3124	0.0007
6	1	5	5	1	4	5696.9547	0.0041
7	0	7	6	0	6	6270.2349	0.0011
7	1	7	6	1	6	6197.5214	−0.0005
7	1	6	6	1	5	6623.8815	0.0007
7	2	6	6	2	5	6435.1684	0.0000
7	2	5	6	2	4	6633.3928	−0.0002
8	0	8	7	0	7	7125.4661	0.0002
8	1	7	7	1	6	7538.2905	−0.0018

continued on next page

J	K_a	K_c	J	K'_a	K'_c	Frequency	$\Delta\nu^a$
8	1	8	7	1	7	7069.3239	−0.0001
8	2	7	7	2	6	7340.1844	0.0029
8	2	6	7	2	5	7605.8638	−0.0007
9	1	9	8	1	8	7938.0568	0.0008
9	0	9	8	0	8	7978.8205	−0.0012
9	2	7	8	2	6	8573.2939	−0.0010
10	1	10	9	1	9	8804.2585	−0.0015
10	0	10	9	0	9	8832.5050	0.0017
11	1	11	10	1	10	9668.4842	−0.0005
11	0	11	10	0	10	9687.3703	−0.0021
11	2	10	10	2	9	10 022.8814	−0.0015
11	1	10	10	1	9	10 190.1427	−0.0012
11	2	9	10	2	8	10 479.3008	0.0021
12	1	12	11	1	11	10 531.2279	0.0023
12	0	12	11	0	11	10 543.5221	−0.0008
12	1	11	11	1	10	11 046.9143	−0.0014
7	3	5	6	3	4	6494.9286	0.0000
7	3	4	6	3	3	6517.9149	0.0006
8	3	6	7	3	5	7425.0992	−0.0016
8	3	5	7	3	4	7469.5995	−0.0039
7	4	4	6	4	3	6490.7416	−0.0002
7	4	3	6	4	2	6491.5472	−0.0011
8	4	4	7	4	3	7425.4432	−0.0010
8	4	5	7	4	4	7423.2486	0.0018
9	3	7	8	3	6	8353.8626	0.0005
9	4	6	8	4	5	8357.3959	0.0006
10	3	8	9	3	7	9280.1342	0.0002
10	4	7	9	4	6	9292.9756	0.0010
10	1	9	9	1	8	9321.5323	−0.0009
10	4	6	9	4	5	9304.0275	−0.0016
10	3	7	9	3	6	9404.2328	−0.0017
10	2	8	9	2	7	9531.9971	−0.0005
11	3	9	10	3	8	10 202.8627	0.0000
11	4	8	10	4	7	10 229.5622	0.0005
11	4	7	10	4	6	10 251.0814	0.0012
11	3	8	10	3	7	10 386.0615	−0.0015
12	2	11	11	2	10	10 906.2358	0.0005

continued on next page

J	K_a	K_c	J	K'_a	K'_c	Frequency	$\Delta\nu^a$
12	3	10	11	3	9	11 121.0994	−0.0003
12	4	8	11	4	7	11 205.3872	−0.0022
13	2	12	12	2	11	11 784.6293	0.0021

[a] $\Delta\nu = \nu_{obs} - \nu_{calc}$

A.2 fenchone$\cdots H_2S$ complex

Table A.2: *The recorded experimental lines of the two fitted states of fenchone$\cdots H_2S$ complex. The difference between predicted and observed frequencies were extracted from the PIFORM formatted output file of SPFIT/SPCAT.*

J	K_a	K_c	J'	K'_a	K'_c	Frequency	$\Delta\nu^a$ (MHz)
				0^- **state**			
7	1	7	6	1	6	7323.8820	0.0000
7	0	7	6	0	6	7354.1858	−0.0002
8	1	8	7	1	7	8351.8020	0.0002
8	0	8	7	0	7	8369.8945	−0.0001
6	1	6	5	1	5	6292.4562	0.0004
6	0	6	5	0	5	6339.4206	−0.0009
5	1	5	4	1	4	5256.4317	−0.0002
5	0	5	4	0	4	5321.5972	−0.0016
9	1	9	8	1	8	9377.2711	−0.0002
9	0	9	8	0	8	9387.5114	0.0000
10	1	10	9	1	9	10 401.1490	0.0001
10	0	10	9	0	9	10 406.7298	−0.0003
11	1	11	10	1	10	11 424.0495	0.0008
11	0	11	10	0	10	11 427.0073	−0.0003
7	1	6	6	1	5	7749.5147	−0.0003
8	1	7	7	1	6	8790.5792	0.0000
9	1	8	8	1	7	9812.1181	0.0002
6	1	5	5	1	4	6685.1051	0.0002
10	1	9	9	1	8	10 822.4934	−0.0002
3	0	3	2	0	2	3245.8707	−0.0002

continued on next page

J	K_a	K_c	J'	K'_a	K'_c	Frequency	$\Delta\nu^a$ (MHz)
4	1	4	3	1	3	4214.9631	0.0007
4	0	4	3	0	3	4293.0248	−0.0002
4	1	3	3	1	2	4495.9260	−0.0018
5	1	4	4	1	3	5599.0302	0.0008
5	2	3	4	2	2	5591.0824	0.0006
6	2	5	5	2	4	6520.6774	0.0001
6	2	4	5	2	3	6739.0933	0.0000
7	2	6	6	2	5	7586.6829	−0.0001
7	2	5	6	2	4	7880.0942	−0.0002
8	2	7	7	2	6	8644.4487	−0.0008
8	2	6	7	2	5	9007.1152	0.0000
9	2	8	8	2	7	9694.1053	−0.0006
9	2	7	8	2	6	10 115.3723	−0.0001
10	2	9	9	2	8	10 736.3466	0.0000
10	2	8	9	2	7	11 200.8145	0.0000
11	2	10	10	2	9	11 772.3038	0.0007
11	2	9	10	2	8	12 260.4197	−0.0003
6	3	4	5	3	3	6590.5674	0.0005
6	3	3	5	3	2	6625.2549	0.0003
7	3	5	6	3	4	7689.6774	−0.0003
7	3	4	6	3	3	7762.4886	−0.0006
5	3	2	4	3	1	5503.0233	0.0004
5	3	3	4	3	2	5489.4830	0.0013
6	4	3	5	4	2	6588.0523	0.0001
6	4	2	5	4	1	6589.5462	−0.0008
7	4	4	6	4	3	7693.4886	0.0004
7	4	3	6	4	2	7698.3771	0.0007
8	4	5	7	4	4	8800.9929	0.0004
8	4	4	7	4	3	8814.0331	0.0001
9	4	6	8	4	5	9909.5427	0.0002
9	4	5	8	4	4	9939.4171	0.0002
10	4	7	9	4	6	11 017.5503	−0.0003
10	4	6	9	4	5	11 077.9267	−0.0001
10	3	8	9	3	7	10 954.6728	−0.0003
10	3	7	9	3	6	11 240.9766	0.0002
11	3	9	10	3	8	12 026.9381	0.0000
11	3	8	10	3	7	12 393.3812	0.0000

continued on next page

J	K_a	K_c	J'	K'_a	K'_c	Frequency	$\Delta\nu^a$ (MHz)
11	4	8	10	4	7	12 123.0068	−0.0004
11	4	7	10	4	6	12 232.0898	0.0001
12	2	11	11	2	10	12 803.3235	0.0000
12	2	10	11	2	9	13 294.3364	0.0001
12	3	10	11	3	9	13 089.8749	−0.0001
12	3	9	11	3	8	13 527.4262	0.0006
12	4	9	11	4	8	13 223.7340	−0.0004
12	4	8	11	4	7	13 401.0153	0.0005
7	0	7	6	1	6	7283.9094	0.0005
7	1	7	6	0	6	7394.1591	−0.0001
7	1	6	6	2	5	7093.4946	0.0016
7	4	3	6	3	4	10 737.0431	0.0002
7	4	4	6	3	3	10 677.4345	−0.0010
8	0	8	7	1	7	8329.9209	−0.0005
8	1	8	7	0	7	8391.7749	0.0000
8	1	7	7	2	6	8297.3898	0.0006
6	0	6	5	1	5	6222.1784	−0.0002
6	1	6	5	0	5	6409.6989	0.0002
4	1	4	3	0	3	4475.4360	0.0012
5	2	4	4	1	3	6419.4792	0.0002
5	1	4	4	0	4	6489.1203	−0.0026
5	2	3	4	1	3	6686.1001	0.0007
5	2	4	4	1	4	7127.1632	0.0004
4	4	0	3	3	0	7431.3813	−0.0009
4	4	1	3	3	1	7432.0046	−0.0005
5	3	2	4	2	2	7596.4865	0.0007
5	3	3	4	2	3	7700.7328	0.0011
6	2	4	5	1	4	7826.1620	−0.0013
6	3	3	5	2	3	8630.6588	0.0002
6	3	4	5	2	4	8844.4358	0.0028
7	2	5	6	1	5	9021.1541	0.0011
6	4	2	5	3	2	9611.0750	0.0000
6	4	3	5	3	3	9627.3605	0.0002
7	3	4	6	2	4	9654.0539	−0.0005
7	3	5	6	2	5	10 013.4318	−0.0016
8	2	6	7	1	6	10 278.7502	−0.0028
7	4	3	6	3	3	10 684.1973	0.0004

continued on next page

J	K_a	K_c	J'	K'_a	K'_c	Frequency	$\Delta\nu^a$ (MHz)
8	3	5	7	2	5	10 689.1248	−0.0003
7	4	4	6	3	4	10 730.2814	−0.0001
8	3	6	7	2	6	11 211.4278	0.0004
9	3	6	8	2	6	11 760.0440	−0.0006
8	4	5	7	3	5	11 841.5968	0.0006
				0^+ **state**			
10	0	10	9	0	9	10 406.8934	0.0000
11	1	11	10	1	10	11 424.2277	0.0009
11	0	11	10	0	10	11 427.1877	−0.0006
8	1	8	7	1	7	8351.9217	0.0000
10	1	10	9	1	9	10 401.3073	−0.0006
7	1	7	6	1	6	7323.9820	−0.0002
8	0	8	7	0	7	8370.0240	0.0004
7	0	7	6	0	6	7354.2968	−0.0001
6	1	6	5	1	5	6292.5361	−0.0003
6	0	6	5	0	5	6339.5121	0.0000
5	1	5	4	1	4	5256.4948	0.0007
5	0	5	4	0	4	5321.6663	0.0008
5	1	4	4	1	3	5599.0117	−0.0005
6	2	4	5	2	3	6739.0288	0.0001
7	2	6	6	2	5	7586.7176	−0.0010
7	4	4	6	4	3	7693.4640	0.0000
7	4	3	6	4	2	7698.3464	−0.0006
7	3	4	6	3	3	7762.4243	0.0001
7	2	5	6	2	4	7880.0285	0.0009
8	2	7	7	2	6	8644.5002	−0.0023
8	4	4	7	4	3	8813.9894	0.0003
9	1	9	8	1	8	9377.4111	0.0000
9	0	9	8	0	8	9387.6573	−0.0001
9	2	8	8	2	7	9694.1789	0.0000
9	1	8	8	1	7	9812.2164	−0.0002
9	4	6	8	4	5	9909.5059	−0.0013
7	0	7	6	1	6	7283.9836	−0.0001
11	4	8	10	4	7	12 122.9718	0.0005
9	2	7	8	2	6	10 115.3343	0.0001
10	2	8	9	2	7	11 200.8098	0.0003

continued on next page

J	K_a	K_c	J'	K'_a	K'_c	Frequency	$\Delta\nu^a$ (MHz)
11	2	9	10	2	8	12 260.4622	0.0019
6	4	3	5	3	3	9627.4351	0.0000
6	4	2	5	3	2	9611.1620	−0.0004
7	4	4	6	3	4	10 730.3463	0.0008
5	3	2	4	2	2	7596.5650	−0.0014
9	3	6	8	2	6	11 760.0530	0.0012
5	3	3	4	2	3	7700.7656	−0.0002
8	4	5	7	4	4	8800.9611	−0.0011
6	2	4	5	1	4	7826.1152	−0.0006
6	3	4	5	2	4	8844.4419	−0.0009
10	4	7	9	4	6	11 017.5131	0.0000
10	4	6	9	4	5	11 077.8308	−0.0002
10	3	8	9	3	7	10 954.6898	0.0021
8	1	7	7	1	6	8790.6418	−0.0004
7	3	5	6	2	5	10 013.4086	−0.0007
11	3	9	10	3	8	12 026.9706	0.0001
11	3	8	10	3	7	12 393.2605	0.0003
7	4	3	6	3	3	10 684.2956	0.0010
11	4	7	10	4	6	12 231.9536	−0.0026
10	1	9	9	1	8	10 822.6222	0.0009
12	2	10	11	2	9	13 294.4264	−0.0008
12	3	10	11	3	9	13 089.9299	0.0006
12	3	9	11	3	8	13 527.3271	−0.0001
12	4	9	11	4	8	13 223.7034	−0.0017
6	2	5	5	2	4	6520.6982	−0.0007
6	0	6	5	1	5	6222.2243	0.0011
10	2	9	9	2	8	10 736.4421	0.0008
11	2	10	10	2	9	11 772.4213	0.0011
8	3	5	7	2	5	10 689.1933	0.0019
8	2	6	7	1	6	10 278.5544	0.0008
7	2	5	6	1	5	9021.0404	0.0012
7	3	4	6	2	4	9654.1497	0.0018
6	3	3	5	2	3	8630.7496	−0.0026
4	4	1	3	3	1	7432.0893	−0.0023
8	0	8	7	1	7	8330.0255	0.0004
4	4	0	3	3	0	7431.4709	0.0016
6	1	6	5	0	5	6409.8259	0.0005

continued on next page

J	K_a	K_c	J'	K'_a	K'_c	Frequency	$\Delta\nu^a$ (MHz)
7	1	6	6	2	5	7093.3555	−0.0004
7	4	4	6	3	3	10 677.5400	−0.0004
10	2	9	9	1	8	10 965.6264	−0.0001

[a] $\Delta\nu = \nu_{obs} - \nu_{calc}$

APPENDIX

B

OBSERVED LINES OF LIMONA KETONE

Table B.1: *The experimental lines of limona ketone as used in the XIAM fit.*

J	$K+$	$K-$	J'	$K+'$	$K-'$	sym.	obs. (GHz)	$\Delta\nu^a$ (MHz)
3	0	3	2	0	2	A	4.158 627 0	−0.0006
3	K	0	2	K	0	E	4.158 494 3	−0.0007
4	0	4	3	0	3	A	5.535 381 5	0.0002
4	K	0	3	K	0	E	5.535 217 2	−0.0008
5	0	5	4	0	4	A	6.904 209 6	0.0002
5	K	0	4	K	0	E	6.904 023 5	−0.0011
6	0	6	5	0	5	A	8.263 517 0	0.0004
6	K	0	5	K	0	E	8.263 318 3	−0.0006
7	0	7	6	0	6	A	9.612 178 1	0.0012
7	K	0	6	K	0	E	9.611 972 6	0.0003
8	0	8	7	0	7	A	10.949 746 1	0.0007
8	K	0	7	K	0	E	10.949 536 5	0.0015
9	0	9	8	0	8	A	12.276 604 4	−0.0002
9	K	0	8	K	0	E	12.276 381 6	0.0001
10	0	10	9	0	9	A	13.593 957 9	−0.0014
10	K	0	9	K	0	E	13.593 706 5	0.0001
11	0	11	10	0	10	A	14.903 644 3	0.0000
11	K	0	10	K	0	E	14.903 331 7	0.0004
12	0	12	11	0	11	A	16.207 792 9	0.0023
12	K	0	11	K	0	E	16.207 370 2	0.0002
13	0	13	12	0	12	A	17.508 466 8	0.0003

continued on next page

J	$K+$	$K-$	J'	$K+'$	$K-'$	sym.	obs. (GHz)	$\Delta\nu^a$ (MHz)
13	K	0	12	K	0	E	17.507 868 7	0.0000
3	1	2	2	1	1	A	4.288 318 8	0.0041
3	K	1	2	K	1	E	4.287 398 3	0.0098
4	1	3	3	1	2	A	5.715 295 1	−0.0004
4	K	1	3	K	1	E	5.714 761 0	−0.0044
5	1	4	4	1	3	A	7.140 072 6	−0.0008
5	K	1	4	K	1	E	7.139 635 3	−0.0006
6	1	5	5	1	4	A	8.561 974 7	−0.0009
6	K	1	5	K	1	E	8.561 544 0	0.0013
7	1	6	6	1	5	A	9.980 247 2	−0.0003
7	K	1	6	K	1	E	9.979 786 2	−0.0011
8	1	7	7	1	6	A	11.394 039 4	0.0020
8	K	1	7	K	1	E	11.393 537 6	−0.0013
9	1	8	8	1	7	A	12.802 388 1	0.0014
9	K	1	8	K	1	E	12.801 849 4	0.0005
10	1	9	9	1	8	A	14.204 229 4	0.0013
10	K	1	9	K	1	E	14.203 656 0	−0.0004
5	2	3	4	2	2	A	6.980 490 8	−0.0007
5	K	2	4	K	2	E	6.970 892 3	0.0017
6	2	4	5	2	3	A	8.394 364 1	−0.0008
6	K	2	5	K	2	E	8.386 921 5	0.0004
8	2	6	7	2	5	A	11.247 958 6	0.0000
8	K	2	7	K	2	E	11.245 302 5	0.0001
10	2	8	9	2	7	A	14.132 393 5	0.0014
10	K	2	9	K	2	E	14.131 083 0	−0.0042
6	3	3	5	3	2	A	8.345 646 3	−0.0006
6	K	3	5	K	3	E	8.344 516 0	0.0006
8	3	5	7	3	4	A	11.139 893 4	0.0002
8	K	3	7	K	3	E	11.135 907 5	0.0026
4	1	4	3	1	3	A	5.387 941 0	−0.0010
4	K	−1	3	K	−1	E	5.388 215 4	−0.0071
5	1	5	4	1	4	A	6.731 310 7	0.0006
5	K	−1	4	K	−1	E	6.731 439 9	0.0001
6	1	6	5	1	5	A	8.072 435 1	0.0003
6	K	−1	5	K	−1	E	8.072 509 0	0.0011
7	1	7	6	1	6	A	9.411 029 1	0.0003
7	K	−1	6	K	−1	E	9.411 088 2	0.0007

continued on next page

J	$K+$	$K-$	J'	$K+'$	$K-'$	sym.	obs. (GHz)	$\Delta\nu^a$ (MHz)
8	1	8	7	1	7	A	10.746 884 8	0.0005
8	K	−1	7	K	−1	E	10.746 956 1	0.0006
9	1	9	8	1	8	A	12.079 877 3	0.0008
9	K	−1	8	K	−1	E	12.079 983 7	−0.0009
10	1	10	9	1	9	A	13.409 963 9	−0.0008
10	K	−1	9	K	−1	E	13.410 135 6	−0.0015
13	1	13	12	1	12	A	17.383 527 2	−0.0012
13	K	−1	12	K	−1	E	17.384 163 7	−0.0027
5	2	4	4	2	3	A	6.940 088 2	0.0015
5	K	−2	4	K	−2	E	6.949 308 3	−0.0022
6	2	5	5	2	4	A	8.324 363 4	0.0000
6	K	−2	5	K	−2	E	8.331 340 1	−0.0015
8	2	7	7	2	6	A	11.086 489 2	0.0000
8	K	−2	7	K	−2	E	11.088 486 8	−0.0018
6	3	4	5	3	3	A	8.343 874 4	0.0005
6	K	−3	5	K	−3	E	8.344 559 4	−0.0024
7	3	5	6	3	4	A	9.737 445 8	−0.0012
7	K	−3	6	K	−3	E	9.739 146 9	−0.0021
8	3	6	7	3	5	A	11.131 963 3	−0.0025
8	K	−3	7	K	−3	E	11.135 339 6	−0.0029
3	1	3	2	0	2	A	6.387 224 4	0.0026
3	K	−1	2	K	0	E	6.386 148 2	0.0009
4	1	4	3	0	3	A	7.616 538 8	0.0025
4	K	−1	3	K	0	E	7.615 874 9	0.0001
5	1	5	4	0	4	A	8.812 465 1	−0.0001
5	K	−1	4	K	0	E	8.812 094 7	−0.0019
6	1	6	5	0	5	A	9.980 693 8	0.0032
6	K	−1	5	K	0	E	9.980 580 2	0.0002
7	1	7	6	0	6	A	11.128 204 1	0.0013
7	K	−1	6	K	0	E	11.128 353 0	0.0044
8	1	8	7	0	7	A	12.262 912 8	0.0026
8	K	−1	7	K	0	E	12.263 333 7	0.0019
9	1	9	8	0	8	A	13.393 042 6	0.0013
9	K	−1	8	K	0	E	13.393 781 3	−0.0001
10	1	10	9	0	9	A	14.526 402 3	0.0008
10	K	−1	9	K	0	E	14.527 538 1	0.0010
6	0	6	5	1	5	A	6.355 261 1	0.0003

continued on next page

J	$K+$	$K-$	J'	$K+'$	$K-'$	sym.	obs. (GHz)	$\Delta\nu^a$ (MHz)
6	K	0	5	K	−1	E	6.355 240 0	−0.0068
7	0	7	6	1	6	A	7.895 002 3	−0.0006
7	K	0	6	K	−1	E	7.894 708 5	−0.0027
8	0	8	7	1	7	A	9.433 718 1	−0.0014
8	K	0	7	K	−1	E	9.433 157 4	−0.0013
9	0	9	8	1	8	A	10.963 440 2	0.0004
9	K	0	8	K	−1	E	10.962 588 8	0.0042
10	0	10	9	1	9	A	12.477 522 9	0.0004
10	K	0	9	K	−1	E	12.476 305 4	−0.0011
3	2	1	2	1	2	A	11.695 757 3	−0.0020
3	K	2	2	K	−1	E	11.729 993 7	−0.0119
4	2	3	3	1	2	A	12.705 700 6	−0.0086
4	K	−2	3	K	1	E	12.677 264 2	0.0036
4	2	2	3	1	3	A	13.227 495 4	−0.0037
4	K	2	3	K	−1	E	13.253 218 5	0.0064
5	2	4	4	1	3	A	13.930 494 1	−0.0063
5	K	−2	4	K	1	E	13.911 806 8	0.0011
5	2	3	4	1	4	A	14.820 041 4	−0.0072
5	K	2	4	K	−1	E	14.835 885 6	0.0054
6	2	5	5	1	4	A	15.114 783 6	−0.0068
6	K	−2	5	K	1	E	15.103 512 7	0.0013
6	2	4	5	1	5	A	16.483 103 0	−0.0004
6	K	2	5	K	−1	E	16.491 366 1	0.0046
7	2	6	6	1	5	A	16.259 425 4	0.0037
7	K	−2	6	K	1	E	16.252 490 3	−0.0033
7	2	5	6	1	6	A	18.227 488 4	−0.0052
7	K	2	6	K	−1	E	18.231 200 6	−0.0009
8	2	7	7	1	6	A	17.365 666 6	0.0032
8	K	−2	7	K	1	E	17.361 203 3	0.0084
9	2	8	8	1	7	A	18.435 316 6	−0.0003
9	K	−2	8	K	1	E	18.432 331 4	−0.0032
4	1	3	3	0	3	A	8.435 176 2	0.0013
4	K	1	3	K	0	E	8.434 966 8	0.0006
5	1	4	4	0	4	A	10.039 867 3	0.0003
5	K	1	4	K	0	E	10.039 387 9	0.0038
6	1	5	5	0	5	A	11.697 631 8	−0.0014
6	K	1	5	K	0	E	11.696 905 7	0.0034

continued on next page

J	$K+$	$K-$	J'	$K+'$	$K-'$	sym.	obs. (GHz)	$\Delta\nu^a$ (MHz)
7	1	6	6	0	6	A	13.414 364 4	0.0003
7	K	1	6	K	0	E	13.413 372 2	0.0016
8	1	7	7	0	7	A	15.196 224 8	0.0002
8	K	1	7	K	0	E	15.194 937 9	0.0008
3	2	2	2	1	2	A	11.685 564 6	−0.0066
3	K	−2	2	K	−1	E	11.651 616 6	−0.0055
3	2	1	2	1	1	A	11.450 095 5	−0.0052
3	K	2	2	K	1	E	11.481 417 9	−0.0018
4	2	2	3	1	2	A	12.736 216 6	0.0025
4	K	2	3	K	1	E	12.760 659 2	−0.0044
4	2	3	3	1	3	A	13.196 994 6	0.0003
4	K	−2	3	K	−1	E	13.169 814 3	0.0052
5	2	4	4	1	4	A	14.749 133 1	−0.0058
5	K	−2	4	K	−1	E	14.730 905 5	0.0084
5	2	3	4	1	3	A	14.001 403 7	−0.0064
5	K	2	4	K	1	E	14.016 789 0	0.0001
6	2	5	5	1	5	A	16.342 193 3	0.0011
6	K	−2	5	K	−1	E	16.330 807 0	0.0081
6	2	4	5	1	4	A	15.255 698 1	−0.0035
6	K	2	5	K	1	E	15.264 076 0	0.0020
7	2	5	6	1	5	A	16.510 550 5	−0.0004
7	K	2	6	K	1	E	16.514 881 8	0.0026
7	2	6	6	1	6	A	17.976 362 9	−0.0015
7	K	−2	6	K	−1	E	17.968 815 4	−0.0004
8	2	6	7	1	6	A	17.778 261 4	−0.0006
8	K	2	7	K	1	E	17.780 394 1	−0.0002
3	3	0	2	2	0	A	16.492 623 3	0.0012
3	K	3	2	K	2	E	16.510 921 7	−0.0035
3	3	1	2	2	1	A	16.494 634 2	0.0045
3	K	−3	2	K	−2	E	16.472 129 4	0.0021
4	3	1	3	2	1	A	17.877 571 8	0.0047
4	K	3	3	K	2	E	17.899 498 6	−0.0008
4	3	2	3	2	2	A	17.887 536 9	0.0039
4	K	−3	3	K	−2	E	17.861 330 7	0.0022
7	2	5	7	1	6	A	6.530 293 6	−0.0098
7	K	2	7	K	1	E	6.535 094 4	0.0024
4	3	2	4	2	3	A	12.333 424 9	0.0032

continued on next page

J	$K+$	$K-$	J'	$K+'$	$K-'$	sym.	obs. (GHz)	$\Delta\nu^a$ (MHz)
4	K	−3	4	K	−2	E	12.299 719 5	0.0040
4	3	1	4	2	2	A	12.303 142 1	0.0030
4	K	3	4	K	2	E	12.332 861 0	−0.0059
6	3	4	6	2	5	A	12.364 142 3	0.0020
6	K	−3	6	K	−2	E	12.315 088 8	−0.0036
6	3	3	6	2	4	A	12.225 887 5	−0.0026
6	K	3	6	K	2	E	12.270 991 0	−0.0028
6	4	3	6	3	4	A	17.247 953 6	−0.0092
6	K	−4	6	K	−3	E	17.224 465 2	−0.0017
6	4	2	6	3	3	A	17.245 325 6	0.0054
6	K	4	6	K	3	E	17.263 256 3	−0.0004
5	3	3	5	2	4	A	12.344 633 9	0.0042
5	K	−3	5	K	−2	E	12.301 869 4	−0.0028
5	3	2	5	2	3	A	12.274 610 1	0.0020
5	K	3	5	K	2	E	12.313 395 7	−0.0038
7	3	5	7	2	6	A	12.394 985 5	0.0052
7	K	−3	7	K	−2	E	12.343 714 4	−0.0022
7	3	4	7	2	5	A	12.150 499 1	0.0077
7	K	3	7	K	2	E	12.197 843 4	−0.0011
8	3	6	8	2	7	A	12.440 458 4	0.0015
8	K	−3	8	K	−2	E	12.390 568 7	−0.0018
8	3	5	8	2	6	A	12.042 419 6	−0.0064
8	K	3	8	K	2	E	12.088 448 8	0.0018
9	3	7	9	2	8	A	12.504 069 9	0.0055
9	K	−3	9	K	−2	E	12.458 842 3	−0.0015
9	3	6	9	2	7	A	11.897 154 7	−0.0076
9	K	3	9	K	2	E	11.938 574 3	0.0026
10	3	8	10	2	9	A	12.589 392 8	0.0060
10	K	−3	10	K	−2	E	12.551 638 6	−0.0038
10	3	7	10	2	8	A	11.712 572 3	−0.0004
10	K	3	10	K	2	E	11.746 564 8	0.0023
8	2	7	8	1	7	A	5.971 620 8	−0.0052
8	K	−2	8	K	1	E	5.967 662 3	0.0062
6	3	4	6	2	4	A	12.223 233 0	0.0040
6	K	−3	6	K	2	E	12.154 532 6	0.0028
7	3	5	7	2	5	A	12.143 854 9	0.0038
7	K	−3	7	K	2	E	12.081 330 5	−0.0004

continued on next page

J	$K+$	$K-$	J'	$K+'$	$K-'$	sym.	obs. (GHz)	$\Delta\nu^a$ (MHz)
6	3	3	6	2	5	A	12.366 803 0	0.0017
6	K	3	6	K	−2	E	12.431 556 6	0.0002
5	3	3	5	2	3	A	12.273 719 9	−0.0002
5	K	−3	5	K	2	E	12.196 889 0	−0.0001
8	3	6	8	2	6	A	12.027 857 2	−0.0011
8	K	−3	8	K	2	E	11.971 370 1	−0.0009
9	3	7	9	2	7	A	11.868 147 7	0.0038
9	K	−3	9	K	2	E	11.819 045 9	−0.0077

[a] $\Delta\nu = \nu_{obs} - \nu_{calc}$

Spectroscopic characterization of molecules of atmospheric interest: internal dynamics and microsolvation with hydrogen sulfide (H_2S)

Abstract

Biogenic volatile organic compounds (BVOCs), and especially monoterpenes ($C_{10}H_{16}$), are molecules naturally occurring in the atmosphere, which have been linked to the formation of secondary organic aerosol (SOA). They can alter the physical and chemical properties in the atmosphere, have negative effects on human health and contribute to climate change. There exists a strong relationship between the structure of a molecular system and the inter- and intramolecular interactions present on the molecular scale. Hence, having in-depth information about the gas phase structure and internal dynamics of these molecules, or their molecular complexes, is important to better understand their reaction pathways and complexation patterns.

The synergic combination of quantum chemical calculations and Fourier transform microwave (FTMW) spectroscopy has been shown to be a reliable approach to examine the conformational landscape, structure and internal dynamics of several types of molecules of atmospheric interest, their oxidation products and their complexes.

In the framework of this thesis, we have applied this theoretical-experimental approach to characterize the complexes of two monoterpenoids: fenchol ($C_{10}H_{18}O$) and fenchone ($C_{10}H_{16}O$) with another atmospheric contaminant: the H_2S molecule. The gas phase stable conformations were identified in the pure rotational spectrum with the support of *ab initio* and DFT calculations. A comparative analysis of the observed complexes with their water analogues confirmed the presence of weaker hydrogen bonds. On top of that, we observed a large amplitude motion, that was qualitatively described. The stabilizing non-covalent interactions of the two complexes were also evaluated.

In a similar manner, and within the same general context, we also characterized the conformational landscape and methyl internal rotation in the case of limona ketone ($C_9H_{14}O$), which is a BVOCs originating from the oxidation of limonene. The experimental barrier height of the methyl torsion showed some deviation from the calculated values, which pushed towards a more thorough examination, that revealed the presence of an intramolecular interaction.

The second part of this thesis was dedicated to the construction and evaluation of a broadband chirped pulse FTMW spectrometer, operating in the range 6-18 GHz. A detailed technical description of the spectrometer is given herein. Moreover, the preliminary tests performed to evaluate the performance of the spectrometer are reported.

Keywords: rotational spectroscopy, quantum chemical calculations, microsolvation, large amplitude motions, chirped-pulse fourier transform microwave spectrometer

---

Physique des Lasers, Atomes et Molécules (PhLAM) UMR 8523
Bâtiment P5 campus Cité Scientifique – 2 Avenue Jean Perrin – 59655 Villeneuve d'Ascq cedex – France

Caractérisation spectroscopique de molécules d'intérêt atmosphérique : dynamique interne et microsolvatation avec le sulfure d'hydrogène (H_2S)

Résumé

Les composés organiques volatils biogéniques (COVBs), et en particulier les monoterpènes ($C_{10}H_{16}$), sont des molécules naturellement présentes dans l'atmosphère, qui sont liées à la formation d'aérosols organiques secondaires (SOA). Ils peuvent altérer les propriétés physiques et chimiques de l'atmosphère, avoir des effets négatifs sur la santé humaine et contribuer aux changements climatiques. Une forte relation existe entre la structure d'un système moléculaire et les interactions inter- et intramoléculaires présentes à l'échelle moléculaire. Par conséquent, l'accès aux informations sur la structure, en phase gazeuse, et à la dynamique interne pourrait être essentiel pour prédire les voies possibles de réaction ou de la formation de complexes et d'agrégats.

La spectroscopie micro-ondes à transformée de Fourier (FTMW) combinée aux calculs de chimie quantique, est une approche fiable pour étudier le paysage conformationnel, la structure et la dynamique interne de plusieurs types des molécules, et notamment les molécules d'intérêt atmosphérique, leurs produits d'oxydation et leurs complexes associés.

Dans le cadre de cette thèse, nous avons appliqué cette approche théorique-expérimentale pour caractériser les complexes de deux monoterpénoïdes : le fenchol ($C_{10}H_{18}O$) et la fenchone ($C_{10}H_{16}O$) avec un autre contaminant atmosphérique, à savoir le H_2S. Les conformations stables en phase gazeuse ont été identifiées dans le spectre de rotation pure à l'aide des calculs *ab initio* et DFT. Une analyse comparative des complexes observés avec leurs analogues hydratés a confirmé la présence d'une liaison hydrogène plus faible. De plus, nous avons observé un mouvement de grande amplitude, décrit qualitativement. Les interactions non covalentes stabilisantes des deux complexes ont également été évaluées.

De manière similaire, et dans le même contexte général, nous avons également caractérisé le paysage conformationnel et la rotation interne du groupe méthyle dans le cas de la limona cétone ($C_9H_{14}O$), qui est un CVOB issu de l'oxydation du limonène. La hauteur de barrière expérimentale de la torsion du méthyle a montré un certain écart par rapport aux valeurs calculées, ce qui nous a poussé vers une investigation plus approfondie, qui a révélé la présence d'une interaction intramoléculaire.

La deuxième partie de cette thèse a été consacrée à la construction et à l'évaluation d'un nouveau spectromètre FTMW à dérive de fréquence, large bande (6-18 GHz). Une description technique détaillée du spectromètre est donnée dans ce manuscrit. De plus, les tests préliminaires effectués pour évaluer les performances du spectromètre sont rapportés.

Mots clés : spectroscopie rotationnelle, calculs de chimie quantique, microsolvatation, mouvements de grande amplitude, spectromètre par dérive de fréquence à transformée de fourier